Studies on Role of Defects in Structural, Photoluminescent and Photocatalytic Behaviours of ZnS Nanoparticles

Thesis submitted to
the University of Calicut for the award of
the degree of
Doctor of Philosophy in Physics
under the Faculty of Science

by

MUHAMMED JUBEER E

under the guidance of
Prof. P. A. SUBHA

DEPARTMENT OF PHYSICS
FAROOK COLLEGE (AUTONOMOUS)
FAROOK COLLEGE,
KOZHIKODE KERALA - 673632

APRIL 2024

CERTIFICATE

Certified that the work presented in this thesis titled ‘Studies on Role of Defects in Structural, Photoluminescent and Photocatalytic Behaviours of ZnS Nanoparticles’ is a bonafide work done by Mr. Muhammed Jubeer E under my guidance in the Department of Physics, Farook College (Autonomous), University of Calicut and that this work has not been included in any other thesis submitted previously for the award of any degree.

Farook College	**Prof. P. A. Subha**
April 2024	(Supervising Guide)

DECLARATION

I hereby declare that the work presented in this thesis titled 'Studies on Role of Defects in Structural, Photoluminescent and Photocatalytic Behaviours of ZnS Nanoparticles' is based on the original work done by me under the guidance of Prof. P. A. Subha, Department of Physics, Farook College (Autonomous), University of Calicut and has not been included in any other thesis submitted previously for the award of any degree.

Farook College **Muhammed Jubeer E**
April 2024

CERTIFICATE

This is to certify that the thesis titled “Studies on Role of Defects in Structural, Photoluminescent and Photocatalytic Behaviours of ZnS Nanoparticles “has been checked for plagiarism using iTHENTICATE software at CHMK library, University of Calicut and found that the similarity index of the work is within acceptable limits fixed by the University

Farook College
April 2024

Prof. P. A. Subha
(Supervising Guide)

CERTIFICATE

This is to certify that the corrections and suggestions recommended by the adjudicators have been incorporated in the thesis of Mr. Muhammed Jubeer E, research scholar under my supervision and that the contents in the Thesis and the soft copy are one and the same.

Farook College	**Prof. P. A. Subha**
06. September 2024	(Supervising Guide)

ACKNOWLEDGEMENTS

I would like to express my heartfelt gratitude to all those who have supported me throughout the journey of completing my thesis. I am truly grateful for the invaluable guidance and encouragement I received from my guide, Prof. P. A. Subha. Her unwavering support and belief in me were the driving force behind my success. With deep appreciation, I thank Dr. Mohamed Aslam M, Assistant Professor at King Khalid University in Saudi Arabia, for his tremendous support and guidance during this study. His knowledge and assistance were really helpful in making this thesis successful. I am profoundly grateful to Dr. Biju K P, Associate Professor, Government Arts and Science College in Kozhikode, for his great support during my study, which was crucial to ensuring the successful completion of my doctoral thesis.

I want to express my deepest gratitude to Principal, Farook College Dr. K A Ayisha Swapna, as well as former principals Prof. E P Imbichikoya and Dr. K M Naseer, for their continuous support in finishing my PhD journey. I also respect the advice and assistance I received from Professor M. M. Musthafa and Professor Mohamed Shahin Thayyil, Department of Physics, University of Calicut. I would also like to extend my gratitude to the Mr. Midhun Shah, Head, Department of Physics, Farook College and previous heads for providing me with the resources and opportunities necessary to complete my research. Special mention to Dr. Sulfikar Ali, Research Coordinator, Department of Physics, Farook College. I am indebted to all the faculties of Department of Physics, Farook College for their cooperation.

A special remark of gratitude and appreciation is extended to the research scholars and faculty members of the Chemistry department, whose crucial assistance and encouragement made the completion of this thesis possible. My sincere gratitude goes out to the whole faculty and staff of Farook College for their commitment and support during my research career. I would also like to extend my appreciation to my friends Dr. Remi, Amal and Thasneem for their support during difficult times and for sharing their valuable ideas and perspectives.

I am grateful to my family for their emotional support and encouragement through the ups and downs of this journey. This voyage would not have been possible without the loving support of my father, Aboobacker E, my mother Maimoona K and my better half, Dr. Junsina K P. With special gratitude to my kids, Aneeqa Yelda E and Adel Yezen E. Their confidence in me served as a source of support and inspiration.

Finally, I express my sincere gratitude to Rashtriya Uchchatar Shiksha Abhiyan (RUSA) for their financial assistance for the project and to the Department of Science & Technology for their funding via the Fund for Improvement of S&T Infrastructure in Universities and Higher Educational Institutions (FIST), which has been instrumental in supporting my research activities.

The most all, I am grateful to Almighty, the Most Gracious and Merciful, for his kindness and graces in helping me to successfully finish my thesis.

Muhammed Jubeer E

ABSTRACT

This study explores the impact of defects on the structural, photoluminescent, and photocatalytic behaviors of ZnS nanoparticles synthesized by two methods: hydrothermal and microwave-assisted co-precipitation method. The defects are induced by varying stoichiometric ratio and by doping rare earth elements.

In the hydrothermal synthesis method, point defects were introduced by varying the S/Zn molar ratio and doping with Ce, La, and Y. These modifications led to the formation of sulphur vacancies and sulphur dangling bonds, which play a crucial role in enhancing photocatalytic activity under visible light. The sulphur defect states and dangling bonds act as trapping sites for charge carriers, facilitating their separation and prolonging their lifetimes, thereby significantly improving photocatalytic efficiency. Photoluminescence (PL) measurements revealed an emission peak around 470 nm, attributed to these sulphur-related defects, further confirming their presence. However, the PL transitions corresponding to La, Ce, and Y dopants were absent in the hydrothermal samples, likely due to the overlapping of emission from the host material, masking the dopant-related emissions but the luminescence intensity tuning is possible by doping. Additionally, the doping process induced a phase transition from cubic to hexagonal structure, which also contributed to the observed changes in material properties.

In contrast, ZnS nanoparticles synthesized using the microwave-assisted method did not exhibit photocatalytic activity despite their smaller crystallite size. The absence of sulphur-related PL emission peaks in these samples indicates lack of active sulphur defects, which explains their inactivity in photocatalysis. However, the PL spectra showed transitions corresponding to the dopants Er and Pr, reflecting the influence of the synthesis method on the nature and distribution of defects.

This study highlights the importance of synthesis methods and conditions in defect engineering, which enhance the photocatalytic and photoluminescence activity. These findings provide a foundation for optimizing ZnS nanoparticles for targeted applications in photocatalysis and optoelectronics.

സംഗ്രഹം

ഹൈഡ്രോതെർമൽ രീതിയിലും മൈക്രോവേവ് അസിസ്റ്റഡ് കോ-പ്രസിപ്പിറ്റേഷൻ രീതിയിലും സംശ്ലേഷണം ചെയ്ത ZnS നാനോകണികകളുടെ ഘടനാപരവും , ഫോട്ടോല്യൂമിനെസെന്റ്, ഫോട്ടോകാറ്റലിറ്റിക് അനുബന്ധമായ സ്വഭാവങ്ങളെയും ക്രിസ്റ്റൽ ഡിഫക്റ്റുകൾ എങ്ങനെ ബാധിക്കുന്നു എന്നതാണ് ഈ ഗവേഷണം പ്രധാനമായും പഠനവിധേയമാക്കുന്നത്. സ്റ്റോയിക്കിയോമെട്രിക് അനുപാതം വ്യത്യാസപ്പെടുത്തിയും റെയർ എർത്ത് എലെമെന്റ്സ് ഡോപ്പിംഗ് ചെയ്തുമാണ് ZnS നാനോകാണികകളിൽ ക്രിസ്റ്റൽ ഡിഫക്റ്റുകൾ സൃഷ്ടിച്ചത്.

ഹൈഡ്രോതെർമൽ സംശ്ലേഷണ രീതിയിൽ, S/Zn മോളാർ അനുപാതം വ്യത്യാസപ്പെടുത്തിയും Ce, La, Y എന്നിവ ഉപയോഗിച്ച് ഡോപ്പിംഗ് ചെയ്തുമാണ് പോയിന്റ് ഡിഫെക്ടുകൾ നിവേശിപ്പിച്ചത് . ഈ മാറ്റങ്ങൾ സൾഫർ വേക്കൻസികൾക്കും സൾഫർ ഡാൻഗ്ലിങ് ബോണ്ടുകളുടെയും രൂപീകരണത്തിന് ഇടയാക്കി, ഇത് ദൃശ്യ പ്രകാശത്തിൽ ഫോട്ടോകാറ്റലിറ്റിക് പ്രവർത്തനം വർദ്ധിപ്പിക്കുന്നതിൽ നിർണായക പങ്കുവഹിക്കുന്നു. സൾഫർ ഡിഫെക്ടുകളും ഡാൻഗ്ലിങ് ബോണ്ടുകളും ചാർജ് വാഹകാർക്ക് ട്രാപ്പിംഗ് സൈറ്റുകളായി പ്രവർത്തിക്കുന്നു, അവയുടെ വേർതിരിവ് സുഗമമാക്കുകയും അവയുടെ ആയുർദൈർഘ്യം വർദ്ധിപ്പിക്കുകയും ചെയ്യുന്നു, ഇത് ഫോട്ടോകാറ്റലിറ്റിക് ക്ഷമത ഗണ്യമായി മെച്ചപ്പെടുത്തുന്നു. സംശ്ലേഷണം ചെയ്ത ZnS നാനോകണികളെ ഫോട്ടോല്യൂമിനെസെൻസ് (PL) സ്‌പെക്ട്രം ഉപയോഗിച്ച് അപഗ്രഥനം നടത്തിയപ്പോൾ, സൾഫർ സംബന്ധമായ ഡിഫെക്ടുകൾക്ക് കാരണമായ 470 nm ചുറ്റുമുള്ള ഒരു ഉദ്ഗമന ശിഖരം ലഭ്യമായത്, ഈ ഡിഫെക്ടുകളുടെ സാന്നിധ്യം കൂടുതൽ സ്ഥിരീകരിച്ചു. എന്നിരുന്നാലും, La, Ce, Y ഡോപ്പന്റുകൾക്ക് അനുയോജ്യമായ PL പരിവർത്തനങ്ങൾ ഹൈഡ്രോതെർമൽ സാമ്പിളുകളിൽ ലഭ്യമായില്ല , ഹോസ്റ്റ് മെറ്റീരിയലിൽ നിന്നുള്ള ഉദ്ഗമനത്തിന്റെ അതിവ്യാപനം കാരണം, ഡോപ്പന്റ് സംബന്ധമായ ഉദ്ഗമനങ്ങൾ ദൃശ്യമാവുന്നില്ല, എന്നാൽ ഡോപ്പിംഗ് ചെയ്യുന്നതിലൂടെ ല്യൂമിനെസെൻസ് തീവ്രത ക്രമീകരിക്കുവാൻ കഴിയും. കൂടാതെ, ഡോപ്പിംഗ് പ്രക്രിയ ക്യൂബിക്കിൽ നിന്നും ഹെക്സഗണൽ ഘടനയിലേക്കുള്ള ഘടനാപരമായ പരിവർത്തനത്തിന് കാരണമായി, ഇത് മെറ്റീരിയൽ ഗുണങ്ങളിലെ മാറ്റങ്ങൾക്കും കാരണമാതായി നിരീക്ഷിക്കപെട്ടു.

മറുവശത്ത്, മൈക്രോവേവ് അസിസ്റ്റഡ് രീതി ഉപയോഗിച്ച് സംശ്ലേഷണം ചെയ്ത ZnS നാനോകണികങ്ങൾക്ക് അവയുടെ ചെറിയ ക്രിസ്റ്റലൈറ്റ് വലിപ്പം ഉണ്ടായിട്ടും ഫോട്ടോകാറ്റലിറ്റിക് പ്രവർത്തനം കാണിച്ചില്ല. ഈ സാമ്പിളുകളിൽ സൾഫർ സംബന്ധമായ PL ഉദ്ഗമന ശിഖരങ്ങളുടെ അഭാവം സജീവമായ സൾഫർ ഡിഫക്റ്റുകളുടെ അഭാവത്തെ സൂചിപ്പിക്കുന്നു, ഇത് ഫോട്ടോകാറ്റലിസിസിൽ അവരുടെ നിഷ്ക്രിയത വിശദീകരിക്കുന്നു. എന്നിരുന്നാലും, PL സ്‌പെക്ട്രം Er, Pr ഡോപ്പന്റുകൾക്ക്

അനുയോജ്യമായ പരിവർത്തനങ്ങൾ കാണിച്ചത് ഡിഫക്റ്റുകളുടെ സ്വഭാവത്തിലും വിതരണത്തിലും സംശ്ലേഷണ രീതിയുടെ സ്വാധീനത്തെ പ്രതിഫലിപ്പിക്കുന്നു.

ഈ പഠനം ഡിഫെക്റ്റ് എഞ്ചിനീയറിംഗിൽ സംശ്ലേഷണ രീതികളുടെയും അവയുടെ സാഹചര്യങ്ങളുടെയും പ്രാധാന്യം അടിവരയിടുന്നു. ഇത് ഫോട്ടോകാറ്റലിറ്റിക്, ഫോട്ടോല്യൂമിനെസെൻസ് പ്രവർത്തനം വർദ്ധിപ്പിക്കുന്നു. ഈ കണ്ടെത്തലുകൾ, ഫോട്ടോകാറ്റലിസിസ്, ഒപ്റ്റോഇലക്ട്രോണിക്സ് എന്നീ മേഖലകളിൽ ZnS നാനോകണികങ്ങൾ ഓപ്റ്റിമൈസ് ചെയ്യേണ്ടതിന്റെ പ്രാധാന്യം വെളിവാക്കുന്നു.

PREFACE

Zinc sulphide (ZnS) nanoparticles have attracted a lot of attention in nanotechnology due to their distinctive features and prospective uses in a variety of industries. The research of ZnS nanoparticles and their photoluminescence behaviour has yielded useful information on their optical characteristics and possible applications in optoelectronic devices. ZnS nanoparticles have also demonstrated significant possibilities in the breakdown of organic contaminants through their photocatalytic activity, which makes them a viable option for water and environmental clean-up.

Water shortage is a significant global concern that affects millions of people. Water purification technologies need to be sustainable and efficient in order to meet the growing demand for safe and clean drinking water. In the area of water purification, semiconductors have shown great promise, especially when used as photocatalysts. These materials, such as zinc sulphide (ZnS) nanoparticles, have the potential to transform solar energy into chemical energy, which is then used to degrade organic contaminants and purify water. The photocatalytic characteristics of semiconductors may be used to effectively remove hazardous impurities from water, providing a cost-effective and ecologically friendly solution to water scarcity.

Photoluminescence is important in optoelectronic applications because it generates and manipulates light. It is a phenomenon in which a substance generates longer-wavelength light after absorbing photons. This characteristic is extremely useful in a variety of optoelectronic devices, including light-emitting diodes (LEDs), lasers, solar cells and sensors. LEDs emit light efficiently and brightly by using photoluminescence to transform electrical energy into light. In lasers, it permits light amplification via stimulated emission, resulting in a coherent and powerful beam. Photoluminescence helps solar cells by facilitating the effective conversion of sunlight into electrical energy. Furthermore, photoluminescence is important in sensors because it allows for the detection and measurement of light, which facilitates applications in imaging, spectroscopy and optical communication.

The present work focuses on the introduction of defects into ZnS nanoparticles and the resulting modifications in optical, structural and photocatalytic properties. To introduce point defects, vary the stoichiometric ratio of ZnS and use rare earth elements as external dopants. Two distinct synthesising techniques were employed in this method 1) Hydrothermal technique and 2) microwave-assisted co-precipitation method. The first work of this thesis uses a low-temperature hydrothermal method to synthesise ZnS nanoparticles with various S/Zn molar ratios. Zn and S defects are introduced into the ZnS crystal using defect engineering, which modifies the band structure of the material. Size strain graphs, Raman analysis and XRD are used to investigate how crystal defects affect the structural properties of the nanoparticles. The S/Zn molar concentration is shown to have an impact on the band gap of the nanoparticles. The fourth chapter focuses on the easy and efficient way to synthesise quantum dots-like ZnS nanoparticles using the microwave-assisted synthesis method at various CTAB concentrations. FT-Raman spectroscopy and X-ray diffraction confirm the formation of ultra-low-dimensional monophasic ZnS nanoparticles. The synthesised ZnS nanoparticles are appropriate for optoelectronic devices because of their tiny dimension, high energy gap, high dielectric constant and low loss values.

In Chapter 5, point defects created by Er doping on ZnS nanoparticles are discussed using a cost-effective microwave-assisted co-precipitation method. The structural, morphological, optical, dielectric and photoluminescent properties of the produced samples were investigated using a variety of characterisation techniques. In contrast to ZnS NP synthesised by hydrothermal technique, ZnS NP with point defects created by Er doping does not exhibit photocatalytic activity.

The main topic of Chapter 6 is the doping of ZnS nanoparticles with Pr to introduce point defects. The XRD pattern, the FESEM, Raman spectrum and the HRTEM investigation all support the development of the nanoparticles in the cubic phase. Photoluminescent emission peaks corresponding to Pr^{3+} transitions are studied using PL spectra. The energy gap values were measured by the Kubelka-Munk technique for the samples. Due to their low dimension, high energy gap, high dielectric constant and low loss values, the synthesised NPs are suitable for optoelectronic devices. Pr doped ZnS nanoparticles also not showing photocatalytic activity either in visible or in UV region.

Chapter 7 focuses on the synthesis using the hydrothermal method and introduction of point defects by La doping. XRD and Raman spectroscopy studied the phase transition during doping. Morphological studies were done using SEM and TEM, whereas the presence of necessary elements is verified by EDAX. The visible light photocatalytic studies of samples were also studied. The amount of point defects introduced has modified the PC activities of ZnS samples. While there are no dopant-specific transitions in the PL spectra, the host material can still affect the overall luminescence of nanoparticles. The results provide insight into potential uses of La-doped ZnS nanoparticles in optoelectronics and other fields, including water purification.

In Chapter 8, point defects are introduced by Ce doping and the synthesis is carried out by the hydrothermal method. The phase change during doping was investigated using XRD and Raman spectroscopy. Both TEM and SEM techniques were used for morphological investigations and EDAX confirms the existence of required elements. The photocatalytic investigations of samples under visible light were also examined. The PC activities of ZnS samples are modified by the amount of point defects added. The total luminescence of nanoparticles can be influenced by the host material even when the PL spectra do not show any dopant-specific transitions. The results give insight into the possible application of Ce doped ZnS nanoparticles in optoelectronics and other domains, including water purification.

In Chapter 9, Y-doped ZnS nanoparticles were synthesised utilising the hydrothermal technique. XRD and Raman spectroscopy were utilised to evaluate the phase shift caused by Y doping. The existence of the necessary elements was verified by EDAX and morphological investigations were carried out using TEM and SEM. The quantity of additional point defects altered the photocatalytic activity of the ZnS samples doped with Y. Even in the absence of dopant-specific transitions in the PL spectra, the host material can affect the overall luminescence of the nanoparticles. The possible uses of Y-doped ZnS nanoparticles in optoelectronics and water purification are affected by these discoveries.

CONTENTS

ZnS Nanoparticles by microwave-assisted method: Point Defects through Pr doping

ZnS Nanoparticles by Hydrothermal Synthesis: Point Defects through Y doping

Summary and Recommendations

LIST OF FIGURES

LIST OF TABLES

ABBREVIATIONS

W-H Method	:	Williamson-Hall method
UDM	:	Unified Deformation Model
UDSM	:	Uniform Deformation Stress Model
UDEDM	:	Uniform Deformation Energy Density Model
SSP	:	Size-Strain Plot
FWHM	:	Full Width Half Maxima
NP	:	Nanoparticles
NM	:	Nanomaterials
SAED	:	Selected area electron diffraction
TO	:	Transverse Optical
LO	:	Longitudinal Optical
LA	:	Longitudinal Acoustic
Ce-ZnS	:	Cerium doped Zinc sulphide

LIST OF PAPERS PUBLISHED/COMMUNICATED

1. **Jubeer, E. M**. *et al.* Optik Microwave assisted synthesis of quantum dots like ZnS nanoparticles for optoelectronic applications: An effect of CTAB concentrations. *Optik (Stuttg).* 240, 166812 (2021).
2. **E. M. Jubeer**., Manthrammel, M. A., Subha, P. A., Shkir, M. & Alfaify, S. A. Microwave-assisted synthesis of praseodymium (Pr) doped ZnS QDs such as nanoparticles for optoelectronic applications. *Luminescence* (2023)
3. **Jubeer, E. M**. *et al.* Defect engineering for enhanced optical and photocatalytic properties of ZnS nanoparticles synthesized by hydrothermal method. *Sci. Rep.* **13**, 16820 (2023).
4. **Jubeer, E. M. *et al***. Er-doped ZnS QDs like NPs for optoelectronic applications: a facile microwave-assisted synthesis. *J. Mater. Sci. Mater. Electron.* **35**, 1317 (2024).
5. **Jubeer, E. M. *et al.*** Enhancement of luminescent and photocatalytic performance of hydrothermally synthesized ZnS NPs using Ce as defect regulator. *Phys. Scr.* **99**, 075964 (2024).
6. **Jubeer, E. M**. *et al.* Synthesis and Characterization of Lanthanum-Doped ZnS Nanoparticles by Hydrothermal Method: Enhanced Properties and Photocatalytic Potential**.** (Communicated)
7. **Jubeer, E. M**. *et al.* Energy-saving synthesis of wurtzite ZnS Nanoparticles using Yttrium as a defect regulator by Hydrothermal method. *Radiat. Phys. Chem.* 112154 (2024).

LIST OF CONFERENCE PRESNTATIONS

1. **Muhammed Jubeer E “**An effect of CTAB concentrations on Microwave assisted synthesis of ZnS nanoparticles”. Sri Ramakrishna college of arts & science, Coimbatore (ICAMAC 2023), Feb 2023
2. **Muhammed Jubeer E et al. “**A Comparative study on tuning the luminescence of ZnS using La, Ce and Y as defect regulators”. International conference on Advanced materials for emerging technologies (ICAMET 23), Netaji Subhas University of Technology, New Delhi, May 2023
3. **Muhammed Jubeer E et al. “**Structural and Optical Properties of Y-Doped ZnS Nanoparticles ", International Conference on Advanced Materials for Sustainability, ICAMS 2023, University of Calicut, December 2023
4. **Muhammed Jubeer E et al. “**Zinc Sulphide Nanoparticles with Tuned Properties for Advanced Photocatalysis in Water Purification”, International conference on advances in interdisciplinary nanoscience (ICAINS-24), Govt. College for women, Thiruvananthapuram, Jan 2024
5. **Muhammed Jubeer E et al** “Structural and Optical Properties of Ce-Doped ZnS nanoparticles”, National conference on Functional materials and applications (NCFMA-24), CUSAT, JAN 2024

Chapter 1

Introduction and Thesis Outline

This chapter covers the fundamentals of nanoscience, the properties of nanomaterials, their various types, the factors that influence their properties, the uses of nanoparticles, defect engineering and a brief overview of the research literature on Zinc sulphide and rare earth elements. The chapter also covers the significance and primary goals of the thesis.

1.1 Introduction

1.1.1 Nanomaterials

Nanotechnology or nanoscience is the branches of research in which the researchers manipulating matter at the molecular or atomic level to achieve material with significantly improved physical and chemical properties. Now a days nanomaterial has great interest, because at the nano regime surface effects and quantization begin to make remarkable change in the measured properties of semi - conductor nanomaterials. Semiconducting nanomaterials have a number of applications in daily life. Materials with dimension 1-100 nm at least in one dimension are normally considered as nanoparticles [1] [2] [3]. These nanomaterials have applications in the development of devices and macroscopic research[4]. Based on the shape, Nanostructures can be classified into Two-Dimensional, One-Dimensional, Zero Dimensional. There is large number applications which could be realised reducing the existing size of the structures in to nanometer size[5].

This study intends to shed light on the fundamental mechanisms that govern the behaviour of ZnS nanomaterials, enabling a better knowledge and opening the way to exploiting their full potential in a variety of applications.

1.1.1.1 Properties of Nanomaterials

Nanomaterials have exceptional characteristics that set them apart from their bulk counterparts. The increasing surface-to-volume ratio at the nanoscale causes dramatic quantum confinement effects, resulting in unique electrical, optical and magnetic characteristics. These size-dependent features have attracted enormous attention and resulted in ground-breaking nanotechnology research.

(i) **Optical Properties**: When compared with bulk materials, the optical characteristics of nanoparticles may differ significantly [6]. The optical properties of nanomaterials can be modified by changing size, shape and surface behaviour and those materials can be make use for various applications [7]. There are different techniques for achieving this modification depending on the arrangement, sizes and orientation. The optical properties of nanomaterials are mainly governed by their electronic structure[8]. Due to their unique optical characteristics, nanomaterials are vital components in sensors, imaging systems and photovoltaic systems.[9].

(ii) **Electronic Properties**: The electronic properties of nanomaterials are unique due to their small size and high surface to volume ratio. Nanomaterials with desired conductivity and band gap can be developed by changing the size[10], shape[11] and composition of nanoparticles[12]. Highly-conductive nanomaterials are employed in electronics [13] and energy storage devices [14] due to their high charge carrier mobility and surface area [15]. The behaviour and arrangement of electrons within an atom or molecule describes the electronic properties of that material.[16]. Quantum confinement causes distinct energy levels in nanomaterials, altering their electronic structure. This impact has resulted in the creation of nano electrical devices with unrivalled performance[17]**.**

(iii) **Mechanical Properties**: Nanomaterials have high mechanical strength and flexibility, making them suitable for reinforcing applications in composites and lightweight materials[18]. Materials have better mechanical properties as their size decreases. From a thermodynamic perspective, crystal defects are extremely energetic and should be removed from ideal crystal structures. Such reduction of defects is made possible by small size. Furthermore, temperature gradients and other inhomogeneities during the synthesis and processing of bulk materials can lead to stresses that result in imperfections like dislocations[18]. In nanomaterials, these stresses and imperfections are unlikely to arise.

(iv) **Chemical Reactivity**: Owing to their large surface area and unsaturated surface bonding, nanomaterials are good catalysts for a variety of chemical processes[19]. Smaller nanocrystals with larger surface areas have larger reaction regions, whereas smaller ones have smaller diffusion barriers[20]. These unique nanoscale phenomena permit numerous chemical reactions to occur at mild conditions, which is not conceivable for bulk materials and are beneficial to chemical change in kinetics.

(v) **Electrical Properties**: Electrical properties include characteristics like resistance and conductivity. Similar to optical or magnetic characteristics, these properties have been seen to change at the nanoscale[21]. The electrical properties of nanoparticles are mainly associated with the mobility of charge carriers. Both the quantum-size effect and the quantum confinement effect are inevitable when a material's dimensions are lowered to the nanoscale range. Certain voltage can lead some conductive metal nanoparticles to become nonconductive due to the quantization of electron energy[11]. In many applications, such as electronics, energy storage and sensing, the electrical characteristics of nanoparticles are essential.

(vi) **Magnetic Properties:** Large surface area to volume ratios in magnetic materials result in a wide range of magnetic properties. Non-magnetic materials can become magnetic at the nanoscale. Magnetic materials are classified based on how they respond to an external magnetic field. Materials are categorised as diamagnetic, paramagnetic, ferromagnetic, antiferromagnetic, or ferrimagnetic based on the direction of the magnetic moments. At the nanoscale, a single particle may be considered as a single magnetic domain. In nanoscale, the magnetic behaviour is demonstrated by a nanoparticle that has a high concentration of atoms of a certain element [22][23]. This domain structure has size-dependent magnetic properties. The size of magnetic domains inside magnetic nanoparticles can also be influenced by other variables, including super exchange forces and particle shape. Researchers have shown that coercivity increases to a maximum when particle size lowers and then drops again, leading to zero[24].

1.1.1.2 Different Types of Nanomaterials

The chemical composition, size and shape of nanomaterials all have a significant effect on their characteristics. This thesis concentrates on nanoparticles and Quantum dots.

(i) **Nanoparticles**: Nano-sized particles composed of metals, metal oxides, or organic compounds[25]. They are used in medicine delivery, catalysis and environmental cleanup. The SEM image of nanowires is shown Figure 1.1a.

(ii) **Nanowires and Nanotubes**: One-dimensional nanomaterials having distinct electrical and mechanical characteristics that are useful in nanoelectronics and nanocomposites[26]. Figure 1.1b shows the 3-D illustration of carbon nanotube.

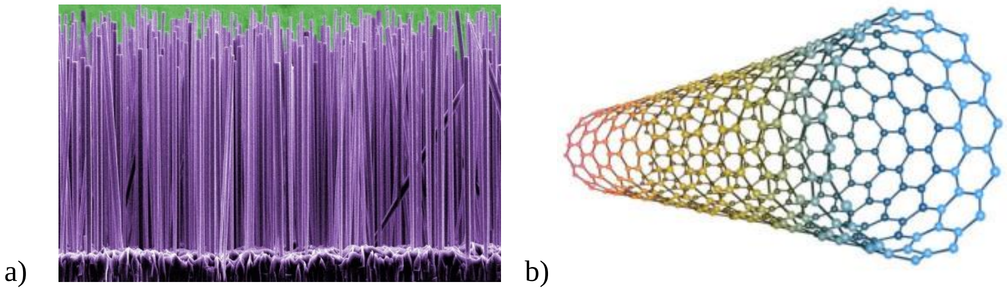

Figure 1.1- a) Nano wires [27] b) Nano tubes [28]

(iii) **Nanocomposites**: Nanomaterials combined with bulk materials to form hybrid structures with customised characteristics[29].

(iv) **Quantum Dots**: Quantum dots are zero-dimensional advanced materials[30]. Quantum dots are promising due to their nanoscale size and ability to be customised for specific applications such as computers[31], electro-optical devices[32] and nonlinear optical devices[33] . Semiconductor nano crystals with programmable bandgaps used in displays and biological imaging[34].

(v) **Nanostructured Thin Films**: Thin films having nano-scale shapes that provide improved mechanical and electrical qualities for advanced coatings and electronic devices[35]. The AFM image of thin film is shown in Figure 1.2.

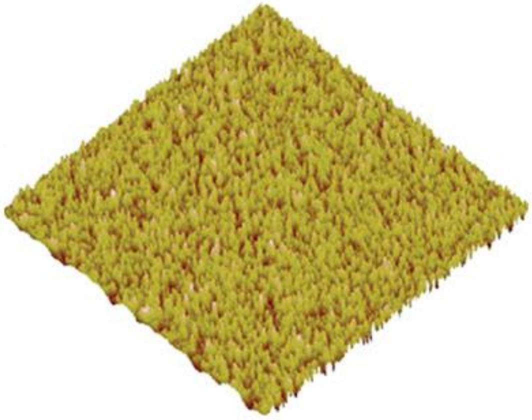

Figure 1.2 AFM image of thin Film [36]

1.1.1.3 Factors Affecting Properties of Nanomaterials

Understanding as well as controlling the characteristics of nanomaterials is critical for their use in real-world applications. Several factors have an impact on their behaviour:

(i) **Dimensionality and Size**: The size of nanomaterials has a direct impact on their characteristics due to quantum confinement effects. Furthermore, their behaviour is dictated by their dimensionality 0D, 1D, 2D, or 3D (as shown in the Figure 1.3) , with distinct applications originating from each kind[37].

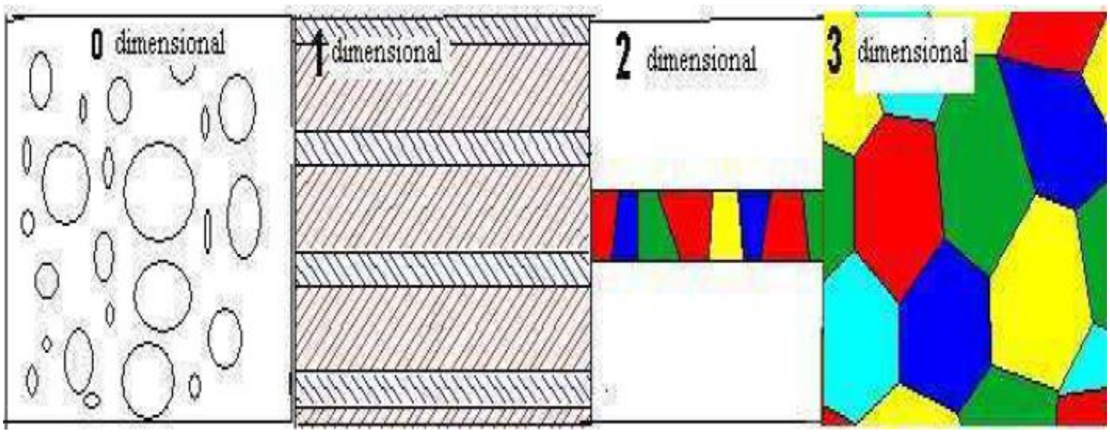

Figure 1.3 Dimensionality of nanoparticles

(ii) **Surface Chemistry**: The surface of nanomaterials influences their reactivity, stability and interactions with their surroundings[38].

(iii) **Crystal Structure:** The arrangements of the atoms in the crystal lattice of nanomaterials has great influence on their optical, electrical and mechanical properties [39].

(iv) **Surface Area**: Higher surface area in nanomaterials gives more active interactions which cause for the greater reactivity and performance which make them suitable for various applications[40].

(v) **Synthesis Methods**: The method used for the synthesis of nanomaterials has important effect on the shape, size and composition of nanomaterials, which modify the characteristics of nanomaterials [41].

(vi) **Physical parameters**: The properties of nanomaterials are influenced by external variables such as humidity, temperature and the exposure to various radiations [42].

The development of nanotechnology and research in nanomaterials offer advancements in technology and solutions for various global issues like energy crisis and water shortage. Analysis of different properties of nanomaterials, studies on various types of nanomaterials and identifying the factors affecting the properties of materials are the essential steps towards reaching their full potential. This study has immense possibilities to contribute to the arena of nanoscience which provides innovations that have the potentials to change our world.

1.2 Applications of Nanoparticles:

Owing to the enhanced physical and chemical properties nanomaterials are used in many industries like electronics, batteries, fuel cells, medicine and food processing. Few applications are listed

1.2.1 Fuel Cell

A fuel cell is a device that convert chemical energy to electricity from fuel and oxidant [43]. A fuel cell consists of two electrodes and electrolyte which enables the movement of hydrogen ions but not the electron [44]. The nanomaterials can be used in the fabrication of electrodes with high electrochemical properties and for developing electrolyte which has enhanced hydrogen ion mobility.

1.2.2 Catalysis

Nanoparticles have applications in many chemical reactions as a catalyst. Owing to their large surface area, nanomaterials have large number of active centres compared to bulk materials[45]. Nanoparticles such as ZnO [46] and TiO_2 [47] have application as photocatalyst, in which the catalyst drive chemical process by absorbing solar energy. Noble metal nanoparticles, such as those of platinum (Pt)[48] and palladium (Pd) [49], have outstanding catalytic activity in the field of electrocatalysis for fuel cell processes. In pharmaceutical synthesis, nanoparticles have been utilised as catalysts for a range of organic reactions and materials like iron nanoparticles are used to breakdown pollutants in water and soil [50][51]. It is possible to modify the size, shape, compositionand surface characteristics of nanoparticles to alter their catalytic ability

1.2.3 Electronics and Optoelectronics:

Nanoparticles have various applications in electronics [52] and optoelectronics[53], making them a suitable topic to develop new products and technology. Nanoparticles have been used in electronics for many different applications due to their high conductivity [54] and adjustable band gaps, which enable the fabrication of high-performance transistors [55], sensors[56] and memory devices[57], Nanoparticles have shown great potential for application in optoelectronics [53], including light-emitting diodes (LEDs)[58], solar cells [59] and photodetectors[60], because of their tunable optical properties and effective light-absorbing and emitting characteristics.

1.2.4 Medical and Healthcare:

Nanoparticles have great interest in various medical and health care applications. It shows the importance of research in this field for improving diagnostics and treatment solutions. Magnetic resonance imaging and fluorescence imaging. Magnetic resonance imaging (MRI) [61] and fluorescence imaging [62] are two diagnostic technologies that use nanoparticles to imaging for diagnosing diseases such as cancer. The use of nanoparticles for the drug delivery system are also studied [63], because it offers precise and regulated delivery of medicines to the infected body parts, which minimise the side effects and enhance the treatment effectiveness. Additionally, nanoparticles have shown possibilities in the field of regenerative medicine[64], where tissue regeneration and repair may be enhanced by their unique properties and interactions with biological systems.

1.2.5 Environmental Pollution Management

Nanoparticles have shown important advantages in the area of environmental cleaning due to their distinctive characteristics and high reactivity [65]. Nanoparticles have been used to remove a variety of pollutants from soil and water such as pathogens[66], heavy metals[67] and organic and inorganic contaminants. The small size and high surface area of nanoparticles increase the interaction with pollutants, which improves the degradation of pollutants[68]. Nanoparticles can be modified with specific coatings or chemicals to target certain pollutant and to increase their effectiveness and selectivity[69]. The use of nanoparticles for the purpose of environmental remediation in the polluted areas helps the preservation and protection of human health and ecosystems.

1.2.6 Surface modifications and Surface Coatings

Nanomaterials are widely used for surface modifications[70] and coatings[71]. The use of nanomaterials improvs the hardness[72], corrosion resistance[73] and scratch resistance[74] of coatings. They can enhance the coating adherence, durability[75] and strength[76] of surfaces. Nanomaterial coatings provide self-cleaning, anti-fouling[77] and anti-microbial qualities [78]. Modifying surfaces with nanoparticles can also produce superhydrophobic[79] or super hydrophilic[80] surfaces with enhanced optical properties. In general, there are several ways of using nanoparticles in coatings and surface modifications to enhance the efficiency and effectiveness of various materials and surfaces.

1.2.7. Sensing and Detection

The applications of nanomaterials for sensing[81] and detection purpose[82] strengthen the biosensing and analytical chemistry sectors. They are ideal for the design of highly sensitive and selective sensing systems due to their unique characteristics, which include adjustable optical and electrical properties[83]. In Chemical sensing, the integration of nanoparticles with specific receptors[84] or ligands[85] helps to detect the minute amounts of poisons[86], pollutants[87] and chemicals[82]. Nanoparticles have been used widely in the biosensing sector to identify infections[88], illnesses[89] and biomarkers[90].

1.2.8. Food and Agriculture

Nanoparticles have several uses in agriculture and food science [91], including food safety, packaging and productivity in agriculture [92][93][94]. Nanoparticles can be used in food safety to detect and remove pollutants like pesticides and hence diseases[95], ensuring the safety and quality of food items[96]. Nanoparticles also be used to improve the quality of food packaging materials [97] to increase the shelf life of perishable foods. Conventional fertilisers can enhance plant nutrition more efficiently and lessen the negative impacts on the environment by using nanoparticles as nano fertilizers[98]. Nanoparticles can also be used to regulate the distribution of pesticides and herbicides, reducing their use and decreasing the probability contaminating the environment.[99].

1.3 Defect Engineering

Defect engineering has developed as a powerful tool in materials science and engineering for altering material properties for specific applications [100]. Defects, which are imperfections in the crystal lattice of materials, can have a significant effect on the electrical characteristics and structural characteristics [101]. Researchers can improve numerous material qualities such as mechanical strength[102], optical activity[103] and catalytic activity[104] by purposefully introducing and manipulating defects, leading to the development of new materials with customised characteristics. This introduction covers defect engineering, different types of defects techniques for creating defects and the influence of defects on various material characteristics. Table 1.1 contains a few reported literatures on defect engineering and improved applications for comparison.

1.3.1 Defects in Materials:

Crystalline materials have a periodic arrangement of atoms in their lattice, however pure crystals are rare in practice due to the existence of imperfections. Point defects, line defects (also known as dislocations), planar defects (such as grain boundaries and interfaces) and Volume defects are the four primary types of defects depending on their dimensions.

a) Point Defects

Point defects develop by the displacement of one or more atoms from their ideal lattice locations. Vacancies (missing atoms), interstitials (additional atoms) and impurities (substitutional or interstitial atoms of other elements) are common forms of point defects[105]. Point defects have a significant impact on material qualities such as mechanical strength[102], thermal conductivity[106] and electrical conductivity[107]. Figure 1.4 shows the point defects in a 2D hexagonal lattice.

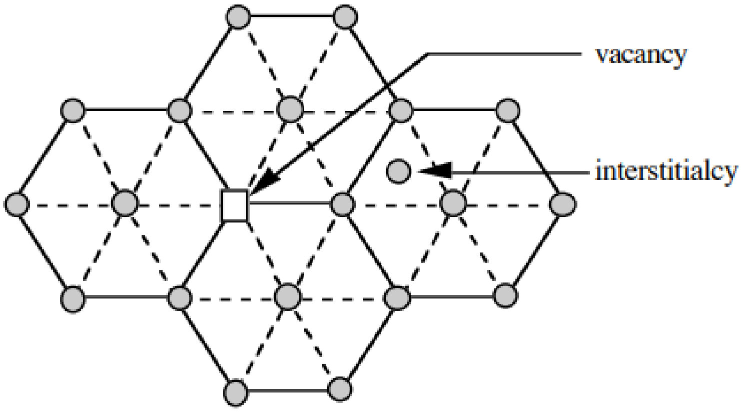

Figure 1.4- Image of an interstitial and vacancy in a two-dimensional hexagonal lattice

b) Line Defects

Line defects are one-dimensional defects in the crystal lattice caused by atom misalignment in certain crystallographic orientations[108]. They are classed as either edge dislocations or screw dislocations[109]. Edge dislocations form when an additional half-plane of atoms is added into the crystal lattice, resulting in a step-like structure. Screw dislocations, on the other hand, feature a spiral-like lattice structural deformation[110]. Dislocations have a major impact on material mechanical characteristics, impacting metrics like as hardness, ductility and yield strength.

c) Planar Defects

Planar defects are two-dimensional atom arrangement irregularities such as grain boundaries in polycrystalline materials or interfaces in heterostructures. These boundaries can happen during crystal growth, as a result of deformation, or as a result of recrystallization[111]. Tilt boundaries, twist boundaries and grain boundary junctions are all examples of planar defects with different structures. Electrical conductivity[112], corrosion resistance[113] and thermal stability[114] are all affected by planar defects.

d) Volume Defects

Three-dimensional atom-or vacancy-based aggregates are known as volume defects in crystals. Voids are the most prevalent kind of volume defect. The origin of voids (also known as pores) can be attributed to either vacancy condensation in the solid state or gases trapped during solidification[115]. These are often undesirable defects. Their main impact is to reduce mechanical strength and increase fracture risk under low loads. The various defects in the crystals are depicted in the Figure 1.5

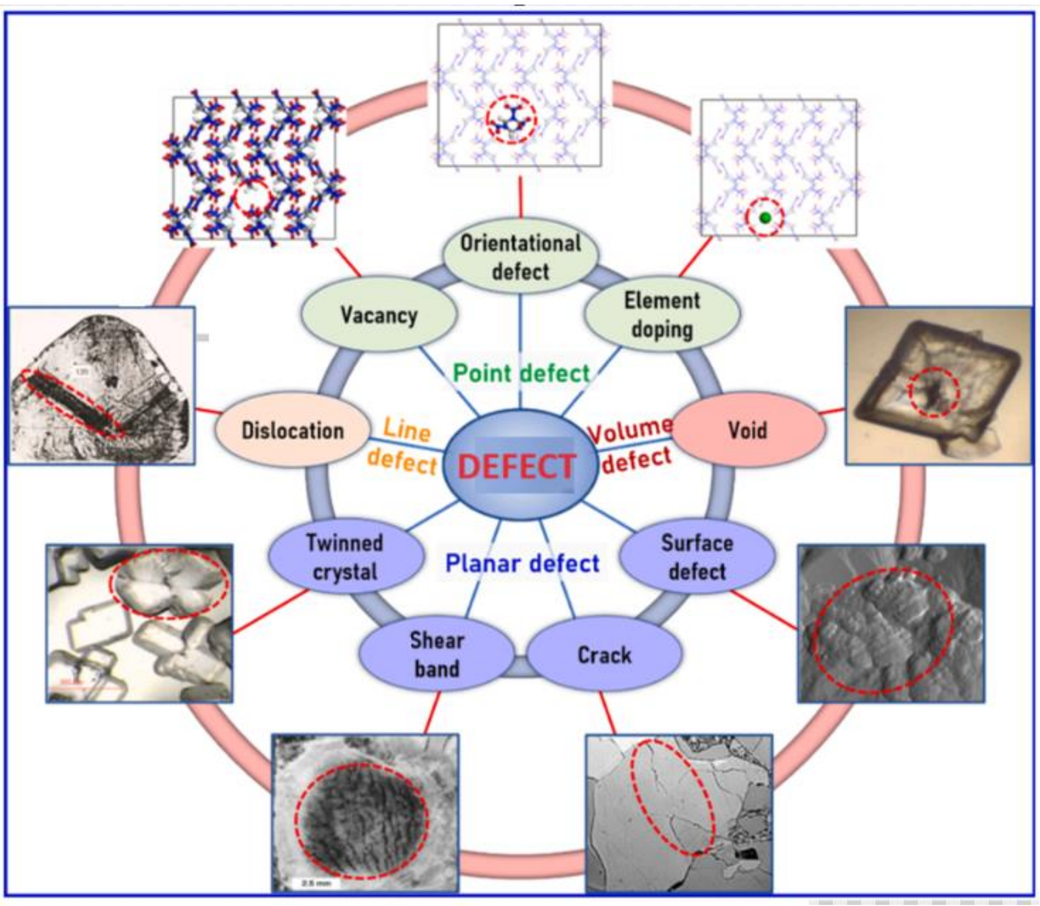

Figure 1.5 Diagrammatic representation of various defects[116]

1.3.2 Methods to Create Defects:

Defects in materials can be created and managed using a variety of methods.

(i) **Ion Implantation**: Ion implantation is a commonly employed technique for introducing controlled defects in materials[117]. Accelerated high energy ions are used for the introduction of point defects and displacements[118]. The depth and concentration of the defect may be precisely controlled by ion implantation.

(ii) **Radiation**: The high energy radiation exposure, such as X-rays or gamma rays, can result in defects in materials [119]. This approach is helpful for researching how radiation-induced defects affect materials used in nuclear and space applications.

(iii) **Mechanical Deformation**: The dislocations and other defects in the materials can be introduced by applying mechanical stress, which affect the hardness and ductility[120] of the material. Methods like plastic deformation[121] and cold working[122] can be used for this.

(iv) **Annealing and Quenching**: Creation and annihilation of defects can be achieved by controlled heating and cooling processes, which regulate the concentration and distribution of defects. Two widely used techniques for controlling defects in metals and alloys are annealing[123] and quenching[124].

(v) **Changing the Concentration of Precursors**: By changing the concentration of precursors and using various stochiometric ratio during material synthesis, one can effectively customise the population of defects[125]. This method is especially relevant to the synthesis of nanomaterials, as defect generation is greatly influenced by high surface-to-volume ratios and quantum confinement effects.

(vi) **Doping**: Doping is the process of adding impurity atoms to a material during synthesis in order to modify its characteristics and produce point defects[126]. One common and adaptable technique for defect engineering is doping, which is the intentional incorporation of impurity atoms into a crystal structure of material. The introduction of energy levels into the bandgap of host materials by the dopant atoms alters the properties of the materials.

(vii) Substitutional Doping: It involves the replacement of host atoms by a foreign element, which produce point defects and affect the thermal stability, optical absorption[127] and electrical conductivity of the material[128]. This method is commonly used in semiconductors to alter their electronic behaviour.[129].

Table 1.1 Delineation of several synthesis techniques for defect creation and applications

Material	**Synthesis Method**	**Defect Created**	**Enhanced Properties**	**Applications**	**References**
ZnS	Chemical Method	S Vacancy, Zn Vacancy	Green and Orange Luminescence	Photoelectrical applications	[130]
ZnS	Hydrothermal Method	Zn Vacancy	charge separation and the electrons transfer are more efficient	Visible Photocatalytic hydrogen evolution	[131]
ZnS	Modified Hydrothermal Method	S Vacancy	photosensitization	Visible light photocatalysis	[132]
ZnS	One Pot Hydrothermal method	S Vacancy, Zn Vacancy	charge separation efficiency	Visible light photocatalysis	[133]
BiOBr	Hydrothermal method	O Vacancy	Enhanced Charge Separation	Photocatalytic N Fixation	[134]
TiO_2	Hydrothermal & photo-assisted reduction	Doped With Transition Metals	electron-hole recombination time	Photocatalytic activity	[135]
FeOOH/rGO composites	Hummer's method	O Vacancy	photogenerated electron-hole separation	photo-Fenton-like catalysts	[136]
MoS_2	Hydrothermal	S Vacancy	Increasing the active sites	Electro Catalytic	[137]
$BaSO_4$	Precipitation method	Ba Vacancy	Improved Adsorption	Photocatalytic removal of NO	[138][139]
ZnCdS/ZnS	Solvothermal Method	Zn Vacancy	Visible light Absorption	Visible Photocatalytic hydrogen evolution	[140]
g-C_3N_4	Hydrothermal	N Vacancy	Visible light Absorption	Visible light photocatalysis	[141]
ZrO_2	Chemical Method	O Vacancy	alteration of electronic structure	photocatalytic activity	[142]

(viii) Interstitial Doping: This process adds dopant atoms to lattice interstitial locations, producing more point defects and changing the characteristics of the material. Materials with better mechanical[143] or catalytic activity[144] can be engineered through the application of interstitial doping.

(ix) Heterostructure Formation: Heterostructures are formed by combining several materials with unique characteristics by doping. Defects in the interfaces allow heterostructures to show improved electronic features, such adjustable bandgaps and greater carrier mobility.

(x) Defect Passivation: Doping can be used to neutralise or passivate certain imperfections, lessening the detrimental effects they have on the performance of the material[145]. This method is frequently applied to increase material stability and boost semiconductor device efficiency.

1.4 Zinc Sulphide

Owing to the distinct properties of II-VI nanostructures they are the potential candidates for the optoelectronic and electronic applications[146].Zinc Sulphide (ZnS)is very old semiconductor having wide varieties of physical and chemical properties. Commonly ZnS has two different allotropes Zinc blend and Wurtzite structure[5] [147] as shown in the Figure 1.6 with a band gap of 3.72eV-3.77eV[148].

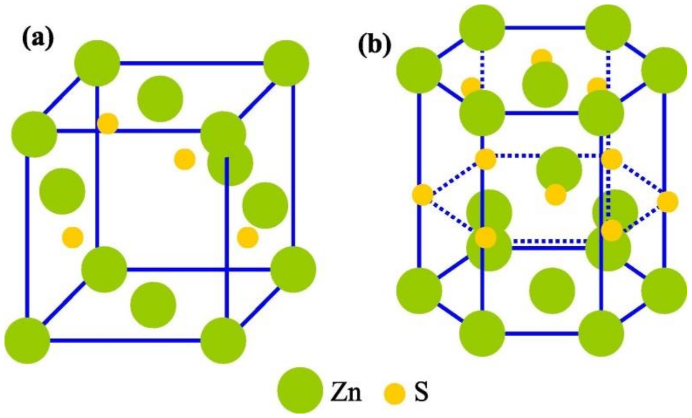

Figure 1.6- Crystalline structure of ZnS a) Cubic b) Hexagonal[149]

Nano ZnS possess enhanced surface volume ratio ,good optical absorption ,high chemical activity, more thermal resistance and low melting point[150] . Different methods have been developed for the synthesis of ZnS nanoparticles. Few research groups successfully synthesized ZnS nanoparticles by chemical co-precipitation method[151]. Hydrothermal method is another way of formation of ZnS nanoparticles [2]. ZnS nanoparticles can also be synthesized using microwave assisted method which takes less time for synthesis. The kinetic enhancement, low reaction temperature and control of aggregation process and hence the control on overall particle size are the advantages of this method[152]. ZnS have applications in optoelectronics[153][154], Field emitters[155], photoluminescence, electroluminance[156]. ZnS nanomaterials can be used as electrocatalyst[157], owing to the high luminescence property of ZnS nanomaterials, they have applications as biosensors[158]. ZnS has application in the construction of photodetectors[159]. ZnS NMs have potential application as photocatalyst[160][161][162][163].

1.5 Rare earth Elements

Rare Earth Elements (REEs) are a group of 17 chemical elements found in the crust of the Earth. They are widely used in a variety of industries and have become known for their unique characteristics[164]. Cerium (Ce), dysprosium (Dy), Erbium (Er), Lanthanum (La), Praseodymium (Pr) and Yttrium (Y) are a few of the common Rare Earth Elements. Because of their electron configurations, they have comparable chemical characteristics that make them difficult to separate and purify[165]. They are very reactive and have high melting points, particularly when divided finely. Strong magnetic properties make rare earth elements valuable in manufacture of magnets for various kinds of applications[166]. They have outstanding luminous properties and are used in the manufacturing of phosphors for lighting and display applications[167]. Rare Earth Elements are additionally noted for their catalytic characteristics, making them useful in a variety of chemical processes[168]. Their great light absorption and emission capabilities and high refractive indices make them stand out in the optical world.

1.5.1 Effect of Rare Earth Elements Doping on Nanoparticles:

Doping Rare Earth Elements in nanoparticles have the ability to modify their characteristics and enhance their performance in a range of applications[169]. Doping can modify structural[170][171], optical[172], magnetic[173] and catalytic properties of nanoparticles[169], making it useful for a specific purpose. Improved luminescence is a property of Rare Earth Elements -doped nanoparticles that makes them suitable for use in optoelectronic devices[174] and sensors[175][176][177][178]. Additionally, doping can strengthen magnetic properties of nanoparticles, which makes them appropriate for use in biomedical[173] and magnetic storage applications[179]. The distinct electrical and surface characteristics of Rare Earth Elements -doped nanoparticles make them effective catalysts for a range of chemical processes.

Erbium (Er) is a rare earth element that finds application in laser and fibre optic communications due to its strong luminescence[180]. Due to its dual ferromagnetic and paramagnetic characteristics, the rare earth element praseodymium (Pr) is crucial for magnetic alloys and materials[181]. Cerium (Ce) is a versatile rare earth element utilised as a dopant in phosphors[182], in catalytic converters[183] and in glass polishing. The rare earth element yttrium (Y) is employed in the synthesis of magnetic[184], sensors[185], phosphors and ceramic stabilisers. The rare earth element lanthanum (La) is utilised as a catalyst in the refining of petroleum[186] as well as in the manufacture of camera lenses[187] and batteries for hybrid vehicles[188]. The band gap energy, PL spectra, crystallite size, already reported for pure ZnS and rare earth metals doped ZnS from literature are listed in the Table 1.2, Table 1.3 and Table 1.4 respectively.

Table 1.2 The band gap energy already reported for rare earth metals doped ZnS from literature

Doped ZnS Nano particles	Zn^{2+}	S^{2-}	Preparation methods	Band Gap(eV)	References
ZnS	$ZnCl_2$	CH_4N_2S	Hydrothermal	3.25	[189]
ZnS	$Zn(CH_3COO)_2$	CH_4N_2S	Solid-state	3.66	[190]
ZnS	$Zn(CH_3COO)_2$	Na_2S	Hydrothermal	3.99	[191]
ZnS:Er	$Zn(NO_3)_2$	Na_2S	Co-Precipitation	3.56	[192]
ZnS:Er	$Zn(CH_3COO)_2$	Na_2S	Co-Precipitation	3.45	[193]
ZnS:La	$Zn(CH_3COO)_2$	CH_4N_2S	Co-Precipitation	4.2(0.5% La)	[194]
ZnS:La	$ZnSO_4$	Na_2S	Co-Precipitation	3.4 (5% La)	[195]
ZnS:Y	$Zn(NO_3)_2$	Na_2S	Co-Precipitation	4.09	[196]

Table 1.3 The PL spectra reported for different rare earth elements doped ZnS

Doped ZnS Nano particles	**Excitation wave length (nm)**	**Emission Wave length (nm)**	**Transitions**	**Nature of the Peak**	**References**
ZnS	255	445	Zinc related defects	Broad	[191]
ZnS	410	486	Emission from Zn vacancy	Narrow	[197]
		530	Emission from S vacancy	Broad	
ZnS	325	407	Emission from S vacancy	Hump like	[190]
ZnS:Pr	325	430	Emission from S vacancy	Broad	[198]
		460,480& 495	Pr-related complexes	Narrow	
ZnS:Eu	325	518	shallow defect state to t2 state of Cu	Broad (Blue-Yellow)	[199]
ZnS:Eu	397	591	$^5D_0 \rightarrow {}^7F_1$ of Eu	Narrow	[200]
		616	$^5D_0 \rightarrow {}^7F_2$ of Eu		
		700	$^5D_0 \rightarrow {}^7F_4$ of Eu		
ZnS:Er	305	400	Emission from S vaccancy	Broad	[201]
ZnS:La	335	414	Trapping of holes at S Vaccancy	Narrow	[195]
		440	S Defects	Narrow	
		506	Elemental sulphur species on the surface of host	Broad	
		570	localized d levels of La2+ ions		
ZnS:Y	325	363	5d→4f transitions in Y^{3+}	8.1(4.09 eV)	[196]
		469			
		601			

Table 1.4 The crystallite size for rare earth metals doped ZnS from literature

Doped ZnS Nano particles	Zn^{2+}	S^{2-}	Preparation methods	Size(nm)	References
ZnS	$ZnCl_2$	CH_4N_2S	Hydrothermal	12.4	[189]
ZnS	$Zn(CH_3COO)_2$	CH_4N_2S	Solid-state	3.7	[190]
ZnS	$Zn(CH_3COO)_2$	Na_2S	Hydrothermal	7	[191]
ZnS:Pr	$ZnSO_4.6H_2O$	S	Hydrothermal	20	[202]
ZnS:Pr	$Zn(NO_3)_2$	Na_2S	Wet Chemical	4	[198]
ZnS:Eu	$Zn(CH_3COO)_2$	Na_2S9H_2O	Precipitation	5	[203]
ZnS:Eu	$Zn(CH_3COO)_2$	TAA	Solid-state	4	[200]
ZnS:Eu	$ZnCl_2$	Na_2S	Precipitation	40	[204]
ZnS:Er	$Zn(NO_3)_2$	Na_2S	Co-Precipitation	4.8	[192]
ZnS:Er	$ZnCl_2$	Na_2S	Chemical Capping	3	[205]
ZnS:Er	$Zn(CH_3COO)_2$	Na_2S	Hydrothermal	10	[201]
ZnS:La	$Zn(CH_3COO)_2$	CH_4N_2S	Co-Precipitation	4	[194]
ZnS:La	$ZnSO_4$	Na_2S	Co-Precipitation	7.6	[195]
ZnS:Y	$Zn(NO_3)_2$	Na_2S	Co-Precipitation	8.1	[196]
ZnS:Tb	$Zn(CH_3COO)_2$	TAA	Co-Precipitation	2.4	[206]

1.6 Thesis outline

This work illustrates role of defects in structural, photoluminescent and photocatalytic behaviours of ZnS nanoparticles. ZnS NP are synthesised using two distinct synthesis methods which are hydrothermal method and microwave-assisted co-precipitation method. The defects are incorporated in to the ZnS crystal lattice by varying stochiometric ratio and by doping rare earth elements which are Er, Pr, La, Ce and Y. This thesis consists of 10 chapters. First chapter gives a general introduction and thesis outline. Synthesis methods and characterisation techniques are discussed in chapter 2.

The Chapter 3 of the thesis uses a low-temperature hydrothermal method to synthesise ZnS nanoparticles and S/Zn molar ratios vary to introduce defects, which modifies the band structure of the material. Size strain graphs, Raman analysis and XRD are used to analyse the modification of crystal defects in the structural properties of the nanoparticles. The morphological studies conducted by TEM and SEM. The S/Zn molar ratios are experimentally verified by ICP-OES and the surface area measurements are done using BET analysis. The impact of defects on Photocatalytic and luminescent properties are also discussed.

The fourth chapter focuses on synthesise of the quantum dots-like ZnS nanoparticles using the microwave-assisted synthesis method at various CTAB concentrations. FT-Raman spectroscopy and X-ray diffraction confirm the formation of low-dimensional monophasic ZnS nanoparticles. The morphological studies are done using SEM analysis. The Optical and Dielectric properties are also studied.

In Chapter 5, point defects created by Er doping on ZnS nanoparticles are discussed using a cost-effective microwave-assisted co-precipitation method. The structural, morphological, optical, dielectric and photoluminescent properties of the samples were investigated. In contrast to ZnS NP synthesised by hydrothermal technique, ZnS NP with point defects created by Er doping does not exhibit photocatalytic activity.

ZnS nanoparticles are synthesised using microwave-assisted co-precipitation method and the defects are introduced by Pr doping in Chapter 6. The XRD pattern, the SEM, Raman spectrum and the TEM investigation all support the development of the nanoparticles in the cubic phase. Photoluminescent emission peaks corresponding to Pr^{3+} transitions are studied using PL spectra. The energy gap values are measured by the Kubelka-Munk technique for the samples. Pr doped ZnS nanoparticles also not showing photocatalytic activity either in visible or in UV region.

Though ZnS NP synthesised using microwave-assisted co-precipitation method doped with Er and Pr are low in dimension, they are not photocatalytically active. In next three chapters we have used hydrothermal method for the synthesis.

Chapter 7 focuses on the synthesis of La doped ZnS using the hydrothermal method. XRD and Raman spectroscopy studied the phase transition during doping. Morphological studies were done using SEM and TEM, whereas EDAX verifies the presence of necessary elements. The visible light photocatalytic behaviour of samples is also studied. The PL spectra, of the samples also analysed.

In Chapter 8, point defects are introduced by Ce doping and the synthesis is carried out by the hydrothermal method. The phase change during doping was investigated using XRD and Raman spectroscopy. Both TEM and SEM techniques were used for morphological investigations and EDAX confirms the existence of required elements. The photocatalytic investigations of samples under visible light were also examined. The Photoluminescence spectra of nanoparticles are analysed.

In Chapter 9, Y-doped ZnS nanoparticles were synthesised utilising the hydrothermal technique. XRD and Raman spectroscopy were utilised to evaluate the phase shift caused by Y doping. The existence of the necessary elements was verified by EDAX and morphological investigations were carried out using TEM and SEM. Point defects altered the photocatalytic activity and photoluminescence of the ZnS samples doped with Y are studied.

The ZnS nanoparticles synthesised using microwave assisted method is suitable for optoelectronic applications, while the ZnS nanoparticles synthesised using hydrothermal method is prominent for making Optoelectronic devices and for water purification

The findings of the thesis and recommendations are presented in chapter 10.

Chapter 2

Synthesis Methods and Characterization Techniques

The chapter covers various synthesis methods that researchers commonly used for achieving doping. The chapter also addresses the advantages of using the hydrothermal route and the microwave-assisted approach over other common techniques. This chapter provides extensive details on several characterization methods and photocatalytic activity measurement.

2.1 Synthesis Methods

The interdisciplinary area of nanomaterials research focuses on developing materials with nanoscale dimensions, which generally span from 1 to 100 nanometres. When compared to their bulk counterparts, these materials display different characteristics and behaviours that make them extremely desirable for a variety of applications[207]. Nanomaterial production is a challenging procedure that demands careful control over a number of factors in order to attain the necessary properties.

There are several methods for the synthesis of nanomaterials. The bottom-up method[208], in which nanoparticles are formed by the assembly of atomic building blocks known as molecules, these methods are common for synthesising nanoparticles. Chemical or biological processes are regulating the development of nanomaterials in this method. Sol-gel synthesis[209], chemical vapour deposition[210] and self-assembly procedures are a few examples of bottom-up synthesis techniques. Through bottom-up synthesis, the characteristics of nanomaterials, such as size, shape, composition and surface chemistry, may be precisely controlled[208], hence bottom-up synthesis are commonly used for the synthesis of complex nanostructures such as nanoparticles, nanowires and nanocomposites with specific features.

The top-down method is an alternative strategy for synthesising nanomaterials[211]. It involves applying physical or mechanical methods to reduce bulk materials to nanoscale dimensions, including milling[212], lithography[213] and etching[214]. This method can be used for the designing and structuring of nanomaterials, making it appropriate for manufacturing nanodevices[215] and nanostructures with specified morphologies. The semiconductor industry frequently uses this method to fabricate integrated circuits and nanoscale electronic components[216]. Top-down and Bottom-up synthesis of nanoparticles is shown schematically in Figure 2.1.

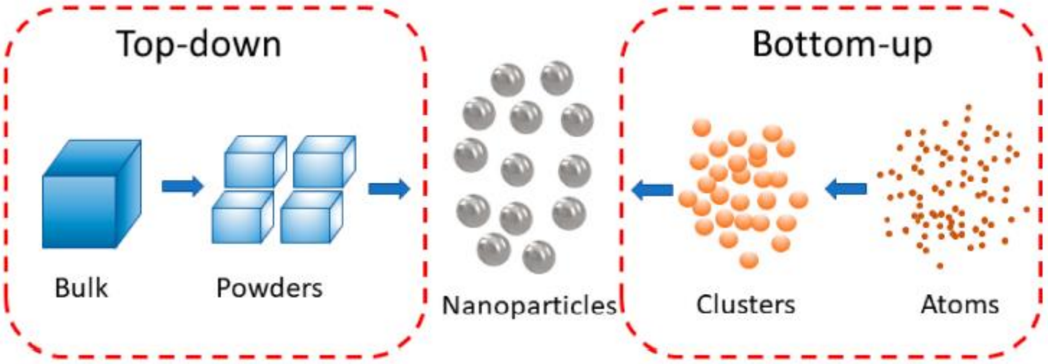

Figure 2.1 Schematic representation of Top-down and Bottom-Up synthesis of Nano particles[217]

The choice of bottom-up or top-down techniques is depending on the specific requirements of the desired nanomaterial and its intended application. Bottom-up synthesis is commonly utilised for applications demanding high purity and well-defined structures, whereas top-down synthesis is best suited for large-scale manufacturing and nanodevice fabrication.

2.1.1 **Liquid-Phase Synthesis**

This method uses several kinds of chemical or physical processes that result in the formation of nanoparticles in liquid media. To synthesise nanoparticles, precursor materials are dissolved or dispersed in a liquid solvent and then exposed to particular parameters including pH, pressure and temperature[218]. This process is known as liquid-phase synthesis.

2.1.1.1 Hydrothermal Method

The hydrothermal method is a common method for synthesising nanomaterials[219]. In this method, the reaction takes place at very high pressure and temperature by keeping aqueous solution of precursor materials inside a sealed autoclave[220]. We can control the size, shape and composition of the nanomaterials by the hydrothermal conditions[219]. High crystallinity [221]with narrow size distributions[222] of nanomaterials are the few advantages of this method. This method is low cost[223] with high quality of product[224], eco-friendly [225]. Hydrothermal method has the capacity for large-scale manufacturing[226]. Figure 2.2 shows photographs of the various stages of the hydrothermal synthesis method.

Figure 2.2 Photographs of phases of hydrothermal synthesis method

2.1.1.2 Microemulsion Method

In microemulsion methods the reactants are dissolved or dispersed in a stable emulsion system composed of oil, water and surfactant [227]. The microemulsion has small droplet size and large interfacial area, which helps for the nucleation and development of nanoparticles. We can synthesis the narrow sized nanoparticles with good control over shape and crystallite size [228]. More Over the nanoparticles synthesised using this method show enhanced performance, which enable the product for the applications including catalysis[229], electronics[230] and medicine[230].

2.1.1.3 Microwave Synthesis:

Microwave synthesis is a fast-developing approach for synthesising nanomaterials in a wide range of scientific fields[231]. In this method the reaction mixture is heated by microwave irradiation for the rapid and uniform heating of the precursors [232]. This method speed up reaction rates and reduce time for the synthesis due to the effective transfer of heat energy to the reaction system by the microwave source [232]. The synthesis of nanomaterials using this technique ensures the excellent purity and crystallinity and the method also has exact control over particle size, shape and composition. Several distinct kinds of nanomaterials, such as metal nanoparticles, metal oxides[233], carbon-based materials[234] and semiconductor nanocrystals[235], have been successfully synthesised via microwave synthesis.

2.1.1.4 Sonochemical Synthesis

The sonochemical synthesis is the process in which the powerful ultrasound radiations are used for the synthesis of nanomaterials. The high intensity ultrasonic waves create transitory microbubbles in liquid medium[236]. The collapse of these microbubbles generates localised hotspots with high temperatures and pressures, providing a perfect environment for nanomaterial manufacturing. Sonochemical synthesis has a number of benefits, such as homogenous particle size distribution[237], rapid response kinetics[238] and controllable particle shape[239]. Many other types of nanomaterials, such as metal nanoparticles[239], metal oxides[240], polymers[241] and hybrid materials[242], have been successfully synthesised using this method.

2.1.1.5 Sol-gel Process

The sol-gel technique is a popular method for synthesising nanomaterials with precise control over their size[243] ,composition[244], structure[245] and morphology[246]. It includes the use of hydrolysis[247] and condensation[248] processes to transform a liquid precursor solution (sol) into a solid gel network. High purity[249], homogeneity[250] and customised characteristics may be achieved in nanomaterials made using the sol-gel technique, which has various benefits. We can easily enhance the properties of synthesised nanomaterials using various dopants and additives. Many different types of nanomaterials, such as metal oxides[251], ceramics[252], glasses[253] and hybrid materials[254], have been successfully synthesised using the sol-gel method.

2.1.1.6 Chemical Co- Precipitation Method

Co-precipitation method is a common technique to synthesise nanomaterials with specific composition and characteristics [255]. It is the simultaneous precipitation of more than one precursor ions from a solution, which results in the production of nanoscale particles. Easiness, cost-effectiveness[256], scalability[257] and suitability for large-scale nanomaterial manufacturing[258] are making this method unique. The properties of the nanomaterials may be tuned by including various dopants and modifiers using this method[259]. Its versatility enables the synthesis of numerous materials, including oxides[260], sulphides[151] and metals, which has applications in various domains like chemical kinetics, electronics and biomedicine.

2.2 Characterization Techniques:

2.2.1 Structural Analysis

The crystalline and molecular structure of a materials is the most important property to study after synthesis. This is significant because the periodic arrangement of atoms and molecules in a substance determines its electrical and optical characteristics.

2.2.1.1 X-ray Diffraction Analysis

Powder X-ray diffraction (XRD) method has importance for the structural analysing of materials, which is a non-destructive method that gives valuable information on atomic arrangement, phase composition and crystal structure of materials[261]. In this work we have used Rigaku Miniflex 600 X-ray diffractometer with Cu Kα (λ= 1.542 Å) radiation which include an X-ray source, sample holder, detector and data analysis system. Generally electromagnetic radiations ranging from 0.02 Å to 100 Å in wavelength are known as X-rays. Which are helpful to study the crystal structures since their wavelength is comparable to atomic size and interatomic distance. The powdered sample is held in a precise orientation by the sample holder to receive the X-ray beam emitted by the X-ray source and to assure optimal X-ray scattering. The detector detects the intensity of the X-rays scattered by the sample at various angles. This information is then used to identify the crystal structure and phase composition of the material. Figure 2.3 displays the schematic diagram of X-ray Diffraction (XRD) Technique.

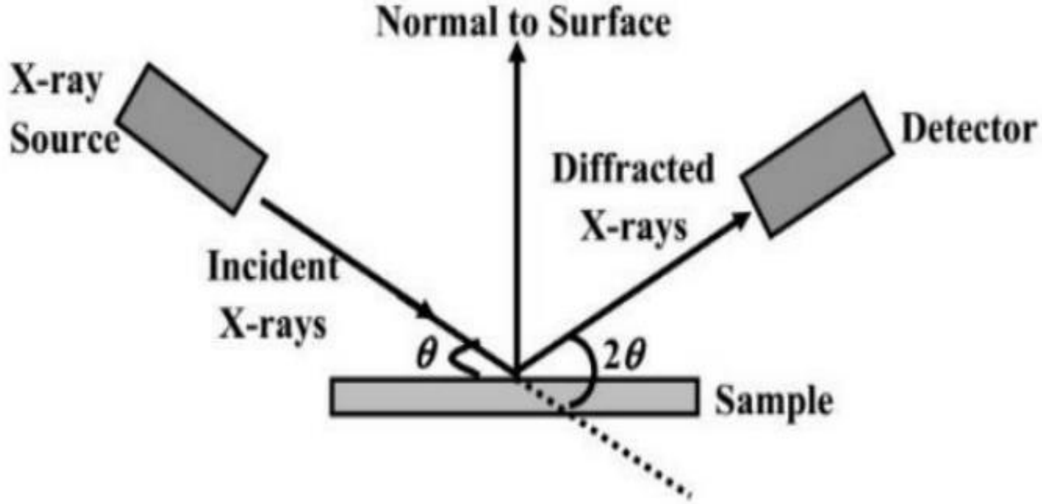

Figure 2.3-Schematic diagram of XRD[262]

The basic principle of XRD is Bragg's Law, which states when the path difference between the X-rays scattered by neighbouring planes of atoms is an integer multiple of the X-ray wavelength is the condition for constructive interference. The Bragg's x-ray reflection from the atomic planes is shown in Figure 2.4.

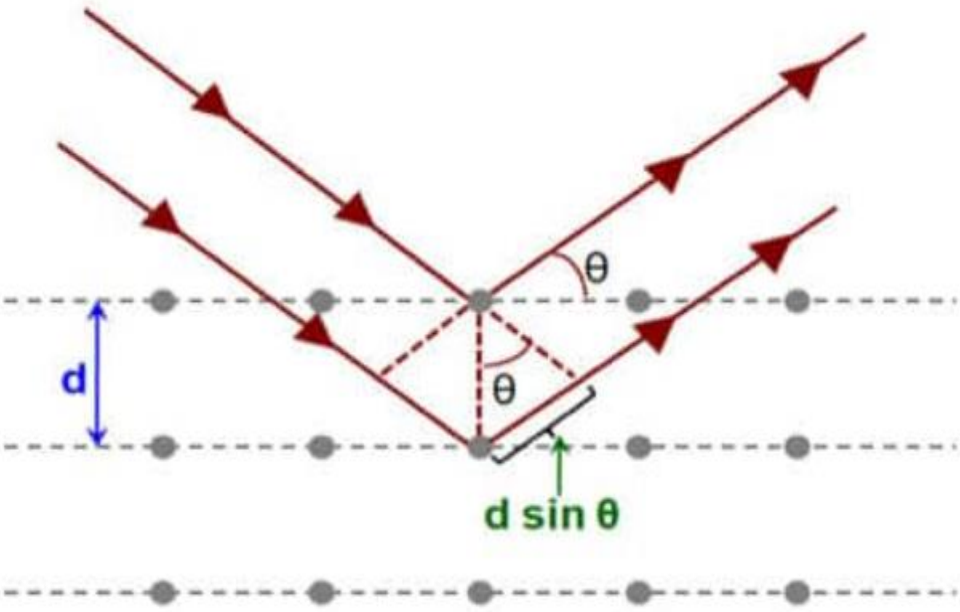

Figure 2.4 Bragg's x-ray reflection from the atomic planes[263].

The mathematical expression of Bragg's law that provides a relationship between the wavelength, interatomic spacing (d) and the angle of diffraction[264] is given as:

$$2d \sin\theta = n\lambda \tag{2.1}$$

These data are used to plot the intensity of diffracted X-rays Vs scattering angle, the plot is composed of a series of peaks, each representing a distinct set of crystal planes in the material. The position and intensity of these peaks reveal the phase composition and crystal structure[264]. The Scherrer equation is commonly employed in XRD investigation to calculate the average crystallite size of a material[264].

$$D = \frac{\boldsymbol{k\lambda}}{\boldsymbol{\beta \cos\theta}} \tag{2.2}$$

where k is a constant 0.9, λ is wave length of X-ray used, β is FWHM of peak in radians and θ is Bragg’s angle in radian.

Equation 2.2 is the relation which connects the size of the crystallites to the peak broadening observed in the diffraction plot. In order to identify the structure of the materials the obtained data can be compared with the reference materials that are kept in data bases. It also provides details about the arrangements of atoms in the crystal lattice, the presence of defects, strain and orientation[265]. XRD is a common technique that can be used for bulk materials, thin films and nanoparticles. The characterization of coatings and their impact on the underlying substrates is another use of XRD. XRD may also measure minute shifts in diffraction lines to infer residual stresses in a crystal lattice[266]. XRD is not only used for crystalline materials, but also provide details about amorphous materials. Figure 2.5 displays photos of the Rigaku Miniflex 600 X-ray diffractometer.

Figure 2.5- Rigaku Miniflex 600 X-ray diffractometer

2.2.2 Morphological Analysis

2.2.2.1 Scanning Electron Microscopy (SEM)

Scanning Electron Microscopy (SEM) is a powerful characterisation method used to study the morphology of materials. SEM works by scanning a concentrated electron beam across the surface of a sample and detecting the signals produced by the interaction of the electrons and the material. SEM theory is based on the interaction of the primary electron beam with the atoms in the sample[267], which results in the emission of different signals like as secondary electrons, backscattered electrons and characteristic X-rays[268]. The electrons emitted by thermionic emission or field emission from a tungsten cathode flow to the anode through electromagnetic fields and lenses. Consequently, the electron beams are directed downward in a vacuum chamber to target a particular sample. When electrons and x-rays hit with the sample, they are ejected from it and collected by detectors. The signals are reconstructed as a final image[269][270]. An image of the surface topography and composition of the sample is produced by collecting the signals produced when the primary electron beam scans the material in a raster pattern. High-resolution imaging capabilities of SEM enable the visualisation of surface features and structures at the nanoscale[271]. SEM is used in many different fields, such as material surface analysis[272], biological sample analysis[273], nanomaterial [274] and thin film research[275]. The schematic depiction of the different components of SEM and the image of ZEISS Gemini SEM 300 are shown in Figure 2.6 and 2.7 respectively.

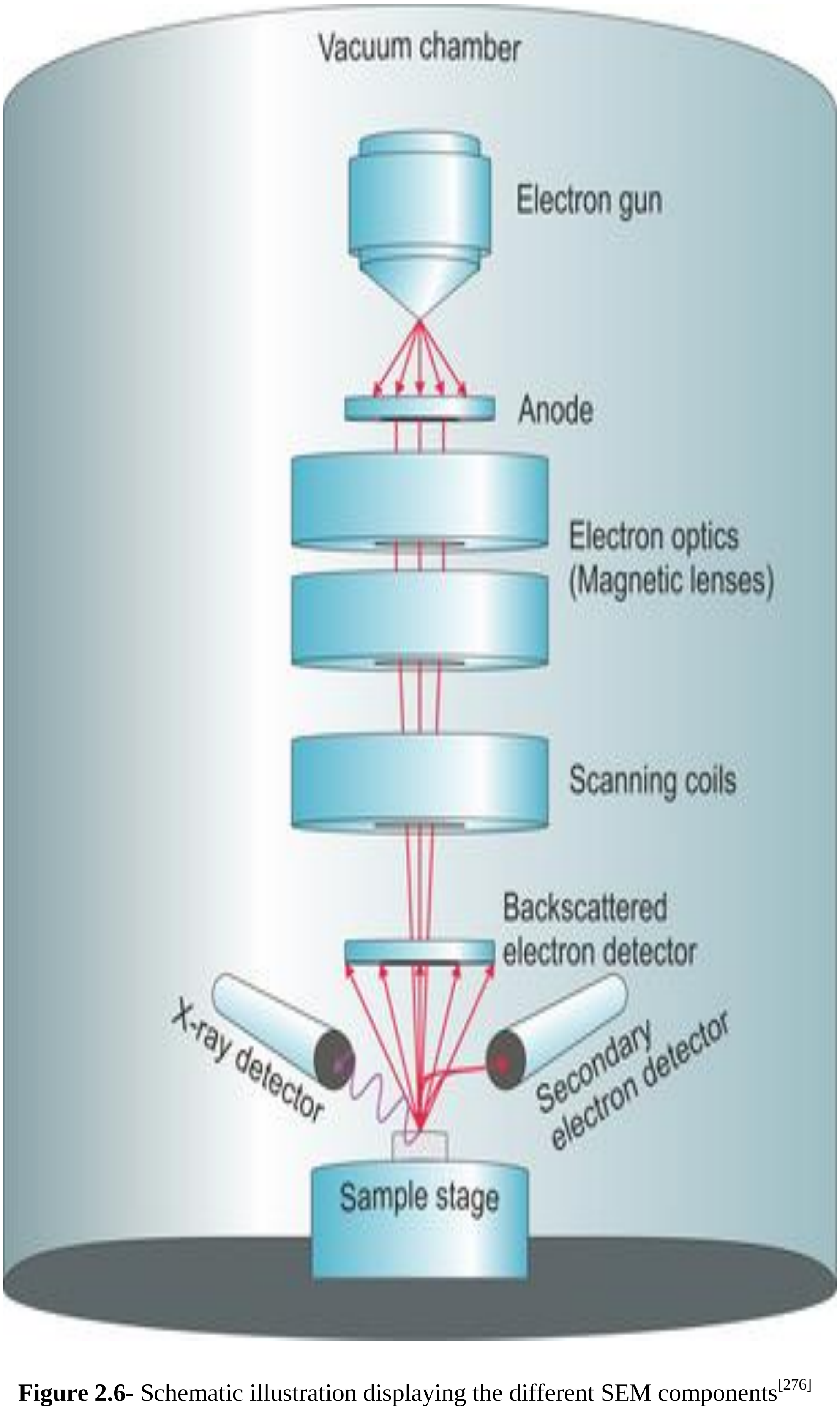

Figure 2.6- Schematic illustration displaying the different SEM components[276]

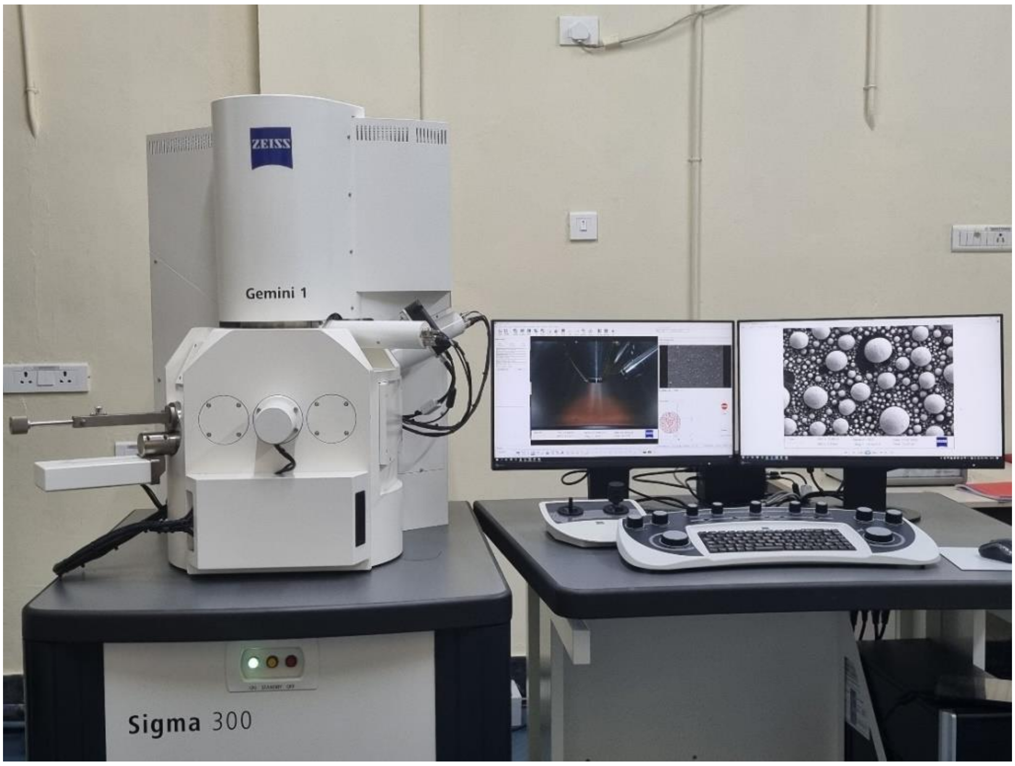

Figure 2.7 Image of ZEISS Gemini SEM 300

2.2.2.2 Transmission Electron Microscopy (TEM)

Transmission Electron Microscopy (TEM) is an effective technique for obtaining detailed information on the morphology, composition and structure of materials. A TEM system consists of an electron source, a detector, a specimen container and a set of electromagnetic lenses[277]. A heated filament or a field emission gun, which generates a stream of high-energy electrons, is commonly used as the electron source in TEM[278]. The electron beam is focused and controlled by the electromagnetic lenses, which enable the beam to pass through the specimen generating an image[278]. The sample is held in place and may be moved inside the microscope by using the specimen holder. The transmitted electrons are collected up by the TEM detector and transformed into a picture that can be examined and studied. Electron-material interaction is the basis of TEM theory[279]. As the electron beam travels through the sample, it scatters and diffractions, yielding information on the atomic structure and crystallographic features of materials. It may be applied to high-resolution imaging of biological samples[280], defect and interface analysis[281], nanoparticle composition [279] and material microstructure testing. Figure 2.8 is schematic depiction of the various TEM components and Figure 2.9 shows image of Tecnai G2 F20.

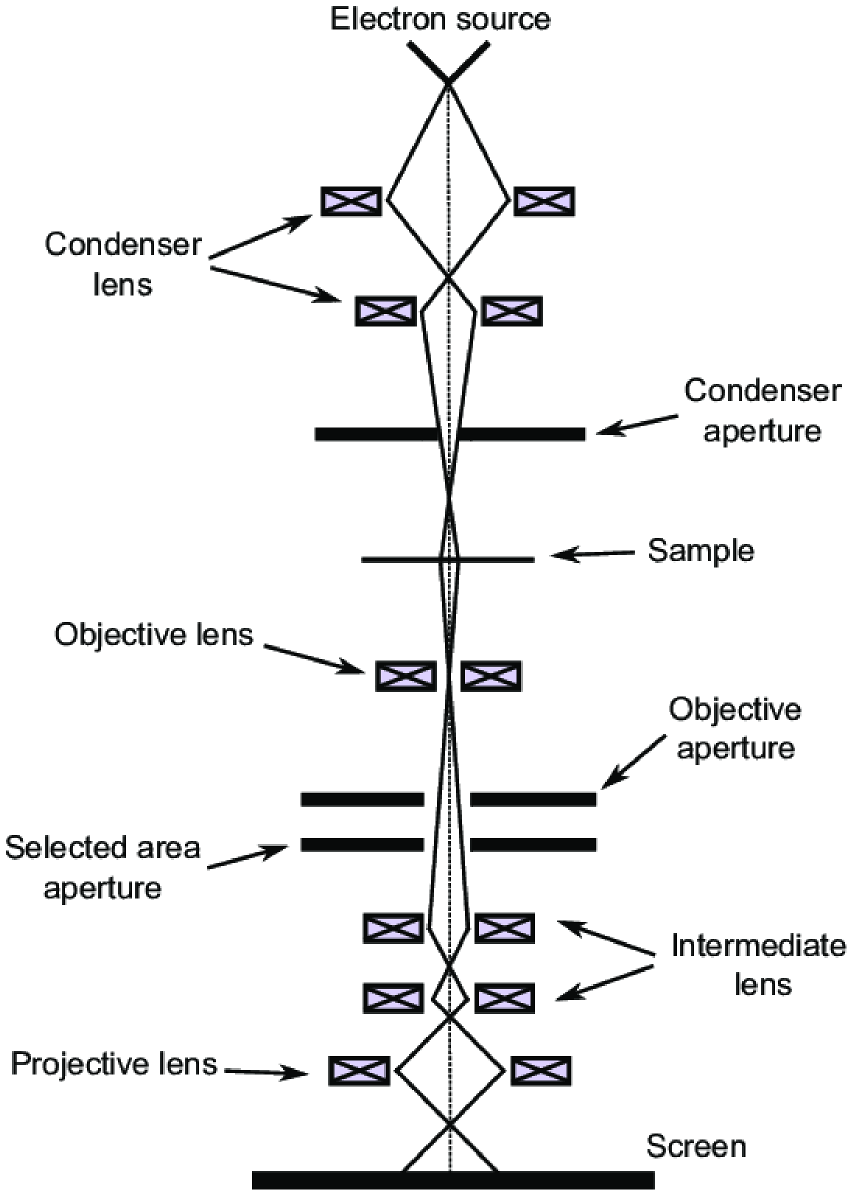

Figure 2.8- Schematic illustration displaying the different TEM components

Figure 2.9 Image of Tecnai G2 F20

2.2.3 Spectroscopic Analysis

2.2.3.1 Raman Spectroscopy

Raman spectroscopy is a method that measures how light scatters from molecules to investigate their vibrational modes[282]. The relationship between light and molecular vibrational modes forms the foundation of the basic theory of Raman spectroscopy[283]. The interaction of monochromatic light with the molecular vibrations of a molecule causes a small percentage of the dispersed light to shift in frequency. This shift in frequency, referred to as the Raman shift, reveals details about the molecular composition and structure. A Raman spectrometer generally consists of a laser source, a sample holder, a monochromator, a detector and a data analysis system. The schematic representation of Raman spectrometer is shown in Figure 2.10. The excitation light is directed onto the sample by the laser source. When a sample is exposed to a monochromatic laser beam in Raman spectroscopy, the molecules in the sample react and generate scattered light. A Raman spectrum is formed by using scattered light with a frequency that differs from the incident light (inelastic scattering). The inelastic collision of incoming monochromatic light with sample molecules produces Raman spectra. The data analysis system processes and interprets the information gathered, while the detector measures the intensity of the dispersed light at each wavelength[284]. There are several uses for Raman spectroscopy in the study of nanomaterials. It may be applied to describe the composition and structure of various nanostructures such as nanotubes and nanoparticles[285][286]. Raman spectroscopy may provide details on the size, shape and surface features of these materials.

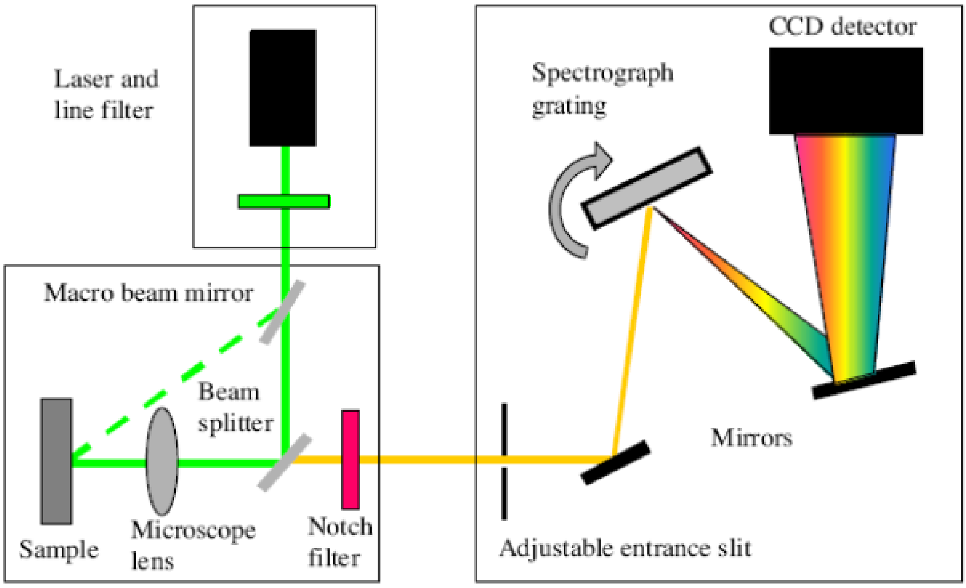

Figure 2.10- Schematic illustration Of Raman Spectrometer [287]

2.2.3.2 Diffused Reflectance Spectroscopy (UV-ViS)

Diffused Reflectance Spectroscopy (UV-Vis) is a commonly used method in materials science and nanotechnology. In diffused reflectance spectroscopy, the reflectance of light from a powder sample for a wide range of wavelengths is measured, since it is extremely challenging to collect transmitted light in solids and powders[288]. Using this method, a broad range wavelengths of light is used to illuminate the sample and the intensity of the reflected light is then measured[289]. The reflectance spectrum gives useful information about the material's absorption and scattering capabilities[290]. There are several parts to a diffused reflectance spectrometer. A tungsten-halogen or UV-Vis lamp is used as the source to excite the atoms of the sample materials. The light from the source is collimated and directed to the sample using lenses and mirrors. The scattered light from the sample is passed through a number of filters and a monochromator to select the required wavelength range and is collected by a detector, like a CCD camera or photomultiplier tube, which is used to measure the intensity of the dispersed light. The diffused reflectance spectroscopy is also used to study the optical characteristics of nanoparticles, nanocomposites and nanostructured materials. This reflectance spectrum analysis provides important insights into the bandgap energy[291], absorption coefficients[292] and electronic transitions of the nanomaterials[293]. The results of this characterisation technique are highly relevant to use the nanomaterials in various applications such as sensors, optoelectronic devices and catalysis. The photograph of the Cary 5000 UV-Vis-NIR spectrophotometer is shown in Figure 2.11.

Figure 2.11 Cary 5000 UV-Vis-NIR spectrophotometer

2.2.3.3 X-ray Photoelectron Spectroscopy (XPS)

X-ray Electron Spectroscopy for Chemical Analysis (ESCA), commonly referred to as Photoelectron Spectroscopy (XPS), is a surface-sensitive method for determining the elemental composition and chemical state of materials. The basis of XPS is the photoelectric effect, which uses X-ray photons from the dual anode X ray source to excite electrons from the inner shells of atom in the samples [294]. The photoelectrons directed to the detector with the help of electron lens system. Electron energy analyser separate electrons with specific energies and then the count of photoelectrons will be measured by the detectors. The kinetic energy of the ejected electrons is then measured, which allows the determination of their binding energy and consequently, the chemical composition of the atoms within the material. XPS can offer useful information regarding the elemental composition, chemical bonding, relative concentration of elements and oxidation states of the surface of a material[295]. XPS can also offer information on electrical structure of materials and band alignment at the surface, which is essential in understanding its electronic and optical characteristics[296]. XPS can be used to study the surface chemistry and composition of materials like thin films, nanoparticles and bulk materials. XPS is used in the semiconductor industry to research the interface characteristics of thin film structures and to characterise and ensure the quality of semiconductor devices[297]. Environmental science[298] and forensic analysis [299]also employ XPS to examine the pollutants, contaminants and trace elements present in different samples.

2.2.3.4 Energy Dispersive Spectroscopy (EDAX)

Energy Dispersive Spectroscopy (EDS), also known as Energy Dispersive X-Ray Analysis (EDX), is a method for determining the chemical composition of materials[294]. The basis of EDS is X-ray fluorescence, which is the process of using a focused electron beam from an electron source to excite atoms in a material to produce distinctive X-rays. The emitted X-rays are then detected by the lithium-based silicon X-ray detector. When the x-rays are incident on the surface of the detector, it will generate charge pulses which are proportional to their energy. This energy yielding information on the elements present in the material as well as their relative concentration. EDS is frequently used together with scanning electron microscopy (SEM)[300]. EDS may provide important details about the elemental composition of a variety of materials, including metals[301], minerals[302], ceramics[303], polymers[304] and biological samples. EDS has extensive applications in many industries. In materials science EDS used to study the material composition ,in geology to analyse the chemical composition of rocks and minerals [305], metallurgy[306], forensics[307] and in semiconductor manufacture to characterise and ensure the quality of semiconductor devices [308]. Figure 2.12 depicts an image of the OXFORD X-Max EDAX.

Figure 2.12 OXFORD X- Max EDAX

2.2.3.5 Photoluminescence Studies

Photoluminescence spectroscopy is a strong technique used for investigating the optical properties of materials by detecting emission spectrum after excitation with photon of suitable wavelength. The basic principle of photoluminescence spectroscopy is the re-emission of light with higher wavelength compared to the wavelength absorbed by the substances for the excitation[309]. When photons incident on the material, the electrons in the material get excited to higher energy levels. These electrons emit photons when they return to their ground state, which gives rise to a distinctive emission spectrum[310]. Photoluminescence spectroscopy is a useful tool for learning electronic structure[311], energy band gaps[312] and defect states[313] of organic compounds[314], semiconductors[315], quantum dots[316] and nanomaterials[317]. In the field of optoelectronics, it is also employed in the development and characterization of light-emitting devices, including lasers and

LEDs[318]. The performance and efficiency of the solar cell can be analysed using photoluminescence spectroscopy by studying recombination processes and defect levels[319]. In biological[320] and medical research[321], photoluminescence spectroscopy is also used for imaging methods like fluorescence microscopy[322] as well as for analysing the fluorescence characteristics of biomolecules like proteins and DNA[323]. The photograph of Agilent Cary fluorescence spectrophotometer is shown in Figure 2.13.

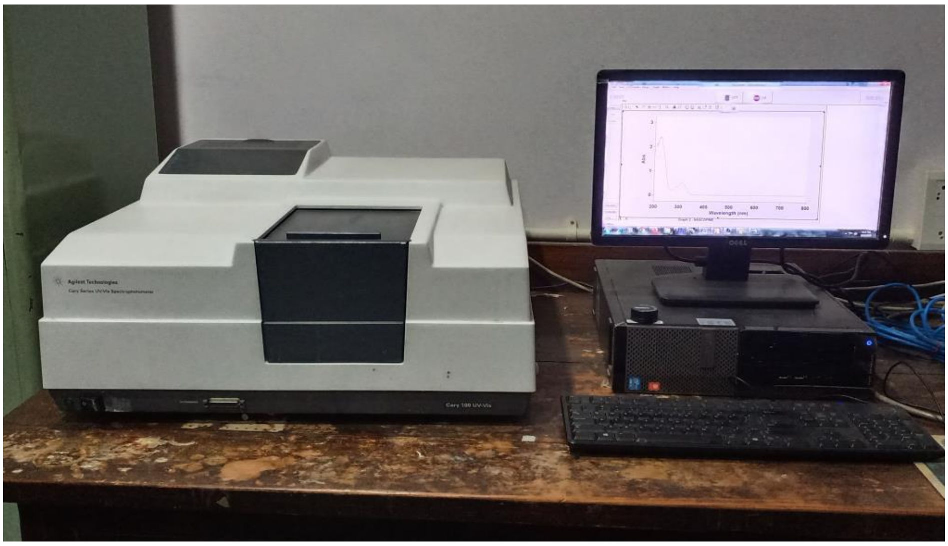

Figure 2.13 Agilent Cary fluorescent spectrophotometer

2. 2.4 Photocatalytic Studies

Photocatalysis (PC) is an exceptional phenomenon that uses light energy to activate chemical reactions on the surface of a catalyst[324]. Visible light photocatalysis has drawn a lot of interest recently because of its potential uses in a variety of industries. The photocatalysis mechanism is based on the excitation of electrons in the catalyst material by photons, which results in the formation of electron–hole pairs[325]. These charge carriers may subsequently participate in redox processes, which allow for the breakdown of organic contaminants[326], the generation of clean energy[327] and the synthesis of useful compounds. Visible light photocatalysis is important because of its capacity to use plentiful and ecologically favourable solar energy for long-term and efficient chemical reactions.

In this thesis the one of the main focuses is the application of visible light photocatalytic activity for water purification, since the global scarcity of freshwater supplies has long been ingrained in the public's eyes. The world is expected to be water-stressed by 2025 [328]. Water pollution harms the ecosystem balance, so humans will be affected by clean water scarcity shortly. Water-related diseases include communicable diseases (waterborne, water-washed, water-based and water-related vector-borne diseases) and noncommunicable diseases caused by chemically polluted water[329]. According to Hermabessiere *et al.*, many plastics in the water are hazardous to a broad spectrum of organisms [330]. Several diseases are caused by chemical waste, including anemia, low blood platelets, headaches, cancer risk and various skin problems [331]. Semiconductor photocatalysis is the most promising and successful approach for competing with water contaminants. ZnS is an important semiconductor photocatalyst in the II-VI group. ZnS is only sensitive to UV light absorption because of its broad bandgap energy. The development of visible-light-active photocatalysts capable of utilizing the greatest amount of solar light is an intriguing research area [332]. It is still challenging to improve visible photocatalytic activity by improving charge transfer and efficient charge separation [333]. The other hurdles in this field are low photocatalytic efficiency for visible-light photocatalysts, low mobility of charge carriers, inferior stability of photocatalyst [334], high recombination rate of electron-hole pairs [335] and cost-effectiveness at the commercial level [336][337]. The primary disadvantage of ZnS catalysts is their irreversible agglomeration during the photocatalytic processes and limited recyclability, which reduces the photocatalytic degradation efficiency [338].

Defect engineering is promising method for improving light harvesting in PC materials [339][340][341][342]. Semiconductor photocatalyst defects can function as adsorption sites for charge transfer that prevent the recombination of photoinduced charge and add new energy levels to narrow the band gap that creates visible-light activity. By creating additional energy levels to photoexcited charge carriers' electronic structure and characteristics, vacancy defects can significantly alter the PC activity of a photocatalyst [343]. Doping is also an effective strategy for inducing these defects. The visible light photocatalysis of ZnS has been reported to be improved by the addition of extrinsic metal elements such as Copper [344], Nickel [345], Cadmium [346], or nonmetal elements Carbon and Nitrogen [347][348]. The inherent characteristics of materials, such as crystalline phases, defect states, exposed facets, etc., of semiconductor photocatalysts are crucial for superior photocatalytic (PC) activities [132] [343]. In this thesis sun light and Xenon short arc lamp of 300W working with 20V, 15A power supply served as visible light sources. Figure 2.14 and Figure 2.15 show the PC activities performed in sunlight and Xenon lamp.

Figure 2.14- PC Experiments performed in Sun light

Figure 2.15- PC Experiments performed using Xenon lamp

Chapter-3

ZnS Nanoparticles by Hydrothermal Synthesis: Point Defects through Stoichiometric Ratio Variation

The photoluminescent and photocatalytic properties of materials like Zinc sulphide (ZnS) can be improved by Defect engineering. Zn and S defects are successfully integrated into the ZnS crystal by altering the S/Zn molar ratio during hydrothermal processes. The addition of defects to the ZnS crystal can modify the band structure of ZnS samples. Defects are formed on the surfaces during the treatment process. XRD and Raman are used for the confirmation of the crystallinity and phase formation of the samples. Using an X-ray peak pattern assessment based on the Debye Scherer model, the Williamson-Hall model and the size strain plot, it is possible to study the influence of crystal defect on the structural characteristics of ZnS nanoparticles. UV-vis diffused reflectance spectroscopy (UV-vis DRS) is used to estimate the band gap (E_g) values and found that the E_g is reduced from 3.49 eV to 3.28 eV by altering the S/Zn molar ratio. Photoluminescence study (PL) shows these ZnS nanoparticles emit violet and blue radiations. In keeping with the results of XRD, TEM demonstrated the nanoscale of the prepared samples and exhibited a small agglomeration of homogenous nanoparticles. Scanning electron microscopy (SEM) was used to examine the surface morphology of the ZnS particles. Inductively Coupled Plasma Optical Emission Spectroscopy (ICP-OES) and X-ray photoelectron spectroscopy (XPS) were used to evaluate and validate the elemental composition. XPS results indicate the presence of defects on the prepared ZnS nanoparticles. For the investigation of vacancy-dependent catalytic activity under exposure to visible light, defective ZnS with different quantities of Zn and S voids are used as catalysts. The lowest S/Zn sample, ZnS0.67 and the highest S/Zn sample, ZnS3, show superior photocatalytic activity.

3.1 Introduction

Zinc sulphide (ZnS) is n-type compound semiconductor with wide direct band gap. ZnS has applications in light-emitting diodes, electroluminescent devices, flat panel displays, infrared windows, sensors, lasers and solar cells [349][350][351]. Various methods are reported for the synthesis of ZnS nanomaterials, including electrochemical deposition, microemulsion [352], solvothermal [353], sol-gel [354], co-precipitation [355], combustion synthesis [356], pyrolysis, hydrothermal, laser ablation and vapor deposition [357], have been used to fabricate ZnS nanostructures. The hydrothermal method does not require any calcination or milling and the method is adaptable, productive and able to be adjusted. Low contamination, cost-effectiveness and ability to regulate the nucleation process [3][353] are the other advantages of hydrothermal method.

Customizing the chromatic discharge of nanomaterials is crucial for their use in light-emitting screens, field emitters, lasers, sensors and optoelectronic devices [358][359]. ZnS nanocrystals exhibit blue, green and orange emissions [360][361]. The luminescence characteristics of ZnS particles have been altered by doping with various transition elements and rare-earth metals [362][363]. The optical characteristics are affected by defects, crystal structure, size and shape. These studies show the ability to adjust several emission characteristics from pure ZnS nanocrystals with various defect features. Despite significant efforts to investigate the optical features, the sources of various photoluminescence (PL) bands from ZnS are infrequently addressed. The ZnS luminescence properties are typically attributed to surface states [364], Sulphur vacancies [365], Zn vacancies [366], elemental Sulphur species, or impurities in ZnS [130]. There are many hanging bands and imperfections in the surface of ZnS due to its diverse interface topologies and larger specific surface areas [367].

The light harvesting properties of photocatalytic materials can be improved by defect engineering [339][340][341][342]. The new energy levels added during the introduction of defects narrows the band gap that induces visible-light activity and in semiconductor photocatalyst defects can function as adsorption sites for charge transfer that prevent the recombination of photoinduced charge. Vacancy defects can significantly alter the PC activity by creating additional energy levels to the electronic structure of photoexcited charge carriers [343]. Doping is also an effective strategy for inducing these defects. The addition of extrinsic metal elements such as Copper [344], Nickel [345], Cadmium [346], or nonmetal elements Carbon and Nitrogen [347][348] improves the visible light photocatalysis of ZnS. The inherent characteristics of materials, such as crystalline phases, defect states, exposed facets, etc., of semiconductor photocatalysts are crucial for superior photocatalytic (PC) activities [132] [343].

This study presents simple hydrothermal method for introducing S and Zn vacancies into the ZnS structure by changing the S/Zn molar ratios. Investigations are made into how vacancy-related features affect the photoluminescence and PC activity of ZnS in visible light.

The results presented in this chapter have already been published as E.M. Jubeer, M. A Manthrammel, P. A Subha, M. Shkir, K.P. Biju and S.A. alFaify,” Defect engineering for enhanced optical and photocatalytic properties of ZnS nanoparticles synthesized by hydrothermal method,”Sci.Rep.,vol.13,no.1,p.16820, Oct.2023, *doi: 10.1038/s41598-023-43735-1*[125].

3.2 Experimental

3.2.1 Synthesis

The nanoparticles (NP) of ZnS were prepared by the hydrothermal method and the brief synthesis procedure followed. The required amount of $ZnCl_2$ and $SC(NH_2)_2$ powder were dissolved in de-ionized water separately and five drops of HCl were added to the $ZnCl_2$ solution and stirred at room temperature for 1 hour. Thiourea solution is then dripped into $ZnCl_2$ solution and the mixture is stirred at room temperature for another 1 hour. 50 ml of the clear mixture was then charged to a Teflon-coated SS autoclave of 100 ml volume. The closed autoclave was placed in a furnace at a temperature of 220 °C for 12 hours and then allowed to cool to room temperature. The nanoparticles in the solution were filtered and washed several times using de-ionized water to remove impurities in the sample. The final whitish product was dried at 60 °C for 1 hour. Five samples were prepared by varying [S]/[Zn] molar ratios using the same procedure. Samples with [S]/[Zn] molar ratios of 0.67, 1, 1.5, 2 and 3 were prepared and named ZnS0.67, ZnS1, ZnS1.5, ZnS2 and ZnS3 for further characterization.

3.2.2 Measurements

The structural studies of prepared samples were carried out by the X-ray diffractometer (XRD) using Rigaku Miniflex 600 X-ray diffractometer with Cu Kα (λ= 1.542 Å) radiation, operating at 15 mA and 40 kV. Cu target and graphite monochromator were used and data was recorded in continuous scan mode from 10° to 80°, with a step size of 0.02° at scan speed of 10° per minute. The vibrational study was carried out for all present samples using the Horiba Lab Ram HR Evolution Confocal Raman Spectrometer. The Raman spectrometer was operated using 532nm (Diode Pumped Solid State Laser) at room temperature and recorded in a scan range of 150 to 450 cm^{-1}. X-ray photoelectron spectroscopy (XPS) of the ZnS nanoparticles was characterized by a Thermo-scientific NEXA Surface analyzer. The determination of the element content was carried out using a Thermo-scientific Icap 6300 ICP-OES. The Photoluminescence study was also carried out using Agilent Cary fluorescent spectrophotometer with an excitation wavelength 280 nm. Optical studies of all ZnS nanostructures were analyzed using The Cary 5000 UV-Vis-NIR spectrophotometer, in the wavelength range of 200–1200 nm at room temperature. The morphological studies of all the synthesized ZnS nanostructures were done using a ZEISS Gemini SEM 300. TEM and EDAX studies by using Tecnai G2 F20, FEI Company operating at 200kV and OXFORD X- Max, respectively. To conduct a PC study, 0.03 g of ZnS photocatalyst is added to 25 ml of Methylene Blue (MB) solution. To prepare the MB dye solution, 10mg of MB was added to 1L of distilled water, resulting in photocatalysts. The mixture was magnetically stirred for 1 hour in darkness to attain adsorption–desorption equilibrium between the MB dye and catalyst. The PC studies were conducted from 11 a.m. to 2 p.m. on sunny days [345]. The solar intensity was measured in each hour during the experiment using a VAR TECH V6610 Digital Lux meter and the intensity values were 56k(lux), 79k(lux), 62k(lux) and 48k (lux), respectively. The specific surface area of the samples is estimated through the Brunauer-Emmett-Teller (BET) method using BELCAT-M.

3.2.2.1 X-Ray Diffraction analysis

The XRD spectra of the ZnS samples are depicted in Figure 3.1a. Every one of the recognizable peaks could be ordered as the cubic ZnS in the standard reference information (ICDD 01-077-2100). Different lattice parameters such as interplanar spacing, unit cell volume and lattice constant were determined from the Bragg condition and the Lattice Geometry conditions [151] of the form :

$$2d_{hkl}\sin\theta = \lambda \tag{3.1}$$

$$V = a^3 \tag{3.2}$$

$$d = \frac{a}{(h^2+k^2+l^2)^{\frac{1}{2}}} \tag{3.3}$$

Where' λ 'is the wavelength of the X-ray used, which is 1.54056Å, (hkl) is the miller index of the crystal plane and θ is Bragg's angle [368]. The lattice parameters of these ZnS powders synthesized using the hydrothermal method were determined utilizing the crystallographic planes relating to the Miller index (111), (220) and (311), which are consistent and in remarkable concurrence with the standard lattice constant value 5.39 nm. A similar finding was reported by T. T. Quynh Hoa *et al.*, well. [369]. The ZnS nanoparticle crystallite size, D, was determined utilizing the standard Scherrer's equation

$$D = \frac{N\lambda}{\beta\cos\theta} \tag{3.4}$$

where β is full-width half maxima and N is the crystallite shape factor [370]. A gaussian fitting with a Chi-square value of more than 0.98 was used in our analysis to determine the peak width. The current analysis used the line broadening of Si single crystal as a reference material to rule out the impact of the instrument. The crystallite size measured by substituting relevant information from the XRD is 2.8

nm, 2.9 nm, 27.2 nm, 36.7 nm and 28.6 nm for the samples ZnS0.67, ZnS1, ZnS1.5, ZnS2 and ZnS3 respectively, from the peak corresponding to (111) plane. For lower S/Zn samples ZnS0.67 and ZnS1, the XRD spectrum shows broad peaks, which indicate the formation of quantum dots like ZnS particles. The crystallite size is more significant when the S/Zn molar ratio exceeds 1. Still, the high intensity of the peaks shows a higher crystallinity nature of the samples with a high S/Zn Molar ratio, M. Thambidurai *et al.*, also reported the same observation [371]. The formation of a little amount of ZnS in the wurtzite structure might also be the cause of the exceptionally weak diffraction signal at 26.93° for S rich sample (#01-075-1547) [130]. The peak positions and intensities are listed in Table 3.1.

3.2.2.1.1 Williamson-Hall (W-H) method

W-H models, for example, a Uniform Deformation Model (UDM) could gauge the lattice strain, which was assessed in the ZnS NP due to the deformation of the grid. Different models, such as the Uniform Deformation Stress Model (UDSM), recognize the stress-strain connection. In contrast, the Uniform Deformation Energy Density Model (UDEDM) assesses the strain and is widely used for finding energy density [372][373]. We have focused on the three prominent peaks in the Williamson-Hall analysis and the other models, which correspond to the (111), (220) and (311) crystallographic planes.

3.2.2.1.2 Unified Deformation Model (UDM)

According to W-H method, the peak widening is owing to the crystal size and the impact of the strain. The influence of the strain is represented by the equation (3.5)

$$\boldsymbol{\beta_{\mathrm{strain}} = 4\varepsilon \tan\theta} \tag{3.5}$$

where, ε is the internal strain.

Hence, the total peak width is shown in eqn. (3.6) represent UDM [374];

$$\boldsymbol{\beta_{\mathrm{hkl}} = 4\varepsilon \tan\theta + \frac{N\lambda}{D\cos\theta}} \tag{3.6}$$

The UDM plot has drawn 4 sin θ along the X-axis and β_{hkl} cos θ along the Y-axis of the prepared samples are shown in Figure 3.1b.

The strain was assessed from the slop of linearly fitted diagrams and normal crystallite size from the Y-intercept [375]. The strain of ZnS nanoparticles is viewed as 2.7 $\times10^{-3}$, - 3.9 $\times10^{-3}$, 0.01 $\times10^{-3}$, -0.25 $\times10^{-3}$, 0.35 $\times10^{-3}$ for ZnS0.67, ZnS1, ZnS1.5, ZnS2 and ZnS3 samples respectively. The negative slope of Williamson and Hall plots for the unit S/Zn molar proportion demonstrates the presence of compressive strain, which could initiate the negative strain mutilation. Nonetheless, the positive slope could be ascribed to the tensile strain or inside stress in the crystal owing to the thermal expansion during the crystal development [195]. In this manner, grid strain differs from a positive to a negative value, explicitly relying upon the S/Zn molar proportion. The crystallite size is obtained as 2.9 nm, 2.7 nm, 26.2 nm, 32.6 nm and 29.7 nm for the ZnS0.67, ZnS1, ZnS1.5, ZnS2 and ZnS3 respectively. The parameters measured are listed in Table3.2

3.2.2.1.3 Uniform Deformation Stress Model (UDSM)

The postulation of homogeneity and isotropy is not satisfied in all cases. To consolidate more sensible circumstances, an anisotropic methodology is taken on; consequently, the W-H condition is altered by an anisotropic strain ϵ. In USDM, the lattice deformation stress is considered uniform in all crystallographic orientations, expecting a little micro strain in the particles. According to Hook's Law

$$\boldsymbol{\epsilon = \frac{\sigma}{Y_{hkl}}} \tag{3.7}$$

where ϵ is the anisotropic strain and Y_{hkl} is Young's modulus in the plane (h k l) and σ is the stress of the crystal.

In this approach, eqn. (3.6) is modified as follows [376]

$$\boldsymbol{\beta_{hkl} Cos\ \theta_{hkl} = \frac{k\lambda}{D} + \frac{4\,\sigma \sin\theta_{hkl}}{Y_{hkl}}} \tag{3.8}$$

Equation (8) is called the Uniform Deformation Stress Model (UDSM). Figure 3.1c shows the UDSM plot of the prepared samples with different S/Zn molar ratios. The slope of the fitted plot will give uniform stress and the particle size can be evaluated from the Y-intercept [377]. The particle sizes are obtained as 2.9 nm, 2.8 nm, 36.7 nm, 51.4 nm and 42.7 nm for ZnS0.67, ZnS1, ZnS1.5, ZnS2 and ZnS3, respectively. The micro strain values of different crystal planes of prepared samples are shown in Table 3.2.

3.2.2.1.4 Uniform Deformation Energy Density Model (UDEDM)

Equation (3.6) is changed to the structure where energy per unit volume (energy density), 'u' is considered. As per Hooke's law, the 'u' as a strain component is u = $\varepsilon^2 Y_{hkl}/2$. In the strain-stress connection, all the proportionality constants become, at this point, not independent when the strain energy density is considered [378]. Thus, the above equation can be written as

$$\boldsymbol{\beta_{hkl} Cos\, \theta_{hkl} = \frac{k\lambda}{D} + \frac{4 \sin \theta_{hkl} (2u)^{\frac{1}{2}}}{(Y_{hkl})^{\frac{1}{2}}}} \tag{3.9}$$

The plot, $\beta_{hkl} Cos\, \theta_{hkl}$ Vs $\frac{4 \sin \theta_{hkl} 2^{\frac{1}{2}}}{(Y_{hkl})^{\frac{1}{2}}}$ is the UDEDM plot [379] of the prepared samples with different S/Zn Molar ratios, shown in Figure 3.1d. The Y-intercept gives the average crystallite size and the values are 2.9 nm, 2.8 nm, 38.9 nm, 55.2 nm and 46.2 nm for ZnS0.67, ZnS1, ZnS1.5, ZnS2 and ZnS3 respectively. The energy density values evaluated from the slopes are listed in Table 3.2.

3.2.2.1.5 Size-Strain Plot (SSP):

The Williamson-Hall plots reveal that the line widening is fundamentally isotropic. This underscores that the diffracting areas are isotropic because of the strain. In instances of isotropic line expansion, a superior assessment of the size-strain boundaries can be obtained by taking into account a SSP. This technique has the advantage that less significance is given to information from reflections at high angles with lower accuracy. In this technique, it is accepted that the 'strain profile' is explained by a Gaussian function and the 'crystallite size' profile by a Lorentzian function [380], which is given by,

$$\boldsymbol{(d_{hkl} \beta_{hkl} \cos\theta)^2 = \frac{K}{D} (d_{hkl}^2 \beta_{hkl} \cos\theta) + (\frac{\varepsilon}{2})^2} \tag{3.10}$$

Where k is the shape factor and D is the crystallite size. The plot ($d_{hkl}^{2}\beta_{hkl}\cos\theta$) along the X-axis and $(d_{hkl}\beta_{hkl}\cos\theta)^{2}$ along the Y-axis, is shown in Figure 3.1 e which is the Size-Strain Plot[381]. The slope of the fitted plot gives the crystallite size and the Y-intercept helps to determine the strain. The calculated strain values for samples ZnS0.67, ZnS1, ZnS1.5, ZnS2 and ZnS3 were 51.2, 36.6, 14.4, 10.5 and 13.8, respectively. The values are listed in Table 3.2.

The crystallite size of these samples was measured using the Scherrer formula and other methods such as UDM, UDSM, UDEDM and Size-Strain Plot (SSP). When different methodologies for estimating crystallite size were evaluated, it was noticed that the SSP model produced more accurate findings than the UDM, UDSM and UDEDM methods. The assessment of the plots revealed that the data were more precisely matched using the SSP model. These results indicate that the SSP technique is a valid method for assessing crystallite size in ZnS samples with varying S/Zn ratios. The accuracy of the SSP model can be ascribed to its capacity to account for lattice strain and give a more thorough understanding of the crystal structure. Overall, this research highlights the need to employ appropriate methodologies for assessing crystallite size in nanocrystals [382][383]. The various models used to estimate strain in nanoparticles generated vary strain values, indicating that strain is not direction-dependent. This finding is crucial because it sheds light on the structural properties of nanoparticles as well as their behaviour under various conditions [376].

Table 3.1 Structural parameters for ZnS NPs

Samples	**2θ (°)**	**Intensity (a.u)**	**Crystallite Size (nm.)**	**Interplanar Spacing d_{111}(Å)**		**Lattice Parameter a (Å)**	
ZnS0.67	28.68	3945	2.8	3.11	Standard d_{111}=3.12	5.39	Standard Value= 5.41
ZnS1	28.60	3543	2.9	3.12		5.40	
ZnS1.5	28.69	32265	27.2	3.11		5.38	
ZnS2	28.64	21354	36.7	3.11		5.39	
ZnS3	28.51	18084	28.6	3.12		5.42	

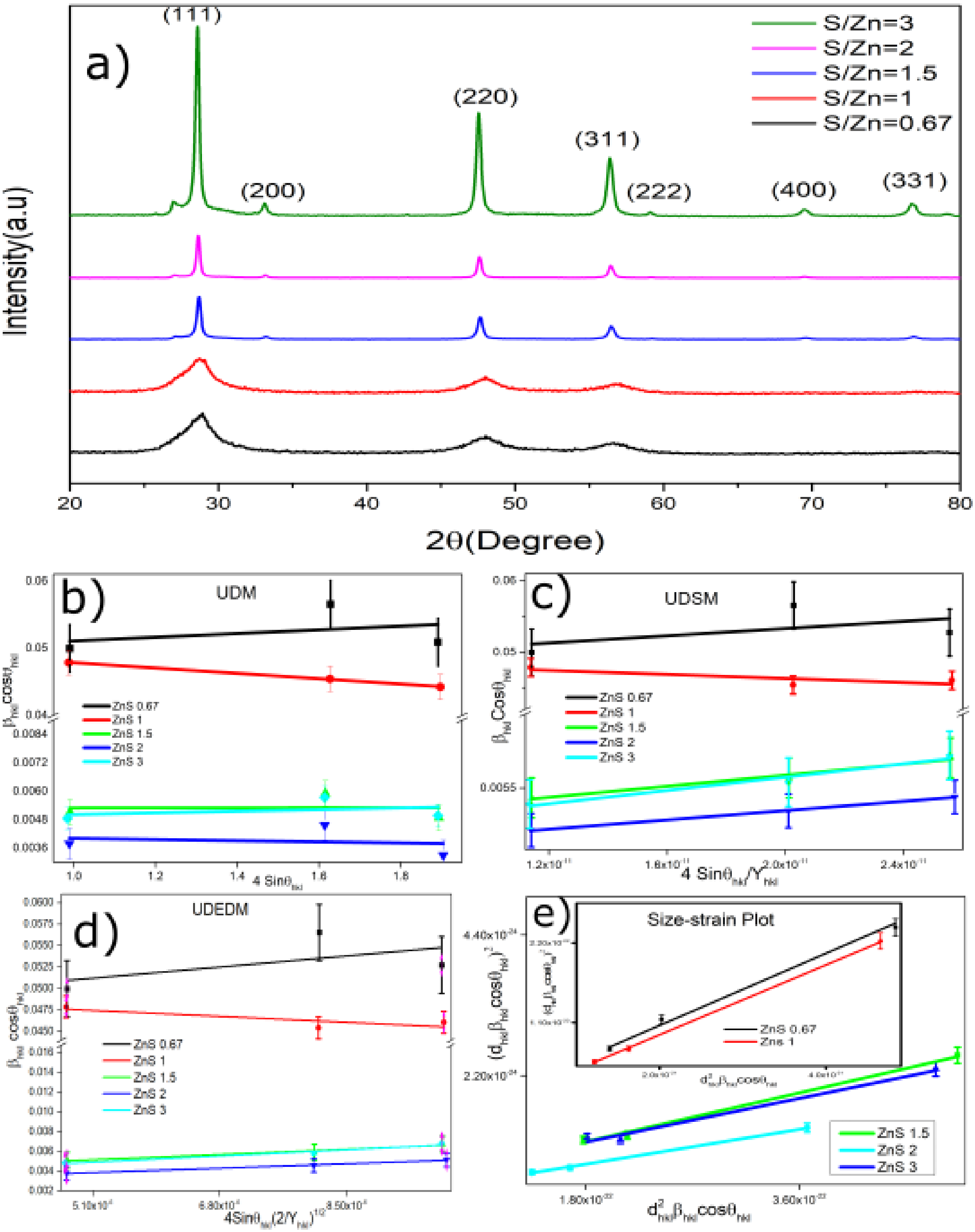

Figure 3. 1. a) XRD pattern of present samples b) UDM, c) UDSM, d) UDEDM, e) Size-Strain Plot of ZnS1.5, ZnS2 and ZnS3 (inset-SSP for ZnS0.67 and ZnS1)

Table 3.2 Structural parameters for ZnS NPs determined using different approaches

Samples	Parameter	Scherrer	UDM	UDSM	UDEDM	SSP
ZnS 0.67	D(nm)	2.8	2.9	2.9	2.9	2.8
	ε (10^{-3})	50.4	2.7	(111) =2.92 (220) =3.15 (311) =3.42	(111) =3.66 (220) =3.80 (311) =3.96	51.2
	σ (G Pa)			0.25	0.3	
	U(kJm^{-3})				582.34	
ZnS 1	D(nm)	2.9	2.7	2.8	2.8	2.9
	ε (10^{-3})	48.4	-3.97	(111) =-1.63 (220) =-1.76 (311) =-1.91	(111) =1.96 (220) =2.04 (311) =2.12	36.6
	σ (G Pa)			-0.15	0.16	
	U(kJm^{-3})				167.513	
ZnS 1.5	D(nm)	27.2	26.3	36.8	38.9	32.7
	ε (10^{-3})	5.15	0.01	(111) =1.29 (220) =1.40 (311) =1.52	(111) =1.49 (220) =1.55 (311) =1.62	14.4
	σ (G Pa)			0.11	0.13	
	U(kJm^{-3})				974.52	
ZnS 2	D(nm)	36.7	32.6	51.4	55.2	46.0
	ε (10^{-3})	3.8	-0. 25	(111) =1.09 (220) =1.17 (311) =1.27	(111) =1.26 (220) =1.31 (311) =1.36	10.5
	σ (G Pa)			0.09	0.11	
	U(kJm^{-3})				693.5	
ZnS 3	D(nm)	28.6	29.7	42.7	46.2	36.6
	ε (10^{-3})	4.9	0.35	(111) =1.55 (220) =1.68 (311) =1.82	(111) =1.78 (220) =1.86 (311) =1.93	13.8
	σ (G Pa)			0.01	0.15	
	U(kJm^{-3})				138.997	

3.2.2.2 Raman Spectra Analysis

Through phonon interactions, changes in surface features can be inferred using the Raman vibrational investigation. The Raman Vibration Modes of the present samples are shown in Figure 3. 2. As Cheng *et al.,* reported, the only permitted modes at the zone centre for the cubic ZnS phase are the longitudinal optical (LO) modes and transverse optical (TO) modes[147]. All samples showed a TO peak mode at around 270 cm^{-1} and LO peak at around 340 cm^{-1}, supporting the cubic phase of ZnS. Notably, for both fundamental modes, there is a peak shift towards the shorter wavelength as the Zn vacancy (V_{Zn}) increases to a certain level and then shifts to a higher wavelength. However, due to surface modulation, it is feasible to observe some other Raman modes at the nanoscale. The overtones of transverse acoustic phonons[384] for all samples except ZnS2 were identified as the sources of the peaks around 235 cm^{-1}. The Raman modes around 427 cm^{-1} for all samples except ZnS3 are due to TO+LA (Longitudinal Acoustic). The identical Raman modes were detected by Nilsen [385], or due to the LO+TA (Transverse Acoustic) vibrational modes as well as, which is in line with reports by S. Dhara *et al. and* Zhiyuan Ye *et al.*, [386][387]. The slight shift in the peaks may be due to the nanoconfinement effect. The other Raman vibration mode that appeared common for all samples is TO+TA mode at 390 cm^{-1} [388]. Raman spectra revealed further information about the lattice defects. Along with the above-mentioned Raman vibration modes, some samples also exhibit defect-induced Raman modes. The samples ZnS0.67, ZnS1, ZnS1.5 and ZnS3 centred at 320 cm^{-1} have a lattice defect-induced phonon mode at X-W-L, as reported by Jun Zhou *et al.*[384]. The cubic crystalline phases are confirmed by Raman analysis, which is in good agreement with the XRD results.

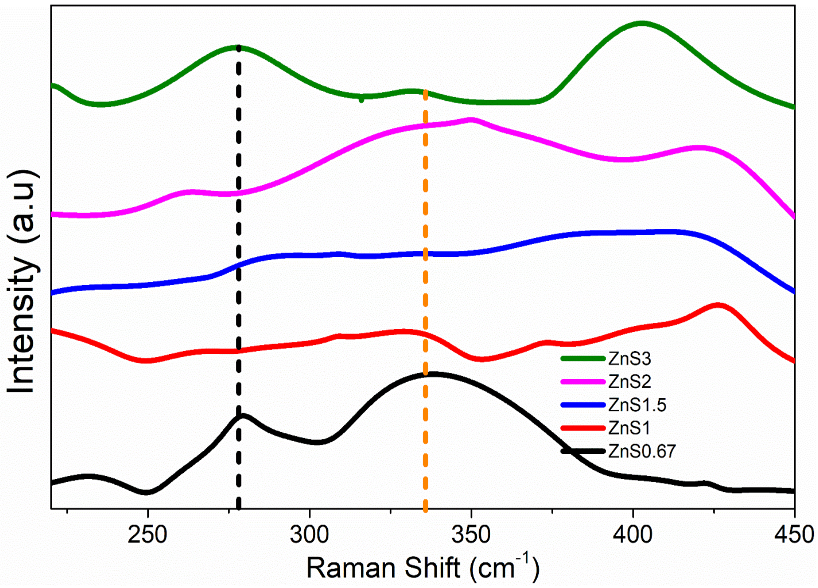

Figure 3.2. Vibrational Raman Spectra of ZnS

3.2.2.3 Scanning Electron Microscopy (SEM)

The morphological study of the ZnS sample synthesized by the hydrothermal method uses SEM images shown in Figure 3.3(a-e). It is obvious that the combination of grains is visible with uniform polygonal-shaped particles. The particles are shaped with a compact morphology and thickly stuffed. Normal grain sizes of the particles were found to be greater than the crystallite size determined from XRD and the values are 25.8 nm, 57.7 nm,93.9 nm,158 nm and 85.4 nm for ZnS0.67, ZnS1, ZnS1.5, ZnS2 and ZnS3 respectively. It is to be noted that the grain sizes assessed by XRD and SEM were exceptionally interesting. In SEM, the grain size was assessed by the differentiation between the clear grain boundaries, while in XRD, the estimation extended to the crystalline region that diffracted X-ray beams coherently. As needed, the XRD assessments provoked a smaller size [389].

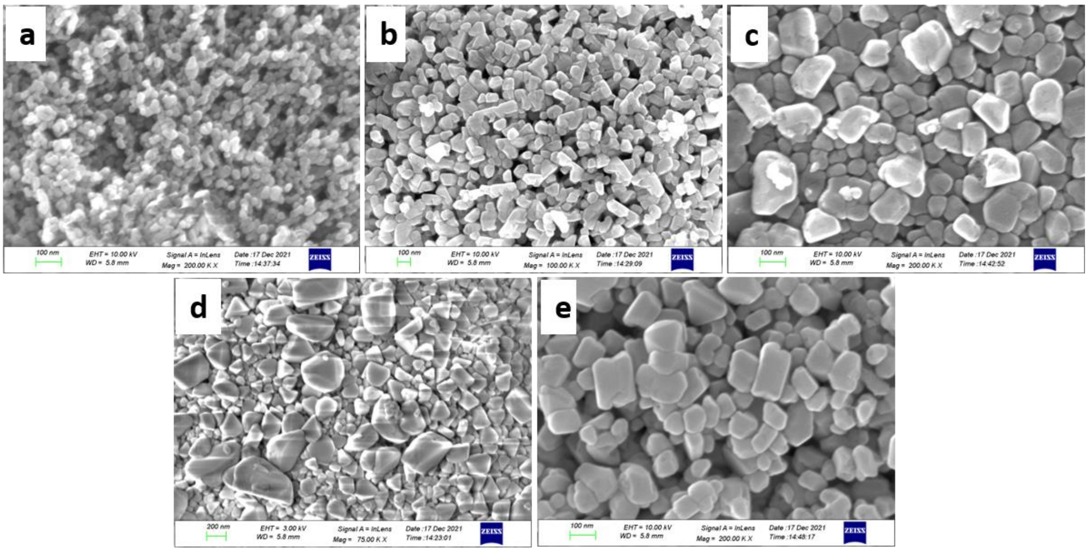

Figure 3.3. SEM image of a) ZnS0.67, b) ZnS1 c) ZnS1.5 d) ZnS2 e) ZnS3

3.2.2.4 Transmission Electron Microscopy (TEM) and Energy-Dispersive X-Ray analysis (EDAX)

The example with ZnS1 was additionally described by TEM (Figure 3.4a) procedure joined by. TEM picture shows that, not every one of the particles is spherical. At the same time, any additional different shapes are scarcely noticed. The normal size of the particles assessed from the TEM images is 46.5 nm in the range of size 15.7-87.3 nm. The size distribution curve of ZnS1 is shown in Figure 3.4b. The particle sizes derived by TEM images are obviously bigger than those from

XRD. This indicates that the synthesis route produces ZnS agglomerate nanoparticles or can also be interpreted as XRD expecting normal atomic distribution in the examples. However, TEM gives the standard size of the particles, including the non-crystalline part [4]. From the selected area electronic diffraction (SAED) in Figure 3. 4c of samples, it was seen that ZnS nanoparticles were polycrystalline and the (111), (220) and (311) planes from the inside ring to the beyond SAED investigation affirm the Zinc blende structure of items, which is consistent with XRD and RAMAN results. A delegate HRTEM picture enlarging a round part of the structure is given in Figure 3.4d. The interplanar distances of the crystal fringes are around 0.209 nm.

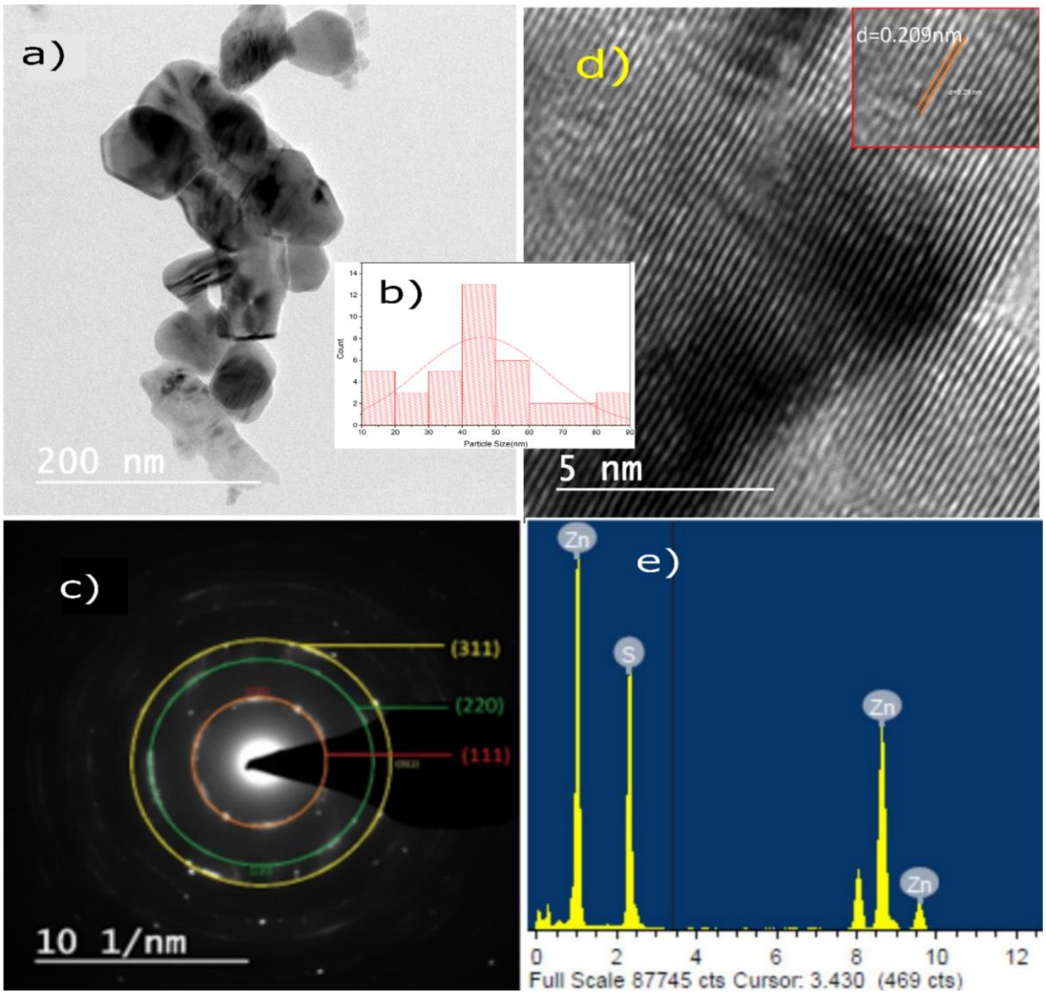

Figure 3.4. a) TEM image of ZnS1 b) Size Distribution Curve of ZnS1 c) SAED Pattern of ZnS1 d) HRTEM image of ZnS1 e) EDAX Spectrum of ZnS1

Typical EDAX analysis was performed to assess the constituents of the synthesized products and the results are presented in Figure 3.4e. Zn and S have produced four distinct signals demonstrating that the product was pure ZnS.

3.2.2.5 Inductively Coupled Plasma Optical Emission Spectroscopy (ICP-OES)

Determining the lighter elements or volatile components in semiconducting materials can be difficult regardless of the analytical approach. High-energy photons, electrons, or ions impact the material during the measurement and may expel lighter or volatile components, damage the surface, or modify the oxidation state and crystal structures. ICP-OES (Inductively Coupled Plasma Optical Emission Spectroscopy) is a technology used for elemental analysis. Environmental analysis, geology, pharmaceuticals and materials research are just a few sectors that use it extensively.

The ICP-OES data reveal that all samples follow the predicted S/Zn ratio trend (Table 3.3). The changes in S/Zn ratios observed by ICP-OES followed the predicted pattern of partial loss of volatile S species during ICP-OES sample preparation [390]. When exposed to acid, semiconductors that generate volatile hydrides, such as H_2S, are vulnerable to elemental loss during digestion [390]. ICP-OES has different detection limits for each element and may be less sensitive than other methods for some elements or at low concentrations. If the concentration of Zn and S in the ZnS nanoparticles is less than the ICP-OES instrument's detection limit, this might explain the lower observed percentage. Moreover, X. Yang *et al.*, reported that the ICP-based overall analysis is not accurate for the S analysis [133].

3.2.2.6 X-RAY Photoelectron Spectroscopy (XPS):

X-ray photoelectron spectroscopy (XPS) is used to investigate the surface composition and chemical state. All binding energy (B.E) values in the XPS spectra were calibrated using the C 1s line at 284.8 eV. Measurements were made of the XPS spectra of ZnS0.67, ZnS1 and ZnS3. The high-resolution XPS spectra (Figure 3.5a) of Zn 2p for ZnS0.67 show two peaks at 1044.48 eV and 1021.26 eV, separated by around 23 eV. Goudarzi *et al. and* Z. Ye *et al.*, stated that these are ascribed to Zn $2p_{1/2}$ and Zn $2p_{3/2}$ [391] [386]. Zn $2p_{1/2}$ and Zn $2p_{3/2}$ peaks of ZnS1 are detected at B.E values of 1021.69 eV and 1044.64 eV, respectively, while the same for ZnS3 is observed at 1022.68 eV and 1045.7 eV. As the S concentration rises, these peaks move slightly to higher B.E. Excess S atoms in S-rich ZnS can create extra chemical bonds or defects in the crystal. These modifications may result in greater binding energy for the Zn 2p electrons in XPS.

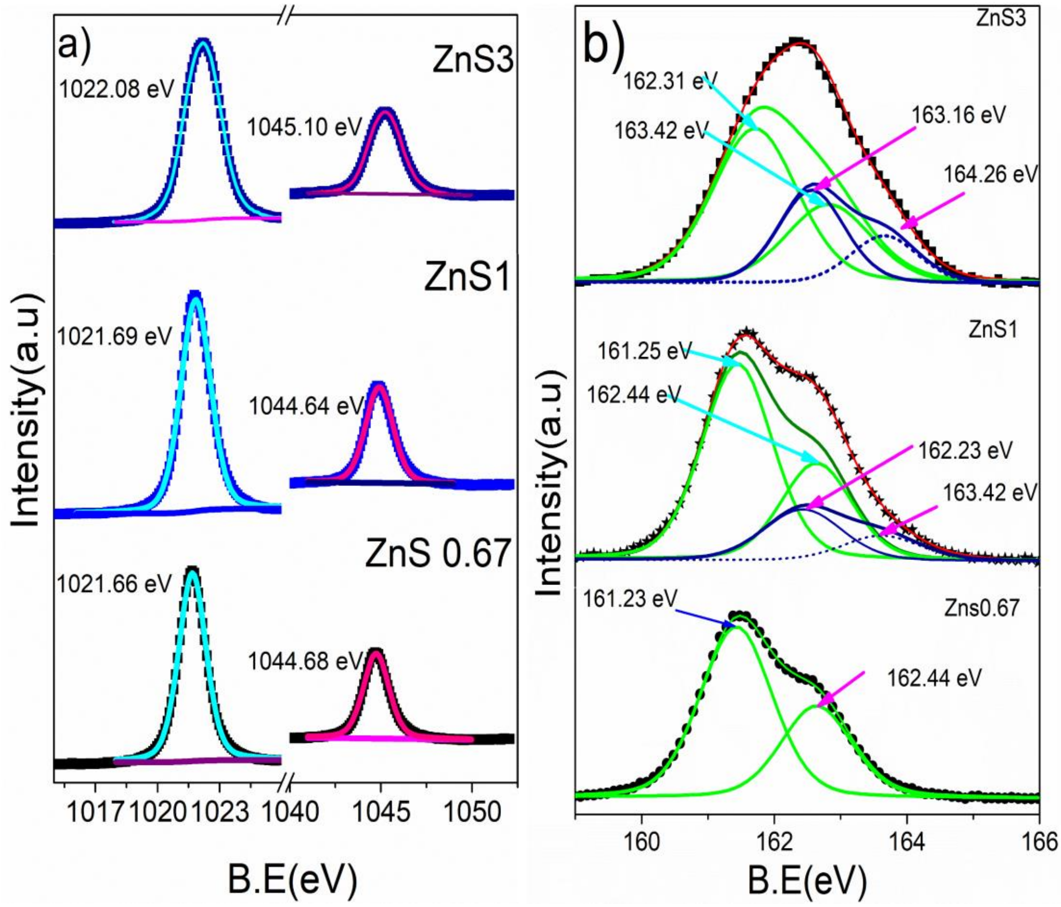

Figure 3.5. XPS spectra of ZnS0.67, ZnS1 and ZnS3 a) Zn2P region XPS Spectra b) S2P region XPS Spectra.

The S $2p_{3/2}$ and S $2p_{1/2}$ peaks for ZnS0.67 are positioned at around 161.23 eV and 162.43 eV, X. Yang et al., also reported the same finding [392], respectively, which are typical ZnS features, however when the S content rises, the of the asymmetric core level XPS spectra of S 2p may be resolved into four peaks (Figure 3.5b). For ZnS1, deconvoluted peaks of core level XPS spectra of S 2p are detected at 161.25 eV, 162.44 eV, 162.23 eV and 163.42 eV. The B.E 161.25 eV and 162.44

eV are derived from S $2p_{3/2}$ and S 2p $_{1/2}$ of S atoms bound in ZnS, whereas 162.23 eV and 163.42 eV are derived from the defect state in ZnS [343]. The defect percentage calculated from the area under the respective peaks in XPS is 18% for ZnS1.

Deconvoluted peaks belonging to core level XPS spectra of S 2p of bonded S are seen at 162.31 eV and 163.42 eV, 163.16 eV and 164.26 eV for sample ZnS3 (Figure 3.5b). The B.E 162.31 eV and 163.42 eV are derived from S $2p_{3/2}$ and S 2p $_{1/2}$ of S atoms bound in ZnS, while peaks relating to defects are observed at 163.16 eV and 164.26 eV. The area of the peaks corresponding to the defects is greater in ZnS3, with 34% of the defects computed for the same. The XPS examination result shows that the defects are in the prepared samples. This implies that the concentration of defects may be regulated to some extent by adjusting the molar ratio of precursors utilized. X. Hao *et al.,* used the same method in their study [343].

3.2.2.7 Diffused Reflectance Spectra Analysis

The prepared ZnS0.67, ZnS1, ZnS1.5, ZnS2, ZnS2.5 and ZnS3 samples' UV-vis DRS are examined to determine the impact of the defects on the electronic and optical properties of ZnS NPs. The DR (Figure 3.6a) shows a sharp hike in the reflection in the UV region, between 330 nm and 350 nm for different samples, corresponding to the transition from the valence to the conduction bands (CB) of the ZnS NPs. It should be also noted that reflection is very high in the wavelength region of 400 and 1200 nm for all samples.

The Kubelka - Munk function was utilized on the diffused reflectance (R) information to appraise the absorption of the sample [393][394]

$$\mathbf{F(R)} = \frac{(\mathbf{1-R}))^{2}}{2R} \qquad (3.11)$$

The band gap (E_g) values can be assessed from Tauc relations (Figure 3.6b) for direct band gap materials in the structure [395][396],

$$\mathbf{(F(R)\ h\ \nu\ )^{2} = A\ (h\ \nu - E_{g})} \qquad (3.12)$$

where 'A' is a constant and 'ν' is the frequency. The band gap values are determined from the extrapolation of the Kubelka-Munk function. The determined E_g for various examples are displayed in Table 3.3. The E_g varies from 3.28 eV to 3.49 eV for different ZnS samples. The E_g value is minimum for the ZnS2 sample and maximum for the ZnS3 sample. The absorbance plot in Figure 3.6c demonstrates that all prepared samples absorb sunlight, showing that all ZnS NPs have visible-light-induced PC activity resulting from the vacancy states in their band structures. Zn deficiency samples show high absorption intensity compared to other samples.

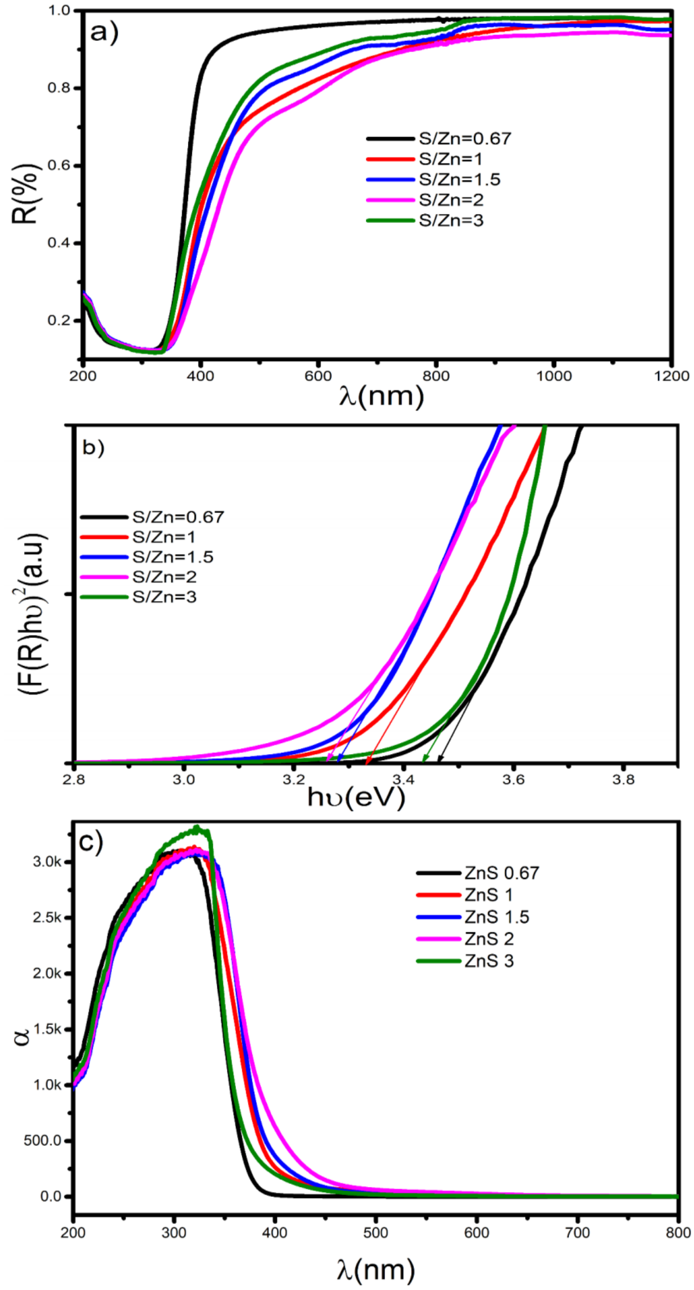

Figure 3. 6. a) Reflectance Spectra of ZnS Samples b) $(F(R)h\nu)^2$ Vs $h\nu$ plot c) Absorption Spectra

3.2.2.8 Photoluminescence Studies

Figure 3.7a shows the Photoluminescence spectra of ZnS nanoparticles with different S/Zn stoichiometric proportions for an exciting wavelength 280 nm. The S/Zn ratio fluctuated from 0.67 to 3 in the precursor medium. According to the report by J. Zhou *et al.*, the point defects that act as luminous centres during photoluminescence processes are linked to defect emission [384]. In pure ZnS, different forms of point defects are commonly found as Sulphur vacancies (Vs), Zinc vacancies (V_{Zn}), interstitial Sulphur atoms (I_S) and interstitial Zinc atoms (I_{Zn}) [343]. According to reports, the point defects that act as luminous sites during photoluminescence processes are linked to defect emission. The PL spectra show the emissions are at 365 nm, 383 nm and 473 nm. The emission wavelengths around 365 nm and 383 nm have arisen due to the transition from interstitial Zn. Transitions corresponding to 365 nm are from I_{Zn} in the samples. The transition at 383 nm corresponds to the transition from I_{Zn} to I_S interstitial states. The same transition is observed by B. L. Devi *et al.*, in their work [397]. The intensity of broad blue emission (473 nm) from the prepared ZnS NPs differed with changes in proportion. According to B. Lalitha Devi *et al.*, the strong emission at 473 nm was caused by the recombination of holes at the surface state (SS) and electrons trapped by Vs sites. ZnS0.67 sample shows a solid blue discharge with the peak extreme at 473 nm. Notwithstanding, as the sulphide fixation is expanded, the intensity of the blue band diminishes impressively and nearly vanishes at an abundance S level for ZnS3. In a pure ZnS, the possible emission sites are related to surface or lattice deformities or local impurities with a low concentration of sulphide particles, during synthesis, the ZnS formed will have a bigger number of Vs, which can serve as doubly ionized donor places. K. Manzoor *et al*. and H. Y. Lu et al., observed that similar variety in the intensities of all emission bands in undoped ZnS with change in stoichiometry suggests their relationship with Vs centres [398][399][5]. The energy level diagram (Figure 3.7b) depicts possible emission processes in ZnS nanoparticles. The crystal defect is responsible for these defect-induced emission peaks and the variations in PL intensity.

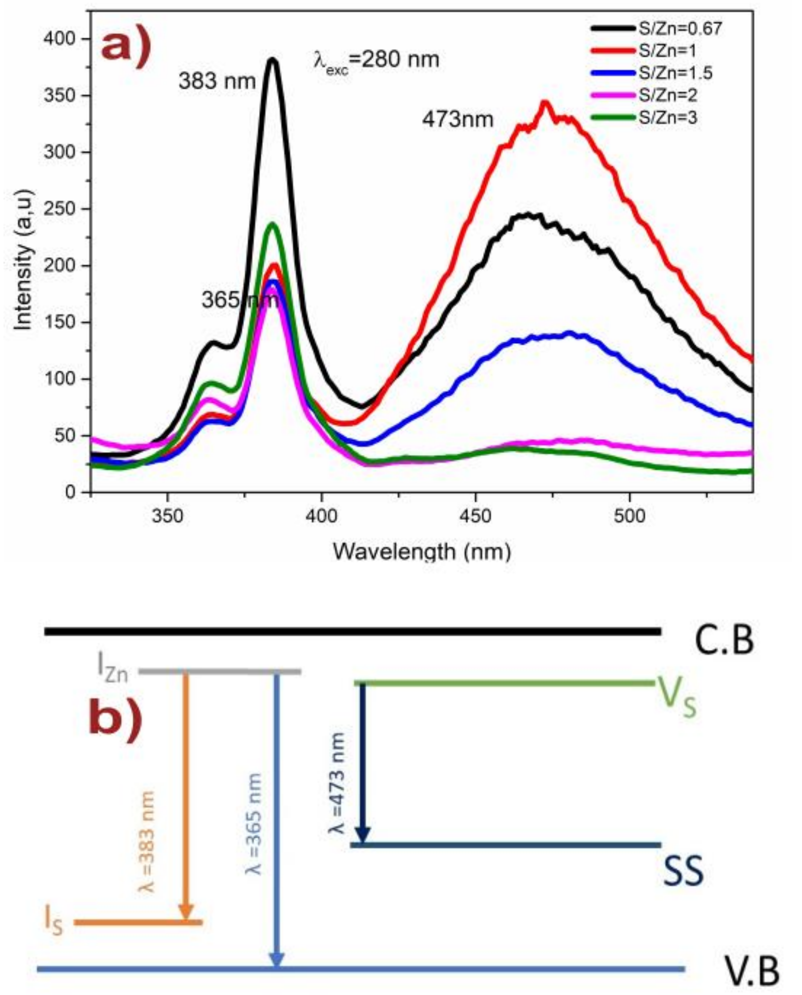

Figure 3.7 a) PL Spectra of ZnS nanostructures**,** b) Energy band gap diagram

3.2.2.9 Photocatalytic Studies

Defect engineering is a low-cost and effective modification technique for designing and developing single-phase catalysts for atomic-scale regulation and the formation of active sites on photocatalyst surfaces [400][401][402]. Of the various defects, surface vacancies can control the surface atomic architecture and local coordination structure of the catalyst, exposing and activating the surface atom to make a single-phase catalyst possess high activity. Furthermore, other than creating defect levels and increasing the photocatalyst's photo absorption capability, the anion and cation vacancy defects have unique impacts [403]. Anion vacancies (S) have been shown to attract photogenerated electrons and limit carrier recombination [404][405], whereas cation (Zn) vacancies can boost surface charge transfer and increase the valence band (VB) position to reduce h^+ oxidation capacity [406][131][407].

As a result, the vacancies enhance the photocatalytic activity and stability of the catalyst.

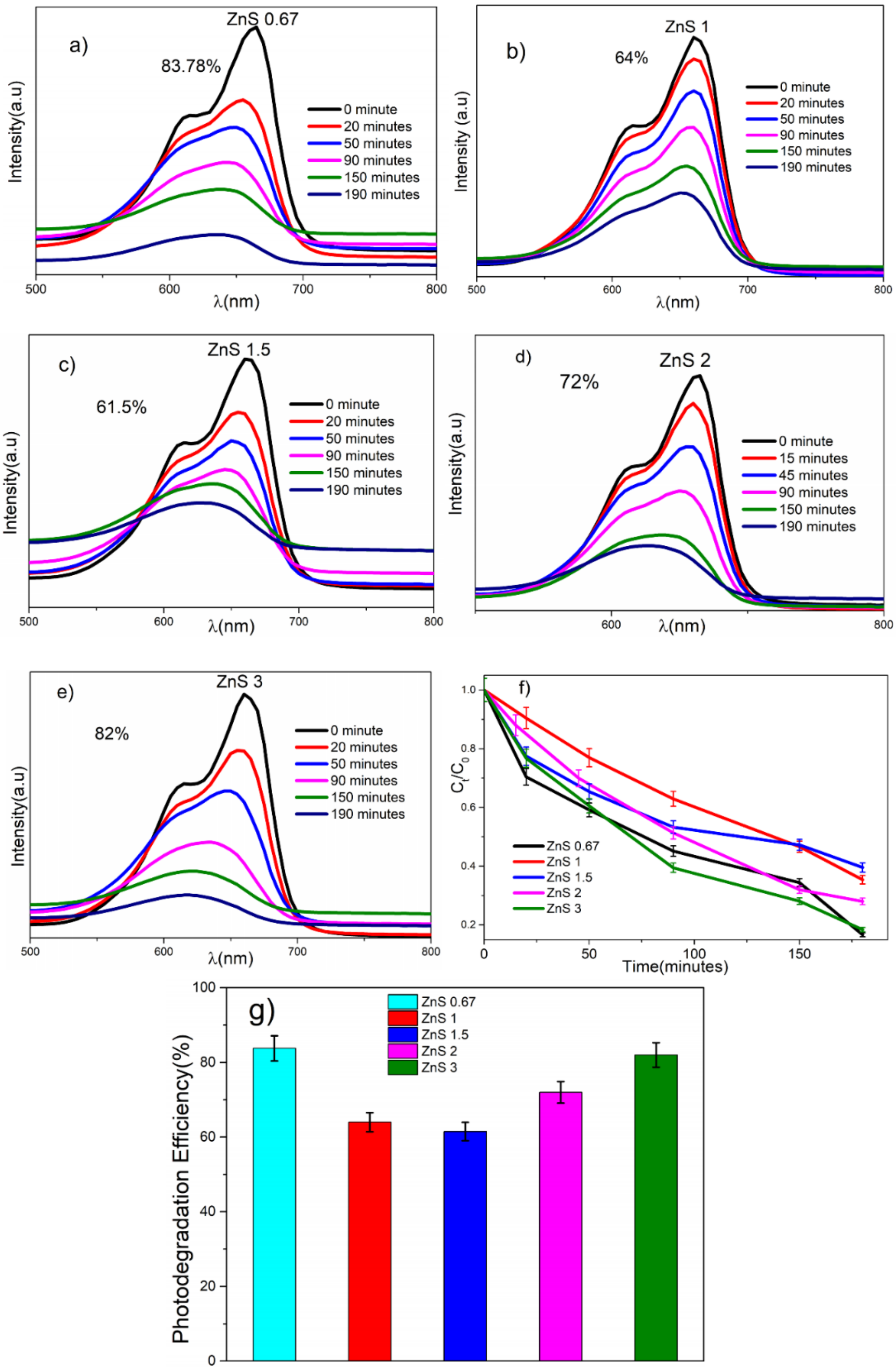

Figure 3.8. a)-e) Time-dependent absorption spectra of photocatalytic degradation of MB dye solution with ZnS photocatalyst f) Photodegradation of MB Dye solution with ZnS photocatalyst g) Percentage Photodegradation Efficiency of ZnS photocatalyst.

The presence of defective states in the synthesized samples are confirmed by Raman spectra, XPS and PL investigations and hence, visible-light PC activities are critical to our investigations. The Figure 3.8 (a-e) shows the time-dependent absorption spectra of PC degradation of MB dye under sunlight irradiation for all samples. Figure 3.8f depicts the MB solution's photodegradation at set intervals of sunshine exposures. The photodegradation efficiency percentage of samples are shown in Figure 3.8g. The crystallinity, surface area and shape are known to affect how the PC process. The PC activity may be enhanced by lowering the recombination of photogenerated electron-hole (e^- -h^+) pairs, stretching out the excitation wavelength to a smaller energy range and expanding surface-adsorbed reactant species [408][132][409]. In general, the system for photocatalysis starts when supra-band hole photons are explicitly absorbed in this manner, creating (e^- -h^+) pairs in the semiconductor particles. Following this, the charge carriers are dispersed across the molecules' surfaces, where they mix with water molecules to produce highly reactive forms of peroxide (O^{2-}) and hydroxyl radical (OH), which cause the degradation of adsorbed molecules. The following diagram demonstrates how methylene blue is photo-catalytically degraded over a ZnS photocatalyst. Adsorption of the dye onto the outer layer of the ZnS nanostructure is the first step [386]. When dye-adsorbed ZnS nanostructures are exposed to sunlight, (e^- -h^+) pairs are formed.

$$ZnS + h\nu \rightarrow e^-(CB) + h^+(VB)$$

The light-induced electrons in the CB of ZnS associate with the oxygen atoms adsorbed on ZnS to shape superoxide anion extremists $(O_2^{\bullet -})$. The holes created in the valence band (VB) of ZnS react with surface hydroxyl groups to deliver extremely reactive (•OH) radicals [332].

$$O_2 + e^- \rightarrow O_2^{\bullet -}$$

$$h^+ + OH^- \rightarrow \bullet\, OH$$

These holes (h^+) can prompt the separation of water atoms in the fluid arrangement, creating radicals. The exceptionally reactive (•OH) radicals and superoxide radicals ($O^{2\bullet -}$) can react with methylene blue dye adsorbed on ZnS nanostructures and lead to its decomposition [345].

$$h^+ + H_2O \rightarrow H^+ + \bullet OH$$

The schematic illustration of the dye degradation process using ZnS is shown Figure 3.9

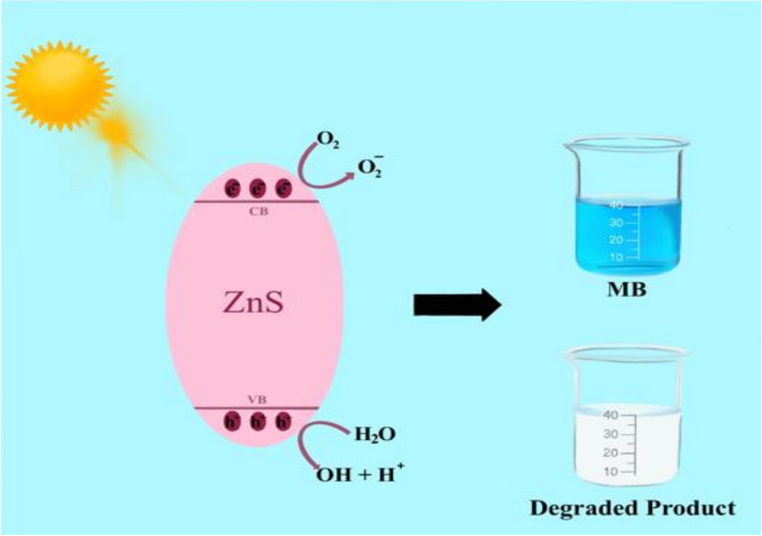

Figure 3.9- Schematic illustration of the dye degradation process using ZnS

The photodegradation efficiency is more for the samples having S/Zn=0.67 and 3. J. Zhou *et al.*, X. Hao *et al. and* F. Chen *et al.*, also used the same strategy to improve the light-harvesting properties of photocatalyst [384][410][343]. The reason for the high PC degradation of the sample with S/Zn=0.67 is S vacancies in the crystal. For ZnS, each S^{2-} ion forms a SZn_4 tetrahedron with four Zn^{2+} ions around it, while each Zn^{2+} ion forms a ZnS_4 tetrahedron with four S^{2-} ions surrounding it. All four Zn atoms around a S vacancy in a SZn_4 tetrahedron transform into a ZnS_4 pyramid with one sp^3 dangling bond when one S atom is removed from the structure. When the composition surrounding the vacancy site is loosened, the symmetry is lowered, which causes the 1t level to split and a huge increase in the energy difference between the 1t and 1a levels. The result is that the three empty levels approach the CB minimum, while the 1a level approaches the VB maximum and becomes doubly filled. Around an S vacancy in the relaxed structure, one ZnS_3 pyramid that becomes powerfully pyramidal in the loosened structure surrounding an S vacancy has its dangling bond double-filled to become a lone pair.

The optical excitations connected to the filled defect level are then close to the VB maximum, while the unfilled defect levels below the CB minimum cause the ZnS samples with S vacancies to absorb visible light [133]. Additionally, these defect states capture photogenerated electrons and holes, which delay their recombination and improve the PC performance of ZnS samples with S vacancies [411][332]. Additionally, S and Zn vacancies could cause a little deviation of the perfect ZnS and lower its volume [412]. After geometric relaxations, the cell volume loss caused by S-vacancy is more noticeable than that caused by Zn-vacancy since it occupies a larger volume. S vacancies in ZnS crystals are more difficult to introduce than V_{Zn}. The energy required to produce S vacancies (7.05 eV) is larger than that required to form V_{Zn} (5.99 eV). Therefore, more V_{Zn} is expected in ZnS crystals than in S vacancies. The V_{Zn} is the reason for the high degradation of sample with S/Zn=3. V_{Zn} in the ZnS photocatalysts is responsible for the higher visible-light absorption and excellent charge separation efficiencies of ZnS catalysts, which result in better visible-light PC activities. The similar observations were reported by X. Hao *et al.* [343]. H. Zhang *et al.,* also conducted Visible light PC activity by varying the molar ratios. They reported maximum PC activity for ZnS with S/Zn=2 prepared by solid-state reaction [408]. Z. Fang *et al.,* adjusted the number of V_S and phase junctions to achieve optimal visible light activity on ZnS synthesized by hydrothermal and solvothermal methods [132]. X. Hao *et al.,* reported high visible light PC activity for ZnS synthesized by hydrothermal technique with Zn/S =2.5 [131]. The luminescence emission spectra (Figure 3.7a) shows the peak around 473 nm corresponding to the transition from sulphur vacancies to dangling sulphur bonds. These sulphur defect states act as trapping sites for charge carriers generated by visible light exposure contributing to their photocatalytic activity.

Under identical settings, the recycling experiments were repeated three times to study the stability of the catalyst using the Xenon lamp [141]. The ZnS1 catalyst was extracted at the end of each cycle for recycling purposes using a centrifuge. Figure 3.10 depicts the results that were obtained after three cycles of testing. The dye degrades with no substantial changes in the rate of degradation up to the third cycle, which is a very important observation. However, a nominal decrease in decay percentage was observed, attributed to partial surface passivation by the decomposed MB dye [410].

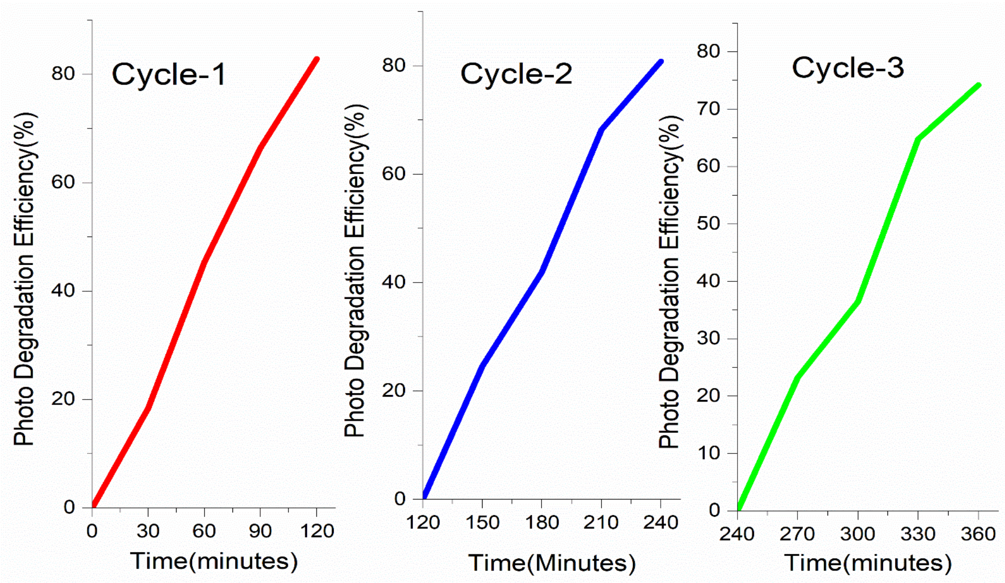

Figure 3.10 Recyclability tests of samples (Three runs) involved with MB degradation.

3.2.2.10 Brunauer-Emmett-Teller Analysis

BET techniques were used to determine the specific surface area of each sample. According to the experimental findings (Table 3.3), the Photodegradation Efficiency of the samples follows the order: ZnS0.67 > ZnS3 > ZnS2 > ZnS1 > ZnS1.5. However, the surface area follows a different trend: ZnS0.67 > ZnS1.5 > ZnS2 > ZnS3 > ZnS1. This disparity shows that defects within the materials have a greater impact on the visible-light photocatalysis of the defective ZnS systems [413] than their surface area. The defects like vacancies or defects created by the dopants can provide energy levels in the band gap making it easier to separate charges and absorb visible light enhancing photocatalytic activity. These findings demonstrate how the defects can be used to tune the photocatalytic activity of ZnS materials under visible-light irradiation.

In the present, work we investigated the effect of parameters including size, band gap energy, strain, surface area and defects on the photocatalytic activity of samples with varied S/Zn ratios. Interestingly, after analyzing the data, we observed that several parameters such as size, band gap energy, strain and surface area are known to affect the photocatalytic activity of the samples. However, the existence of defects in the samples appeared to play an important role in determining their photocatalytic activity. Increased defect densities resulted in increased photocatalytic activity. It suggests defects, rather than size, band gap energy, strain or surface area may be the most important parameter impacting this photocatalytic efficiency of samples. These findings emphasize the relevance of defect engineering into photocatalytic material design and development. It may be feasible to increase the photocatalytic activity and overall performance of materials by deliberately introducing and controlling defects. In order to optimize the design of effective photocatalysts, further research is needed to understand the unique function of defects and their impact on photocatalytic mechanisms.

Table 3.3 Band Gap energy from DRS, Compositional for ZnS NPs from ICP-OES and BET analysis result

Samples	**E_g(eV)**	**ICP-OES (Atomic %)**			**BET**	**Photodegradation Efficiency (%)**
		Sulphur	**Zinc**	**S/Zn**	**S.A(m^2g^{-1})**	
ZnS0.67	3.46	17.78	82.21	0.22	16.77	83.78
ZnS1	3.32	27.66	72.34	0.38	5.57	64
ZnS1.5	3.30	28.77	71.22	0.40	14.233	61.5
ZnS2	3.28	42.19	57.8	0.73	10.652	72
ZnS3	3.49	65.48	34.52	1.89	10.534	82

3.4 Conclusion

ZnS NPs with different S/Zn molar ratio have been synthesized using a low-temperature hydrothermal route for photocatalysis applications. Through defect engineering, the Zn and S defects are successfully introduced into the ZnS crystal, which also alters the band structure of ZnS. The defects are generated on the surface during the synthesis, which is evident from RAMAN, XPS and PL. The crystallinity and phase formation of the samples have been confirmed through XRD and Raman analysis. Through Scherrer, W-H model and size strain plot, the impact of crystal defect on the structural characteristics of ZnS nanoparticles was studied. There is a strong effect of S/Zn molar concentration on the energy gap and the band gap has been reduced from 3.49 eV to 3.28 eV ($\Delta E = 0.21$ eV). The ICP-OES data reveal that all samples follow the predicted S/Zn ratio trend. The PL spectra show that the ZnS nanoparticles emit dual colors which are violet and blue. The NPs agglomeration can be seen in TEM images; however, the size of synthesized NPs is in the quantum dots range. SEM study reveals the different morphology of the synthesized ZnS NPs. The vacancy-dependent visible light photocatalytic activity has been studied. The photocatalysis degradation activity was very high for Sulphur defect-rich sample ZnS0.67 and Zn defect-rich ZnS3 samples. Our study reveals that the developed NPs of ZnS with rich defects are stable photocatalysts and highly applicable for waste-water treatment.

Chapter-4

Microwave assisted synthesis of quantum dots like ZnS nanoparticles

Nanoparticles of ZnS with different weights of CTAB (cetyltrimethylammonium bromide) have been successfully synthesized by Microwave assisted co-precipitation method. The x-ray diffraction pattern exhibits a cubic phase crystal structure with a crystal size of ~3 nm. The morphological properties of prepared samples were investigated using Scanning electron microscopy (SEM). Ultra-violet-visible absorbance spectra were recorded and calculated energy gap for the samples are in the range of 3.56 to 3.6 eV. Raman spectra confirm the synthesis of ZnS nanoparticles at all CTAB contents and it contains two major Raman modes at ~ 264 and 346 cm^{-1} *related to TO and LO modes which are shifted to lower wavenumbers indicates phonon confinement in the final products. The variation of the dielectric constant and dielectric loss was studied. The dielectric constant* ε' *is higher in the lower frequency region almost stable between 1MHz and 5 MHz and is increasing at higher frequencies. The dielectric study reveals that the samples possess high values of dielectric constant which are between 27 to 35 and lower loss values. The electrical conductivity is noticed to be increased with increasing the frequency and also noticed to be varied with varying the CTAB content in ZnS. The synthesized low dimension NPs, with high energy gap, high dielectric constant and lower loss values signify that the prepared NPs are suitable for optoelectronics.*

4.1 Introduction

The ZnS nanoparticles are very important II-VI semiconducting materials with anomalous physical and chemical properties such as: chemical activity, the quantum size effect, enhanced surface to volume ratio, more optical absorption, thermal resistance, surface and volume effect, macroscopic quantum tunnelling effect, catalysis and the low melting point compared to its bulk[150]. ZnS has great importance due to the elegance in chemical and physical properties, which is useful for wide range of applications [5]. The doping with different elements alter physical , chemical and optical properties , which can be used in applications like biosensing, imaging[150], solar cell[414] and UV-visible-NIR light photo detection[415]. We can tune different properties like structural and [4]photovoltaic properties of ZnS[332], using different modification technique and adding different chemical additives.

The preparation added with surfactants modifies the morphology and hence the different physical properties such as, photovoltaic [416] and magnetic properties of various nanomaterials [417]. Surfactants control the size and the uniformity of nanomaterials[418]. For the preparation of nanoparticles with uniform spherical and mesostructured morphology [418] suitable surfactants were added during synthesis. Surfactants can change the morphology of the hydroxyapatite and we can alter other properties such as surface area, Ca/P ratio, acid sites distribution and strength which consequently affects the catalyst activity of the hydroxyapatite sample in oxidation reactions[419].

Cetyl trimethyl ammonium (CTAB) bromide is a cationic surfactant which gets ionised when it dissolves in water. It contains a lipophilic radical at one end and a positively charged hydrophilic radical at the other end. CTAB is in high coordination with non-ionic amphoteric surfactants. CTAB has high resistivity against pressure, heat, light, static electricity and strong acidic/alkaline nature and has high chemical stability, therefore CTAB based nanohybrids widen its application range [420]. The concentration of CTAB can control the size of synthesised ZnS nanoparticle, which has great influence in the study of photocatalysis and luminescent properties[421]. CTAB can be used for reconstruction of microstructure and morphology of transition metal oxide nanomaterials to enhance the electrochemical performance for energy storage[422].

Microwave assisted method is a simple, uniform, quick and efficient synthesis technique for synthesis of nanomaterials. Since the reaction rate of the microwave assisted method is high, the synthesis time is comparatively less. This method is very simple and requires only minimum equipment [423]. In this chapter, we aim to study the effects of CTAB on the structural, optical and dielectric properties of ZnS nanoparticles prepared by microwave assisted co-precipitation route.

The results presented in this chapter have already been published as E. M. Jubeer, M. A. Manthrammel, M. Shkir, P. A. Subha, I. S. Yahia and A. Alfaify, "Optik Microwave assisted synthesis of quantum dots like ZnS nanoparticles for optoelectronic applications : An effect of CTAB concentrations," *Optik (Stuttg).*, vol. 240, no. March, p. 166812, 2021, doi: 10.1016/j.ijleo.2021.166812[368]

4.2 Experimental

4.2.1 Synthesis

The nanoparticles of ZnS were prepared by microwave assisted co-precipitation synthesis method. The brief procedure of synthesis is as follows. 0.5M Zinc Acetate and 0.5M Na_2S precursors were prepared separately in double distilled water (DDW) under continuous magnetic stirring at 60^{o}C for ~30 minutes. Then separately prepared CTAB solutions were added to the 0.5M Zinc Acetate precursors by weighing 0.0, 0.025g, 0.1g, 0.5g, 1g, 2.5g and 5gm, respectively CTAB in 100 mL each deionized water and continued the stirring for uniform mixing. They were mixed with 0.5M Na_2S precursors and the reactions were continued for 1 hour at 60^{o}C. The obtained solutions were microwave treated at 700 W microwave power for15 minute and the solutions were allowed to cool to room temperature naturally. The white products were systematically washed with DDW[424]. All chemicals used in the experiment were of analytic grade. Thus, pure ZnS and 6 different samples with different weights of CTAB were prepared.

4.2.2. Measurements

For Structural confirmation of prepared sample of pure ZnS and ZnS with different weights of CTAB the powder X-ray diffraction (PXRD) patterns were recorded using a Shimadzu X-600 Japan powder X-ray diffractometer (PXRD) having CuKα radiation and wavelength $\lambda = 0.1543$ nm and operated at 40 kV, 30 mA, at the scan rate of 0.02°/m over the angular range of 10°to 70° at 300 K. The morphological analyses for all the prepared nanostructures were done by using a scanning electron microscope (SEM). The dielectric measurement on pure ZnS and CTAB added ZnS nanostructures synthesized by microwave assisted technique have been carried out in the frequency range 3 kHz to 10 MHz at room temperature. The measurements were done using SCS 4200 semiconductor characterization system. Studies are made on pellet samples. The vibrational study was carried out at room temperature for all the nanostructures using a RAMAN spectrometer. The Raman system was operated at 0.2 mW laser power (532 nm laser). The room-temperature optical absorption spectra of the films were determined using a double beam UV-VIS spectrophotometer in the wavelength range of 200–1200 nm.

4.3 Results and discussion

4.3.1 X-Ray Diffraction analysis

The information about the crystal structure and the grain size of the nanoparticles will give by the X-ray diffraction pattern. Figure 4.1 shows the XRD patterns of pure ZnS, ZnS with 0.025g CTAB, ZnS with 0.1g CTAB, ZnS with 0.5g CTAB, ZnS with 1g CTAB, ZnS with 2.5g CTAB and ZnS with 5g CTAB. From the figure it is clear that there are three different diffraction peaks at 2θ values 29.08^0, 48.480 and 57.07^0. The diffraction peaks are due to reflection from (111), (220), (311) planes of cubic phase of ZnS. The XRD patterns of prepared samples are matched with standard ICDD (# 00-005-0566). It is clear that the ZnS grown with cubic phase, since no other phases have been observed. The significantly broadened diffraction peaks show the very small size of nanoparticles. The XRD pattern of all samples no show extra peaks due to impurity. No significant shifts in peaks and broadening have been observed with addition of CTAB. The lattice parameter (a) is observed using following equation

$$\mathbf{a} = \frac{\lambda}{2sin\theta}(\mathbf{h}^2+\mathbf{k}^2+\mathbf{l}^2)^{1/2} \qquad (4.1)$$

where λ is wavelength of X-ray used which is 1.54056Å, θ is Bragg’s angle and (hkl) is miller index of crystal plane. ’a’ was found to be very close to the reported value of cubic blend ZnS with standard ICDD (Reference code-00-005-0566). The average particle size was estimated using Debye-Scherrer equation.

$$D=\frac{k\lambda}{\beta\cos\theta} \tag{4.2}$$

where k is a constant 0.9, λ is X-ray wavelength, β is full width at half maxima of peak in radians and θ is Bragg's angle in radian. The various parameters measured from the XRD data are listed in the Table 4.1

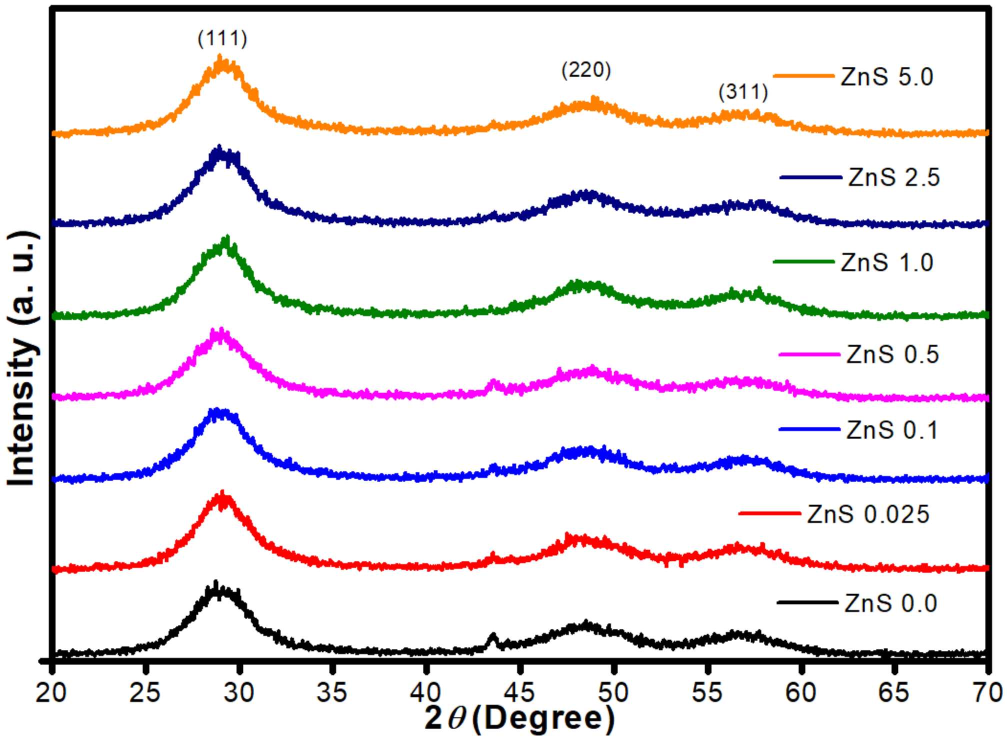

Figure 4.1 XRD patterns of ZnS:CTAB nanoparticles

Table 4.1: grain size, dislocation density and micro-strain values of ZnS: CTAB samples estimated from the XRD data.

CTAB quantity	D (nm)	δ (10^{-3}) nm^{-2}	ε (10^{-3})	a (nm)	V (nm^3)
0 g	1.92	286.010	51.039	0.5339	0.1522
0.025 g	2.16	217.319	45.265	0.5326	0.1512
0.1 g	2.04	257.372	48.949	0.5331	0.1515
0.5 g	1.81	330.304	54.332	0.5328	0.1513
1 g	2.09	234.770	46.562	0.5327	0.1511
2.5 g	1.965	269.547	49.374	0.5324	0.1509
5 g	2.039	248.980	47.502	0.5324	0.1509

4.3.2 Scanning Electron Microscopy (SEM)

The SEM image of pure ZnS, ZnS with 0.025g CTAB, ZnS with 0.1g CTAB, ZnS with 0.5g CTAB, ZnS with 1g CTAB, ZnS with 2.5g CTAB and ZnS with 5g CTAB is shown in Figure 4.2. The SEM analysis shows that the synthesized samples contain mainly the grains of ZnS particles (crystallite) with regular shape and uniform size. One can see that nearly spherical nanoparticles have an almost homogenous size distribution with a mean size of 100nm. SEM image shows general view of ZnS nanoparticles in large area. The ZnS products are aggregation of these small nanospheres which shows small dimensions and high surface energy.

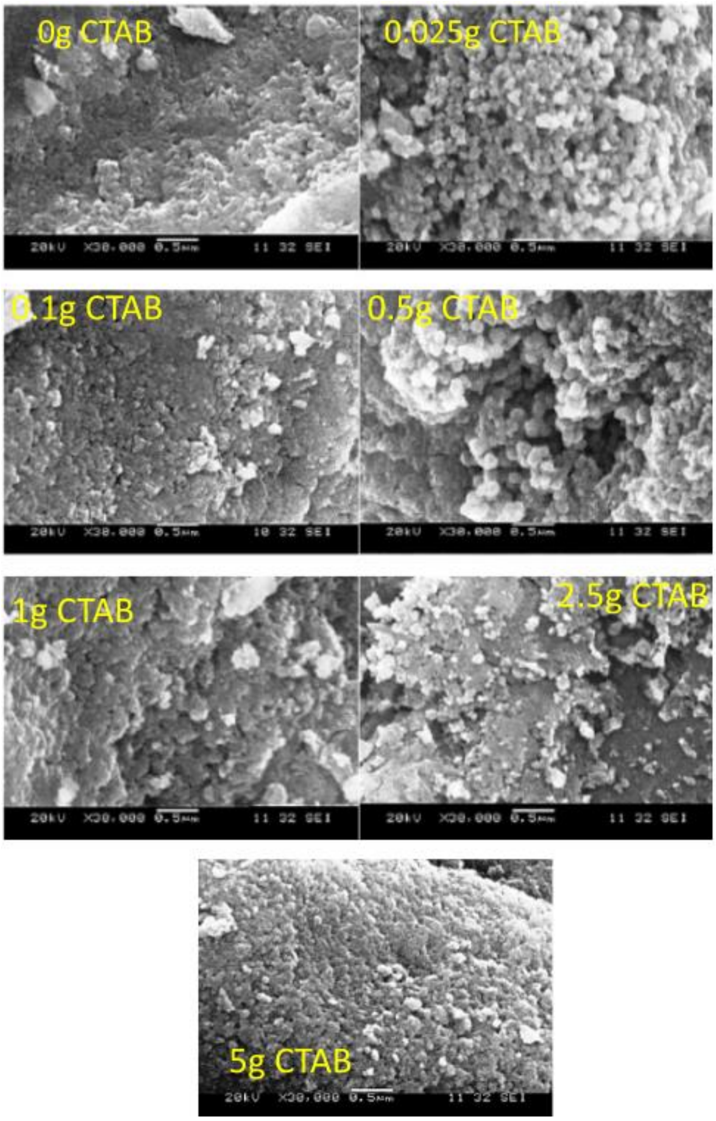

Figure 4.2 SEM images of ZnS:CTAB nanoparticles

4.3.3 Raman Spectra Analysis

The vibrational analysis has been performed through recording the FT-Raman spectra of the prepared different CTAB content assisted ZnS NPs as displayed in Figure 4.3. It is visible from figure that there are two major Raman modes in all prepared NPs of ZnS, however the intensity variation can be seen. The intensity variation indicates the variation in FWHM of the peaks, however it depends on the used excitation source and its power. The two major Raman bands are noticed at ~ 264 and 346 cm^{-1} which are related to fundamental Raman modes and are assigned to transverse optic (TO) and longitudinal optic (LO) phonon modes of ZnS[425]. In previous study these modes are reported at 260 and 341 cm^{-1} by Lalithadevi et al. [426]. The currently observed modes are noticed to be shifted towards lower wavenumber compared to bulk values reported at 274 and 351 cm^{-1}[425]. Such shift in Raman modes is linked with the phono confinement effect owing to nano size.

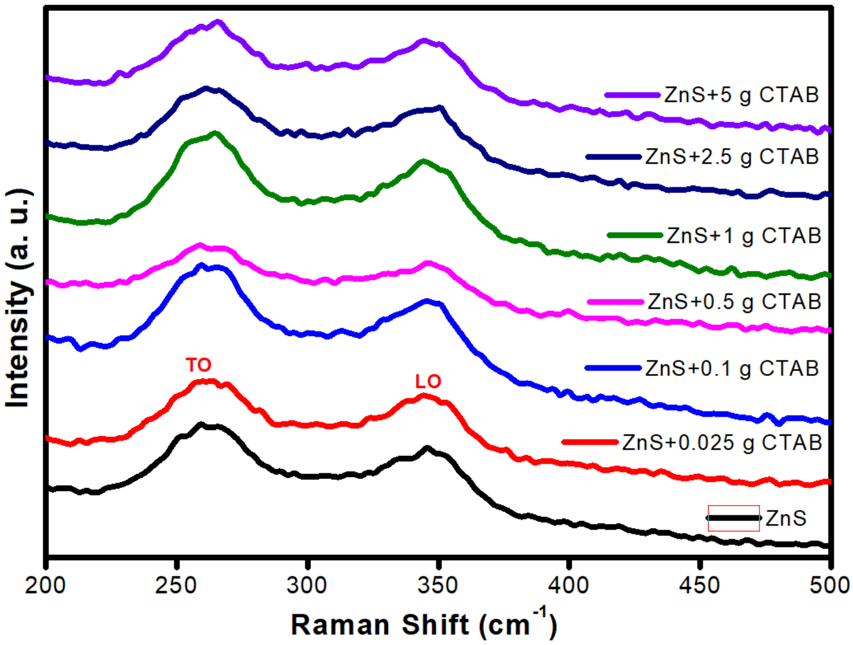

Figure 4.3 Raman spectra of the ZnS: CTAB nanoparticles

4.3.4 Optical Properties

Figure 4.4a show the diffuse reflection spectrum of sample pure ZnS, ZnS with 0.025g CTAB, ZnS with 0.1g CTAB, ZnS with 0.5g CTAB, ZnS with 1g

CTAB, ZnS with 2.5g CTAB and ZnS with 5g CTAB. It shows a sharp increase in reflection in the UV range approximately up to 400 nm., corresponding to the valence to-conduction band transitions of the ZnS nanostructure [369]. In order to verify absorption of the sample, the Kubelka - Munk function was used

$$\mathbf{F(R)} = \frac{(1-R)^2}{2R} \qquad (4.3)$$

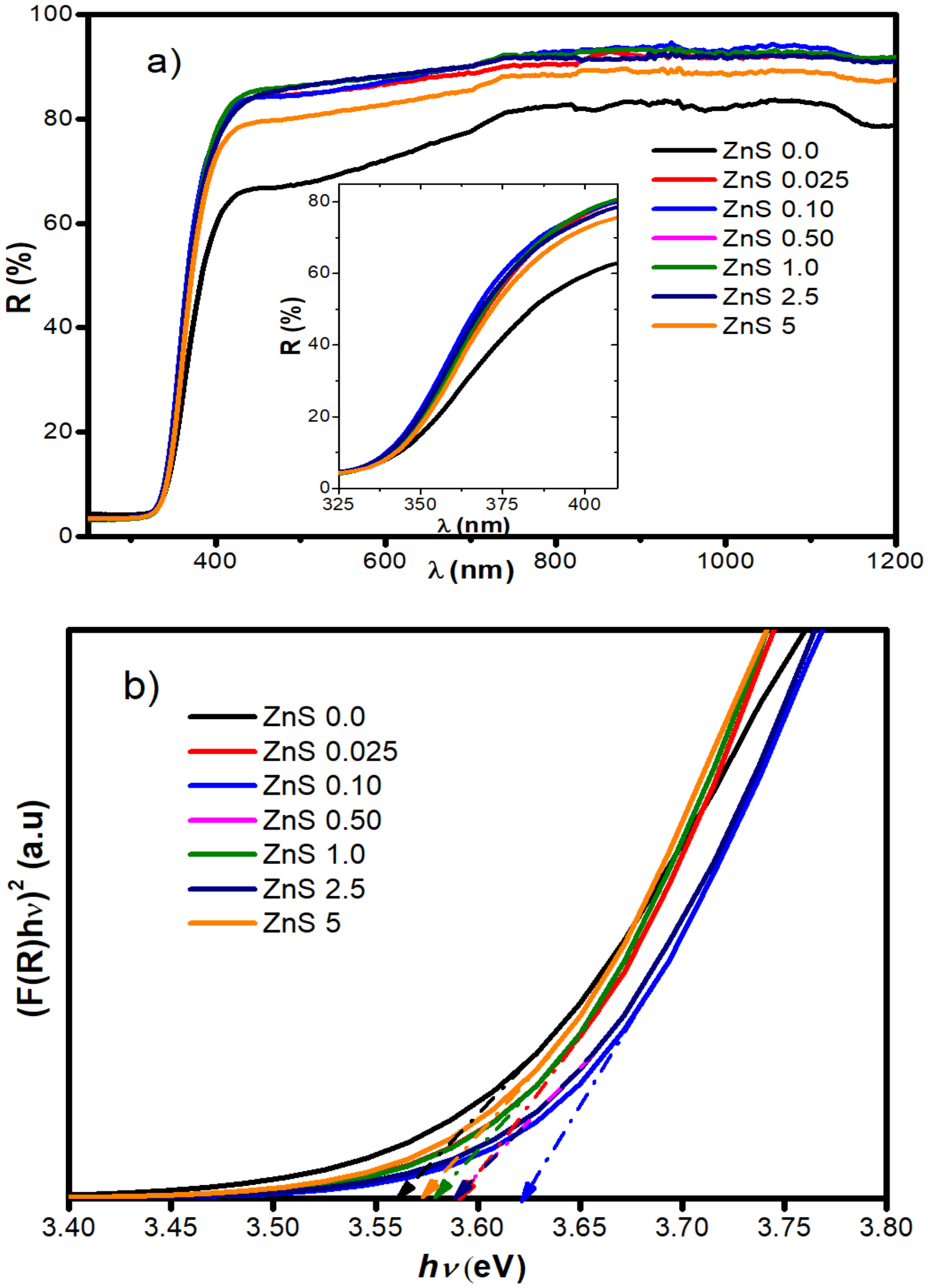

Figure 4.4 a) Reflectance Spectra (inset-magnified plot of reflectance for the wavelength range 325 nm to 425 nm) b) $(F(R)h\nu)^2$ Vs h ν plot of the ZnS: CTAB nanoparticles

The value of the optical band gap can be calculated by extrapolating the Kubelka - Munk function (Figure 4.4b). The calculated band gaps for different samples are shown in the Table 4.2.

Table 4.2 Band Gap energy from DRS

S. No.	Sample	Bandgap(eV)
1.	Pure ZnS	3.56
2.	ZnS +0.025g CTAB	3.59
3.	ZnS +0.1g CTAB	3.61
4.	ZnS+0.5g CTAB	3.59
5.	ZnS+1g CTAB	3.58
6.	ZnS+2.5g CTAB	3.59
7.	ZnS+5g	3.57

4.3.5 Dielectric Property Analysis

The dielectric constant (ε′) and loss (ε″) parameters were estimated from the measured capacitance (C) and loss tangent (tan (δ)) data using the relations

$$\boldsymbol{\varepsilon' = \frac{Cd}{\varepsilon_0 A}} \qquad (4.4)$$

$$\boldsymbol{\varepsilon'' = \tan(\delta) \times \varepsilon'} \qquad (4.5)$$

where d and A are the thickness and cross-sectional area of the pellet samples[427]. The Figure 4.5a shows the variation of dielectric constant ε’ with frequency. From the graph, it is observed that the dielectric constant ε’ has higher values at the low frequency regime, which becomes nearly stable between 1 MHz and 5 MHz and is then increasing at higher frequency range. This observed behaviour of ε’ at the low frequencies is due to the contributions from all four frequency dependent charges such as space charge polarization, ionic, electronic and dipolar [428]. The reason for the observed initial decreasing of ε’ with frequency for the pure and CTAB added ZnS NPs followed by the nearly stable state within ~ 1–6 MHz could be attributed to the special characteristics of the electric field dipoles, that cannot follow the alternating field beyond certain frequencies.

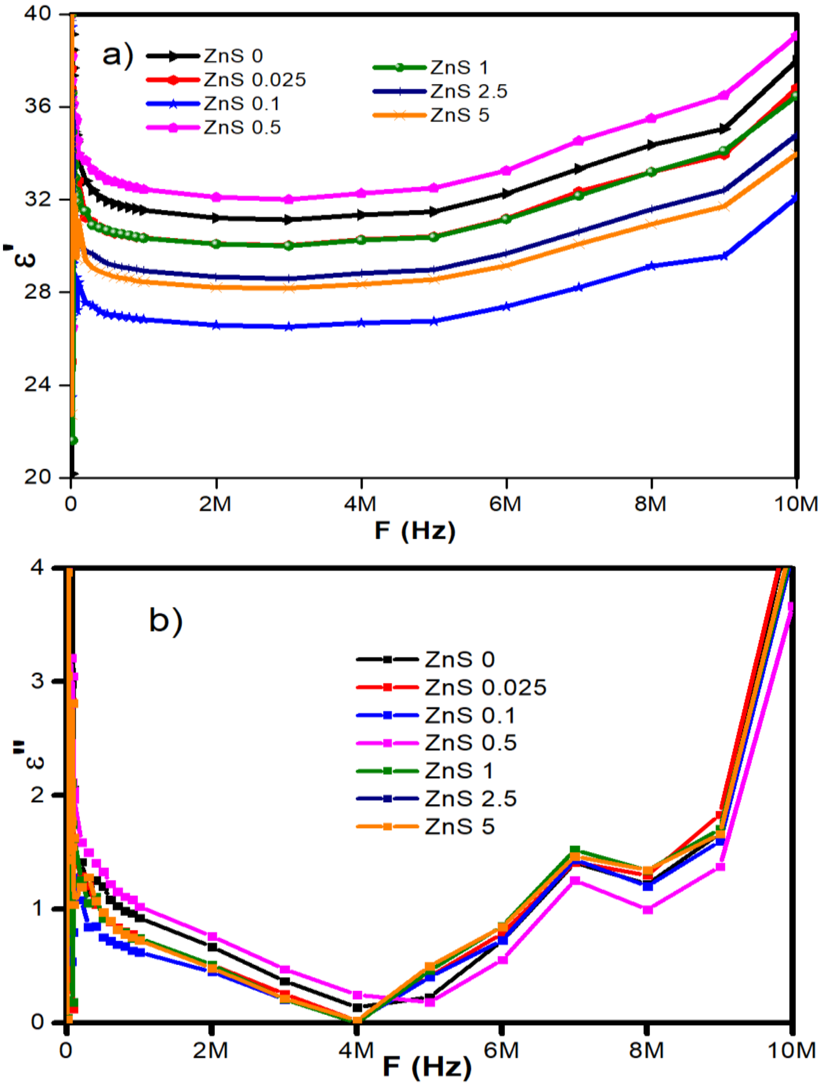

Figure 4.5 Variations of a) dielectric constant and b) dielectric loss vs. frequency.

The values of ε′ are found within the range 26–39 in the frequency range 1 kHz to 10 MHz. These values express slight enhancement in ε′ compared to the most of the previous works on ZnS based nanoparticles and thin films, in the range 103–107 Hz [429][430]. This could be due to the fact that most of the atoms in NPs reside on the grain boundaries where the charge trapping makes them electrically active sites. Also, contributions from space charge and rotation polarizations are also prominent at the interfaces. Thus, nanostructured particles exhibit comparatively larger ε' values. The ε' values of 30–40 has been reported by Suresh et al. in wide range of frequencies 10^4- 10^7 Hz, at 40–150 °C [146]. Figure 4.5b represents the variations of the dielectric loss with respect frequency. From the figure, the dielectric loss values showed a clear decreasing tendency with frequency for all the samples and observed their minimum at 4 MHz However, the dielectric loss values are increasing sharply above 4 MHz. The maximum value of dielectric constant was observed for 0.5 g CTAB: ZnS sample and the same sample displayed the maximum dielectric loss below 4 MHz frequency whilst it exhibited the minimum dielectric loss beyond 4 MHz. The changes in dielectric loss properties are related to various factors like grain sizes, lattice vibration mode and contributions from various polarization mechanisms [429].

4.3.6 Electrical Conductivity Analysis

The following relations were employed to extract the useful information regarding the total ac conductivity ($\sigma_{ac.tot}$).

$$\boldsymbol{\sigma}_{\mathbf{ac.tot}} = \frac{\mathbf{1}}{\boldsymbol{ZXA}} \tag{4.6}$$

$$\boldsymbol{\sigma}_{\mathbf{ac}} = \boldsymbol{\sigma}_{\mathbf{dc}} + \mathbf{B}\boldsymbol{\omega}^{\mathbf{s}} \tag{4.7}$$

where the latter is the Jonscher law that connects the ac conductivity, σ_{ac} with dc conductivity, σ_{dc} and angular frequency ω. Here B and exponent s are constants [431], (l is the thickness = 1.35 mm and A is the area = 7.85×10^{-5} m^2). The plot of ac conductivity vs. frequency for all the prepared NPs is shown in Figure 4.6. The figure clearly shows that the results obey the frequency power law and increasing of the σ_{ac} with frequency. The maximum ac conductivity was observed for the 0.5 g CTAB content added ZnS NPs. The exponent values were also computed for all the samples from the slope of above plots in Figure 4.6 and are obtained to be 0.986,0.988,0.992,0.984,0.992,0.988,0.989 for pure ZnS, ZnS with 0.025 g CTAB, ZnS with 0.1 g CTAB, ZnS with 0.5 g CTAB, ZnS with 1 g CTAB, ZnS with 2.5 g CTAB and ZnS with 5 g CTAB.

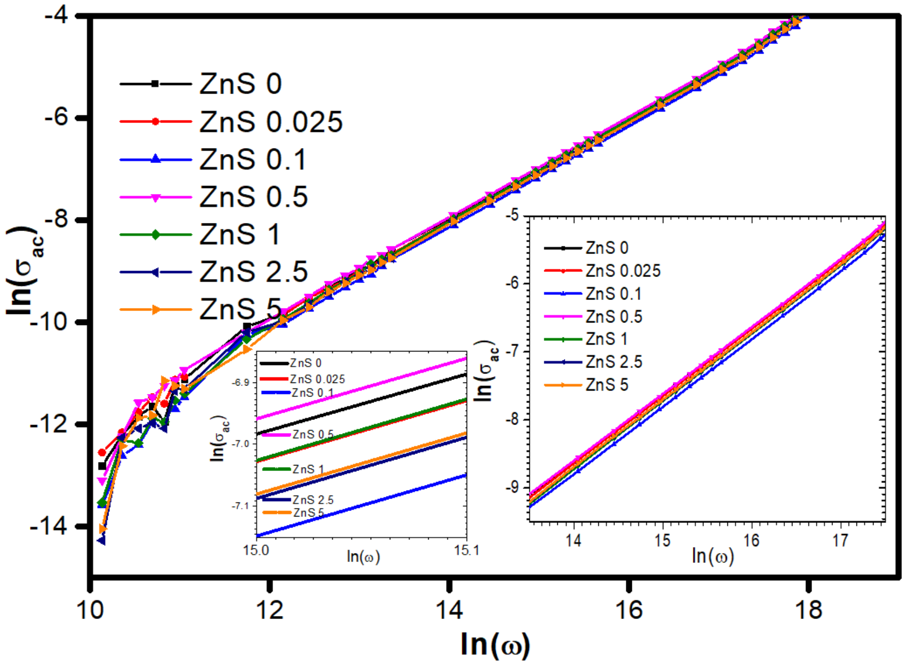

Figure 4.6 Variation of ac conductivity with angular frequency, (the inset shows two magnified plots for frequency between 13to19 and 15.0 to 15.1)

The 0.5 g CTAB concentration in ZnS nanoparticles has been identified as the optimum, as it results in the highest dielectric constant and maximum ac conductivity. This optimized concentration leads to enhanced dielectric properties, making it particularly suitable for applications in capacitors and other high-frequency electronic devices. Additionally, the high ac conductivity suggests potential use in energy storage systems and advanced electronic materials.

4.3.7 Photocatalytic Studies

The photocatalytic tests were conducted for the ZnS sample with optimum CTAB concentration. The effective use of ZnS with 0.5g of CTAB as photocatalysts for the breakdown of Methylene Blue (MB) dye was investigated by photocatalytic (PC) examinations. For the experiment, 10 mg of MB was dissolved in 1 L of distilled water to prepare the MB dye solution. Then, 0.03 g of photocatalyst was added to 25 ml of this solution. The mixture was magnetically agitated in the dark for an hour to attain an adsorption-desorption equilibrium between the dye molecules and the catalyst surface. Photocatalytic activity was tested on sunny days between 11 a.m. and 2 p.m. However, no significant degradation of the MB dye was found in the presence of ZnS, indicating that these materials do not exhibit effective photocatalytic activities as shown in the Figure 4.7.

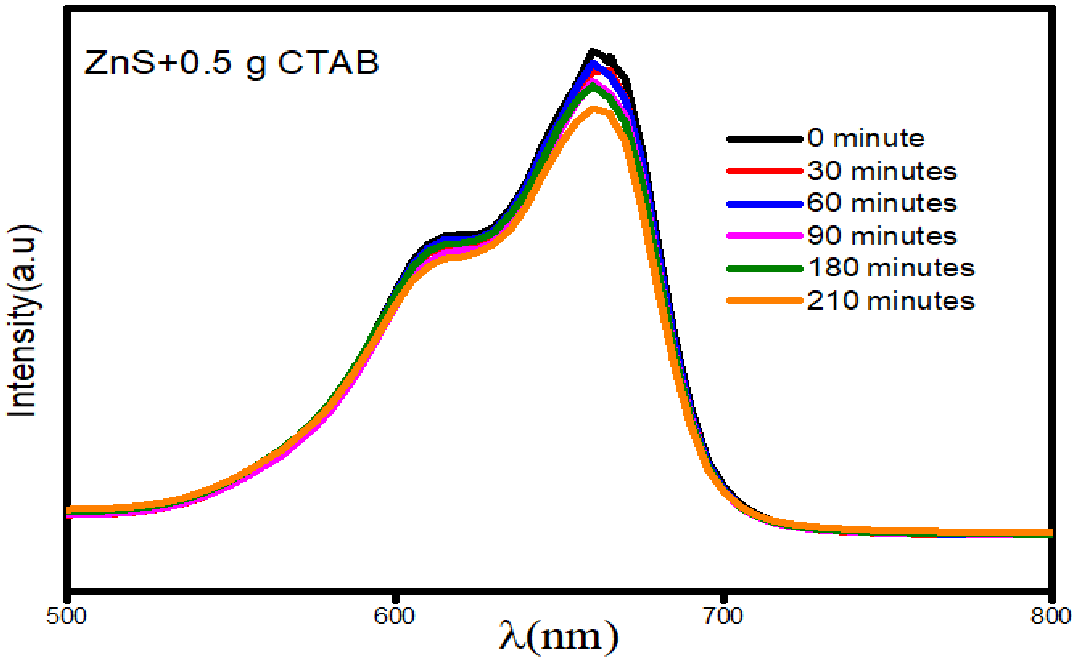

Figure 4.7 Photodegradation of MB dye with ZnS as photocatalyst

4.4 Conclusion

In previous chapter we discussed the synthesis of ZnS nanoparticles using hydrothermal method. Point Defects are introduced using stochiometric ratio variation. In this chapter a facile and successful preparation of quantum dots like ZnS nanoparticles has been synthesized at different CTAB concentrations. X-ray diffraction and FT-Raman spectroscopy approves the synthesis of monophasic ZnS with very low dimension. FT-Raman spectra contain two major Raman modes at ~ 264 and 346 cm^{-1} related to TO and LO modes which are shifted to lower wavenumbers compared to bulk values indicates phonon confinement in the final products. SEM study reveals that the prepared nanostructures are nanoparticles of very low dimension and the size is also varying slightly with CTAB content in ZnS. Kubelka-Munk method was used to determine energy gap and noticed between 3.56

to 3.6 eV at different CTAB contents in ZnS. The ZnS nanoparticle synthesized were not showing photocatalytic activity. The dielectric study reveals that the samples possess high values of dielectric constant which are between 27 to 35 and los loss values. The electrical conductivity is noticed to be increased with increasing the frequency and also noticed to be varied with varying the CTAB content in ZnS. The 0.5 g CTAB concentration in ZnS nanoparticles has been identified as the optimum suitable for the formation low dimension NPs with higher energy gap, higher dielectric constant and lower loss values. These properties make ZnS NPs suitable for optoelectronics devices.

Chapter-5

ZnS Nanoparticles by microwave-assisted method: Point Defects through Er doping

The rare earth element Er is doped into the CTAB optimised zinc sulphide nanoparticles prepared by microwave-assisted co-precipitation route. XRD and Raman studies confirm the crystalline nano growth of the prepared nanostructures. The stress-strain analysis of the samples was made using Williamsons-Hall (UDM, USDM and UDEDM) plots. The Raman bands at 257 and 340 cm^{-1} *are associated to transverse optic (TO) and longitudinal optic (LO) phonon modes of ZnS. SEM/EDX/SEM e-mapping micrographs and compositional analyses approve the formation of nano-scale materials with proper elemental composition and homogeneity. Band gap values of the prepared samples were estimated in the range of 3.61-3.64 eV using the Kubelka-Munk Plots derived from the experimental diffused reflectance data. The photoluminescence spectra of Er doped ZnS nanoparticles were studied at 320nm and 400 nm excitation wavelengths. The emission peaks of 320 nm excitation were observed at 364nm, 380nm, 423nm, 438 nm and 520 nm. The dielectric values are found within the range 15–23 in the frequency range 1 kHz to 10 MHz which are slightly lower compared to pure ZnS nanoparticles in the same range and the reason is attributed to the effects of Er doping.*

5.1 Introduction

Rare earth elements (REEs) are a collection of seventeen chemically related metallic elements that are essential for many modern technologies[432]. These elements, which have unique magnetic, luminous and catalytic characteristics that are useful in numerous applications[433], hence the rare earth element doping improves the electrical conductivity[434], Optical[435], electrochemical[436],thermoelectric[437] and magnetic properties of nanomaterials[438]. Zinc sulphide (ZnS) nanoparticles have attracted a lot of attention recently because of their unique properties and their uses in a variety of industries[439]. These nanoparticles are extremely attractive for a variety of applications, including optoelectronics[440], photonics[441], sensors[442] and catalysis[443], because to their exceptional optical, electrical and mechanical capabilities. The electrical and optical characteristics of nanoparticles can be greatly impacted by point defects like vacancies or interstitials[444]. Doping with rare earth elements and adding point defects to ZnS nanoparticles have been investigated as ways to improve their characteristics more significantly[445]. The electrical and optical characteristics of nanoparticles can be greatly impacted by point defects like vacancies or interstitials[444]. In this thesis we introduced point defects by doping with rare earth elements. ZnS nanoparticles may be doped with rare earth elements, such Erbium (Er), to change their photocatalytic, luminous characteristics and add other energy levels[446]. This allows ZnS nanoparticles to be used in lasers, telecommunications[205] and displays[447]. Synthesis of ZnS nanoparticles with regulated size, shape and composition is critical for customising their characteristics. Microwave-assisted co-precipitation has become a promising method among many synthesis techniques. This method has a number of benefits, such as the capacity to produce nanoparticles with narrow size distributions, accurate control over reaction conditions and quick and uniform heating[231].

5.2 Experimental

5.2.1 Synthesis

The nanoparticles of Erbium (Er) doped ZnS were prepared by microwave assisted co-precipitation method. Prior to reaction 0.5M Zinc Acetate solution was prepared under magnetic stirring followed by addition of 0.5g/100 ml CTAB and the stirring continued for 30 min at 60^{o}C. Separately prepared 0.5M Na_2S precursor solution in double distilled water (DDW) was added to the above solution at 60^{o}C to form the ZnS. Er doping has been achieved by mixing the required amount of Erbium nitrate hexahydrate to the Zinc acetate and CTAB mixture before reacting with the Na_2S precursor to synthesize 0.25%, 0.5%, 1%, 2.5% and 5% Er doped ZnS Nanoparticles. The reaction was allowed to continue for 1 hr and then cooled to room temperature naturally and treated with 700 W microwave power for 15 min. The obtained ZnS nanoparticles were then meticulously cleaned using standard procedures to remove the undesirable constituents present.

5.2.2 Measurements

The structural and compositional studies of Er doped ZnS nanoparticles were done using the powder XRD (PXRD), The diffraction patterns of prepared samples of Er doped ZnS nanoparticles were recorded using a Shimadzu X-600 Japan powder X-ray diffractometer (PXRD) having Cu-Kα radiation and wavelength λ = 0.1543 nm and operated at 40 kV,30 mA, at the scan rate of 0.02°/m over the angular range of 10°to 70° at 300 K. The morphological analyses for all the synthesised Er doped ZnS nanostructures were done by JSM 6360 LA, Japan scanning electron microscope (SEM). The dielectric measurements on all nanostructures synthesized by microwave assisted technique have been carried out in the frequency range 3 kHz to 10 MHz at room temperature. The measurements were done using SCS 4200 semiconductor characterization system. Studies are made on pellet samples. The vibrational study was carried out at room temperature for all the nanostructures using a THERMO SCIENTIFIC, DXRFT-Raman spectrometer. The Raman system was operated at 0.2 mW laser power (532 nm laser). The room-temperature optical absorption spectra of the nanostructures were determined using a double beam UV-VIS spectrophotometer a Shimadzu UV-3600 spectrophotometer in the wavelength range of 200–1200 nm.

5.3. Results and discussion

5.3.1 X-Ray Diffraction Analysis

5.3.1.1 Scherrer method

The PXRD patterns of 0.25%, 0.5%,1%,2.5%,5% by weight of Er doped ZnS nanoparticles are shown in Figure 5.1. The PXRD pattern of undoped ZnS is already depicted in Figure 4.1 and discussed in the section 4.3.1. From the figure it is clear that all the XRD peaks of the prepared sample could be indexed as the cubic Zinc blend structure of ZnS. It could be seen that the broadened three peaks are correspond to (111), (220), (311) planes of cubic phase of Er doped ZnS nanoparticles (ICDD (# 01-080-0020). The peaks are observed at 2θ values 28.97^0, 48.32^0 and 56.98^0 respectively. The absence of other peaks shows that no other Er compounds are observed and it is evidence for the successful dispersion of Er in the ZnS matrix. However, no systematic peak shifts is observed towards lower 2θ values, the reason might be that the amount of Er^{3+} is so little that it could not be detected by XRD[448]. The average crystallite size of pure and Er doped ZnS were calculated by Scherrer equation and it is found to be 2.84n.m. The lattice parameter ‘a’ is measured using following equation

$$\mathbf{a} = \frac{\lambda}{2sin\theta}(h^2+k^2+l^2)^{1/2} \tag{5.1}$$

where λ is wavelength of X-ray used which is 1.54056Å, (hkl) is miller index of crystal plane and θ is Bragg’s angle. The measured values of lattice parameter are 5.34 Å which is very close to the reference (ICDD # 01-080-0020) values. No significant changes observed in the value of ‘a’ with increasing Er doping ratio, Which might be due to the replacement of the Zn^{2+} ions with Er^{3+} ions[389].

5.3.1.2 Williamsons-Hall plot

The strain and dislocation density of the samples are computed by Williamson and Hall plots and are shown in Figure 5.2.

5.3.1.2.1 Uniform Deformation Model (UDM)

UDM (Uniform deformation model) is based on the homogeneity and isotropic nature of the crystals. The observed broadening β_{hkl} is the sum of the size broadening and strain broadening.

ie. $$\beta_{hkl} = \frac{k\lambda}{D\,cos\theta} + 4\epsilon\tan\theta \tag{5.2}$$

By rearranging the above equation

$$\beta_{hkl}\cos\theta = \frac{k\lambda}{D} + 4\epsilon\sin\theta \tag{5.3}$$

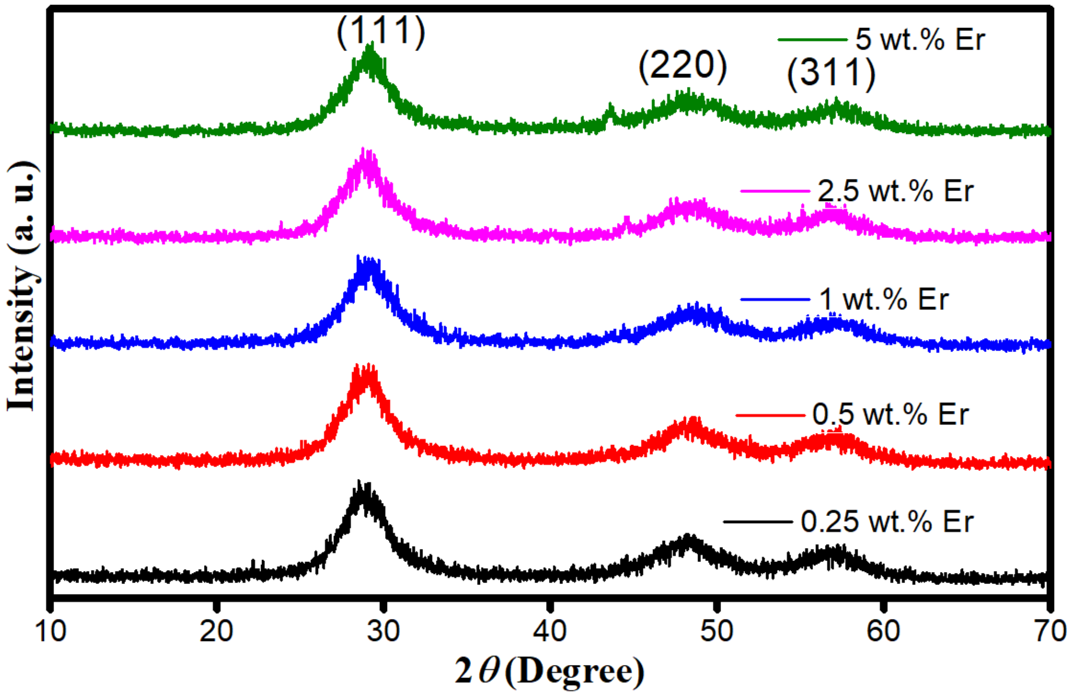

Figure 5.1: XRD patterns of Er doped ZnS nanoparticles

This is modified Williamsons-Hall equation, which is also called UDM. The plot drawn 4 sinθ along X-axis and β_{hkl} cosθ along Y-axis of prepared samples are shown in the Figure 5.2a. The strain was estimated from the slopes of linearly fitted graphs and average crystallite size from the Y- intercepts. The strain values of prepared ZnS:Er nanoparticles are listed in Table 5.1 and is found to be positive for all Er concentrations. The positive slopes of Williamsons Hall plot indicate the presence of tensile strain appeared due to the thermal expansion which is associated with the crystal growth[195]. The crystallite size determined from the Y-intercept of the UDM plot is well matched with that obtained from Scherrer method.

5.3.1.2.2 Uniform Deformation Stress Model

In reality the Youngs modulus is anisotropic in nature. In UDSM (Uniform Stress Deformation Model) the anisotropic strain is considered instead of isotropic strain and uniform stress is considered in all crystallographic directions[449]. By Hook’s law anisotropic strain is related to uniform stress by the relation.

$$\epsilon = \frac{\sigma}{Y_{hkl}} \tag{5.4}$$

Where σ is uniform Stress and Y_{hkl} is Young's modulus of the given (hkl)plane. Hence equation (5.3) will modify as

$$\boldsymbol{\beta_{hkl}\cos\theta = \frac{k\lambda}{D} + \frac{4\,\sigma\sin\theta}{Y_{hkl}}} \tag{5.5}$$

The calculated values of Young's modulus of ZnS for different orientation planes are Y(111)=86.8GPa, Y(220)=80.3GPa and Y(311)= 74 GPa [373].The UDSM plots are drawn with $\frac{4\sin\theta}{Y_{hkl}}$ along X-axis and $\beta_{hkl}\cos\theta$ along Y-axis are shown in Figure 5.2b . The stress and average crystallite size of samples were estimated (Table 5.1) from the slop and Y-intercepts values of linearly fitted plots.

5.3.1.2.3 Uniform Deformation Energy Density Model

UDM is based on the isotropic nature of the crystal and the UDSM assumes linear relationship between stress and strain, but in reality, due to the various defects, dislocation and agglomeration creates imperfections in almost all crystals. Here UDEDM (Uniform deformation energy density model) model can be used to determine the deformation energy density, average crystallite size, stress and strain parameters. When the strain energy density 'u' is considered all the proportionality constants associated with stress-strain relation is now dependent[450]. Energy density u is related to strain by the relation

$$\boldsymbol{u = \frac{\epsilon^2}{Y_{hkl}}} \tag{5.6}$$

Then equation (5.3) become

$$\boldsymbol{\beta_{hkl}\cos\theta = \frac{k\lambda}{D} + 4\sin\theta\ \left(\frac{2u}{Y_{hkl}}\right)^{\frac{1}{2}}} \tag{5.7}$$

The plots are drawn with $\left(\frac{4\sin\theta}{Y_{hkl}}\right)^{\frac{1}{2}}$ along X-axis and $\beta_{hkl}\cos\theta$ along Y axis as shown Figure 5.2c. The intercept of linearly fitted plot provides average crystallite size and the deformation energy density (Table 5.1) calculated from the slope.

5.3.1.2.4 Size -Strain Plot

Size-strain plot (SSP) can be used to measure the average size -strain parameters. It needs to check the values obtained from Williamsons-Hall plot though it has low precision [451]. Average size and strain parameters can be evaluated using the equation

$$(\boldsymbol{d_{hkl}\beta_{hkl}\cos\theta})^2 = \frac{\boldsymbol{K}}{\boldsymbol{D}}\,(\boldsymbol{d_{hkl}^2\beta_{hkl}\cos\theta}) + (\frac{\epsilon}{2})^2 \qquad (5.8)$$

Figure 5.2d shows the size -strain plot drawn with $d_{hkl}^2\beta_{hkl}\cos\theta$ along the X-axis and $(d_{hkl}\beta_{hkl}\cos\theta)^2$along Y-axis. The D and ϵ extracted (Table 5.1) from the Y-intercept and Slop of the fitted plot respectively. The crystallite size obtained is well matched with that obtained from W-H plot.

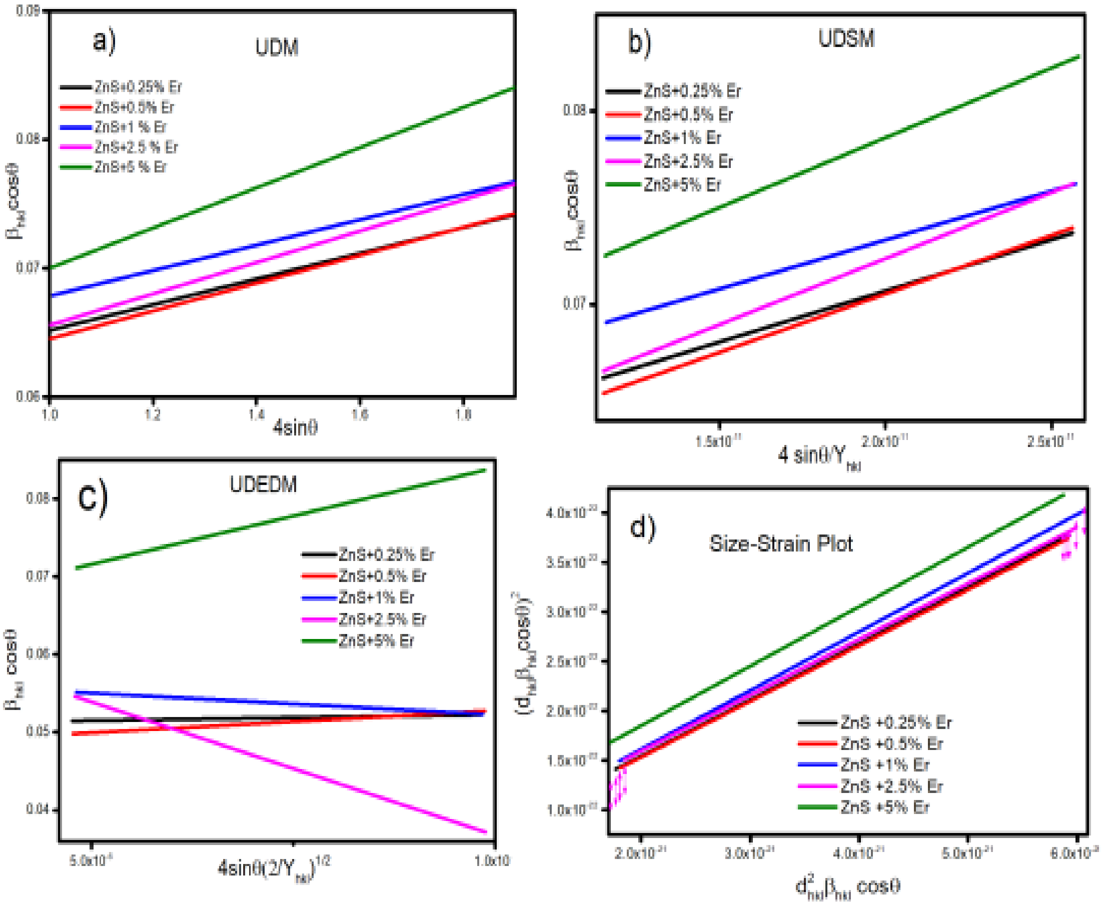

Figure-5.2: a) UDM b) UDSM c) UDEDM d) Size-strain plot 0.25 %, 0.5 %, 1 %, 2.5 %, 5 % Er doped ZnS

Table 5.1 The calculated value from UDM, UDSM, UDEDM and Size -Strain plot is listed

Samples	Parameter	Scherrer	UDM	UDSM	UDEDM	SSP
ZnS+0.25% Er	D(nm)	2.78	2.51	2.31	2.73	2.44
	$\varepsilon(10^{-3})$		9.98	6.01(ε_{111}) 6.59(ε_{220}) 7.15(ε_{311})	0.723(ε_{111}) 0.753(ε_{220}) 0.784(ε_{311})	1.28E-08
	σ(GPa)			0.053	0.06	
	U(KJ/m^3)				22.74	
ZnS+0.5% Er	D(nm)	2.78	2.58	2.31	2.73	2.46
	$\varepsilon(10^{-3})$		10.83	6.97(ε_{111}) 7.53(ε_{220}) 8.18(ε_{311})	2.76(ε_{111}) 2.87(ε_{220}) 2.99(ε_{311})	1.273E-08
	σ(GPa)			0.061	0.23	
	U(KJ/m^3)				332.51	
ZnS+1% Er	D(nm)	2.67	2.39	2.19	2.73	2.34
	$\varepsilon(10^{-3})$		9.87	5.83(ε_{111}) 6.30(ε_{220}) 6.84(ε_{311})	2.67(ε_{111}) 2.77(ε_{220}) 2.89(ε_{311})	1.463E-8
	σ(GPa)			0.05	0.22	
	U(KJ/m^3)				309.6	
ZnS+2.5% Er	D(nm)	2.7	2.66	2.36	1.95	2.46
	$\varepsilon(10^{-3})$		12.18	7.87(ε_{111}) 8.51(ε_{220}) 9.23(ε_{311})	16.44(ε_{111}) 17.10(ε_{220}) 17.81(ε_{311})	1.365E-8
	σ(GPa)			0.07	1.37	
	U(KJ/m^3)				11743.90	
ZnS+5% Er	D(nm)	2.66	2.54	2.16	2.34	2.31
	$\varepsilon(10^{-3})$		15.61	8.31(ε_{111}) 8.98(ε_{220}) 9.74(ε_{311})	11.91(ε_{111}) 12.38(ε_{220}) 12.91ε_{311})	1.612E-8
	σ(GPa)			0.07	0.99	
	U(KJ/m^3)				6162.44	

5.3.2 Scanning Electron Microscopy

The SEM images of the synthesized products are displayed in Figure 5.3 A(a-e) which reveals that the synthesized materials of are of very low dimension i.e. below 10 nm. Moreover, slight increment in size was seen or cluster formation was observed with doping of Er in ZnS. The compositional and e-mapping analysis has been performed by EDX/SEM. The compositional analysis confirms the composition of Zn and S along with the presence of Er in the final products in the Figure 5.3B (a-b), moreover the mapping analysis (Figure 5.3C(a-d)) confirms the homogeneous presence of Zn, S and Er in the final product.

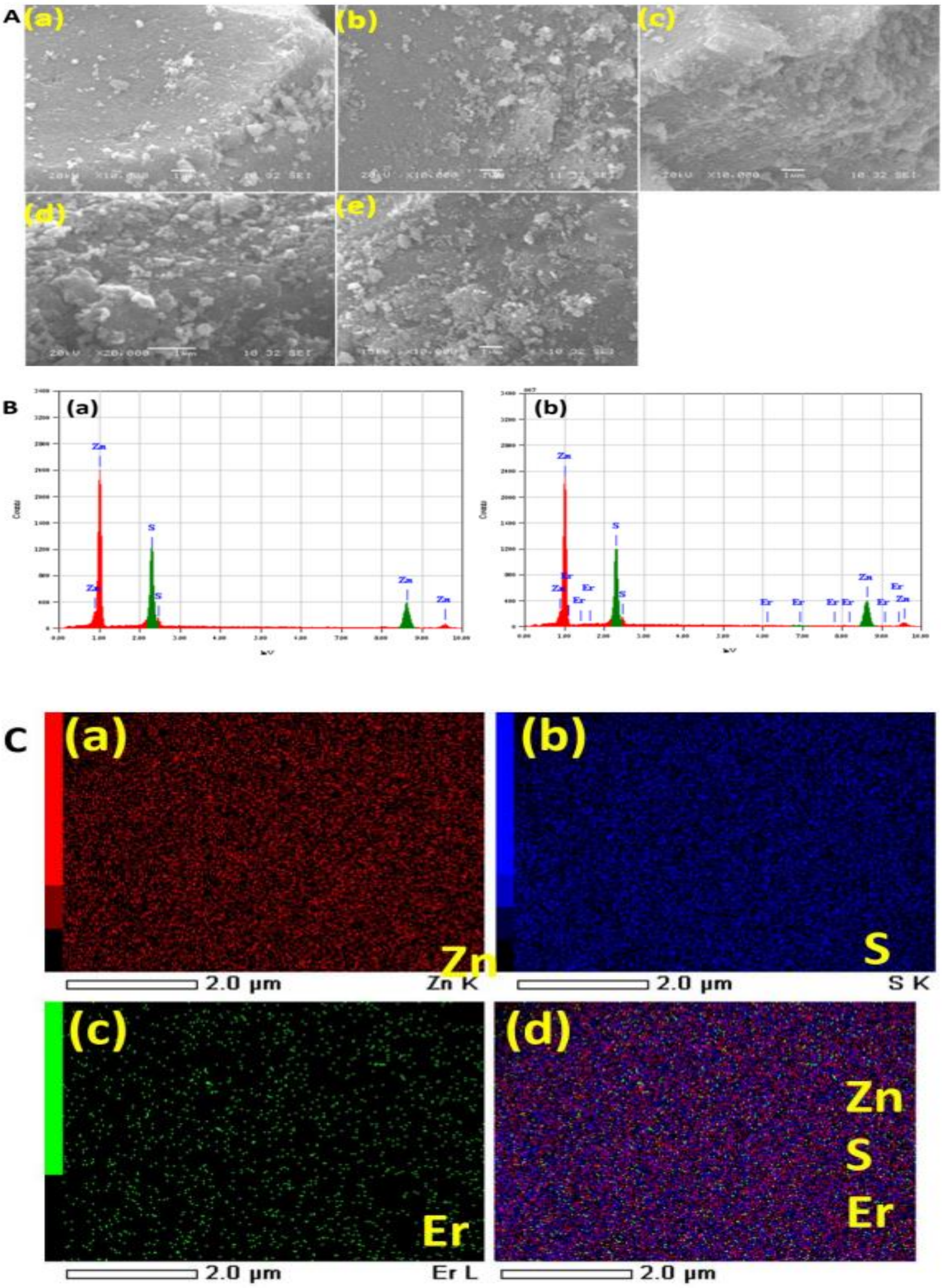

Figure 5.3 A (a-e) SEM images of Er doped ZnS nanoparticles, B(a-b) EDX for pure and 1.0 wt.% Er doped ZnS and C(a-d) e-mapping image for Zn, S, Er and overlay

5.3.3 Transmission Electron Microscopy (TEM)

TEM pictures of the ZnS and 5% Er doped ZnS nanoparticles are shown in Figure 5.4a and 5.4b respectively. According to the TEM images, the synthesised particles have a uniform distribution and a spherical shape. The TEM images of ZnS and Er doped ZnS particles show clear grain boundaries with an average crystallite size of 11.7 nm and 28.4 nm, respectively. Figures 5.4c and 5.4d show delegate HRTEM images of ZnS and 5% Er doped ZnS. The interplanar spacing calculated from the HRTEM image of ZnS is 2.87 Å which corresponds to planes of miller index 200. The d-spacing calculated for the plane illustrated in the picture is 1.62Å for the 5% Er doped ZnS sample, which correlates to 311 plane of ZnS grown in cubic phase that enlarges a portion of the structure.

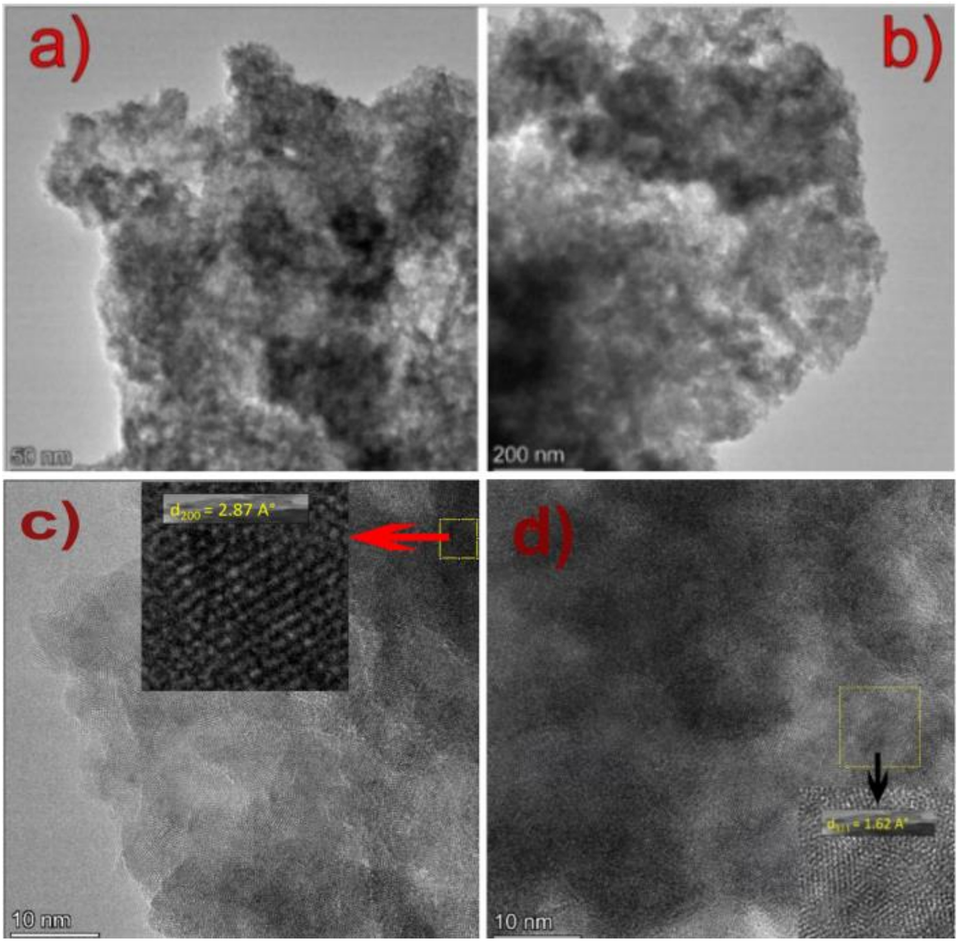

Figure 5.4 a), b) TEM image of ZnS & 5% Er-doped ZnS c), d) HRTEM image of ZnS & 5% Er-doped ZnS

5.3.4 Optical Properties

The reflectance spectra of present samples are shown in Figure 5.5a. The optical properties of Er doped ZnS nanoparticles were measured using U.V-Visible spectroscopy in a diffuse reflectance mode. The Kubelka-Munk relation shown below is used to calculate the optical bandgap of prepared samples,

$$\alpha h\nu = C_1(h\nu - Eg)^n \tag{5.9}$$

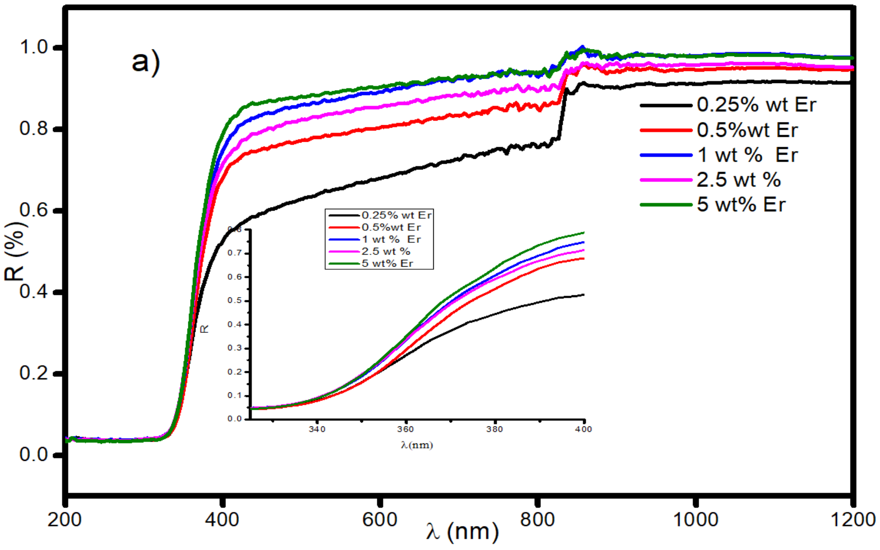

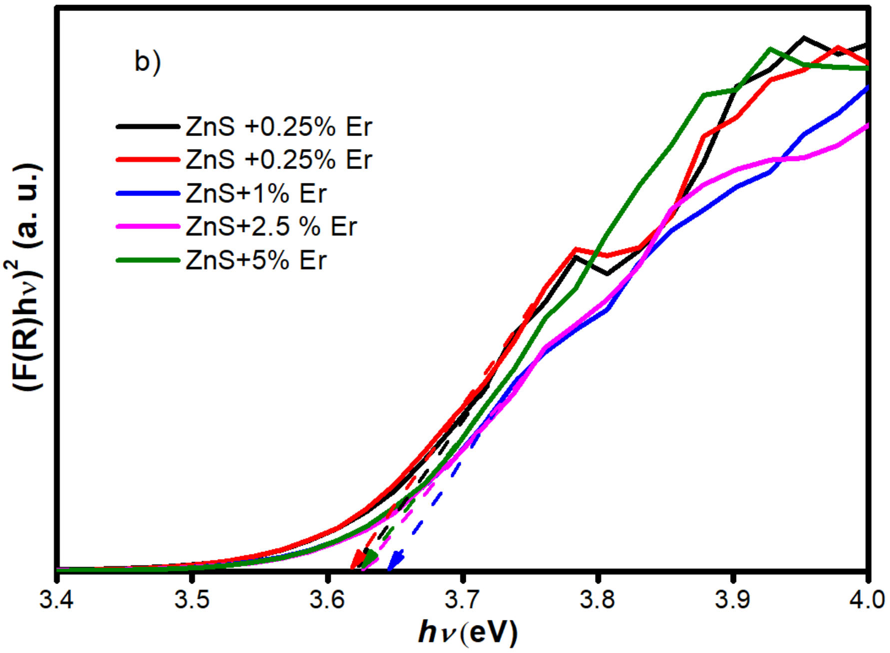

Figure 5.5 a) Reflectance Spectra b) $(F(R)h\nu)^2$ Vs h ν plot of Er doped ZnS

where α is the linear absorption coefficient of the material, hν is the photon energy, C_1 is a proportionality constant, E_g is the optical band gap and n is a constant associated with different kinds of electronic transitions (n = 1/2, 2, 3/2 or 3 for direct allowed, indirect allowed, direct forbidden and indirect forbidden transitions, respectively)[152]. The value of the optical band gap can be calculated by extrapolating the Kubelka - Munk function shown in Figure 5.5b. The measured band gap values are varying between 3.61-3.64eV.

The introduction of dopant related energy levels between the host related energy levels are the reason for the change in band gap energies. This can be explained using Urbach energy[452].

$$\boldsymbol{\alpha = \alpha 0\ e^{\frac{Eg}{Eu}}} \tag{5.10}$$

The Urbach energy is determined using the hν Vs ln α plot and is shown in Figure 5.6. The Urbach energy is the reciprocal of the slope of the linear portion of the curve below the bandgap. The change in Urbach energy with the band gap energy is due to the formation of sub band states between the valance and conduction band[453],[454].The values are tabulated in Table 5.2.

Table 5.2 Band gap energy and Urbach energy values of Er doped ZnS

S. No.	Samples	Band gap in eV	Urbach Energy in eV
1	0.25 wt% Er	3.62	0.9998
2	0.5 wt % Er	3.61	0.8889
3	1 wt % Er	3.64	1.6704
4	2.5 wt % Er	3.62	1.2252
5	5 wt % Er	3.62	1.30841

The relationship of the band gap with Urbach energy for different samples are shown in Figure 5.7.[453]

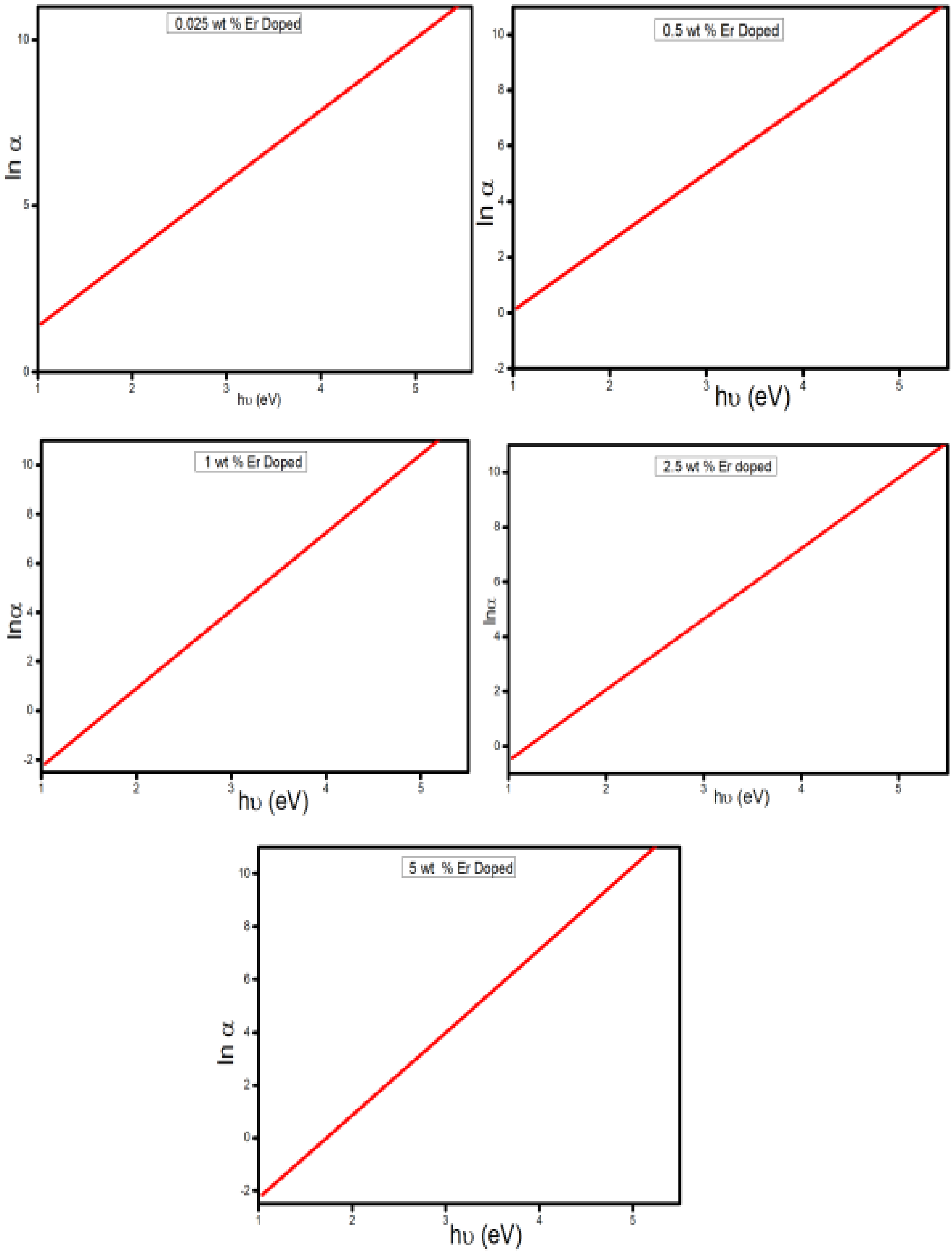

Figure-5.6 Urbach energy plots of Er doped ZnS

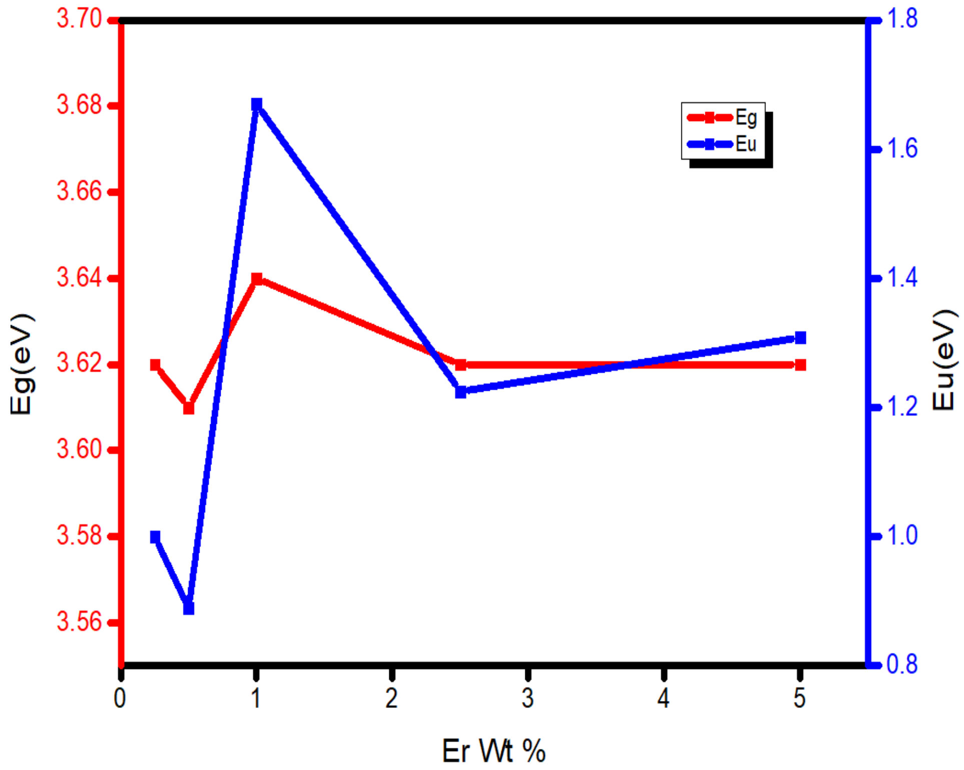

Figure 5.7 -Variation of band gap and Urbach energy for different concentrations of Er.

5.3.5 Raman Spectra Analysis

The FT Raman spectroscopy was used to the Vibrational analysis of Er doped ZnS nanoparticles. FT Raman recordings are displayed in Figure 5.8. From the figure it is clear that two major Raman peaks are noticed in all prepared Er doped ZnS NPs samples. The peaks are observed at ~ 257 cm^{-1} and ~ 340 cm^{-1} ,These peaks are related to fundamental Raman modes and are attributed to transverse optic (TO) and longitudinal optic (LO) phonon modes of ZnS[393][368].Variation of FWHM of peaks is the reason for the variation of the intensity indicating that the interaction between Er ions and the ZnS lattice affects the vibrational modes however, it depends on the used excitation source and its power. We have not detected any secondary peaks related to Er or its oxide phase. Phonon confinement effect in the nano regime is the reason for the shift of the

Raman peaks to the lower wave number side in comparison to the bulk values which are reported at 274 and 351 cm^{-1}[425].

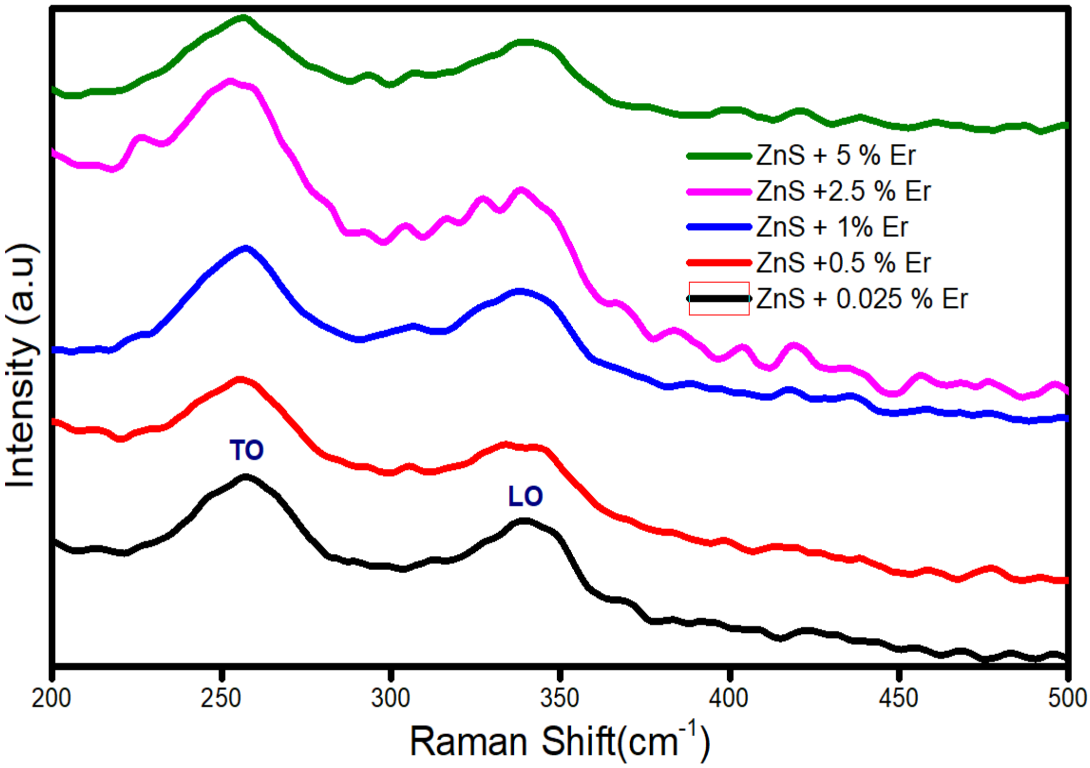

Figure 5.8-Raman Spectra of Er doped ZnS nanoparticles

5.3.6 Photoluminescence Studies

The photoluminescence spectrum of Er doped ZnS nanoparticles corresponding to the 320 nm excitation wavelength are shown in the Figure 5.9a. The asymmetric and broad spectra shows that more contributors are there to the intensity of PL spectra. The deconvoluted PL curve using Gaussian fitting of 5% Er doped sample is shown in the figure as a test sample. The emission peaks are located at 364nm, 380nm, 423n.m, 438 nm and 520 nm. The emission band centred around 364 nm is attributed due to the transition from the interstitial Zn[397]. The peak around 380 nm arises due to Zinc vacancies and peak around 423 nm is due to sulphur vacancies. The emission band centred on 438 nm corresponds to a self-activated centre assumably formed between a shallow donor associated with a sulphur vacancy and a Zn vacancy. The green emission around 520nm is due to the deep level emissions which are potentially induced and may have been arise due to the point defects[455][399][456].The deconvoluted PL plot of 5% Er doped ZnS shows that it is 3 level laser active material.

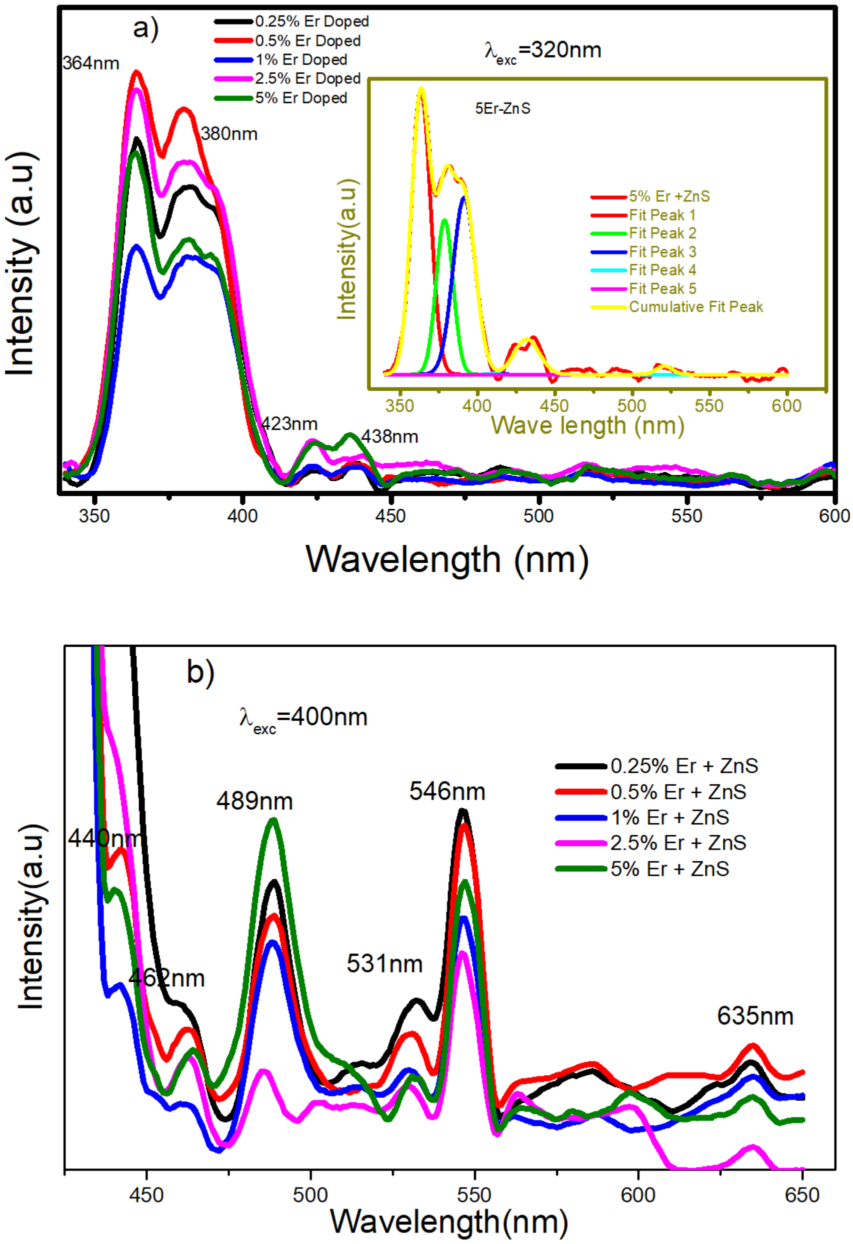

Figure-5.9. The photoluminescence spectrum of Er doped ZnS nanoparticles (a) excited at 320nm and (b) excited at 400 nm.

The PL emission spectra of Er doped ZnS nanoparticles corresponding to 400 nm excitation wavelength are shown in Figure 5.9b. The luminescence transition corresponding to Er is more dominant for excitation wavelength 400 nm.

The peaks are located at 444nm, 462nm, 489nm, 531nm, 546nm and 635nm. The PL peak around 444nm ascribed to interstitial void defects due to sulphur vacancies.[457] The hanging sulphur bonds in the interface of crystal grains might be the reason for peak centred around the 464 nm[399]. The PL peaks around 489 nm,531 nm,546 nm and 635 nm might be corresponding to Er^{3+} transitions ${}^{4}_{\frac{7}{2}}F \rightarrow {}^{4}_{\frac{15}{2}}I$, ${}^{2}_{\frac{11}{2}}H \rightarrow {}^{4}_{\frac{15}{2}}I$, ${}^{4}_{\frac{3}{2}}\mathrm{S} \rightarrow {}^{4}_{\frac{15}{2}}\mathrm{I}$, ${}^{4}_{\frac{9}{2}}\mathrm{F} \rightarrow {}^{4}_{\frac{15}{2}}\mathrm{I}$ [458][459][460][461]. The intensity of PL peaks corresponding to ${}^{2}_{\frac{11}{2}}H \rightarrow {}^{4}_{\frac{15}{2}}I$, ${}^{4}_{\frac{3}{2}}S \rightarrow {}^{4}_{\frac{15}{2}}\mathrm{I}$ transitions are decrease as the doping percentage of Er increases till 2.5%, up on doping with Er there is a significant PL quenching by 40%, but for the 5% Er doping ZnS Sample there is slight increase in the intensity. The PL quenching attributed to some non-radiative recombination in the Er-ZnS interface after the electron transfer from excited ZnS to Er.

5.3.7 Dielectric Property Analysis

Wider band gap semiconductors can be used in capacitors like Barrier layer capacitors. The electrical and Optical properties of nanoparticles can be control by varying the amount and type of dopant[462]. The dielectric measurement on Er doped ZnS nanostructures synthesized by microwave assisted method has been carried out in the frequency range, 1kHz to 10MHz at room temperature. The dielectric constant (ε′) and loss (ε″) parameters were calculated from the measured capacitance value (C) and loss tangent (tan (δ)) data using the relations

$$\boldsymbol{\varepsilon'} = \frac{\boldsymbol{Cd}}{\boldsymbol{\varepsilon o A}} \tag{5.11}$$

and

$$\boldsymbol{\varepsilon'' = \tan(\delta) \times \varepsilon'} \tag{5.12}$$

where A and ‘d’ are the cross sectional area and thickness of the pellet samples[463]. The Figure 5.10a shows the variation of dielectric constant ε' with frequency. From the graph it is clear that the dielectric constant ε' is higher value in the lower frequency region almost stable between 1MHz and 5 MHz and ε' is increasing at higher frequencies. The all four frequency dependent charges such as space charge polarization, electronic, dipolar and ionic are the reason for observed behaviour of ε’ at the low frequencies [368]. The electric field dipoles cannot follow the alternating field beyond certain frequencies, this special characteristic is the reason for the observed initial decreasing of ε’ with frequency for the Er doped ZnS NPs followed by the nearly stable state within ~ 1–5 MHz [431]. The values of ε′ are found within the range 15–23 in the frequency range 1 kHz to 10 MHz. These values express slight diminution in ε′ compared to pure ZnS nanoparticles in our previous work [368]on ZnS in the range 10^3 –10^7 Hz, The doping with Er is the reason for the diminution of dielectric constant[464].

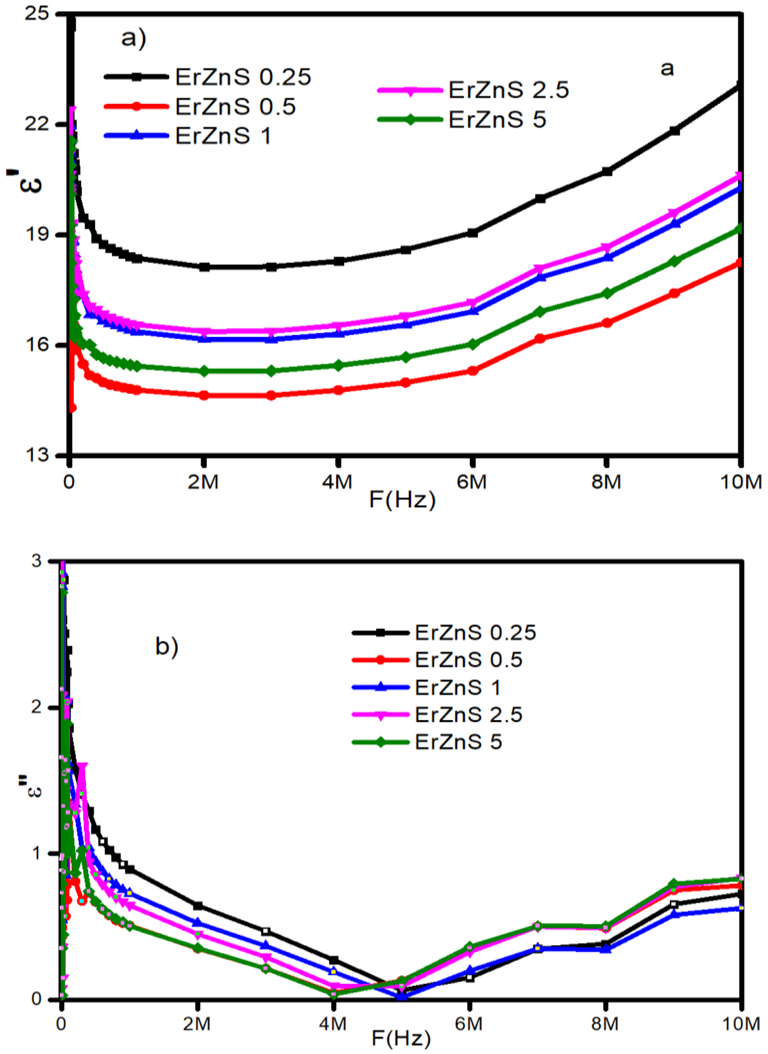

Figure 5.10- Variations of a) dielectric constants b) dielectric loss with frequency

Figure 5.10b presents the variations of the dielectric loss with respect frequency of Er doped ZnS nanoparticles. From the figure, for all samples the dielectric loss values showed a clear decreasing tendency with frequency and observed their minimum loss between 4 MHz-5MHz for various samples. However, the dielectric loss values are increasing after the minimum value. The maximum value of dielectric constant was observed for 5% Er doped ZnS sample. 0.25% Er doped ZnS displayed the maximum dielectric loss below 5 MHz frequency. 1% Er doped ZnS sample along with 0.25% Er doped ZnS sample exhibited the minimum dielectric loss beyond 4 MHz-5MHz. Various factors like lattice vibration mode, contributions from various polarisation mechanisms and grain sizes are the reason for the changes in dielectric loss properties[429].

5.3.8 Electrical conductivity Analysis

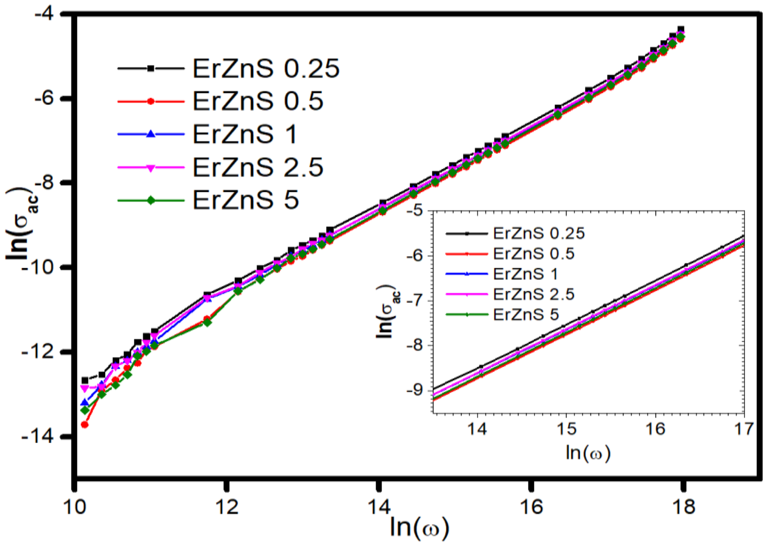

Figure 5.11: -Variation of ac conductivity with angular frequency, (inset shows the magnified plots for the value of ln(ω) from 13 to 17)

The information regarding the total ac conductivity ($\sigma_{ac.tot}$) were extracted by employing the following relations.

$$\boldsymbol{\sigma_{ac.tot} = \frac{l}{XAZ}} \tag{5.13}$$

$$\boldsymbol{\sigma_{ac} = \sigma_{dc} + B\omega^{s}} \tag{5.14}$$

where the latter is the **Jonscher law** which connects the ac conductivity, σ_{ac} with dc conductivity, σ_{dc} and angular frequency, ω, here B and exponent s are constants. Figure 5.11 shows the variation of σ_{actot} with frequency for all the prepared Er doped ZnS NPs. The plot itself is an evident that all samples obeying the frequency power law and increasing of the σ_{ac} with frequency. The maximum ac conductivity was observed for the 0.25 Er doped ZnS NPs. The exponent values were also computed for all the samples from the slope of above plots in Fig. 9 and are obtained to be 0.988, 0.993, 0.988, 0.991, 0.997 for 0.25%, 0.5%, 1% ,2 .5%, 5% Er doped ZnS NPs respectively.

5.3.9 Photocatalytic Studies

Photocatalytic (PC) experiments were carried out to determine the effectiveness of pure ZnS and 5% Er-doped ZnS as photocatalysts for the degradation of Methylene Blue (MB) dye. MB dye solution was prepared by dissolving 10 mg of MB in 1 L of distilled water and 0.03 g of each photocatalyst was added in 25 ml of it for the experiment. The mixture was magnetically stirred for an hour in the dark to ensure an adsorption–desorption equilibrium between the dye molecules and the catalyst surface. However, no substantial degradation of the MB dye was seen in the presence of pure or Er-doped ZnS, suggesting that these materials do not have efficient photocatalytic capabilities under the tested conditions as shown in Figure 5.12a and 5.12b. This finding indicates that neither pure ZnS nor Er-doped ZnS are appropriate for photocatalytic degradation of MB dye under visible light irradiation.

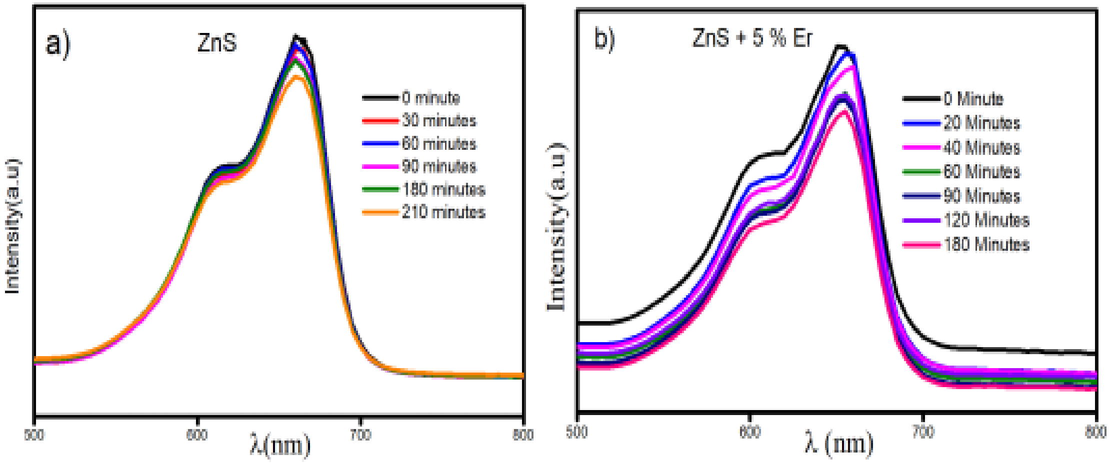

Figure 5.12 Photodegradation of MB dye a) with ZnS b) with 5% Er doped ZnS photocatalyst

The PL spectra of pure ZnS and Er-doped ZnS nanoparticles synthesized via the microwave assisted method do not exhibit transitions from sulphur vacancy to dangling sulphur bonds were as the samples synthasised using hydrothermal method exhibit these transitions. These sulphur defect states in the hydrothermal samples act as trapping sites for charge carriers generated by visible light, contributing to their photocatalytic activity. In contrast, the lack of these trapping sites in the microwave-assisted samples explains their absence of photocatalytic activity.

5.4. Conclusion

In this chapter low-cost microwave-assisted co-precipitation route has been successfully used for the production of Er doped ZnS nanoparticle samples with optimum CTAB concentration. Various characterization methods were applied to study their structural, morphological, optical, dielectric and photo luminous characteristics of the prepared samples. Band gap values were obtained in the range 3.61-3.64eV from the Kubelka-Munk Plots. The samples were found to be highly luminescent when excited at 320nm and 400 nm excitation wavelengths. The emission peaks of 320nm excitation were observed at 364nm, 380nm, 423nm, 438 nm and 520 nm. The dielectric values are found to be tunable with Er doping concentrations, which are varying between 15 and 23 in the frequency range 1 kHz to 10 MHz which are slightly lower compared to pure ZnS nanoparticles in the same range and the reason is attributed to the effects of Er doping. The pure and Er doped ZnS nanoparticles were not photocatalytically active either in Visible region or in UV region.

Chapter-6

ZnS Nanoparticles by microwave-assisted method: Point Defects through Pr doping

In this chapter we are discussing about the introduction of point defects by doping with Pr. Pr-doped ZnS nanoparticles were synthesized using a low-cost microwave assisted technique and investigations on their structure, morphology, optical properties, Raman resonance, dielectric properties and luminescence were conducted. Broad XRD peaks suggested the formation of low-dimensional Pr-doped ZnS nanoparticles with a cubic structure which was validated by TEM/HRTEM analysis. The energy gaps were identified using diffuse reflectance spectroscopy and it was found that the values varied between 3.54 and 3.61 for different samples. Vibrational experiments on Pr doped ZnS nanoparticles revealed significant Raman modes at ~ 270 and ~350 cm -1 associated to TO and LO modes that are shifted to lower wavenumbers, indicating phonon confinement in the synthesised products. The PL spectra of all samples demonstrate that the pure and Pr doped ZnS nanoparticles are three level laser active materials. EDX and mapping study confirms the homogeneous presence of Pr in ZnS. TEM study shows that the particles are of very small size and cubic phase. The samples have high dielectric constant values between 13 and 24 and low loss values, according to the dielectric analysis. With an increase in frequency and a change in the Pr content of ZnS, an intense peak can be seen in the PL spectra at a wavelength of 360 nm and some other peaks observed correspond to the transition of Pr^{3+}*. The produced NPs are appropriate for optoelectronic applications due to their short dimension, high energy gap, high dielectric constant and low loss values.*

6.1 Introduction

There are several synthesis methods developed for the synthesis of nanomaterials. The physical and chemical properties of the nanomaterials can be altered by changing the experimental conditions used for the synthesis of nanomaterials[465].

ZnS is II-VI semiconductor and have wide applications in photonics, optoelectronics such as Laser diode, LED, photodetectors [389][466]. Recently ZnS nanostructures are also used in nanogenerators, biosensors, chemical sensors, UV-light sensors, nanostructure-based field emitters, field emitter transistors and as catalyst in chemical kinetics due to its rich morphologies at the nanoscale [5]. Post annealing procedure with sufficient temperature can be used to improve the crystallinity and the conductance of ZnS heterostructure films , which has applications in the fabrication of optoelectronic structures[467][429]. Rare earth elements doped Zn based nanomaterials systems have prospective uses in spintronics and fabrication of magnetic nanostructures[438]. Zinc blend structure and wurtzite structure with wide band gap energy (E_{g}.) of 3.68 eV and 3.72 eV respectively[151][429] are the two possible phases of ZnS. Hydrothermal method[190], Microwave assisted method, Precipitation method, Solgel method, Wet chemical method, Spin coating method and Spray pyrolysis method [197] etc are the various methods reported for the synthesis of ZnS nanomaterials. Doping with cationic elements modify the physical and chemical properties of nanomaterials [468]. La doping enhance the photocatalytic activity of ZnS thin films [469] whereas the Mn doping improves optical, luminescence, chemical properties and it also modify the band gap [150]. It is also reported that, Cu doping increases the visible light emission of ZnS [470], whereas the dielectric properties can be increased by doping with Pb[462]. The doping with Pr enhance the photocatalytic property of ZnS [202]. Pr doping can be used to create lattice distortion in certain materials which will enhance the gas sensing performance, electroluminescence and optoelectronic properties[471][472][473][474]. In our previous study[368] we successfully synthesised pure ZnS with very small crystallite size, high dielectric constant low dielectric loss using

CTAB as a surfactant which is suitable for optoelectronic devices. The Pr dopant shows various energy level transitions corresponding to blue, green, orange, red and deep red spectral regions [474]. In this work we study the effect of Pr doping on Optical, Luminescent and dielectric properties of ZnS nanoparticles.

The results presented in this chapter have already been published as E.M. Jubeer, M. A Manthrammel, P. A Subha, M. Shkir and S.A. alFaify,” Microwave-assisted synthesis of praseodymium (Pr)-doped ZnS QDs such as nanoparticles for optoelectronic applications,” Luminescence, Sep. 2023, doi: 10.1002/bio.4577[475]

6.2. Experimental

6.2.1 Synthesis

For the preparation of Praseodymium (Pr) doped nano-powders of ZnS, the microwave assisted co-precipitation method is used. The three precursors 0.5 M Zinc Acetate, 0.5 M Na_2S and 0.5 M Praseodymium (III) Nitrate (NO_3), which were prepared separately in double distilled water (DDW) with continuous magnetic stirring at 60 ^{o}C for 30 minutes. The CTAB solutions were prepared by weighing 0.5 g CTAB in 100 mL of DDW and stirring for uniform mixing, The CTAB solutions were added to the 0.5 M Zinc Acetate precursors. Pure ZnS, 0.5, 1, 2.5 and 5 weight percent Pr doped ZnS are also synthesised. The resulting solutions were microwaved for 15 minutes at 700 W microwave power and allowed to cool to room temperature naturally. The white products were systematically washed with DDW. All the chemicals used in the experiment were of analytical quality.

6.2.2 Measurements

Optical studies of present samples were carried out by using Shimadzu double beam UV-3600 spectrophotometer in the wavelength range of 200–1200 n.m at Room Temperature (RT). The Photoluminescence study was carried out using Agilant Cary fluorescent spectrophotometer. The structural, compositional and crystallographic orientational studies of prepared nanoparticles were done using the Shimadzu X-600 Japan powder XRD (PXRD), having Cu-Kα radiation of

Wavelength equal to 0.1543 nm, at the sweep pace of 0.02°/m over the angular scope of 10°to 70° at 300 K worked at 40 kV, 30 mA. The morphological studies of all the synthesised Pr doped ZnS nanostructures were done by JSM 6360 LA, SEM and Tecnai G2 F20, FEI company operating at 200 kV used for the TEM images. 'SCS-4200' semiconductor measurement system is used for the dielectric measurement of all nanostructures in the frequency interval 3 kHz-10 MHz at RT. The Studies are made on the pellet samples. The vibrational study was carried out for all the Pr doped ZnS nanostructures as done in the article [368] at RT

6.3. Result and discussions

6.3.1 Structural and Particle size distribution

6.3.1.1 Scherrer Method

The XRD patterns of pure and Pr doped ZnS nanoparticles are shown in the Figure-6.1a. All the diffraction peaks could be indexed to Cubic ZnS structure (ICDD (# 01-080-0020). The absence of other phases in the diffraction pattern confirms the purity of prepared samples. The observed three broad peaks correspond to lattice planes of (110), (220), (311) at 2θ values 29°,48.5°and 57.7°respectively. The absence of other peaks indicates that the doping using Pr does not alter the structure of ZnS and it also indicates that Zn ions in the crystals are getting replaced the by the Pr ions. The significant broadness (breadth) of the recorded peaks indicates the nanometric crystallite size. The crystallite size of the synthesised particle is determined by using Debye- Scherrer formula[476].

$$\mathbf{D}=\frac{k\lambda}{\beta \cos\theta} \tag{6.1}$$

where k is a constant with a value equal to 0.9, λ is the wavelength of X-ray used, β is FWHM (full width at half maxima) of peak in radians and θ is Bragg's angle in radian. The average particle size measured using the above equation is 2. 13nm.

The following equation is used for the estimation of lattice constant

$$\mathbf{a} = \frac{\lambda}{2\sin\theta}\,(h^2+k^2+l^2)^{1/2} \tag{6.2}$$

The calculated lattice constant value a=5.32 nm is in well agreement with ICDD (# 01-080-0020). The current samples have the lowest crystallite size and as a result, the highest surface-to-volume ratio among the cited literatures.

6.3.1.2 Williamsons-Hall plot

6.3.1.2.1 Unified Deformation Model

Williamsons Hall (W.H) plot is one of the mostly dependable and steady techniques for stress-strain estimation. According to WH method, the micro strain and size of the crystallite contribute to the line broadening and the contributions are

$$\boldsymbol{\beta_{\varepsilon} = 4\varepsilon\, tan\theta} \tag{6.3}$$

and

$$\boldsymbol{\beta_{D} = \frac{k\lambda}{D\cos\theta}} \tag{6.4}$$

respectively.

Hence the total peak broadening

$$\boldsymbol{\beta_{hkl} = \beta_{D} + \beta_{\varepsilon}} \tag{6.5}$$

Put (6.3) and (6.4) in (6.5)

$$\boldsymbol{\beta_{hkl} = \frac{k\lambda}{D\cos\theta} + 4\varepsilon\, tan\theta} \tag{6.6}$$

Re arranging above equation

$$\boldsymbol{\beta_{hkl} cos\,\theta = \frac{k\lambda}{D} + 4\varepsilon\, sin\theta} \tag{6.7}$$

$\text{equations (6.6) and (6.7) are Williamsons} - \text{Hall equations.}$

The above condition that ensures uniform strain in all Crystallographic Directions (CDs), demonstrates the isotropic behaviour of crystals. Hence this model is known as UDM. The UDM plot by taking 4sinθ and βcosθ along X and Y-axes respectively is shown in Figure 6.1b. The Y-intercept of the UDM plot gives the crystalline size and the slope[477][375] yields the micro strain. All the Pr doped ZnS nanoparticles have positive slopes which indicate tensile strain(s). The tensile stress is due to the thermal expansion associated with the crystal growth[195].

6.3.1.2.2 Uniform Deformation Stress Model

In reality, the assumption of isotropy and homogeneity is not always true. Therefore, the UDM equations are altered by considering anisotropic strain ϵ, whereas in UDSM, uniform deformation stress is considered in all CDs.

By Hooke's Law, the direct proportionality connection between the stress and strain can be composed as:

$$\epsilon = \frac{\sigma}{Y_{hkl}} \tag{6.8}$$

Where σ is uniform stress of the crystal and Y_{hkl} is Young's modulus. In this approach eq (7) can be modified by using (8) as

$$\beta_{hkl} \cos \theta_{hkl} = \frac{k\lambda}{D} + 4\frac{\sigma \sin\theta_{hkl}}{Y_{hkl}} \tag{6.9}$$

The reported value of Y_{hkl} for ZnS nanoparticles are 86.8 GPa, 80.3 GPa and 74 GPa for (111), (220) and (311) crystallographic directions respectively[373]. The plot drawn with (4sinθ /Yhkl) and β_{hkl} Cosθ along the X & Y axes respectively is the UDSM plot. The UDSM plots of Pr doped nanoparticles are shown in Figure 6.1c. The stress and crystallite size were determined from the slope and the intercept of the fitted line respectively[372][374].

6.3.1.2.3 Uniform Deformation Energy Density Model

The assumptions of isotropy and homogeneity considered in UDM and UDSM are not fulfilled in many cases. In UDEDM, the deformation energy density 'u' is considered to be uniform in all CDs. In accordance with Hook's law, the deformation energy per unit volume (u) is given by

$$u = \frac{\varepsilon^2 Y_{hkl}}{2} \tag{6.10}$$

so eq (7) can be modified as

$$\boldsymbol{\beta_{hkl} \cos\theta = \frac{k\lambda}{D} + 4\sin\theta \left(\frac{2u}{Y_{hkl}}\right)^{0.5}} \tag{6.11}$$

The $\beta_{hkl}\, Cos\,\theta$ V/s $4\, sin\theta\, (\frac{2}{Y_{hkl}})^{0.5}$ plot shown in Figure 6.1d is fitted linearly to find the crystallite size and anisotropic deformation energy [381].

6.3.1.2.4 Size-strain Plot

Size-strain plot (SSP) can also be used for obtaining the size and strain parameters. Size-strain analysis gives less importance to the values from the high inclination reflections at which have lower precision. In this plot the strain portrait is illustrated by Gaussian Function and size of the crystallite by Lorentz function as shown in equation (12) [[378][379].

$$\boldsymbol{(d_{hkl}\beta_{hkl}\cos\theta)^2 = \frac{k}{D}\,(d_{hkl}^2\beta_{hkl}\cos\theta) + \left(\frac{\varepsilon}{2}\right)^2} \tag{6.12}$$

The Slope of the plot (Figure 6.1e) provides information regarding the size of the crystallite whereas Y-intercept gives the strain values. The parameters obtained using different models are listed in Table 6.1

The Scherrer's equation, SSP and modified W-H models including UDM, UDSM and UDEDM were used to analyse the peak broadening. The crystallite size D obtained from different W-H methods and SSP methods are almost similar and are in good agreement with the values obtained from TEM, which indicates that the average crystallite size D obtained using various W-H and SSP methods is essentially identical to the values obtained using TEM, indicating that the incorporation of strain in these methods has very little impact on the average crystallite. The lattice strain computed using the various W-H approaches was discovered to be equivalent and congruent of strain in various forms of W-H methods has a very small effect on the average crystallite. The lattice strain calculated from the different W-H methods was found to be comparable and in agreement with each other. All three models are proven to be effective in this study for estimating crystallite size and strain.

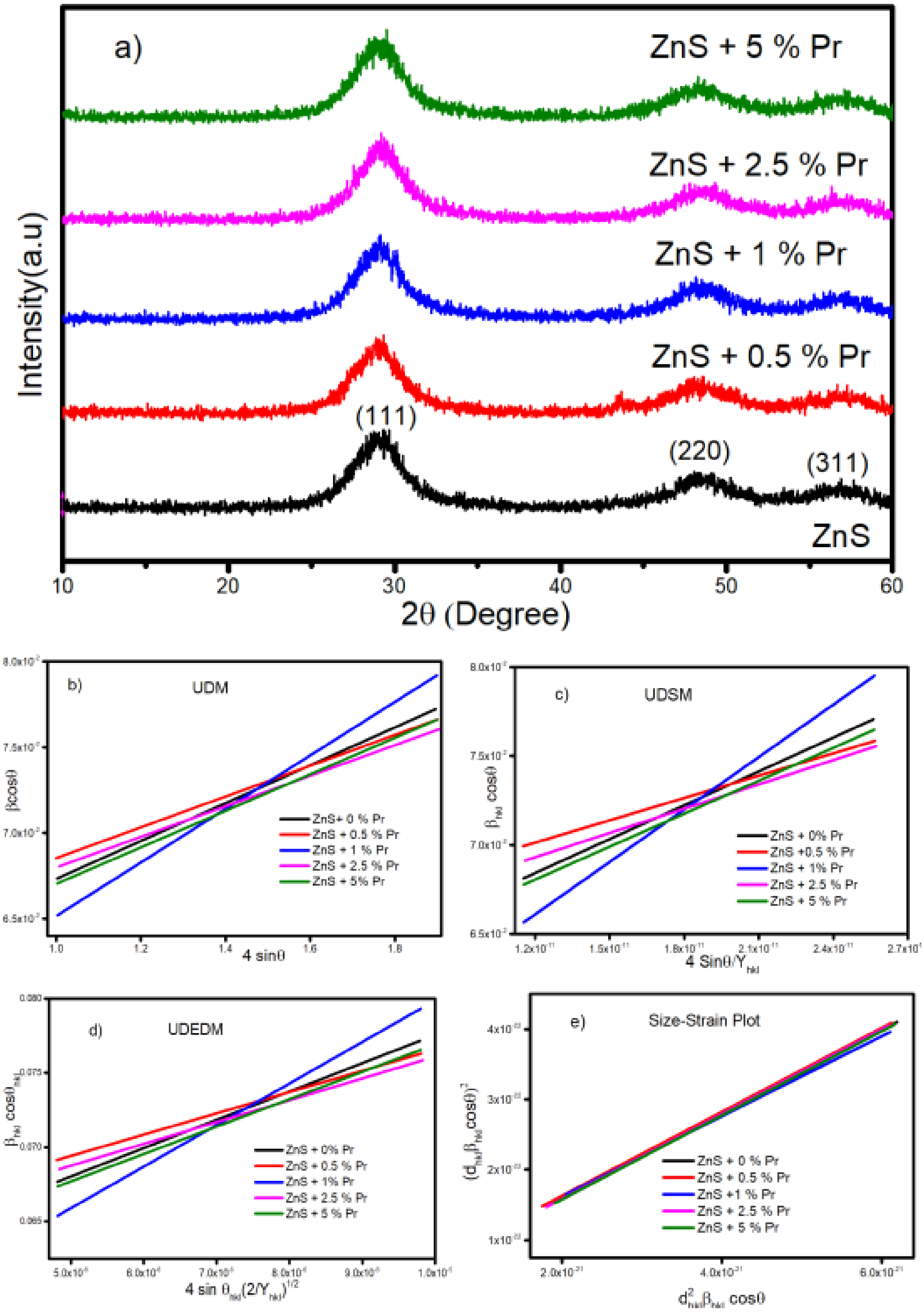

Figure 6.1: a) XRD patterns of Pr doped ZnS nanoparticles b) UDM, c) UDSM, d) UDEDM e) Size-strain plot of Pr doped ZnS

Table 6.1 Structural parameters for Pr doped ZnS NPs determined using different approaches

Samples	Parameter	Scherrer	UDM	UDSM	UDEDM	SSP
ZnS	**D(nm)**	2.12	2.46	2.28	2.37	2.32
	ε(10^-3)		11	(110) =7.312 (220) =7.904 (311) =8.577	(110) =9.14 (220) =9.505 (311) =9.902	
	σ(10^9)			6.35E-01	0.763	
	U(10^3)				3627.556	
ZnS+0.5% Pr	**D(nm)**	2.15	2.33	2.13	2.23	2.32
	ε(10^-3)		8.97	(110) =4.821 (220) =5.211 (311) =5.655	(110) =6.871 (220) =7.144 (311) =7.442	
	σ(10^9)			4.18E-01	0.573	
	U(10^3)				2049.345	
ZnS+1% Pr	**D(nm)**	2.14	2.79	2.55	2.67	2.43
	ε(10^-3)		15.59	(110) =11.324 (220) =12.24 (311) =13.282	(110) =13.4207 (220) =13.953 (311) =14.535	
	σ(10^9)			9.83E-01	1.12	
	U(10^3)				7817.025	
ZnS+2.5% Pr	**D(nm)**	2.13	2.35	2.17	2.26	2.3
	ε(10^-3)		8.9	(110) =5.245 (220) =5.67 (311) =6.153	(110) =7.004 (220) =7.327 (311) =7.633	
	σ(10^9)			4.55E-01	0.588	
	U(10^3)				2155.699	
ZnS+5% Pr	**D(nm)**	2.12	2.46	2.29	2.37	2.32
	ε(10^-3)		10.64	(110) =7.114 (220) =7.69 (311) =8.345	(110) =8.8485 (220) =9.2 (311) =9.583	
	σ(10^9)			6.18E-01	0.739	
	U(10^3)				3398.069	

6.3.2 EDX mapping Analysis

The elemental composition and doping homogeneity in the final product were studied on JEOL6360 SEM/EDX system as displayed in Figure 6.2 (a-a’) and (b-b’). Figure 6.2 (a) and (b) reveal that the Zn, S and Pr elements are present in pure and doped samples. The composition of Zn, S and Pr elements are provided in tables. Furthermore, the Figure 6.2(a') and (b') show the mapping of elements in pure and doped samples which indicate that all these elements are homogeneously distributed throughout the samples. Hence, it is confirmed that the Pr doping has been taken place successfully homogeneously in ZnS.

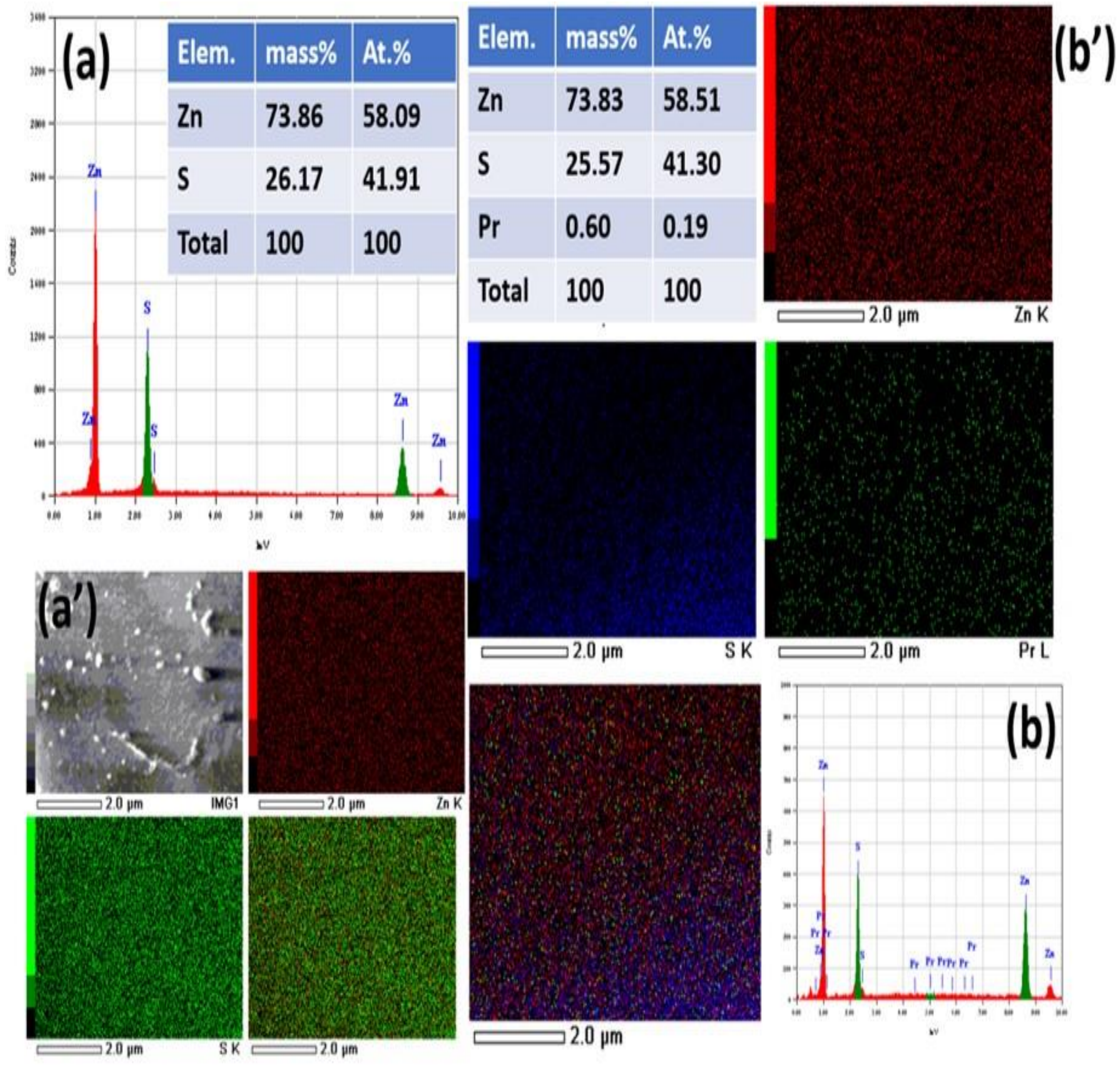

Elem.	mass%	At.%
Zn	73.86	58.09
S	26.17	41.91
Total	100	100

Elem.	mass%	At.%
Zn	73.83	58.51
S	25.57	41.30
Pr	0.60	0.19
Total	100	100

Figure 6.2 EDX spectra, elemental composition and e-mapping plots for (a.a') pure and (b,b') 1.0% Pr doped ZnS NPs

6.3.3 Transmission Electron Microscopy Analysis

The HRTEM image of pure ZnS samples prepared by microwave assisted method is shown in Figure 6.3. The TEM images (Figure 6.3a) indicate the nanocrystalline structure of samples with distinct well defined grain boundaries.

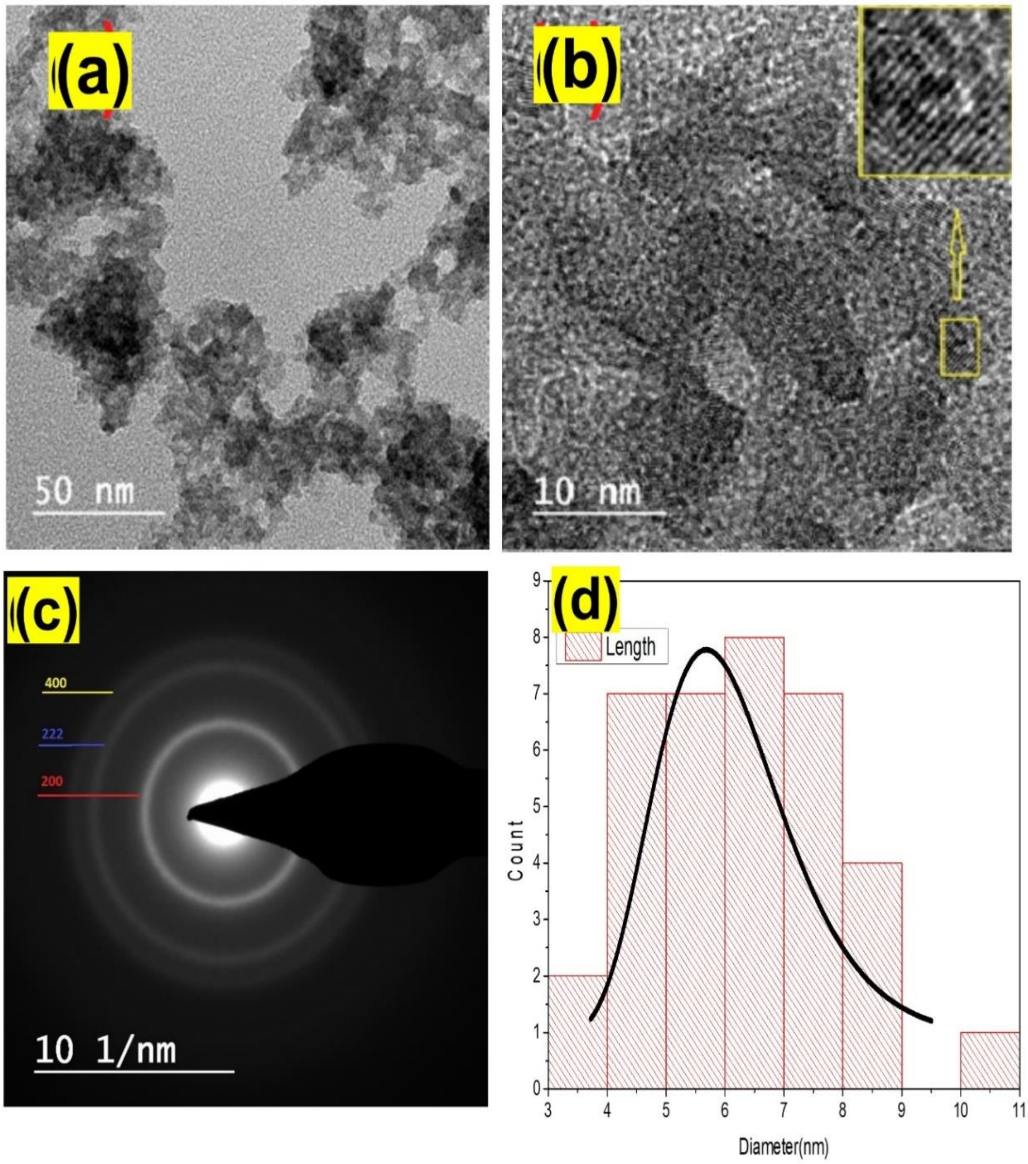

Figure 6.3: a) TEM, b) HRTEM (inset shows magnified image of (200) plane), c) SAED pattern and d) size distribution curve of pure ZnS

The average size of the particle calculated from the TEM image is 4.54 nm, which exactly matches with the XRD data. The d-spacing evaluated for the plane shown in the Figure 6.3b is 2.64Å for the pure sample which corresponds to (200) Plane. From the TEM image, it is clear that the pure ZnS nanoparticles are formed in almost spherical shape. The Selected Area Electron Diffraction (SAED) pattern of the same sample is also shown in Figure 6.3c. It can be seen that, the pure ZnS particles are polycrystalline and the rings from inside to outside correspond to

200, 220, 400 lattice planes of cubic. The size distribution plot of ZnS is shown in Figure 6.3d.

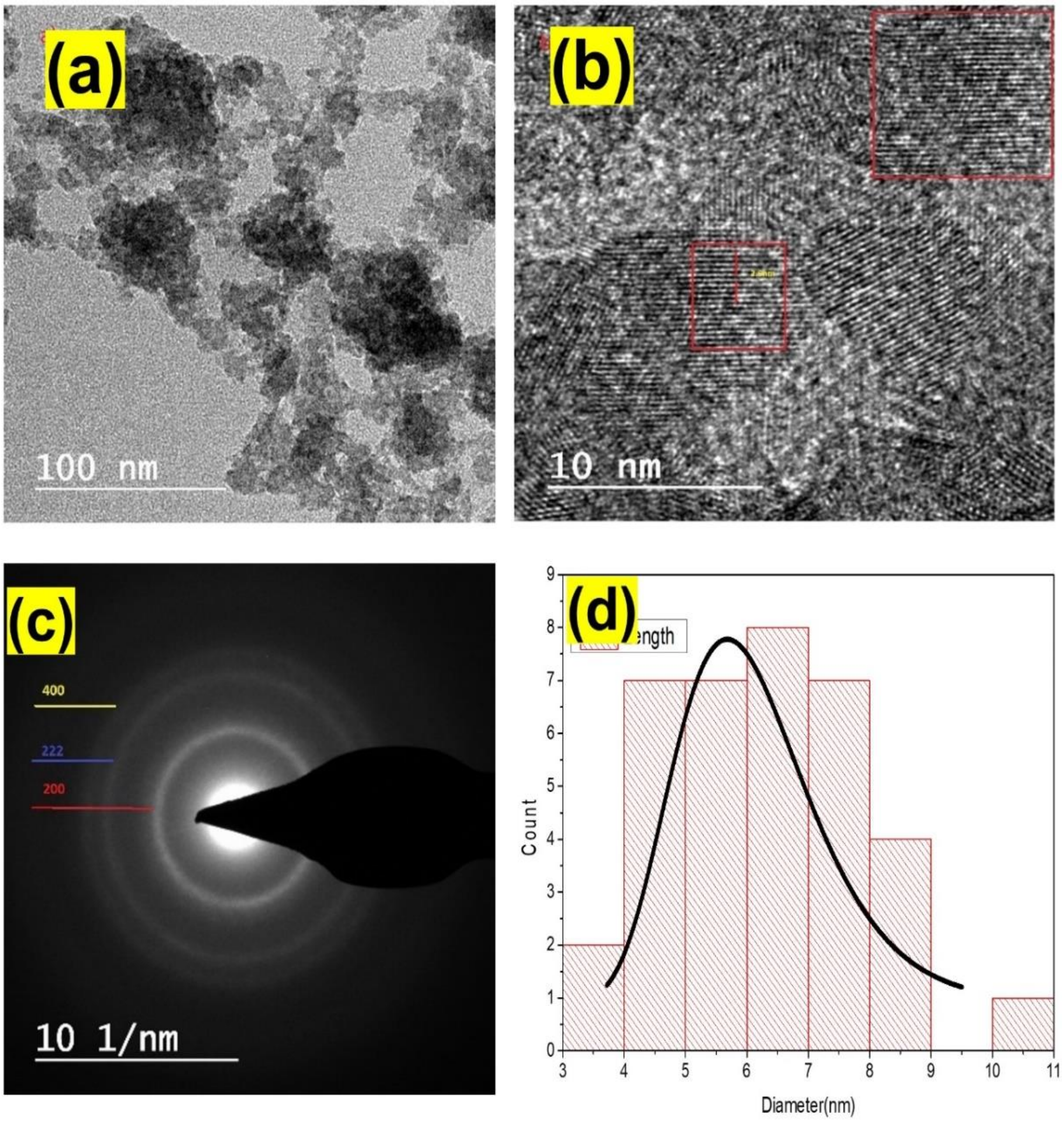

Figure 6.4. a) TEM, b) HRTEM (inset shows magnified image of (200) plane), c) SAED pattern and d) size distribution curve of 5% Pr doped ZnS sample.

The TEM image of 5% Pr doped ZnS sample is displayed in Figure 6.4. The measured average size of the spherically shaped particles from the Figure 6.4a is 6.31nm which is in well agreement with XRD values. The interplanar spacing is evaluated from the HRTEM image (Figure 6.4b) and the value obtained is 2.58Å which corresponds to 200 plane. The prepared samples are polycrystalline and the rings of SAED (Figure 6.4c) patterns from inside to outside correspond to 200, 220, 400 lattice planes of cubic. The size distribution plot of 5% Pr doped ZnS is shown in Figure 6.4d.

6.3.4. Diffused Reflectance Spectra Analysis

The diffused reflectance spectra of Pr doped ZnS nanoparticles are portrayed in Figure 6.5a. The plot shows that the reflectance values are less in the band gap region >350 nm and there is a rapid increase appeared in the range (350-420 nm.). The reflectance is maximum in the visible region and less in the U.V region. The 5% Pr doped ZnS sample has minimum reflectance value among the prepared samples, (and) the pure ZnS has maximum reflectance value and hence having minimum light harvesting ability. The band gap (E_g) of the samples from diffused reflectance evaluated using and Tauc relation. Kubelka-Munk relation is utilized to evaluate absorption coefficient. The F(R) (Kubelka-Munk function) is [354]

$$\mathbf{F(R)}=\boldsymbol{\alpha}=\frac{(\mathbf{1}-\boldsymbol{R})^{\mathbf{2}}}{\boldsymbol{R}} \tag{6.13}$$

Where ‘α’ is absorption coefficient and ‘R’ the reflectance.

The Optical band-gap can be evaluated using Tauc’s equation is of the form:

$$\boldsymbol{\alpha h\nu = L\ (h\nu - E_g)^s} \tag{6.14}$$

Where hν is the incident photon energy, L is a constant [389]. The value of s is ½ for direct band gap energy semiconductors and 2 for indirect band semiconductors. The Tauc’s plot ($(\alpha h\nu)^2$ - hν) of Pr-doped ZnS is portrayed in in Figure 6.5b. The value of E_g is assessed by extrapolating the linear part of $(\alpha h\nu)^2$ to zero α value. The measured E_g values are tabulated in Table 6.2.

The Figure 6.5c shows the extinction coefficient dispersion of prepared samples. From the figure it is clear that the extinction coefficient reaches maximum value at UV region and then decreases as wavelength increases. The 5% Pr doped ZnS nanoparticles has minimum extinction coefficient and 2.5% Pr doped ZnS has maximum values among the synthesized samples. The Function F(R) is proportional to the absorbance. The absorbance plot of Pr doped ZnS are shown in the Figure 6.5d. The 5%Pr doped ZnS has minimum absorption coefficient and 2.5%Pr doped ZnS nanoparticles has maximum absorption coefficient.

Table 6.2 Band gap and band edge of Pr doped ZnS

S. No.	Sample	Band Gap in (eV)	Band Edge (nm)
1	ZnS +0.5% Pr	3.6	322.93
2	ZnS +1% Pr	3.59	322.09
3	ZnS +2.5% Pr	3.61	321.97
4	ZnS +5% Pr	3.54	321.42

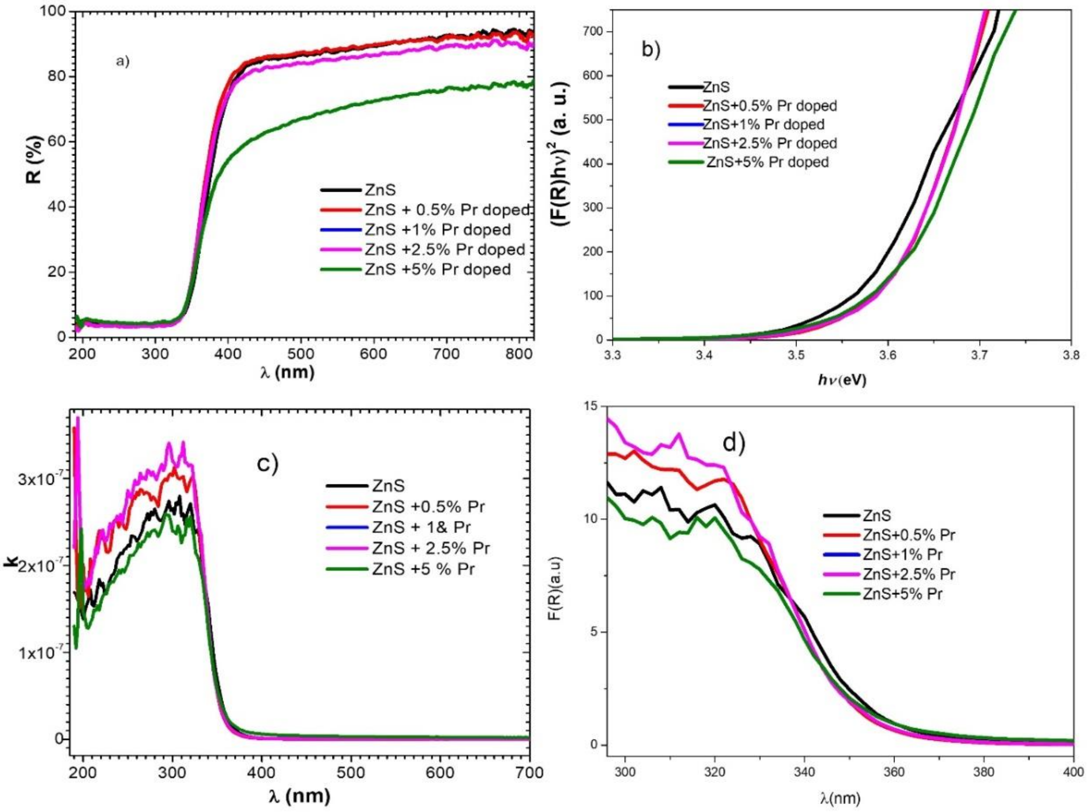

Figure 6.5: - Diffused Reflectance, a) Reflectance b) Tauc's Plot c) extinction coefficient dispersion d) Absorbance of present samples

6.3.5 Raman Spectra Analysis

The Raman spectra of Pr doped ZnS samples prepared by microwave assisted method measured in the range of 200-500 cm^{-1} is shown in the Figure-6.6. Raman Spectra of samples have two prominent peaks around 255 cm^{-1} and 341 cm^{-1} which corresponds to the fundamental transverse Optic (TO) and longitudinal Optic (LO) phonon modes of ZnS respectively. The Raman Spectra of pure ZnS displayed in Figure 4.3 and discussed in section 4.3.3. The Raman spectra of bulk cubic ZnS had reported by Nelson et al [385].The TO phonon mode and LO phonon mode of bulk cubic ZnS have been observed at 270 $cm^{-1}$and 350 cm^{-1} respectively. The shifting of Raman peaks towards lower energy compared to the reported values of bulk ZnS indicates the quantum confinement effect in Pr doped ZnS nanoparticles[466].The formation of Pr doped cubic ZnS nanostructures were confirmed by both XRD and Raman Spectra.

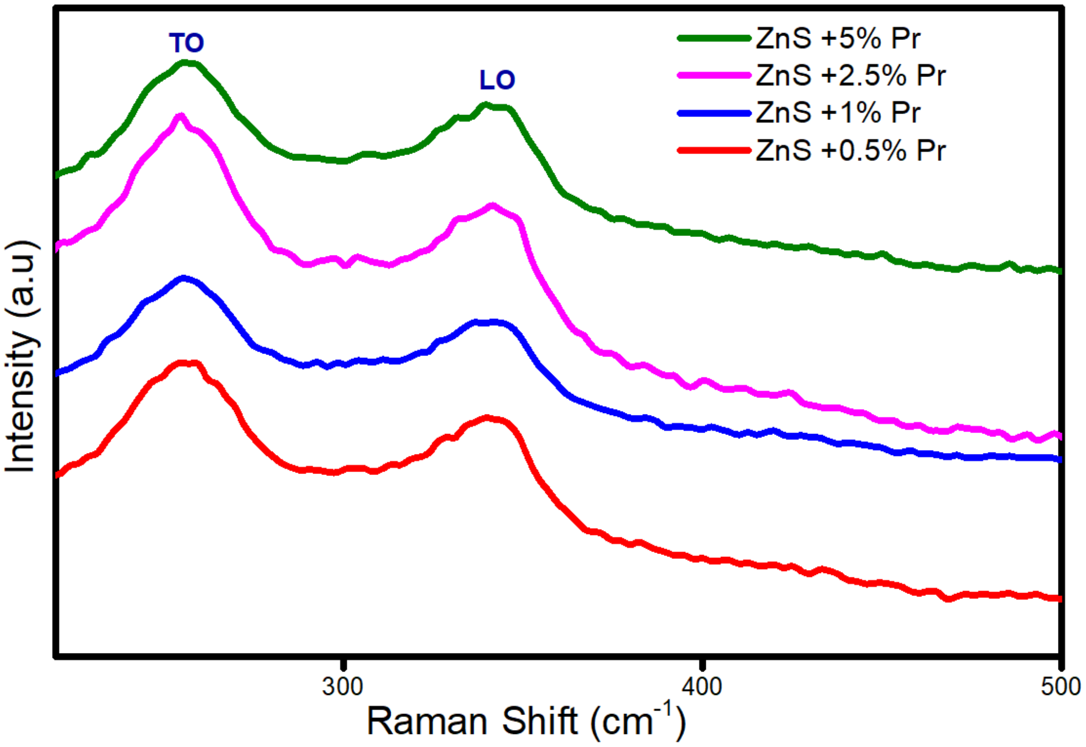

Figure-6.6: Raman Spectra of Pr doped Samples

6.3.6 Dielectric and Electrical Conductivity Studies

The dependence of frequency on the real part of dielectric constant ε̇ and imaginary part of dielectric constant ε̈ (dielectric loss) are shown in Figure 6.7a and 7b respectively. It has been observed that the value of ε̇ is very high at very low frequencies, after that the dielectric value is almost constant for a frequency range of 1MHz~5MHz as shown in Figure 6.7a. At high frequencies above 6MHz the value increasing with frequency. The value of dielectric constant is more than that of bulk. This can be explained by the Maxwell-Wagner model. As per this model high value of dielectric might be due to the induced interfacial polarization caused by larger grain boundary among the modest grain boundaries[397][478]. The 5% Pr doped ZnS sample has least έ value and 0.5% Pr doped ZnS has maximum dielectric values among the prepared samples.

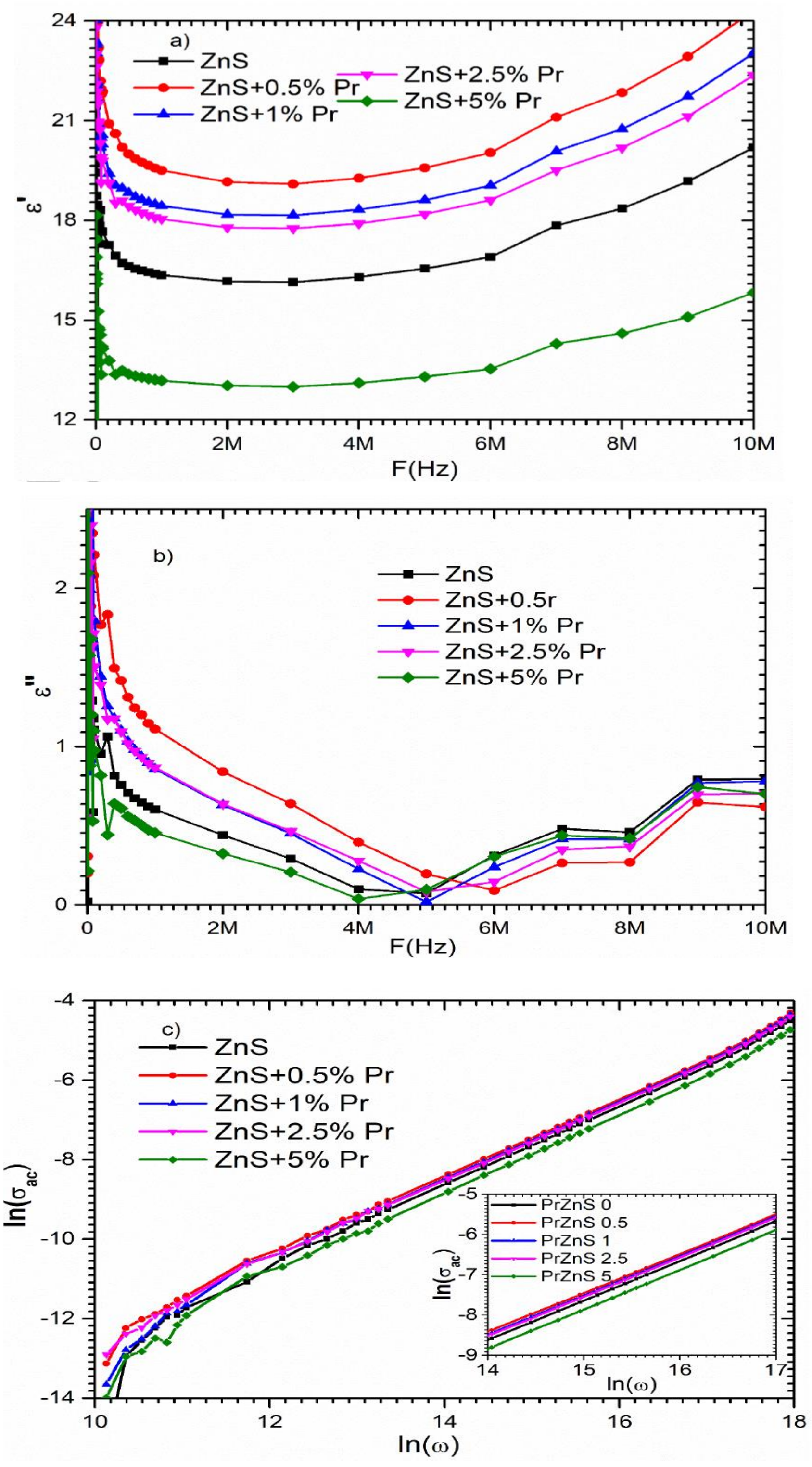

Figure 6.7: Variations of (a) dielectric constant vs frequency (b) dielectric loss vs. frequency c) Variation of ac conductivity vs angular frequency

The values of $\ddot{\epsilon}$ (dielectric loss) are very high at low frequencies and gradually decreasing to a minimum value. All the samples reach the minimum value around 5MHz, but 5% Pr doped ZnS attain the minimum at 4MHz itself. The dielectric loss also pursued the almost identical path to that of the dielectric constant as seen in Figure 6.7b[479].

The variation of ac conductivity (σ_{ac}) with frequency for all the prepared NPs are displayed in Figure 6.7c. Jonscher's law is used to study the relation between the ac conductivity, d.c conductivity and angular frequencies[480]. The figure clearly indicates that the increasing of the σ_{ac} with frequency is in accordance with the frequency power law. The least value noticed for the 5% Pr doped ZnS and greatest for 0.5% Pr doped ZnS NPs. Using the slopes of the above plots, the exponent values evaluated for all the samples within $\ln(\omega)$ range 14 to 17 are 0.9865, 0.9738, 0.9815, 0.9818, 0.9855 for pure ZnS, 0.5%Pr, 1% Pr, 2.5% Pr, 5% Pr doped ZnS NPs respectively.

6.3.7 Photoluminescence Studies

The photoluminescence emission spectrum of Pure and Pr doped ZnS samples synthesised by microwave assisted method for an excitation wavelength 320 nm is shown in the Figure 6.8. The de convoluted plots of the PL spectra using Gaussian fitting shows peaks common to all samples which are centred at ~ 362nm, 380 nm,394 nm, 425 nm and 437 nm. It is also noted that, the peaks at 394 nm, 425 nm and 437 nm are very weak or absent for the sample 2.5%Pr ZnS samples. The reason for emissions around 360 nm and 380nm are the transitions from the interstitial Zn[397].The emission peak at 394 nm and 425 nm arise due to the optical activation of sulphur vacancies[455]. The photoluminescence emission peak corresponding to the peak around 437 nm is attributed to transition between shallow donor associated with sulphur vacancies and Zn vacancies[481]. There are some peaks corresponding to the transitions of Pr^{3+} for all samples doped with Pr. The photoluminescence emission peaks correspond to Pr^{3+} transitions are seen at 497 nm,505 nm, 520nm, 540 nm and 558nm for different Pr doped samples. These peaks are corresponding to ${}^{3}_{0}P \rightarrow {}^{3}_{4}H$, ${}^{3}_{0}P \rightarrow {}^{3}_{4}H$, ${}^{1}_{6}I \rightarrow {}^{3}_{5}H$, ${}^{3}_{1}P \rightarrow {}^{3}_{5}H$ and ${}^{3}_{0}P \rightarrow {}^{3}_{5}H$ respectively[482][483][484][485][486].The de convoluted PL spectra of all samples shows that the Pure and Pr doped ZnS nanoparticles are three level laser active materials. The deconvoluted PL spectrum of 5 % Pr doped ZnS is shown in the inset.

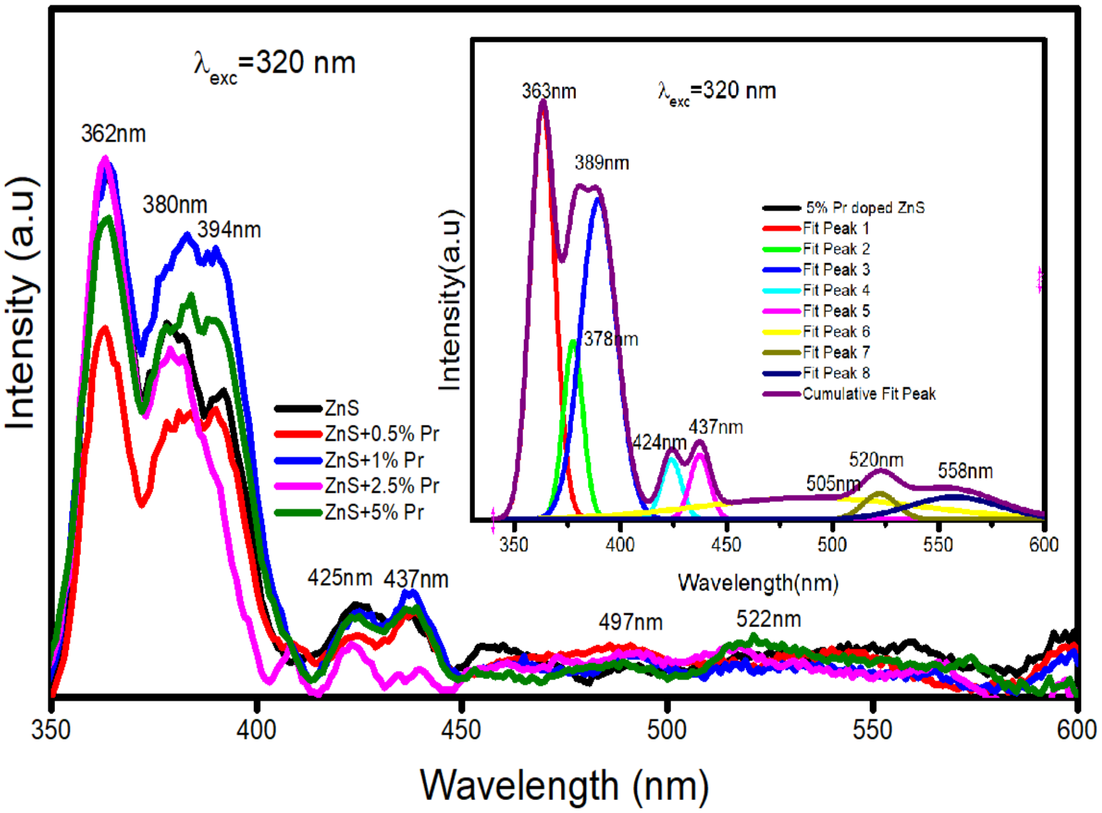

Figure 6.8 PL spectra of pure and Pr doped ZnS corresponding to λ_{exc}= 320 nm, deconvoluted PL plot of 5% Pr doped ZnS using Gaussian Fitting(inset)

6.3.8 Photocatalytic Studies

Photocatalytic (PC) experiments were conducted to assess the effectiveness of pure ZnS and 5% Pr-doped ZnS as photocatalysts for degrading Methylene Blue (MB) dye. The MB dye solution was prepared by dissolving 10 mg of MB in 1 L of distilled water and 0.03 g of each photocatalyst was added to 25 ml of this solution. The mixture was stirred magnetically in the dark for one hour to achieve adsorption–desorption equilibrium between the dye molecules and the catalyst surface. However, no significant degradation of the MB dye was observed in the presence of either pure ZnS or Pr-doped ZnS, indicating that these materials do not exhibit effective photocatalytic properties under the tested conditions, as illustrated in Figures 6.9a and 6.9b. This observation implies that neither pure ZnS nor Pr-doped

ZnS are appropriate for photocatalytic degradation of MB dye when exposed to visible light.

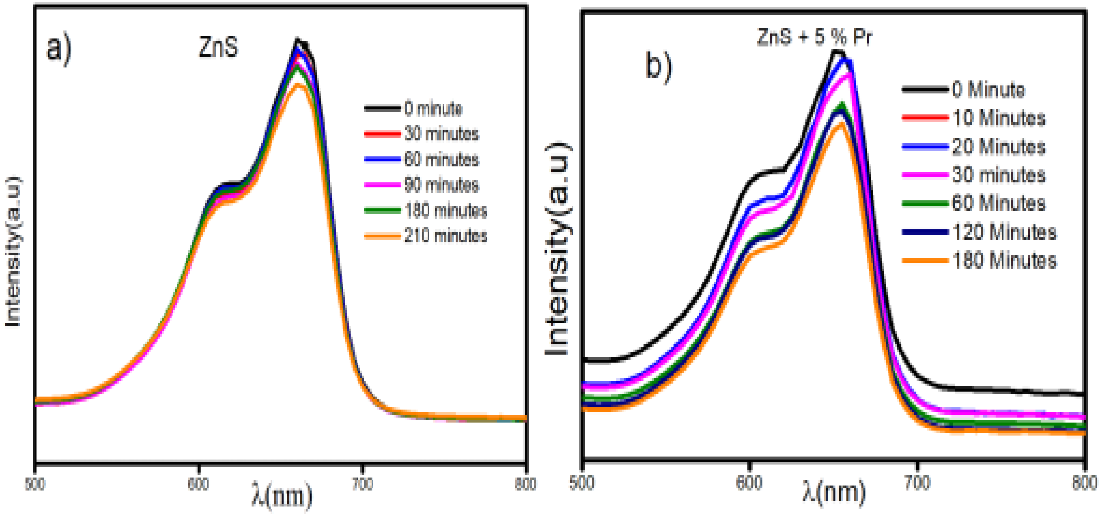

Figure 6.9 Photodegradation of MB dye a) with ZnS b) with 5% Pr doped ZnS photocatalyst

The PL spectra of pure ZnS and Pr-doped ZnS nanoparticles synthesized via the microwave assisted method do not exhibit transitions from sulphur vacancies to dangling sulphur bonds. These sulphur defect states in the hydrothermal samples act as trapping sites for charge carriers generated by visible light, contributing to their photocatalytic activity.

6.4 Conclusion

In this chapter we discussed the introduction of point defects on ZnS nanoparticles by doping with Pr. The growth of the nanoparticles in the cubic phase is indicated by the XRD pattern, FESEM and HRTEM. The Scherrer's equation, SSP and modified W-H models including UDM, UDSM and UDEDM were used to analyse the peak broadening. Raman spectrum of the samples reveals the two fundamental modes of Zinc blend structure, TO at 255 cm^{-1} and LO at 341 cm^{-1}. These values are in good agreement with the values previously obtained using Raman measurements. The nanocrystalline size was found to be ~ 2 nm. The PL spectrum shows the photoluminescent emission peaks that correspond to Pr^{3+} transitions. The Kubelka-Munk method was used to compute the energy gap. The band gap energy of the present samples at varied Pr concentrations in ZnS is in the range 3.54 to 3.64 eV. The results of the dielectric analysis show that the samples have low loss values and high dielectric constant values between 13 and 24. It is observed that the electrical conductivity also rises with frequency and Pr content. It is suitable for optoelectronics devices due to the low dimension synthesized NPs, high energy gap, dielectric constant and low loss values. Pr doped ZnS samples synthesised using microwave assisted co-precipitation method not showing PC activity like Er doped ZnS Samples.

Chapter-7

ZnS Nanoparticles by Hydrothermal Synthesis: Point Defects through La doping

In this work, point defects are introduced by La doping in ZnS nanoparticles synthesized using hydrothermal method. The structural, photoluminescent and photocatalytic properties of La doped ZnS NPs are studied. ZnS nanoparticles and La-doped ZnS nanoparticles with different doping concentrations (0.5, 1%, 2.5% and 5%) were synthesized. Pure ZnS nanoparticles showed a cubic phase as shown by X-ray diffraction (XRD) analysis, whereas doped ZnS nanoparticles showed a phase change to wurtzite, which was further supported by Raman spectroscopy. The size, form and distribution of the nanoparticles were revealed by morphological analysis conducted using scanning electron microscopy (SEM) and transmission electron microscopy (TEM). Photoluminescence (PL) spectra reveal no transitions related to the dopant. The existence of the required elements was verified using energy-dispersive X-ray spectroscopy (EDAX). An ideal degradation efficiency of 94% was achieved at a 1% doping concentration, according to an evaluation of the photocatalytic activity of nanoparticle under visible light. The samples synthesised by microwave assisted method are not photocatalytically active whereas samples prepared using hydrothermal are photocatalytically active. This study effectively illustrates the phase shift, shape, elemental composition, photoluminescent and photocatalytic activity of La-doped ZnS nanoparticles. Although no dopant-specific transitions were seen in the PL spectra, the overall luminous behaviour of the nanoparticles may be impacted by the host material's luminosity. These results offer insightful information on the possible uses of these nanoparticles in optoelectronics and other domains, including photocatalysis.

7.1 Introduction

Nanoparticles are getting a considerable amount of attention in recent years due to their unique features and wide-ranging applications in a variety of industries[487]. Zinc sulphide (ZnS) nanoparticles are a potential option among semiconducting materials since they have their exceptional optical[488][489], electrical[490][491] and catalytic characteristics[190][492]. In this work, we primarily studied the hydrothermal synthesis of Zinc Sulphide (ZnS) nanoparticles and the possible characteristics enhancement by lanthanum (La) doping. Doping ZnS nanoparticles with Lanthanum has a number of advantages. The rare earth element lanthanum is well-known for its distinct optical and electrical characteristics. The structure[493][494], optical absorbance[495][496] and charge carrier dynamics[494] of the nanoparticles may all be altered by adding lanthanum to the ZnS lattice .The purpose of lanthanum doping of Zinc Sulphide (ZnS) nanoparticles is to enhance their optical, structural and photocatalytic properties[497][195][498], rendering them more appropriate for use in optoelectronics, photocatalysis and sensing. The hydrothermal method is a widely accepted method for synthesising nanoparticles with regulated size, shape and crystallinity. Accurate control over the production of ZnS nanoparticles may be obtained by adjusting reaction parameters, including temperature, pressure and reactant concentrations[499]. The hydrothermal approach has been successfully used to synthesise ZnS nanoparticles in several research, indicating its effectiveness[500][501][189].

7.2 Experimental

7.2.1 Synthesis

ZnS nanoparticles (NPs) were prepared using the hydrothermal technique in accordance with a concise procedure. For the preparation of the solution, separate solutions of $ZnCl_2$, $SC(NH_2)_2$ powder and La $(NO_3)_3.6H_2O$ Lanthanum (III) nitrate hexahydrate) were prepared in de-ionized water. The $ZnCl_2$ solution was then mixed with five drops of hydrochloric acid and stirred at room temperature for an hour. After progressively incorporating the $ZnCl_2$ solution into the Thiourea solution, the mixture was subjected to magnetic stirring at room temperature for a further hour.

The resultant clear liquid was then put into a 100 cc Teflon-coated SS autoclave. After that, the autoclave was heated for 12 hours at 220 °C in a furnace. The autoclave was then taken out and left sealed to cool to ambient temperature. The $ZnCl_2$ solution was combined with an appropriate volume of Lanthanum (III) nitrate hexahydrate solution while being stirred magnetically in order to synthesise La-ZnS samples. Before being placed in the autoclave, this combined solution was blended with the thiourea solution and stirred.

7.2.2 Measurements

The structural analysis of the synthesized nanoparticles was performed using a Rigaku Miniflex 600 X-ray diffractometer with Cu K radiation. The data was collected in the range of 10° to 80°, with a scan speed of 10° per minute. Raman vibrational analysis was conducted using a Horiba Lab Ram HR Evolution Confocal Raman Spectrometer, powered by a 532nm Diode Pumped Solid State Laser. Photoluminescence investigation was carried out using an Agilent Cary fluorescence spectrophotometer. Optical examinations of the ZnS nanostructures were performed using The Cary 5000 UV-Vis-NIR spectrophotometer in the range of 200-1200 nano-meters. Morphological examinations were conducted using a ZEISS Gemini SEM 300, while TEM and EDAX studies were performed using Tecnai G2 F20, FEI Company at 200kV and OXFORD X-Max, respectively. Photocatalytic studies were conducted by adding 0.03 g of ZnS photocatalyst to 25 ml of Methylene Blue (MB) solution, using a Xenon short arc lamp as the visible light source. The MB dye solution was prepared by mixing 10mg of MB with 1L of distilled water

7.2.2.1 X-ray Diffraction Analysis

This study emphasises the hydrothermal synthesis of pure ZnS and La-doped ZnS nanoparticles because it gives fine control over the size, shape and properties of the nanoparticles. The structural characterisation of the synthesised nanoparticles was carried out utilising X-ray diffraction (XRD) investigations. XRD is a strong method that may offer information about the crystal structure and phase composition of materials. The XRD pattern of pure ZnS nanoparticles revealed three unique peaks at 28.72°, 48.06° and 56.87° as shown Figure 7.1. These peaks matched to the

(111), (220) and (311) planes of the cubic phase of ZnS semiconductor. The existence of these peaks suggests that the produced nanoparticles have a clearly Cubic crystal structure.

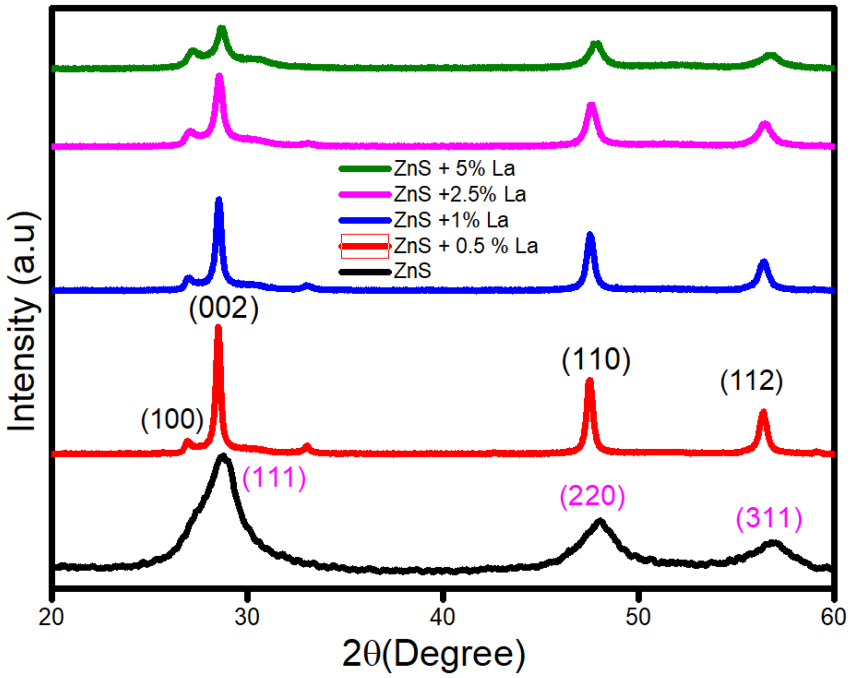

Figure 7.1 X-ray diffractometer pattern of ZnS and La doped ZnS

Interestingly, when ZnS nanoparticles were doped with La, the phase of the nanoparticles changed from cubic to hexagonal. The (100), (002), (110) and (112) planes of the wurtzite ZnS structure matched to the peaks seen in the XRD pattern of La-doped ZnS nanoparticles at 26.88°, 28.53°, 47.44° and 56.41°. The change in crystal structure shows that the integration of La into the ZnS lattice impacted the arrangement of atoms, resulting in the production of hexagonal ZnS nanoparticles. The hexagonal characteristics of La doped ZnS (La-ZnS) were determined using X-ray diffraction (XRD) data. It was found that the parameters were c=6.24 Å and a=3.82 Å. Doping ZnS nanoparticles allow for the management of their crystal structure, which creates new opportunities for modifying their characteristics and investigating their uses. The intensity of the XRD peaks decreased as the La concentration increased, which might be attributed to lattice instability caused by dopant atom occupancy in the ZnS host matrix [502].

The "Debye-Scherrer equation" was used to calculate the average crystallite size.

$$\mathbf{D} = \frac{k\lambda}{\beta\, cos\theta} \tag{7.1}$$

Where k is a constant of 0.9, λ is the X-ray wave length, β is the FWHM of the peak in radians and θ is the Bragg's angle in radians. The calculated crystallite size for pure ZnS is 2.95nm. The crystallite size of different doping concentrations (0.5%, 1%, 2.5% and 5%) was measured using the Debye-Scherrer equation. The crystallite sizes found were 27.2 nm, 23.73 nm, 18.96 nm and 16.39 nm, respectively. These results offer insightful information on the structural characteristics of La-ZnS and how doping concentration affects crystallite size.

7.2.2.2 Raman Spectra Analysis

The structure and vibrational properties of pure ZnS were examined in this research paper using Raman vibration investigations. The findings from Figure 7.2 verified that pure ZnS had a cubic structure. The transverse optical (TO) and longitudinal optical (LO) modes of vibration have been observed as the vibrational modes seen at 276 cm^{-1} and 337 cm^{-1}, respectively[147]. A peak seen at 248 cm^{-1} additionally pointed to an overtone of the transverse optical phonon mode[388]. The X-W-L point's lattice defect-induced phonon mode was shown by the peak at 308 cm^{-1}[147], emphasising the influence of structural defects on the material's vibrational properties. Moreover, it was found that a peak at 401 cm^{-1} was consistent with cubic ZnS TO+LA vibrations[388].

5% La-doped ZnS was analysed using Raman analysis in order to study its structural characteristics. The wurtzite structure of the 5% La-doped ZnS was validated by the findings, which showed distinct vibrational modes. It was found that the vibration detected at 270 cm^{-1} matched either the A1 or E1 modes of the transverse optical (TO) modes in wurtzite ZnS[147][503][504]. Similarly, in wurtzite ZnS, the vibration detected at 352 cm^{-1} was shown to be the E1 or A1 modes of the longitudinal optical (LO) modes[504][503][147]. In addition, a 431 cm^{-1} vibration was detected, which is consistent with the TA+LO modes of wurtzite ZnS[147]. Moreover, the second-order LA vibrations of wurtzite ZnS were shown by the peak that was present at 235 cm^{-1}[505][147]. Our results validate the wurtzite structure of 5% La-doped ZnS and offer important insights into its structural properties.

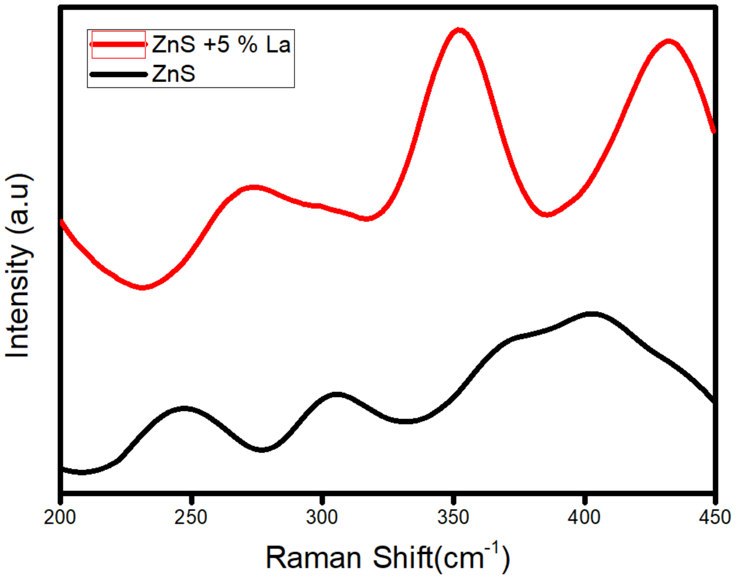

Figure 7.2. Vibrational Raman Spectra of ZnS and 5% La doped ZnS

7.2.2.3 Diffused Reflectance Spectra Analysis

The article focuses on estimating the band gap of pure ZnS and ZnS doped with La using diffused reflectance data. The Kubelka-Munk relation is used to calculate the absorption coefficient. The Kubelka-Munk function, or F(R),[475] is.

$$\mathbf{F(R)}=\boldsymbol{\alpha} = \frac{(1-R)^2}{R} \qquad \mathbf{(7.2)}$$

Where ‘α’ -absorption coefficient and ‘R’ the reflectance.

Tauc's equation could be used to calculate the optical band gap[368]

$$\boldsymbol{\alpha\, h\, \nu = L\, (h\, \nu\text{-}E_{g)}\,^{s}} \qquad \mathbf{(7.3)}$$

Where hν denotes incoming photon energy and L denotes a constant. For direct band gap energy (E_g) semiconductors, s is ½while for indirect band semiconductors it is 2, the reflectance spectra shown in Figure 7.3.

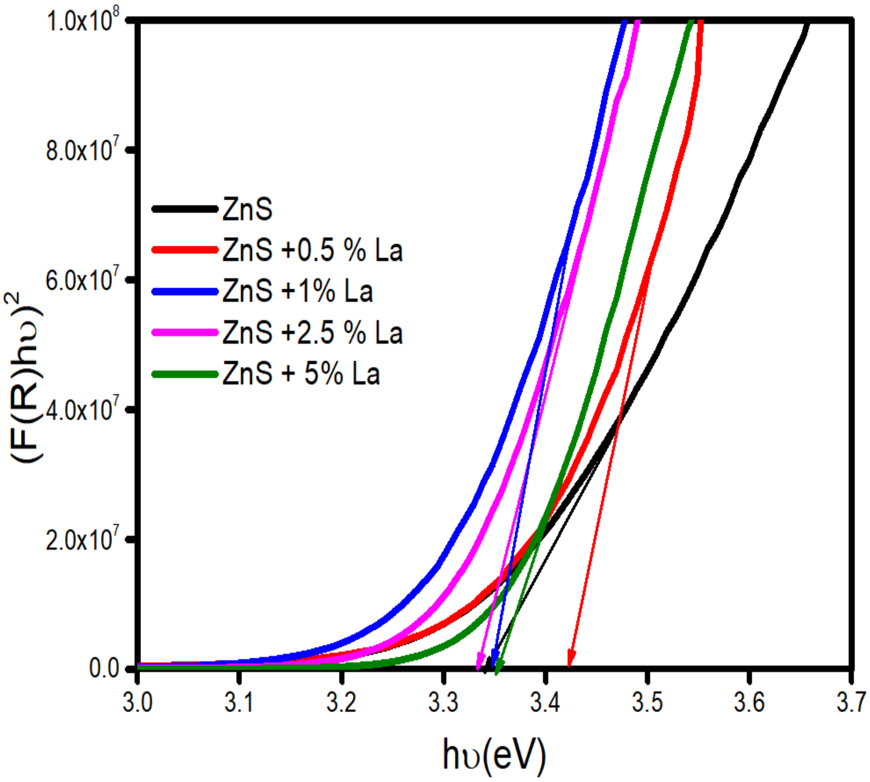

Figure 7.3. Reflectance Spectra of La doped ZnS Samples

Pure ZnS has a E_g value of 3.34 eV, showing the energy necessary for an electron to pass from the valence band (V.B) to the conduction band (C.B). However, when ZnS is doped with 0.5 % La, the E_g rises to 3.43 eV. The Burstein-Moss effect, which describes the expansion of the band gap or blue shift caused by the Pauli exclusion principle, can be related to the enhance in E_g caused by doping[506][507][508][509]. The Burstein-Moss effect occurs when doping provides more charge carriers, causing the absorption edge to move to higher energy. When all states near the conduction band get occupied in degenerately doped semiconductors, the optical band gap tends to widen. On the other hand, the band gap begins to contract with additional increases in doping percentage. Band gap shrinkage happens in highly doped semiconductors as a result of band gap renormalization[510][511][512][513]. Overall, the work sheds light on how ZnS behaves in terms of its band gap and how La doping may alter it. This information has consequences for designing and perfecting semiconductor materials for a range of uses. The measured bandgap values are listed in Table 7.1

Table 7.1 Band gap Values of La doped ZnS

S.No	Samples	E_g (eV)
1	ZnS	3.34
2	ZnS+0.5% La	3.43
3	ZnS+1% La	3.34
4	ZnS+2.5% La	3.32
5	ZnS+5% La	3.35

7.2.2.4 Transmission Electron Microscopy &EDAX

The morphology of pure ZnS nanoparticles and ZnS nanoparticles doped with 5% Lanthanum (La) was investigated using TEM. It was evident from the TEM scans that the shape of some of the pure ZnS nanoparticles was not uniform, since some of them had a spherical shape. It had been found that the interplanar spacing between the crystal fringes in the pure ZnS nanoparticles was 2.1 Å from the HRTEM image (Figure 7.4a and b), which is equivalent to the 220 planes in the ZnS cubic phase. The average particle size from the Figure 7.4c of the pure ZnS nanoparticles was 46.5 nm, with a size range of 15.7-87.3 nm. The range of particle sizes was visible in the size distribution curve from Figure 7.4 d. The cubic structure of pure ZnS was validated by the SAED pattern shown in Figure 7.4 e. In the pure ZnS nanoparticles, Zinc (Zn) and Sulphur (S) were detected by EDAX analysis (Figure 7.4 f)

On the other hand, a nanocrystalline structure with defined grain boundaries was seen in the TEM image Figure 7.5 of the La-doped ZnS nanoparticles. The d-spacing for the plane shown in the HRTEM image (Figure 7.5 a and b) was 3.1 Å, showing hexagonal development along the (002) plane. The average particle size of the La-doped ZnS nanoparticles measured from Figure 7.5c was 37.65 nm and the size distribution plot is shown in Figure 7.5d. The hexagonal phase was confirmed and the crystallographic orientation was determined using SAED (Figure 7.5e) pattern analysis. In the La-doped ZnS nanoparticles, Zn, S and La were detected by EDAX analysis from Figure 7.5f.

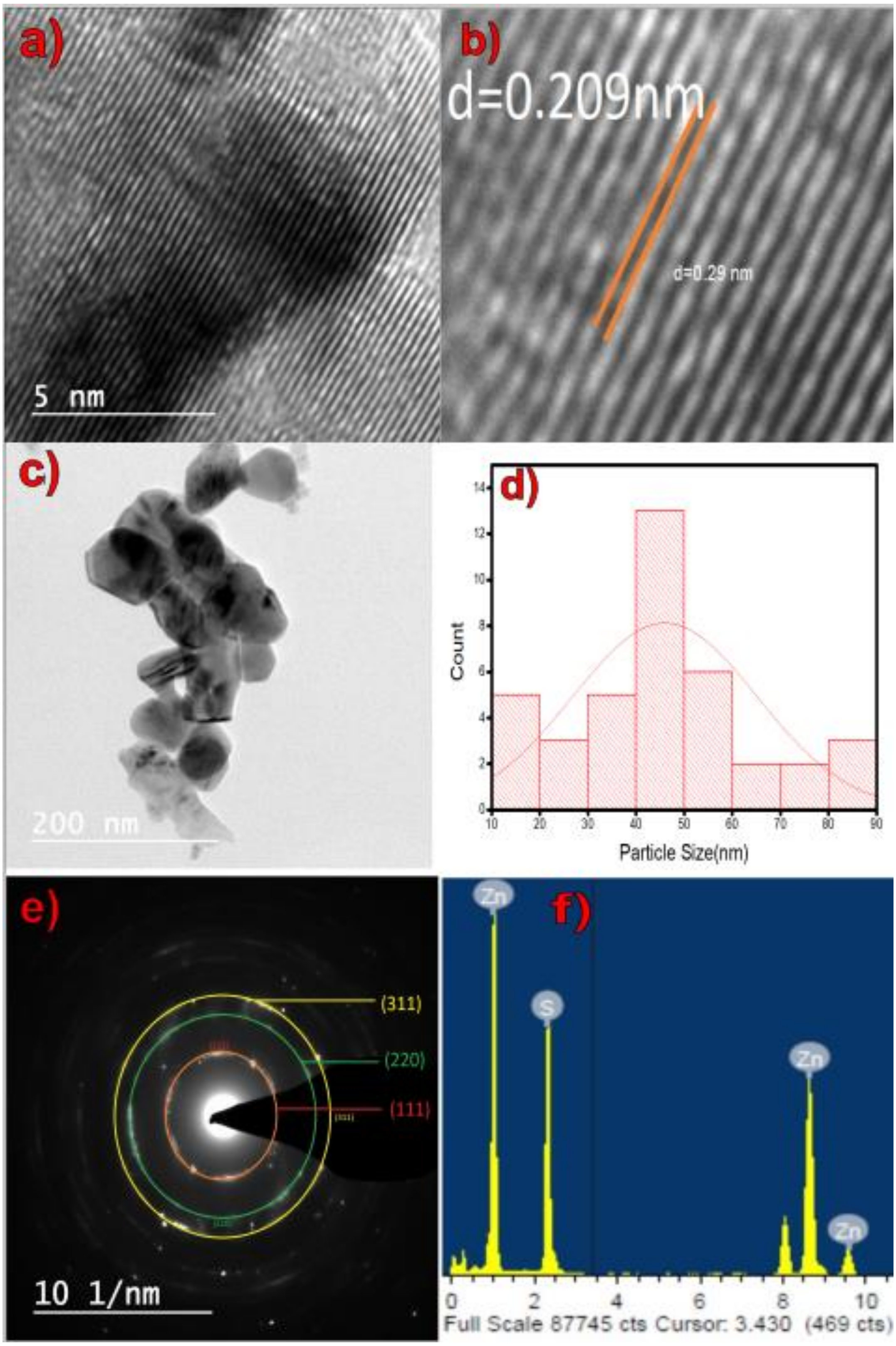

Figure 7.4. a), b) HRTEM image & c) TEM image d) Size Distribution Curve e) SAED pattern f) EDAX Spectrum of ZnS

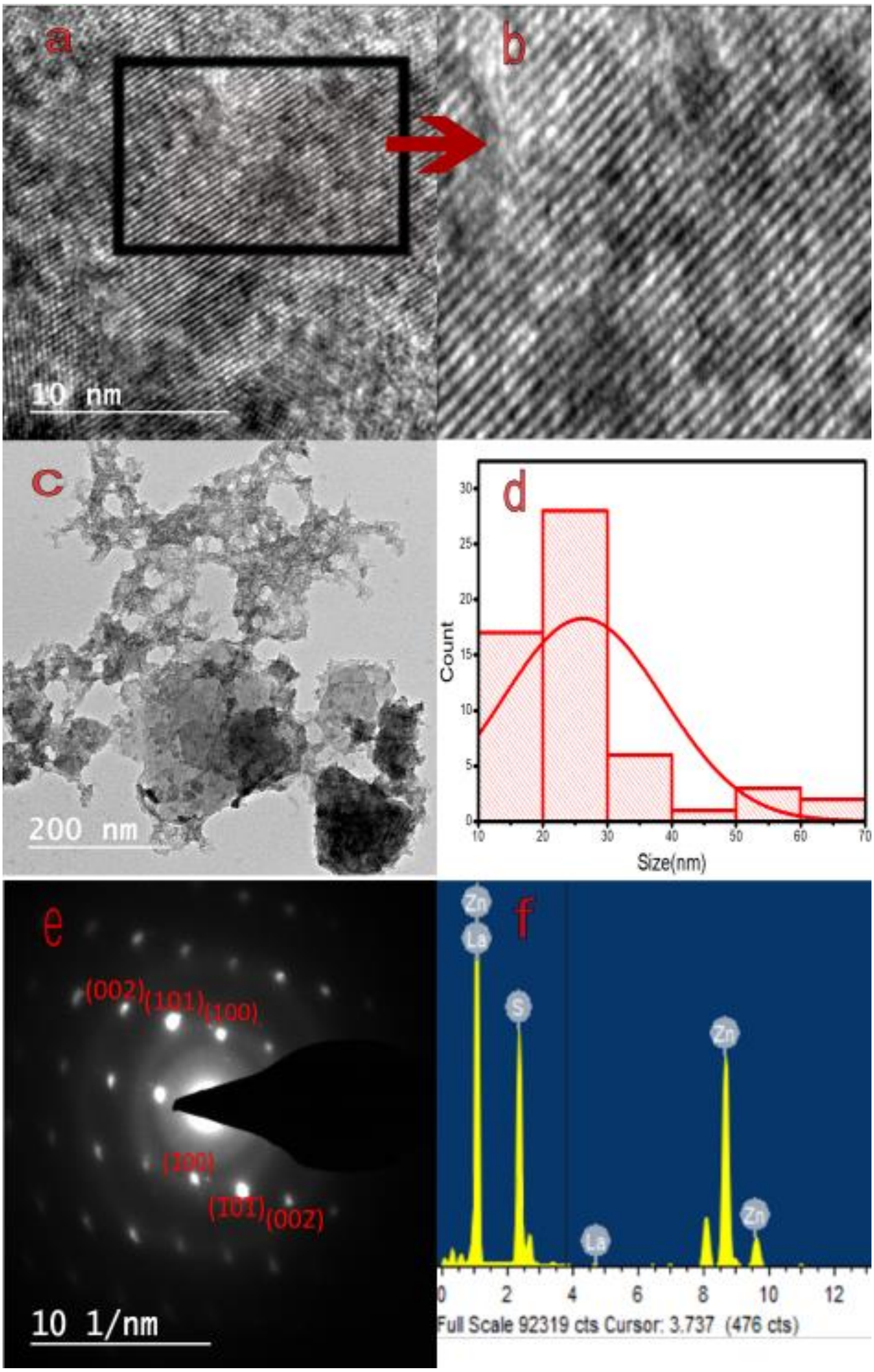

Figure 7.5. a), b) HRTEM image c) TEM image d) Size Distribution Curve e) SAED pattern f) EDAX Spectrum of 5% La doped ZnS

7.2.2.5 Scanning Electron Microscopy

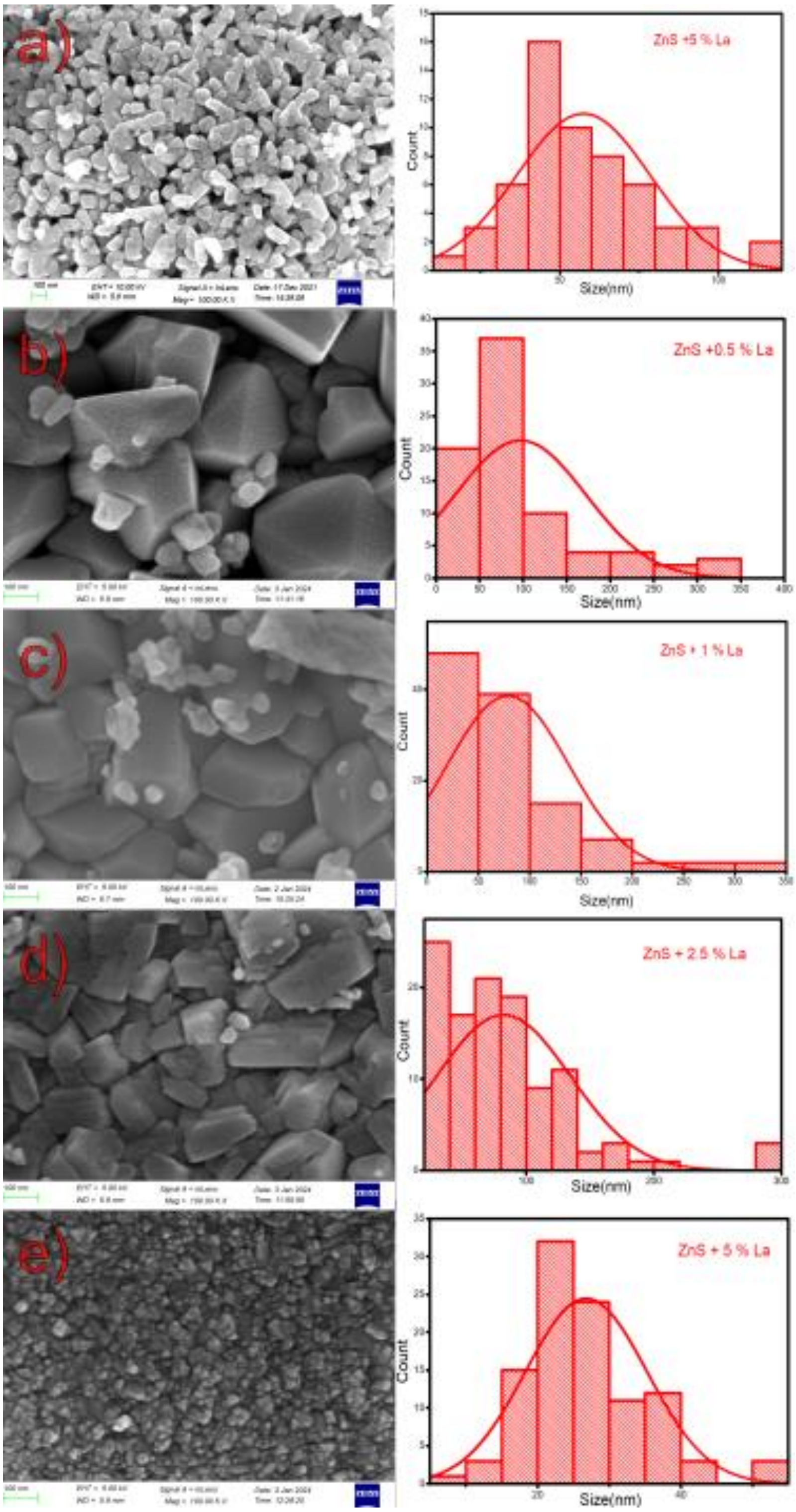

Figure 7.6. SEM image of a) ZnS, b) ZnS+0.5% c) ZnS+1% d) ZnS+2.5% e) ZnS+5% La doped

SEM analysis was used in this study to examine the morphology of pure and La-ZnS nanoparticles. The SEM pictures Figure 7.6 (a-e) showed that the majority of the particles grew in a polygonal pattern rather than having a regular shape. For varying La doping concentrations in ZnS, the average crystallite size was determined. The average crystallite size for the pure ZnS sample was measured and found to be 52.67 nm. The average crystallite diameters measured at 0.5%, 1%, 2.5% and 5% La doping concentration were 94.94 nm, 77.56 nm, 80.1 nm and 26.85 nm, respectively. It's noteworthy to notice that the sizes found through SEM examination were significantly larger than those found through XRD analysis. SEM measurements are routinely carried out on the surface of the sample, where particle agglomeration or clustering can occur, resulting in larger apparent particle sizes[514].

7.2.2.6 Photoluminescence Studies

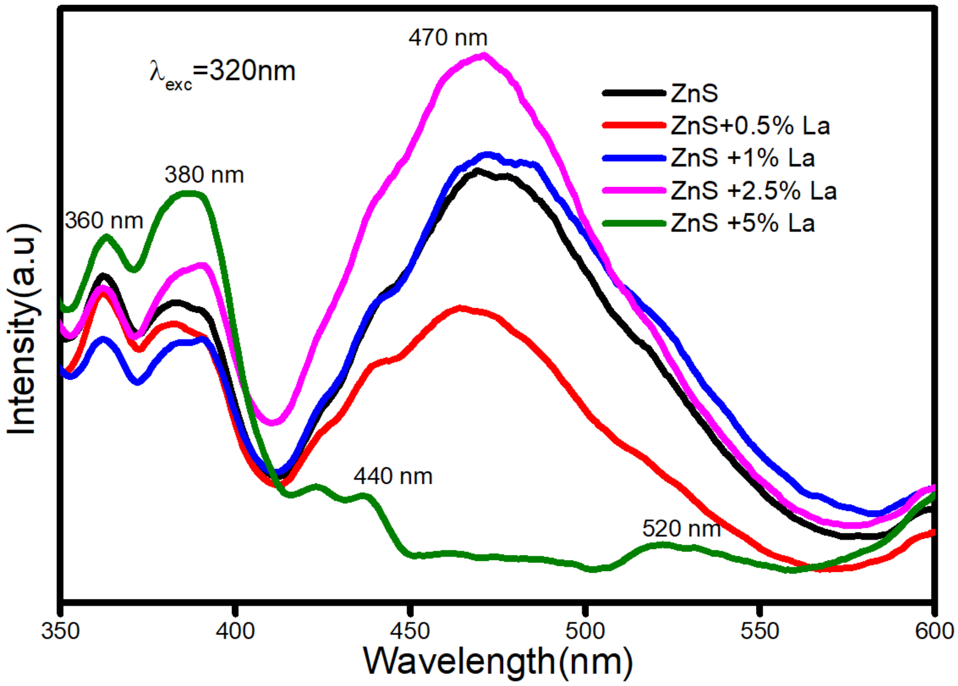

Figure 7.7. PL Spectra of ZnS and La doped ZnS nanostructures

This study used the hydrothermal technique for synthesising ZnS and La-doped ZnS nanoparticles. These nanoparticles were subjected to a photoluminescence study corresponding to an excitation wavelength 320 nm, which revealed several peaks at different wavelengths. The peak at 360 nm in the Figure

7.7 represented the transition from interstitial zinc to the V.B, demonstrating the existence of zinc atoms in the interstitial sites[397]. Peaks at 380 and 390 nm were seen, corresponding to the transitions from the C.B to zinc vacancy and interstitial zinc to interstitial sulphur, respectively, indicating the presence of crystal lattice defects[515]. The shift from the sulphur vacancy to the V.B, which implies vacancies in the sulphur atoms, was shown by another peak at 440 nm[516]. A signal at 470 nm indicated a transition from surface vacancy to dangling surface bonds on the boundaries, indicating the presence of surface defects[516]. The shift from sulphur to zinc vacancies was finally revealed by a peak at 520 nm, indicating vacancies in both zinc and sulphur atoms[456]. These findings provide insights into the optical properties and structural aspects of the synthesised nanoparticles, pointing to their potential uses in optoelectronic devices and related domains.

Upon increasing the doping percentage, the luminescence peak intensity at 360 nm and 380 nm increases, after first decreasing with La doping. This intensity shift may be explained by the addition of La, which modifies the energy level of Zinc Sulphide (ZnS), or by the addition of La to its own energy level[517]. It is noticed that when the doping percentage grows, the strength of the peaks at 440 nm, 470 nm and 520 nm decreases dramatically which is called as concentration quenching[516]. The two reasons for this decrease in intensity are the La ion doping-induced distortion of the lattice structure and the elimination of interstitial ions like S and Zn. A key factor in influencing the strength of the peaks is the configuration of dopants on the host material and their spatial distribution[518]. It is observed that the intensity is highest for samples with 2.5% La doped. The improvement of radiative recombination in the luminescent process at lower doping percentages is responsible for the increase in intensity[519].Transitions corresponding to the La dopant were not observed.

7.2.2.7 Photocatalytic Studies

The PC research is started by mixing a 25 ml solution of Methylene Blue (MB) with 0.03 grammes of photocatalytic pure and La-ZnS material. One litter of distilled water is used to dissolve 10 mg of dye in order to produce the dye solution.

In the absence of light, the resulting mixture including the photocatalyst and MB solution is subjected to magnetic agitation for one hour. The adsorption and desorption of the MB dye on the catalyst surface can more easily reach an equilibrium condition during this stirring period.

Upon exposure to visible light, ZnS nanostructures containing adsorbed dye produce electron-hole pairs (e--h+)[386] .

$$ZnS + h\gamma \rightarrow e^{-}(CB) + h^{+}(VB)$$

When oxygen atoms attached to ZnS interact with the e-generated in the C.B of ZnS, superoxide anion radicals ($^{\bullet}O_2^{-}$) are created. Simultaneously, the positively charged holes produced in the V.B of ZnS react with hydroxyl groups on the surface to produce exceptionally reactive hydroxyl radical ($^{\bullet}$OH) species[332] . When MB dye is attached to ZnS nanostructures, it can interact with the highly reactive hydroxyl radicals ($^{\bullet}$OH) and superoxide radicals ($^{\bullet}O_2^{-}$), causing the dye to degrade. By doping ZnS with ions of rare earth metals, charge carriers may be trapped and their lifetimes can be prolonged. By trapping the electrons and lowering the recombination of photogenerated electron-hole pairs, rare-earth metal ions may effectively separate the photoinduced electrons and prevent charge recombination in the electron-transfer processes. Dopants thus improve photocatalyst efficiency[520][521]. The PL spectra of La-doped ZnS nanoparticles synthesized using the hydrothermal method do exhibit transitions from sulphur vacancy to dangling sulphur bonds. These sulphur defect states in the hydrothermal samples act as trapping sites for charge carriers generated by visible light, contributing to their photocatalytic activity.

The photodegradation efficiency of ZnS is significantly affected by lanthanum (La) doping, as in Figure 7.8a. For this process to take place, only a small amount of lanthanum atoms must be added to the ZnS structural configuration. Researchers found that implementing this strategy improved the capacity of ZnS to breakdown environmental contaminants and cleanse water significantly [522]. The maximum photodegradation efficiency in this study is attained when ZnS nanostructures are doped with 1% lanthanum. The most effective breakdown of target compounds seems to occur at this particular doping concentration, which is thought to be the optimum level due to the synergistic actions of lanthanum and zinc. It is thought that the easier electron-hole pair separation made possible by the presence of lanthanum atoms at this level will increase photocatalytic activity. However, in comparison to pure ZnS, the photodegradation efficiency steadily declines above the ideal doping concentration of 1% lanthanum and for 0.5% doping as shown in Figure 7.8b. This unexpected observation might be attributable to the creation of unwanted recombination centres associated with lanthanum or changes in the electronic structure of the ZnS lattice[523] .The recombination rate increases as the dopant concentration goes over the ideal level.

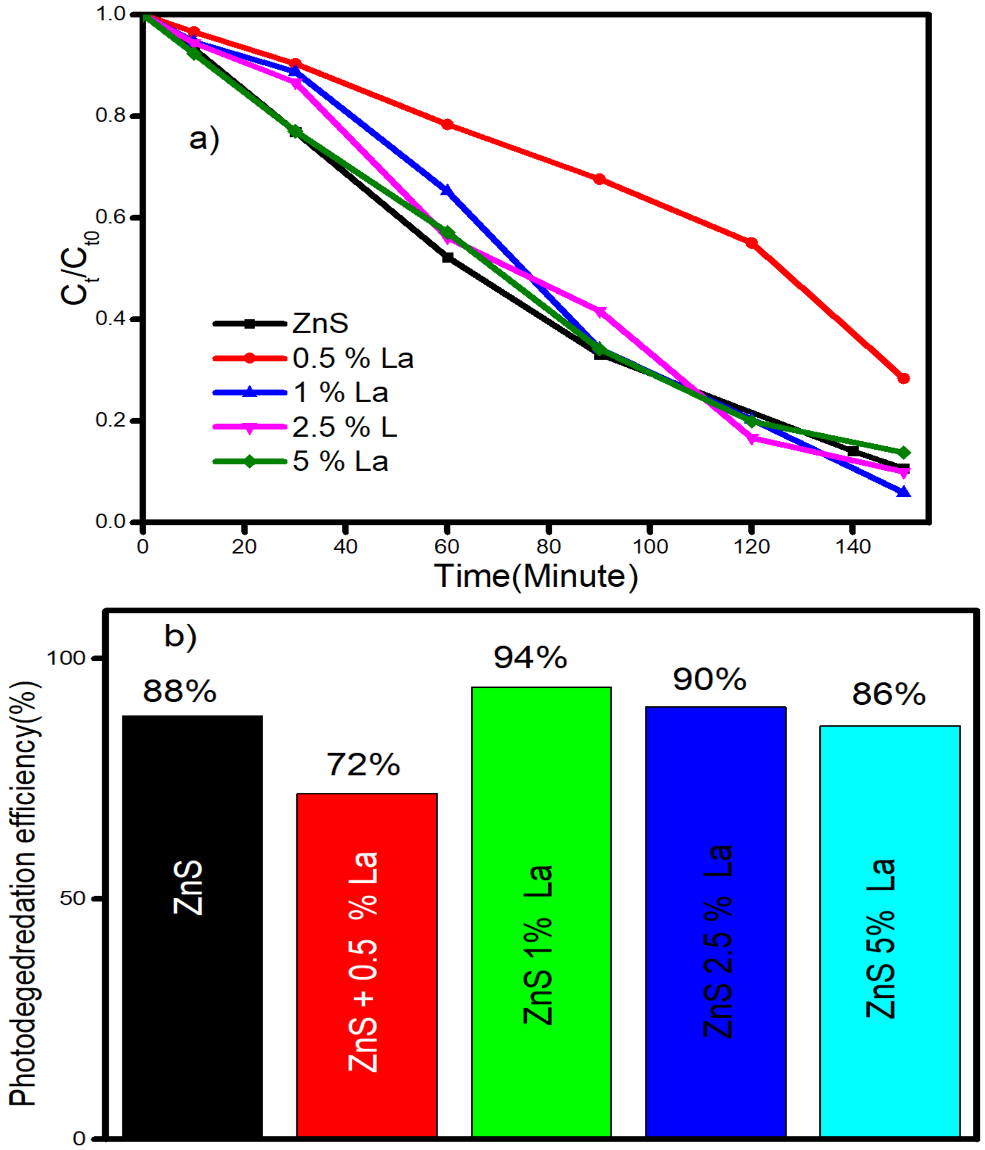

Figure 7.8. a) Photodegradation of MB Dye solution with ZnS and La doped ZnS catalyst b) Photodegradation efficiency of present photocatalyst.

7.3 Conclusion

In this work, the hydrothermal method is used keeping equal stochiometric ratio for Zn and S for the introduction of point defects by doping with La. XRD and Raman spectroscopy verified that the doping of La caused a phase transition from cubic to wurtzite. The size, shape and distribution of the nanoparticles were determined by morphological analysis and the presence of the necessary elements was verified by EDAX. The La doped ZnS NPs show enhanced photocatalytic activity. Upon evaluating the photocatalytic activity of the nanoparticles, the maximum degradation efficiency was observed at a 1% La doping concentration. Despite the absence of dopant-specific transitions in the PL spectra, the host material could still have an impact on the general luminescence of nanoparticles. The possible uses of La-doped ZnS nanoparticles in photocatalysis and other domains, such optoelectronics, are further illuminated by our results. The synthesis, characterization and possible applications of La-doped ZnS nanoparticles are better understood as a result of this work, which also highlights the phase change, shape, elemental composition and photocatalytic activity of the particles.

Chapter-8

ZnS Nanoparticles by Hydrothermal Synthesis: Point Defects through Ce doping

In this chapter we are discussing about the introduction of point defects by Ce doping as we discussed La doping in Chapter 7. ZnS Using the hydrothermal technique, we synthesized ZnS and Ce-doped ZnS nanoparticles with various doping concentrations (0.5%, 1%, 2.5% and 5%). X-ray diffraction (XRD) analysis indicated that pure ZnS nanoparticles exhibited a cubic phase, but when doped with Ce, the phase changed to wurtzite. The phase shift in the doped ZnS nanoparticles was also verified by Raman spectroscopy. In the photoluminescence (PL) spectra, however, no transitions matching to the dopant were identified. Morphological examinations were carried out using scanning electron microscopy (SEM) and transmission electron microscopy (TEM), which revealed information about the size, shape and distribution of the nanoparticles. Energy-dispersive X-ray spectroscopy (EDAX) was used to confirm the elements. The visible light photocatalytic activity of the nanoparticles was examined and it was discovered that the photocatalytic efficiency initially increased with doping concentration and then decreased. A 1% doping concentration was determined to be the optimum level for 99% degradation efficiency. The success of the synthesis and characterization of Ce-doped ZnS nanoparticles is highlighted in this work, which demonstrates their phase change, shape, elemental composition and photocatalytic activity. Although no transitions matching to the dopant were seen in the PL spectra, The overall luminous behaviour of the nanoparticles may still be influenced by the luminescence of the host material. the findings give important insights into the possible uses of these nanoparticles in photocatalysis and other domains like optoelectronics.

8.1 Introduction

In light of the rapid breakthroughs and technical advances in science and technology, the research community is highly interested in studying innovative areas of nanotechnology[524]. Nanotechnology is the alteration of materials so that any of their dimensions fall inside the nanometre range of 1 nm to 100 nm[525]. Materials generated at the nanoscale exhibit a range of unique properties (optical[526], magnetic[527], electrical[528] and so on) due to their extremely high surface energy, very high surface area and quantum confinement. Nanomaterials (NMs) are of significant scientific importance due to their being able to bridge the gap between bulk materials and atomic or molecular structures. [529]. Owing to their unique physicochemical properties, NMs have numerous applications in electronics[530], the oil industry[531], medicine[532], photocatalysis[533] and cosmetics[534]. Nanomaterials can be developed by various types of processes, like chemical[535], physical[536] and biological methods[537].

Defect engineering is a possible approach for increasing light capturing in photocatalytic materials. In our earlier work, during hydrothermal processes, defects are effectively incorporated into the ZnS crystal. and it exhibits greater photocatalytic activity[125]. Doping is an excellent another tool for defect engineering[538] . Recently, much work has been focused to the preparation and investigation of rare earth metal doped chalcogenide nanoparticles due to quantum confinement and surface effects, chalcogenides show exceptional electrical, optical, optoelectronic[475] and magnetic properties at the nanoscale as compared to bulk material[539]. Because of its enormous exciton binding energy and broad band gap, Zinc Sulphide is one of the ideal phosphor materials[200] among the many chalcogenide materials. At room temperature (RT), ZnS has two crystal phases: cubic (C-Phase) and wurtzite (W-Phase) [201]. ZnS has several potential uses due to its large band gap, including solar cells[202], optoelectronic devices[540][368], sensors[194], flat panel displays[386], led and transducers[541], spintronics [195] and so on. Many synthesis approaches, including precipitation[196], hydrothermal[199] and mechanochemical methods[542], were used for the synthesis of doped and undoped ZnS nanosized structures.

The band gap of ZnS may be further modified by doping it with proper impurities, allowing it to be altered and improved in terms of electrical, optoelectronic and other properties. Rare Earth doping is a promising approach for improving magnetic, optical and electrical properties of the ZnS for the forthcoming era of spintronics and optoelectronics [543]. La-doped ZnS samples provide the opportunity to enhance ZnS's solar energy use[514]. Tb-doped ZnS has the potential for applications in light-emitting diodes, biomarkers and photocatalysis[544]. Eu doped ZnS nanomaterials could be a promising candidate for semiconductor optoelectronic applications[545]. Gd-doped ZnS nanoparticles are suitable for IR detector applications[546]. The incorporation of Sm obviously changes the host ZnS lattice, leading to a significant impact on the fabricated device's photo-detecting activity[547]. Doping ZnS with Pr improves its optoelectronic capabilities, making it suitable for use in sensors and photodetectors[471][475]. We may employ Nd doped Zn based nanomaterials as a dominating luminescent material in luminescence performances and it improves photochemical properties as well as light emission electronics[548]. Dy doped Zn based nanomaterials exhibits a high efficiency photocatalytic activity making them suitable for the gas sensor applications[548].

Ce is an interesting dopant in rare-earth element and by doping Ce, the size of the material can be reduced while the specific surface can be enhanced[549][550]. As a result, visible light-emitting fluorescent powder of the display[379], high-power laser, light-emitting diode [551]are widely used and can function as the most advanced luminous nano-opto and NMO (nano-mechano-optical) devices available today[552]. In our study, we investigated the structural, optoelectronic and photocatalytic performance of ZnS and Ce doped ZnS (Ce-ZnS) nanoparticles synthesized using hydrothermal method.

8.2 Experimental

8.2.1 Synthesis

The hydrothermal approach was used to create ZnS nanoparticles (NP) and the brief synthesis procedure followed. Five drops of Hydrochloric acid were added to the $ZnCl_2$ solution and stirred for an hour at RT after the requisite amounts of $ZnCl_2$, $SC(NH_2)_2$ powder and Ce $(NO_3)_{3.}6H_2O$ (Cerium (III) nitrate hexahydrate) were separately dissolved in de-ionized water. The $ZnCl_2$ solution is then dripped into the Thiourea solution, which continues to stir for an hour at RT. The clear liquid was then put into a 100 cc Teflon-coated SS autoclave. After being in a furnace heated at 220 °C for 12 hours, after being removed, the closed autoclave was left to cool to room temperature. A sufficient amount of Cerium (III) nitrate hexahydrate solution was added to $ZnCl_2$ solution and mixed together under magnetic stirring for the synthesis of Ce-ZnS samples. This solution was combined with the thiourea solution and then stirred before being poured into the autoclave.

8.2.2 Measurements

The structural analysis, Raman vibrational analysis, photoluminescence, diffused reflectance ,SEM,TEM,EDAX and photocatalytic studies are conducted as in literature [125].The structural analyses of prepared NMs were carried out using a 'Rigaku Miniflex 600 X-ray diffractometer' with Cu K (= 1.542 Å) radiation, running at 15 mA and 40 kV. Data was collected using a Cu target and a graphite monochromator in continuous scan mode from 10° to 80°, with a increment of 0.02° and a scan speed of 10° per minute. The Horiba Lab Ram HR Evolution Confocal Raman Spectrometer was used to conduct vibrational analysis on all of the materials. At ambient temperature, the Raman spectrometer was powered by a 532nm (Diode Pumped Solid State Laser). The Agilent Cary fluorescence spectrophotometer was also used in the photoluminescence investigation. Optical examinations of all ZnS nanostructures were performed at RT using 'The Cary 5000 UV-Vis-NIR spectrophotometer' in the range of 200-1200 n.m. Morphological examinations of all synthesised ZnS nanostructures were performed using a ZEISS Gemini SEM 300, while TEM and EDAX studies were performed using Tecnai G2

F20, FEI Company working at 200kV and OXFORD X- Max, respectively. A PC investigation is carried out by adding 0.03 g of ZnS photocatalyst to 25 ml of Methylene Blue (MB) solution, Xenon short arc lamp of 300W working with 20V, 15A power supply served as visible light resource. For the preparation of the MB dye solution, 10mg of MB were mixed with 1L of distilled water, yielding photocatalysts. For 1 hour in the dark, the mixture was magnetically stirred to attain adsorption-desorption equilibrium between the MB dye and catalyst.

8.2.2.1 X-ray Diffraction Analysis

The X-ray diffraction (XRD) pattern of ZnS and Ce-ZnS nanoparticles synthesized with varied Ce concentrations is shown in Figure 8.1. The XRD patterns showed peaks related to cubic-structured for pure ZnS sample (01-077-2100). There were no XRD peaks associated to other impurities. The peaks have matching hkl values of (111), (220) and (311). Lattice constant for the sample was computed using the hkl values. The calculated lattice constant value is 5.4 Å for pure ZnS NPs, which is well matched with the standard value 5.41 Å. However, after cerium (Ce) dopants were added, the study took an unexpected turn. Unusually, the C-Phase ZnS experienced a metamorphosis into the W-Phase that had hardly ever been described in the literature. It has been shown that the doping of Mn^{2+} and Cl^{-} ions in ZnS nanocrystals changes its zinc blend phase to W-phase [553][554]. But normal ZnS C-Phase to W-Phase transitions take place at a high temperature 1296 K [555] which requires a lot of energy and sophisticated anti-oxidation machinery. Therefore, in this study we report an extremely desirable, simple and energy-saving technique for producing hexagonal ZnS at low temperatures. The nanocrystalline character of the samples was shown by the broadened XRD peaks of the prepared samples. The intensity of XRD peaks, reduced as Ce concentration increased, which could be attributed to lattice instability generated by the occupancy of dopant atoms in the ZnS host matrix[502].The average crystallite size was determined using ‘Debye-Scherrer equation’.

$$\mathbf{D} = \frac{k\lambda}{\beta \cos\theta} \tag{8.1}$$

where k is a constant 0.9, λ is wave length of X-ray used, β is FWHM of peak in radians and θ is Bragg’s angle in radian. The measured crystallite size corresponding to pure, ZnS is 2.95nm.

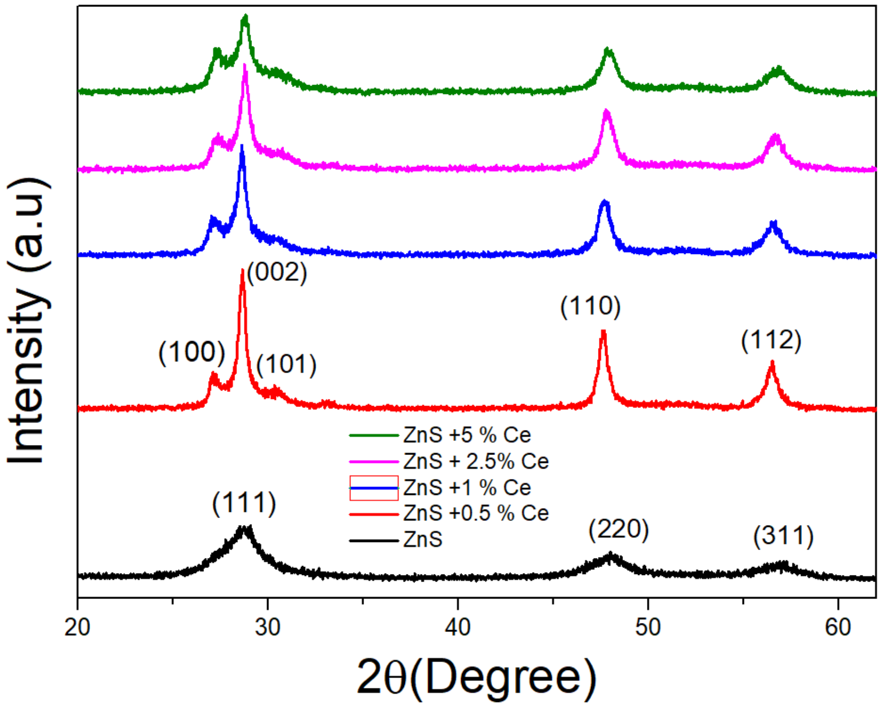

Figure 8.1. X-ray diffraction spectrum of ZnS and Ce doped ZnS samples

Four prominent peaks are seen in the XRD spectrum of Ce-ZnS samples at around 27.23°, 28.59°, 47.72° and 56.18° , which aligns to the (100), (002), (110) and (112) planes of the ZnS W- phase[556] (00-036-1450). This is probably due to the dopant atoms forming more nucleating centres, which is advantageous for the growth of the ZnS crystal phase. The hexagonal structure of nanocrystalline films may also be inferred from the observation of the characteristic plane (101) of hexagonal ZnS in XRD spectra[353].The lattice parameters of Ce-ZnS Hexagonal structured nanoparticles a and c are evaluated using equation (2)[514].

$$\frac{1}{d_{hkl}^{2}} = \frac{4}{3}\frac{(h^{2}+hk+k^{2})}{(a^{2})} + \frac{l^{2}}{c^{2}} \tag{8.2}$$

Where d_{hkl} is the interplanar spacing of the plane having miller index (hkl). The average values of c and a are 6.283 Å and 3.80 Å correspondingly, which are in correspond to the standard (JCPDS number 36- 1450) values 6.26 Å and 3.82 Å.

The measured crystallite size corresponding to 0.5, 1, 2.5 and 5 weight % Ce-ZnS are 19.49nm,16.87nm,17.32nm and 13.01nm respectively.

This work not only improves our understanding of crystal phase dynamics, but also offers new possibilities for creating functional materials with tailored characteristics for a broad variety of industrial uses.

8.2.2.2 Raman Spectra Analysis

In this work, we report a comprehensive Raman spectroscopy investigation of pure ZnS and cerium (Ce) doped ZnS in Figure 8.2. Our research provides crucial details about the material's crystal structure. The Raman spectrum of pure ZnS contains various unique peaks, each of which reveals important information about the characteristics of the material. Only longitudinal optical (LO) and transverse optical (TO) modes are permitted at the zone centre for the C-Phase ZnS phase[147]. The C-Phase of ZnS has been confirmed by sample exhibiting a TO peak mode at about 276 cm^{-1} and a LO peak mode at around 337 cm^{-1}. Notably, the presence of an overtone of the transverse optical phonon mode is indicated by a peak at 248 cm^{-1}, offering insights into the lattice dynamics of ZnS [388]. Furthermore, the presence of a peak at 308 cm^{-1} indicates the existence of a lattice defect-induced phonon mode at the X-W-L point, emphasising the impact of structural defects on the vibrational characteristics of the material[147]. Finally, the peak observed at 401 cm^{-1}, compatible with TO+LA vibrations of cubic ZnS[388] and confirmed XRD data.

The Raman spectrum of Ce-ZnS shows distinct peaks at 275, 297, 349, 377 and 430 cm^{-1}, which offer important information regarding the vibrational modes and lattice properties of Ce-doped ZnS. Notably, the existence of a peak at 275 cm^{-1} indicates the presence of either the A1 or E1 vibration of the transverse optical (TO) phonon mode[147][503][504], whereas the peak at 297 cm^{-1} corresponds to the E2 vibration of the TO mode[557] . Furthermore, the occurrence of peaks at 349 cm^{-1} indicates the presence of both A1 and E1 vibrational modes related with the LO phonon mode[147][503][504] . Additionally, a combination of TO modes and transverse acoustic (TA) modes (TO +TA)[558] and TA+LO[147] vibration modes of the hexagonal ZnS lattice are credited with developing the peaks at 377 and 430 cm^{-1}, respectively. These findings obviously confirm the wurtzite crystal structure of Ce-doped ZnS, revealing insight on its structural and vibrational characteristics, both of which are critical for a wide range of technological applications.

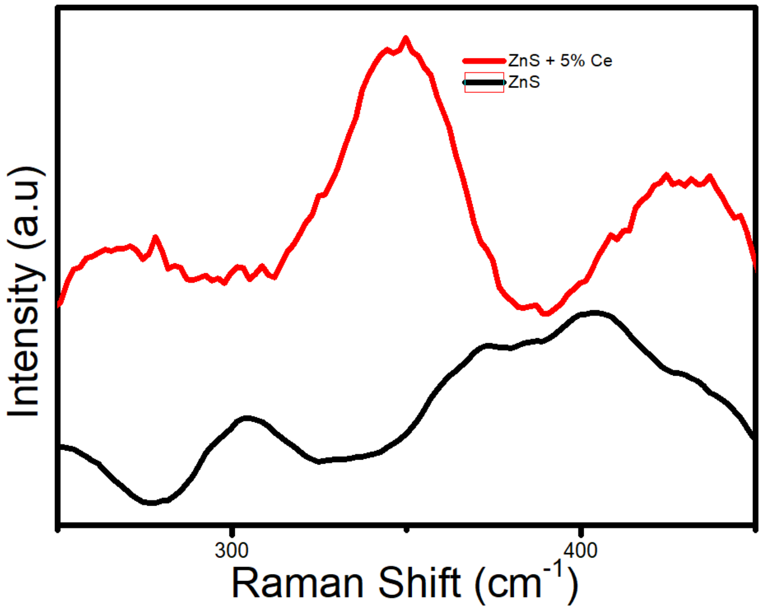

Figure 8.2. Vibrational Raman Spectra of ZnS and 5% Ce doped ZnS

8.2.2.3 Diffused Reflectance Spectra Analysis

The Tauc relation was utilised to get the band gap (E_g) from the diffused reflectance of samples. The absorption coefficient was obtained using the 'Kubelka-Munk relation'. The Kubelka-Munk function, F(R), is given

$$\mathbf{F(R)} = \alpha = \frac{(1-R)^2}{R} \tag{8.3}$$

Where 'α 'represents the absorption coefficient and 'R' the reflectance.

Tauc's equation, which is of the following form, can be used to calculate the optical band-gap

$$\alpha h\nu = L\,(h\nu - E_g)^{s} \tag{8.4}$$

Where hν denotes incident photon energy and L denotes a constant. For direct band gap energy semiconductors, s is $\frac{1}{2}$ while for indirect band semiconductors, it is 2. The Tauc's plot of Ce-doped ZnS is displayed in in Figure 8.3. Extrapolating the linear portion of $(\alpha h\nu)^2$ to zero value yields the value of E_g. Table 8.1 displays the measured E_g values. Doped ZnS samples have slightly higher E_g values than E_g value of pure ZnS.

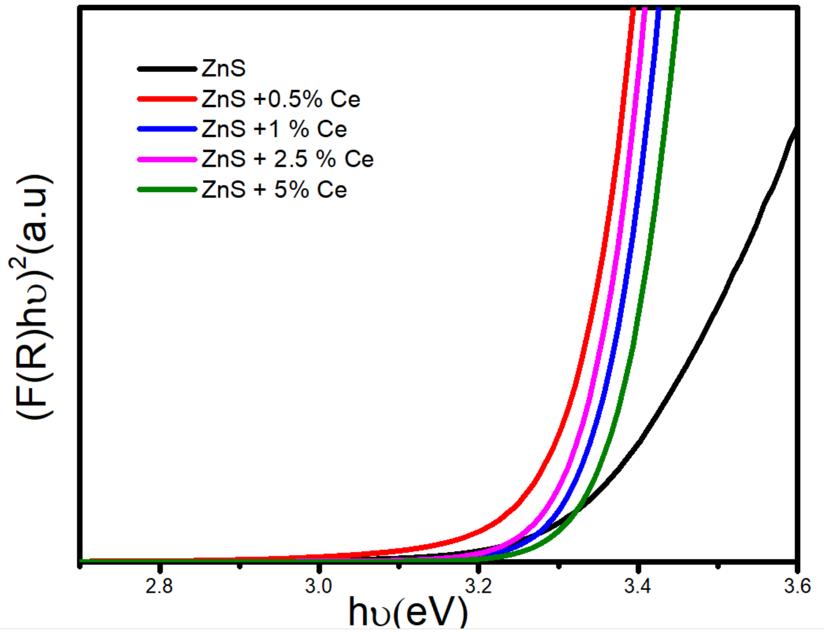

Figure 8.3. Reflectance Spectra of Ce doped ZnS Samples

Table 8.1 Band gap Values of Ce doped ZnS

Samples	**E_g (eV)**
ZnS	3.33
ZnS+0.5% Ce	3.36
ZnS+1% Ce	3.37
ZnS+2.5% Ce	3.35
ZnS+5% Ce	3.37

8.2.2.4 Scanning Electron Microscopy

Figure 8.4a-e depicts a morphological analysis of a ZnS sample synthesised by the hydrothermal method. With regular polygonal-shaped particles, the grain combination is easily observed. The particles are packed closely and have a compact shape. For pure, 0.5, 1, 2.5 and 5% Ce-ZnS, the normal grain sizes of the particles were found to be higher than the crystallite size calculated from XRD, with values of 57.7, 86.2, 55.7, 67.4 and 30.2 nm, respectively.

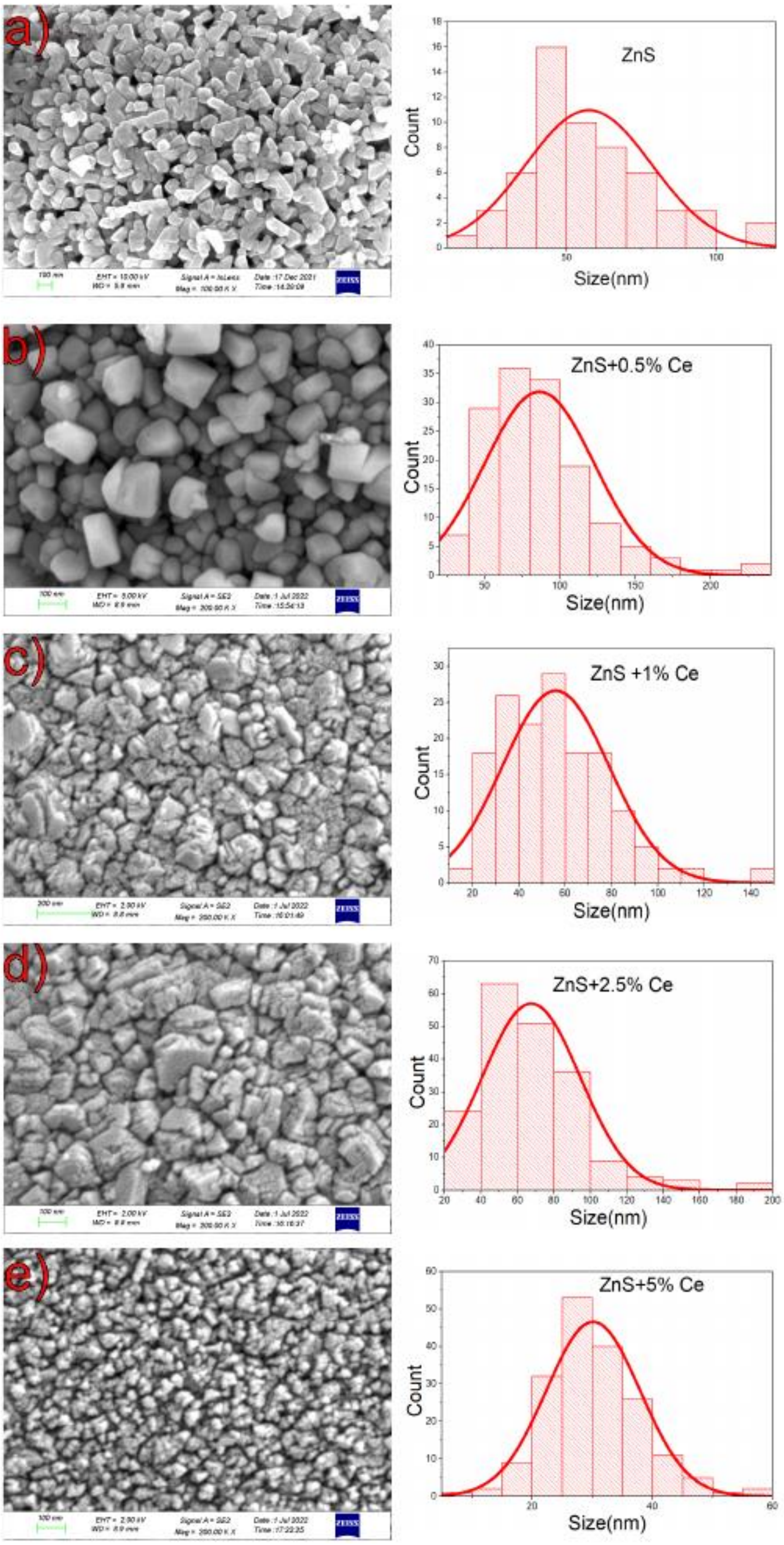

Figure 8.4. SEM image of a) ZnS, b) ZnS+0.5% c) ZnS+1% d) ZnS+2.5% e) ZnS+5% Ce doped

It must be mentioned that the grain sizes found by XRD and SEM were quite fascinating. In order to estimate the grain size in XRD, the crystalline area that coherently diffracted X-ray beams was included in the estimation as opposed to SEM, which only included the evident grain boundaries. The XRD analyses led to the production of reduced sizes. The size distribution profile is also shown in the figure 8.4.

8.2.2.5 Transmission Electron Microscopy and EDAX

The TEM (Figure 8.5a) view was also used to explain the case with pure ZnS. The TEM image demonstrates that not all of the particles are spherical. Additionally, any more distinct forms are hardly discernible. The average particle size determined by transmission microscopy images is 46.5 nm, with a size that varies from 15.7-87.3 nm. A delegate HRTEM image that enlarges a circular section of the structure is provided in Figure 8.5b. This study examines the presence of various elements in ZnS and Ce-doped ZnS nanoparticles using EDAX. EDAX analysis (Figure 8.5c) indicated the presence of Zinc and Sulphur in ZnS nanoparticles, validating the material's composition.

The crystal fringes have interplanar lengths of around 0.209 nm which corresponds to (220) planes of cubic ZnS. Figure 8.6 shows HRTEM images of 5% Ce-ZnS samples synthesized by hydrothermal route. The TEM image (Figure 8.6a and b) shows that the samples have a nanocrystalline structure with prominent and well-defined grain boundaries. The average particle size determined from the TEM picture is 85.39 nm. The d-spacing calculated for the plane illustrated in the Figure 8.5c is 3.01Å for the sample, which correlates to (002) Plane of ZnS grown in hexagonal phase. EDAX analysis (Figure 8.6c) revealed the existence of Zn, S and Ce in Ce-doped ZnS nanoparticles, confirming the effective integration of Ce as a dopant in the ZnS lattice. The finding implies that the Ce dopant was successfully incorporated into the ZnS nanoparticles.

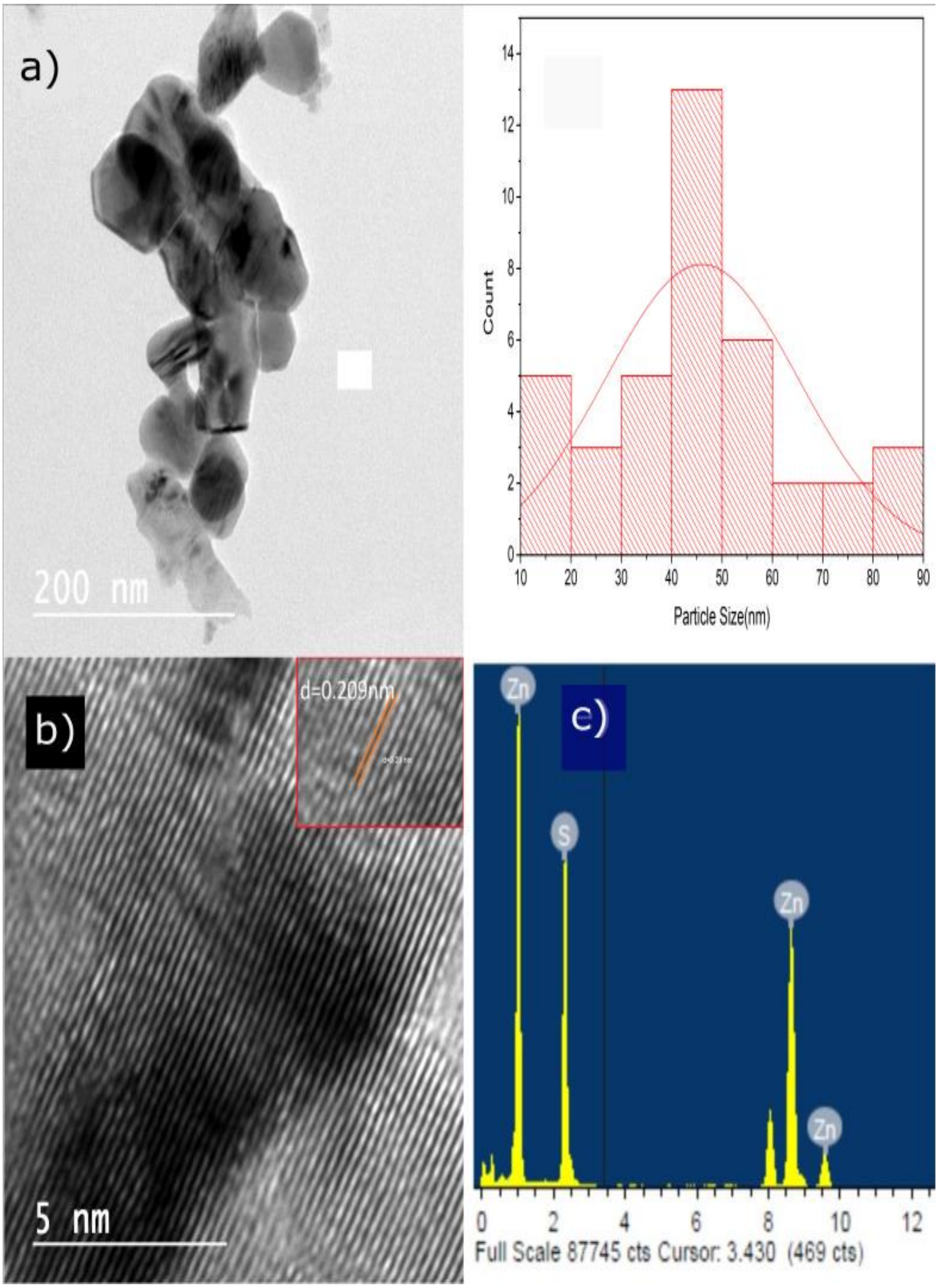

Figure 8.5. a) TEM image of ZnS & Size Distribution Curve of ZnS b) HRTEM image of ZnS c) EDAX Spectrum of ZnS

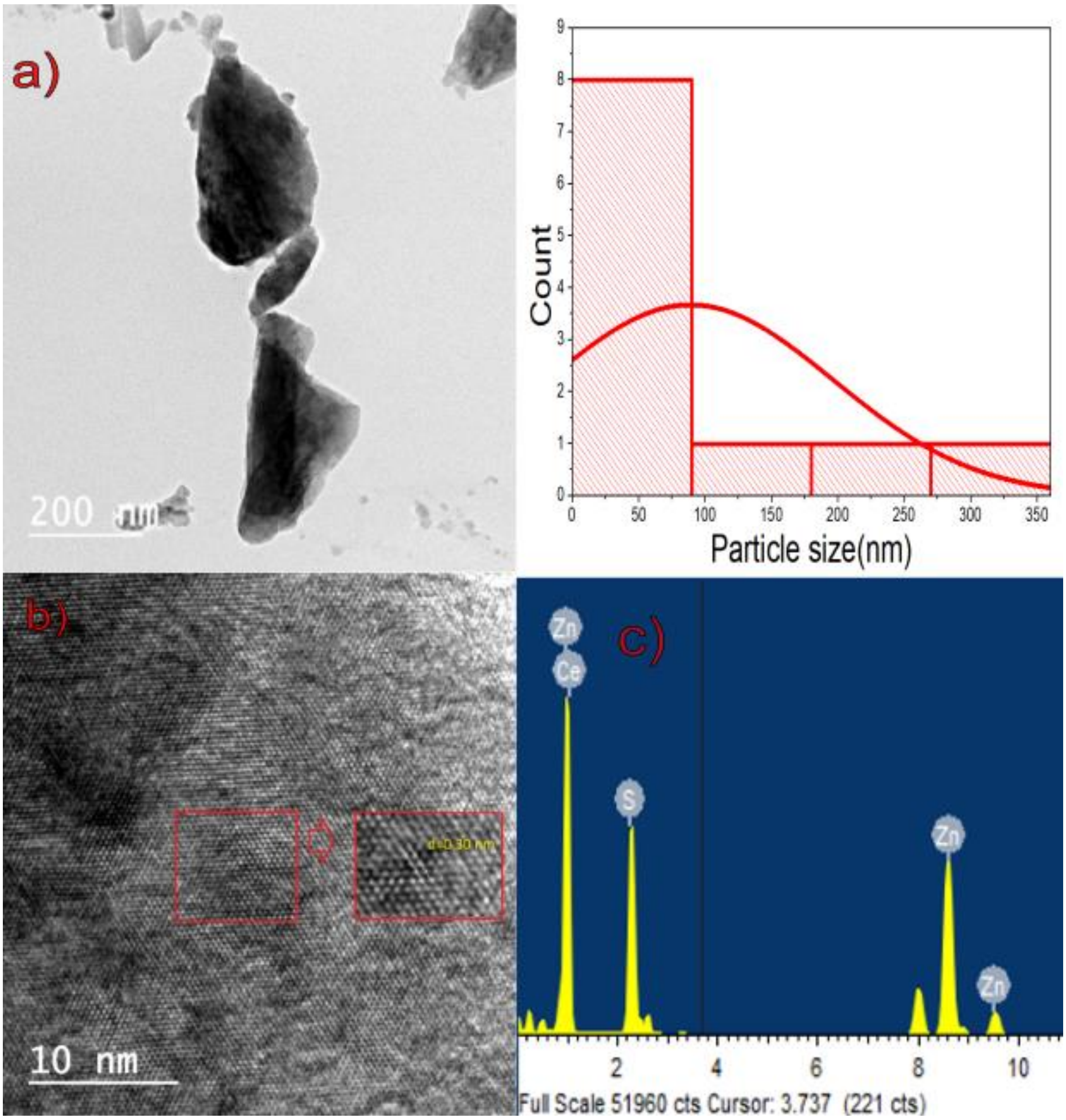

Figure 8.6. a) TEM image of 5% Ce doped ZnS & Size Distribution Curve of ZnS b) HRTEM image of 5% Ce doped ZnS c) EDAX Spectrum of 5% Ce doped ZnS

8.2.2.6 Photoluminescence Studies

The photoluminescence pattern of undoped ZnS and Ce-ZnS is depicted in the Figure 8.7a. Excitation of the 320 nm wavelength yielded the emission spectrum. The emissions are seen in the PL spectra at 363 nm, 383 nm,390 nm,437 nm, 466 nm and 517 nm. The photoluminescence (PL) is sensitive to the defects. Pure ZnS normally has four types of point defects: ‘sulphur vacancies’ (Vs), ‘zinc vacancies’ (V_{Zn}), ‘interstitial Sulphur atoms’ (I_S) and ‘interstitial Zinc atoms’(I_{Zn})[131]. The emission wavelengths at 363nm,383nm and 390nm should be attributed to stoichiometric vacancies (defect states) or interstitial impurities, potentially at the surface of ZnS nanoparticles[397][515]. V_S is thought to be responsible for transitions at 437 and 517 nm. Sulphur bonds dangling at the Zinc Sulphide grain (SS) interface were the origin of the 466 nm PL peak[399].

The relative emission intensity of Ce- ZnS nanoparticles is higher than that of pure ZnS for the peaks about 363 nm, 383 nm and 390 nm. For the peak about the 363 nm, when the Ce doping percentage increases, the intensity also increases due to the improvement of radiative recombination in the luminescent process at lower doping percentage[519]. As the doping concentration grows, the Ce atoms begin to interact with one another, resulting in energy transfer mechanisms that reduce the luminescence intensity. This is known as concentration quenching and it occurs when dopant atoms are close enough to produce non-radiative energy transitions that causes to diminish the luminosity[399]. When the doping percentages are greater than 2.5, concentration quenching is observed. As cerium concentration increases, the intensity of the emission rises in a nonuniform manner.

In the case of peaks around 383nm and 390 nm, for 0.5% and 1%, the dopant serves as a radiative recombination centre which enhances the charge carrier recombination and the intensity of the defect emission band until it is quenched for x = 2.5%. For 5% doping, the PL emission intensity increases again. At this concentration, radiative recombination centres increase in number compared to nonradiative ones due to the spatial distribution of the dopants and their placement on the host material[518]. The concentration quenching is evident for the peaks at 437 nm, 466 nm and 570 nm as the doping percentage increases.

The transition corresponding to Ce ion is not evident. According to KR Bindhu et al ., the transitions corresponding to 2 D → 2 $F_{5/2}$ and 2 D → 2 $F_{7/2}$ of Ce^{3+} ion are at 514 nm and 556 nm, correspondingly[559]. Due to energy level coupling or energy level hybridization, transitions corresponding to dopant elements may be masked or altered by transitions of the host material in the same energy level. When the energy levels of the dopant ions and the host material are near to or overlap, their transitions could combine or interact, resulting in alterations in the photoluminescence spectrum. Figure 8.7b displays an energy level diagram of expected emission paths in ZnS nanoparticles.

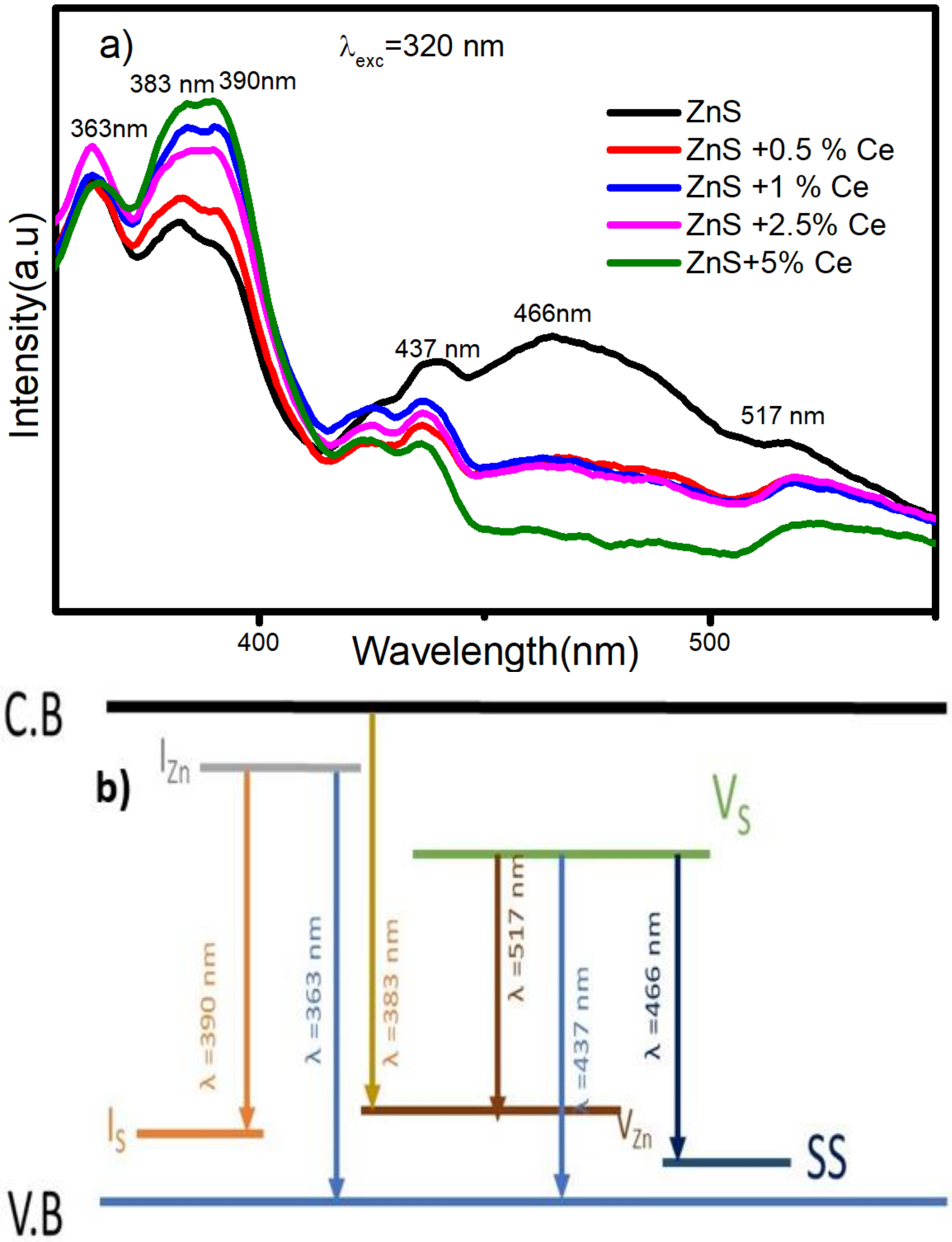

Figure 8.7 a) PL Spectra of ZnS and Ce doped ZnS nanostructures b) Energy band gap diagram

8.2.2.7 Photocatalytic Studies

To initiate a PC investigation, 0.03 grams of photocatalytic pure and Ce doped Zinc sulphide (ZnS) material is mixed with a 25-milliliter solution of Methylene Blue (MB). To formulate the solution of dye, 10 milligrams of dye is dissolved in 1 litter of distilled water. The resultant mixture containing the photocatalyst and MB solution undergoes magnetic agitation for 1 hour in the absence of light. This stirring duration facilitates the attainment of an equilibrium state between the adsorption and desorption processes of the MB dye on the catalyst surface.

When ZnS nanostructures with adsorbed dye are exposed to visible light, electron-hole pairs (e^--h^+) are generated[386].

$$ZnS + h\gamma \rightarrow e^-(CB) + h^+(VB)$$

Superoxide anion radicals ($\bullet O^{2-}$) are created when oxygen atoms bound to ZnS interact with the e^- generated in the conduction band (CB) of ZnS. Simultaneously, the positively charged holes formed in the valence band (VB) of ZnS react with hydroxyl groups on the surface, producing highly reactive hydroxyl radical (•OH) species[332].

$$O_2 + e^- \rightarrow \bullet\, O_2^-$$

$$h^+ + OH^- \rightarrow \bullet\, OH$$

These holes (h+) can instigate the splitting of water molecules in the liquid, resulting in radical formation[560].

$$h^+ + H_2O \rightarrow H^+ + \bullet\, OH^-$$

The extremely reactive hydroxyl radicals (•OH) and superoxide radicals (•O2−) can engage with MB dye anchored on ZnS nanostructures, leading to the degradation of the dye.

$$h^+ + H_2O \rightarrow H^+ + \bullet\, OH^-$$

The PL spectra of Ce-doped ZnS nanoparticles synthesized using the hydrothermal method do exhibit transitions from sulphur vacancy to dangling sulphur bonds. These sulphur defect states in the hydrothermal samples act as trapping sites for charge carriers generated by visible light, contributing to their photocatalytic activity. Charge carriers can be trapped and their lifetimes can be increased by doping ZnS with rare earth metal ions. Rare-earth metal ions may efficiently separate the photoinduced electrons and restrict charge recombination in the electron-transfer processes by trapping the electrons and reducing the recombination of photogenerated electron-hole pairs. As a result, dopants improve photocatalyst efficiency[520][561].

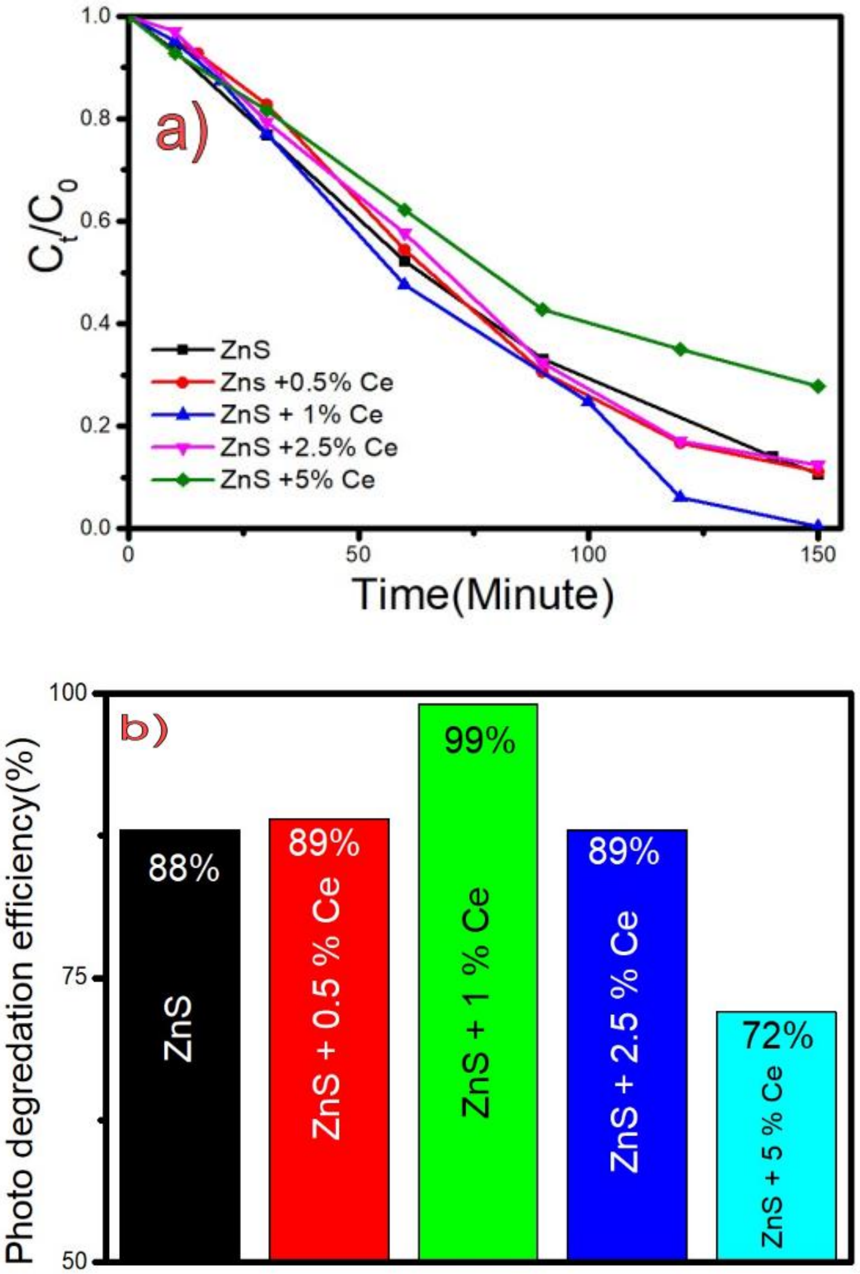

Figure 8.8.a) Photodegradation of MB Dye solution with ZnS and Ce doped ZnS catalyst b) Photodegradation Efficiency of present photocatalyst

Doping with cerium (Ce) has a considerable impact on the photodegradation efficiency of ZnS as shown in Figure 8.8 a-b. A small amount of cerium atoms must be introduced to the ZnS lattice structure in order for this process to take place. Through the application of this approach, researchers have seen a notable improvement in ZnS's photodegradation skills, particularly when it comes to the elimination of environmental pollutants and the purification of water[522].In this study when 1% cerium is doped into ZnS nanostructures, the highest photodegradation efficiency is attained. The optimum doping concentration at which the synergistic actions of ZnS and Ce lead to the most efficient disintegration of target compounds appears to be at this particular doping concentration. The separation of electron-hole pairs is assumed to be made easier at this level by the Ce atoms, which eventually results in more effective photocatalytic activities. The photodegradation efficiency gradually decreases over the 1% Ce doping limit. When the doping percentage of Ce is higher than the optimum doping percentage, the photodegradation efficiency is decreased than the pure ZnS. The creation of undesirable Ce-related recombination centres or changes in the electronic structure of the ZnS lattice might be two possible causes of this paradoxical discovery[523]. The recombination rate will rise and compete with the redox processes when the dopant concentration is too high because the distance between trapping sites will reduce[562][561].

8.3 Conclusion

As in the previous chapter we successfully introduced point defects by doping with Ce. Our study gives the information that the careful choice of dopants is essential for the phase transitions in nanomaterials at low temperatures. XRD and Raman spectroscopy indicated a phase shift in the doped ZnS nanoparticles. The doping impact on ZnS semiconductor nanocrystals is not limited to changing the electrical, magnetic, optical and luminescence characteristics, but also for promoting structural alteration. Though PL spectra revealed no dopant-related transitions, it is crucial to highlight that the luminous characteristics of the host ZnS material may still contribute to the overall luminescent behavior of the nanoparticles. The results of this work give important insights into the possible uses of these Ce-doped ZnS nanoparticles, notably in photocatalysis. The nanoparticles demonstrated visible light photocatalytic activity, with a 1% doping percentage generating 99% degradation efficiency. The optoelectronic properties and photocatalytic activity of the ZnS nanoparticles have been enhanced by the application of Ce as a defect regulator.

Chapter-9

ZnS Nanoparticles by Hydrothermal Synthesis: Point Defects through Y doping

As in previous chapters here we are discussing the introduction of point defects by doping with Y. In this work, Y-doped ZnS nanoparticles were synthesized using the hydrothermal method with doping percentages of 0.5%, 1%, 2.5% and 5%. XRD studies revealed that doping caused a phase transition from cubic to hexagonal, which was further confirmed by Raman analysis and TEM images. The EDAX analysis confirmed the successful integration of Y as a dopant in the ZnS lattice. Morphological studies conducted by SEM and TEM provided insights into the structural changes. Diffused reflectance studies were used to evaluate the band gap, with values obtained as 3.33 eV, 3.45 eV, 3.45 eV, 3.44 eV and 3.37 eV for pure ZnS, 0.5% Y-doped ZnS, 1% Y-doped ZnS, 2.5% Y-doped ZnS and 5% Y-doped ZnS, respectively. Photoluminescence analysis revealed the presence of defect states in ZnS nanoparticles, indicated by peaks at 362 nm, 383 nm and 390 nm in both pure and doped samples. The intensity of these peaks increased with Y doping, reaching its highest at 1% Y doping, while concentration quenching was observed at higher doping percentages. Additionally, the strength of the peak at 470 nm decreased as the doping percentage increased. These findings highlight the importance of optimizing the doping concentration to achieve the desired luminous features and provide valuable insights into the doping-dependent luminescence behaviour of Y-doped ZnS nanoparticles. The visible light photocatalytic activity of the nanoparticles was investigated and it was revealed that the photocatalytic efficiency increased initially and then declined as increasing doping concentration. It was found that the ideal doping concentration for 93% degradation efficiency was 1%. The novelty of this work lies in the development of a simple and energy-saving method for the synthesis of hexagonal ZnS at low temperatures, which avoids the need for high temperatures and advanced anti-oxidation apparatus.

9.1 Introduction

Nanoparticles have garnered a lot of interest in recent years because of their distinctive characteristics and wide-ranging applications in a variety of industries[563]. Because of their exceptional optical[564], electrical[565], thermistor[566] and catalytic capabilities[567], Zinc Sulphide (ZnS) nanoparticles have emerged as a potential choice among the many semiconducting materials. In this work, we focused on the hydrothermal production of ZnS nanoparticles and explored a potential enhancement of their characteristics by doping with Yttrium (Y). The goal of Yttrium doping ZnS nanoparticles is to increase their structural[568], optical[569] and photocatalytic properties[570]. The doping of ZnS nanoparticles with Yttrium, as a rare earth element, it has unique electrical and optical characteristics that may be used to alter the properties of ZnS nanoparticles[571]. Yttrium doping is intended to improve ZnS nanoparticle photo absorption and photoconversion efficiency[572], making them more appropriate for optoelectronics[573], photocatalysis[574] and photovoltaic applications[575]. Furthermore, the addition of Yttrium may affect the crystal structure[543], bandgap[552] and charge carrier dynamics[576] of ZnS, opening up the possibility of tailoring the characteristics of ZnS nanoparticles for specific applications.

The hydrothermal method is a popular approach for preparing nanoparticles with regulated size, shape and crystallinity. The high temperature and pressure inside the hydrothermal reactor encourage the synthesis of ZnS nanoparticles with better structural purity[379]. The hydrothermal approach has been used successfully in several research works for the synthesising ZnS nanoparticles[577].

9.2 Experimental

9.2.1 Synthesis

Zinc chloride ($ZnCl_2$), Thiourea ($CS(NH_2)_2$) and Yttrium nitrate hexahydrate ($Y(NO_3)_3.6H_20$) dissolved in distilled water were used for the synthesis of Y dopped ZnS nanoparticles by hydrothermal method at 220°C .The synthesis route is discussed in detail in our previous work titled Defect engineering for enhanced optical and photocatalytic properties of ZnS nanoparticles synthesized by hydrothermal method[125].

9.2.2 Measurements

The structural analyses of prepared NMs were carried out using a ‘Rigaku Miniflex 600 X-ray diffractometer’ with Cu K (= 1.542 Å) radiation, running at 15 mA and 40 kV. Data was collected using a Cu target and a graphite monochromator in continuous scan mode from 10° to 80°, with an increment of 0.02° and a scan speed of 10° per minute. The Horiba Lab Ram HR Evolution Confocal Raman Spectrometer was used to conduct vibrational analysis on all of the materials. At ambient temperature, the Raman spectrometer was powered by a 532nm (Diode Pumped Solid State Laser). The Agilent Cary fluorescence spectrophotometer was also used in the photoluminescence investigation. Optical examinations of all ZnS nanostructures were performed at RT using ‘The Cary 5000 UV-Vis-NIR spectrophotometer’ in the range of 200-1200 n.m. Morphological examinations of all synthesised ZnS nanostructures were performed using a ZEISS Gemini SEM 300, while TEM and EDAX studies were performed using Tecnai G2 F20, FEI Company working at 200kV and OXFORD X- Max, respectively. A PC investigation is carried out by adding 0.03 g of ZnS photocatalyst to 25 ml of Methylene Blue (MB) solution, Xenon short arc lamp of 300W working with 20V, 15A power supply served as visible light resource. For the preparation of the MB dye solution, 10mg of MB were mixed with 1L of distilled water, yielding photocatalysts. For 1 hour in the dark, the mixture was magnetically stirred to attain adsorption-desorption equilibrium between the MB dye and catalyst.

9.2.2.1 X-ray Diffraction Analysis

The study investigates the synthesis and characterisation of pure ZnS and Y-doped ZnS nanoparticles using X-ray diffraction (XRD). For pure ZnS (01-077-2100), the XRD patterns revealed cubic-structured peaks as in Figure 9.1. The XRD study of the pure ZnS nanoparticles showed that a cubic phase existed, with distinct peaks at 2 theta values of 28.6°, 47.72° and 56.58°, which correspond to the (111), (220) and (311) planes, respectively. However, a phase change from cubic to hexagonal was seen in Y-doped ZnS nanoparticles. The XRD peaks for the (100), (002), (101), (110) and (112) planes of the hexagonal phase were seen at a doping level of 5% at 2θ values 27.07°,28.66°,30.29°,47.82°and 56.60°respectively (01-070-2552). The XRD investigation revealed the existence of both cubic and hexagonal phases for doping levels of 0.5%, 1% and 2.5%. The existence of (200) planes demonstrated that the cubic phase was still dominating at low doping percentages (0.5%, 1% and 2.5%). Notably, we observed a significant phase transition to a hexagonal structure at a higher doping level of 5%, with discrete peaks corresponding to (100), (002), (101), (110) and (111) planes. This finding indicates that the presence of yttrium ions caused a phase change in the ZnS lattice, resulting in the coexistence of cubic and hexagonal phases. The study, however, changed in an unanticipated way with the addition of Yttrium (Y) dopants.

Surprisingly, the cubic ZnS phase experienced a transformation into the wurtzite structure, which had rarely been observed in the literature. Mn^{2+} and Cl^{-} ions in ZnS nanocrystals have been found to be vital for the transition from cubic to hexagonal phase[553]. Normal ZnS cubic to hexagonal phase transitions, however, occur around 1296 K [578]. It goes without saying that synthesis at such a high temperature demands a lot of energy and can necessitate the use of very advanced anti-oxidation apparatus. As a result, research on a simple, energy-saving method for the synthesis of hexagonal ZnS at low temperatures is desirable. The widened XRD peaks of the produced samples demonstrated the nanocrystalline nature of the materials. The strength of XRD peaks decreased as Y content increased, which might be attributed to crystalline instability caused by dopant atoms in the sample. The presence of dopant atoms in the ZnS host lattice caused lattice instability, which was the cause of the decreasing XRD peaks intensity as Y concentration increases [502]. The Debye-Scherrer equation was used to calculate the average particle size. Pure ZnS crystallite sizes were 2.8 nm, 0.5% doped crystallite sizes were 18.95 nm, 1% doped crystallite sizes were 19.04 nm, 2.5% doped crystallite sizes were 17.75 nm and 5% doped crystallite sizes were 2.65 nm. The cubic phase lattice parameters of pure ZnS nanoparticles were measured to be 5.40 Å, which is extremely near to the standard value. The average lattice parameters 'a' and 'c' for the hexagonal phase of Y-doped ZnS nanoparticles were 3.81 Å and 6.26 Å, which are as well close to the standard values. Overall, the study gives extensive details on the phase transition, crystallite size and lattice properties of pure ZnS and Y-doped ZnS nanoparticles based on XRD examination.

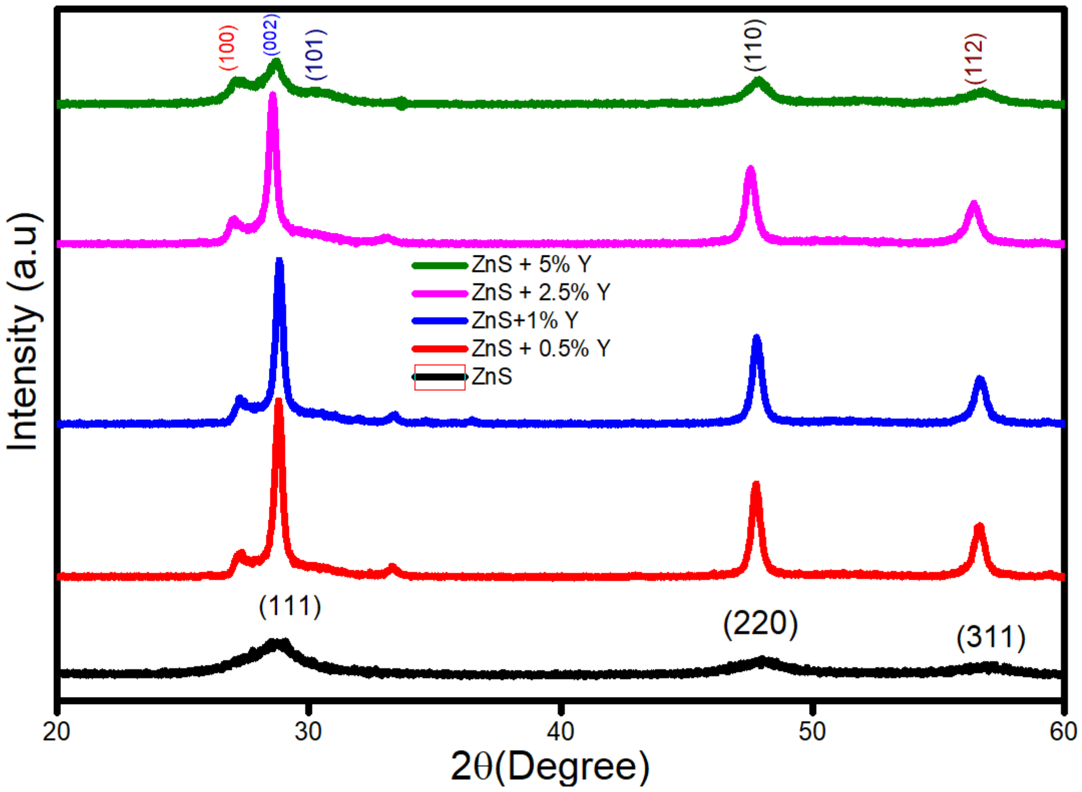

Figure 9.1. X-ray diffraction spectrum of ZnS and Y doped ZnS samples

9.2.2.2 Diffused Reflectance Spectra Analysis

Figure 9.2 shows the diffused reflectance spectra of Y doped ZnS nanoparticles. The band gap (E_g) of samples was calculated using the Tauc's relation from diffused reflectance spectra. The Kubelka-Munk relation is used to calculate the absorption coefficient. The F(R) (Kubelka-Munk function) is

$$\mathbf{F(R)}=\boldsymbol{\alpha} = \frac{(\mathbf{1}-\boldsymbol{R})^{\mathbf{2}}}{\boldsymbol{R}} \qquad (9.1)$$

Where 'α' -absorption coefficient and 'R' the reflectance.

The Optical band-gap can be evaluated using Tauc's equation is of the form:

$$\mathbf{A\ h\ \nu = L\ (h\ \nu\text{-}E_{g)}\ ^{s}} \qquad (9.2)$$

Where hν denotes incoming photon energy and L denotes a constant. For direct band gap energy semiconductors ‘s’ is ½, while for indirect band semiconductors the same is 2. Figure 9.2 depicts the Tauc's plot $((\alpha\ h\ \nu)^2 - h\ \nu)$ of Y-doped ZnS. Extrapolating the linear portion of $(\alpha\ h\ \nu)^2$ to zero value yields the value of E_g.

The band gap energy of pure ZnS and Y-doped ZnS samples were calculated using the Kubelka-Munk relation and the values obtained were 3.33 eV, 3.45 eV, 3.45 eV, 3.44 eV and 3.37 eV for pure ZnS, 0.5% Y-doped ZnS, 1% Y-doped ZnS, 2.5% Y-doped ZnS and 5% Y-doped ZnS, respectively (Table 9.1). Our findings demonstrated that the band gap initially increased with Y doping and reaches maximum at 3.45 eV for samples of ZnS that was 0.5% Y-doped and remains same for 1% Y doped. However, the band gap began to decrease with further doping at higher Y concentrations. With the 2.5% and 5% Y-doped ZnS samples having somewhat lower band gap values of 3.44 eV and 3.37 eV, respectively. The Burstein-Moss effect can be used to explain the broadening of the band gap or blue shift, which is a consequence of the Pauli exclusion principle[506][507][508][509]. The Fermi energy level (EF), which is present in the valence band for p-type doping or the conduction band for heavy n-type doping, causes the shift. Therefore, the filled states prevent optical or thermal stimulation. In contrast, as a result of the exchange and Coulomb interactions between the extra free electrons in the conduction band and electron-impurity scattering, band gap shrinking also occurs in heavily doped semiconductors (band gap renormalization)[510][511][512][513].

Table 9.1 Band gap values Y doped ZnS

S. No.	**Sample**	**Bandgap(eV)**
1.	ZnS	3.33
2.	ZnS+0.5% Y	3.45
3.	ZnS+1% Y	3.45
4.	ZnS+2.5% Y	3.44
5.	ZnS+5% Y	3.37

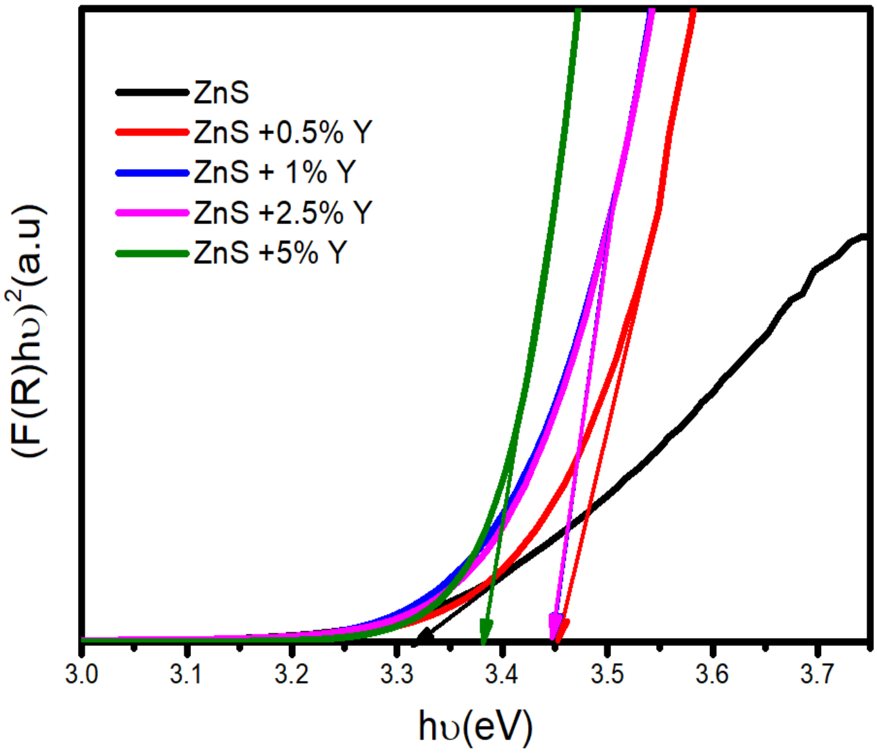

Figure 9.2. (F(R)h ν)^2 Vs h ν plot of Y doped ZnS

9.2.2.3 Scanning Electron Microscopy

In the present investigation, ZnS and different concentrations (0.5%, 1%, 2.5% and 5%) of Y-doped ZnS samples were synthesised. The morphology of all the samples was investigated using SEM (Figure 9.3 a-e), which revealed that there was no uniform shape seen and that some samples displayed agglomeration. The particle diameters assessed by SEM were 57.67 nm, 67.24 nm, 53.05 nm, 65.09 nm and 39.21 nm for ZnS and 0.5%, 1%, 2.5% and 5% Y-doped ZnS samples, respectively, which were greater than the values obtained from XRD analysis. SEM measurements are often taken on the surface of the sample, where particle agglomeration or clustering might occur, resulting in greater apparent particle sizes. This aggregation may be missed mostly by XRD analysis[389]. These findings imply that the presence of Y dopants in the ZnS samples altered particle size and morphology, resulting in agglomeration and bigger particle sizes as compared to the pure ZnS sample.

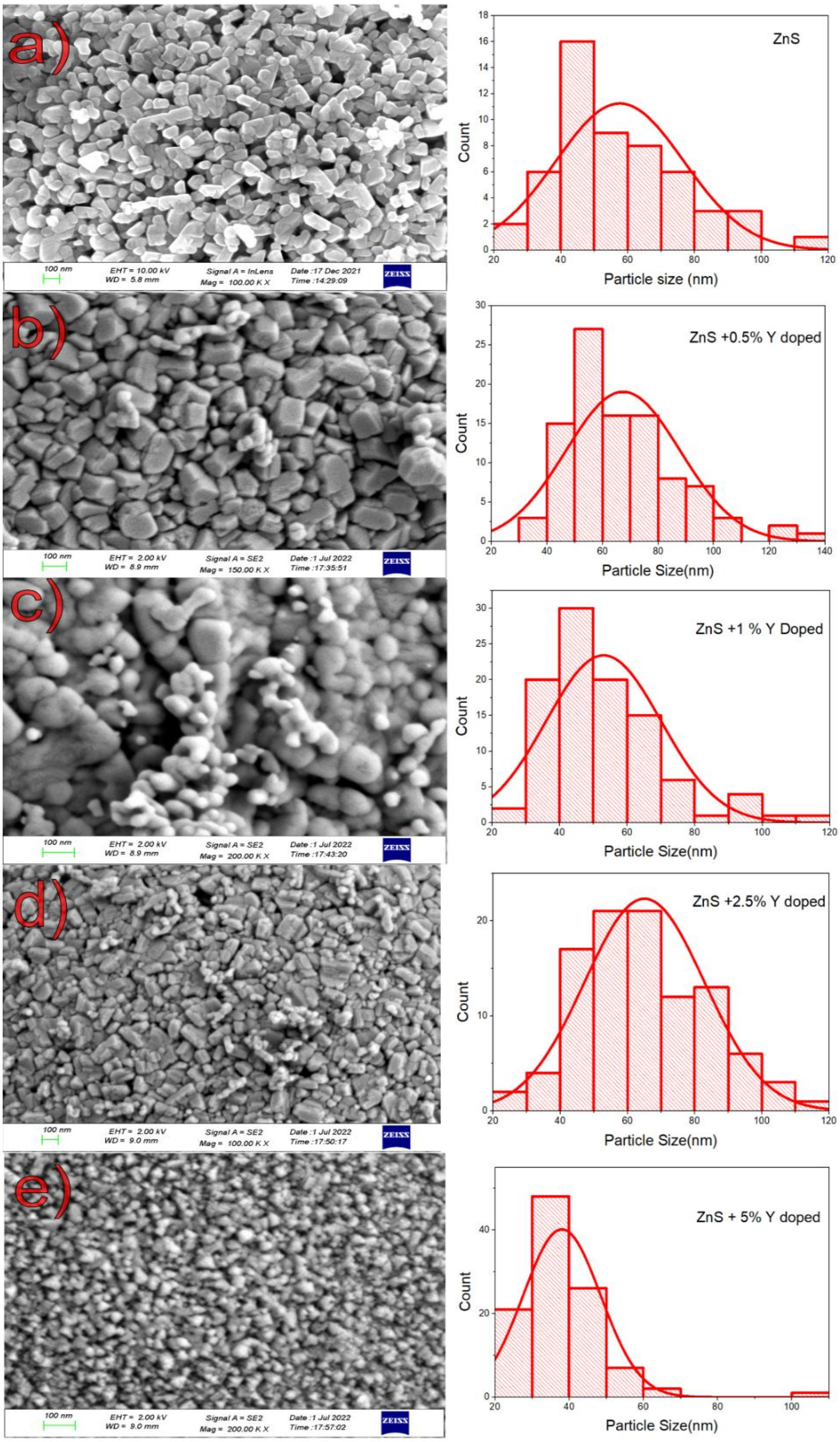

Figure 9.3. SEM image of a) ZnS, b) ZnS+0.5% c) ZnS+1% d) ZnS+2.5% e) ZnS+5% Y doped

9.2.2.4 Transmission Electron Microscopy & EDAX

The morphology of pure ZnS nanoparticles and ZnS nanoparticles doped with 5% Yttrium (Y) has been studied using TEM examination. About 2.09 Å was discovered to be the interplanar distance between the crystal fringes in the pure ZnS nanoparticles from Figure 9.4a which corresponds to 220 plane (Figure 9.4b) in the ZnS cubic phase .The TEM images (Figure 9.4c) showed that some of the pure ZnS nanoparticles had a spherical shape, indicating that their shape was not uniform. The pure ZnS nanoparticles were found to have an average particle size of 46.5 nm and a size range of 15.7-87.3 nm. The size distribution curve Figure 9.4d of pure ZnS nanoparticles exhibited the variety in particle sizes.the SAED pattern Figure 9.4e confirms the cubic structure of pure ZnS. EDAX analysis was used to analyse the presence of various elements in pure ZnS nanoparticles shown in Figure 9.4f.

In contrast, a nanocrystalline structure with distinct grain boundaries was seen in the TEM picture Figure 9.5 of the Y-doped ZnS nanoparticles. From Figure 9.5a it was found that the d-spacing for the plane seen in the TEM picture of the Y-doped ZnS sample was 2.2 Å, showing that ZnS grew along the 102 plane in the hexagonal phase (Figure 9.5b). The Y-doped ZnS nanoparticles were found to have an average particle size of 37.65 nm from Figure 9.5c and the size distribution curve is shown in Figure 9.5d. Additionally the SAED pattern (Figure 9.5e) analysis of Y doped ZnS sample is one of the main focus of the work. The crystal structure of the 5% Y doped ZnS was shown by the SAED pattern. which verified that the sample was produced in the hexagonal phase. The identified planes were labbeled in the SAED pattern diagram, the analysis made it possible to fully comprehend the sample's crystallographic orientation. This study is significant because it offers insightful details on the structural characteristics of the 5% Y doped ZnS material, which may have consequences for its possible uses in a variety of industries.

The EDAX analysis of the Y-doped ZnS nanoparticles showed (Figure 9.5f) the presence of Zn, S and Y, suggesting that Y was successfully integrated as a dopant in the ZnS lattice. This result further supports the successful synthesis of Y-doped ZnS nanoparticles by offering compelling evidence that the Y dopant was successfully integrated into the ZnS nanoparticles.

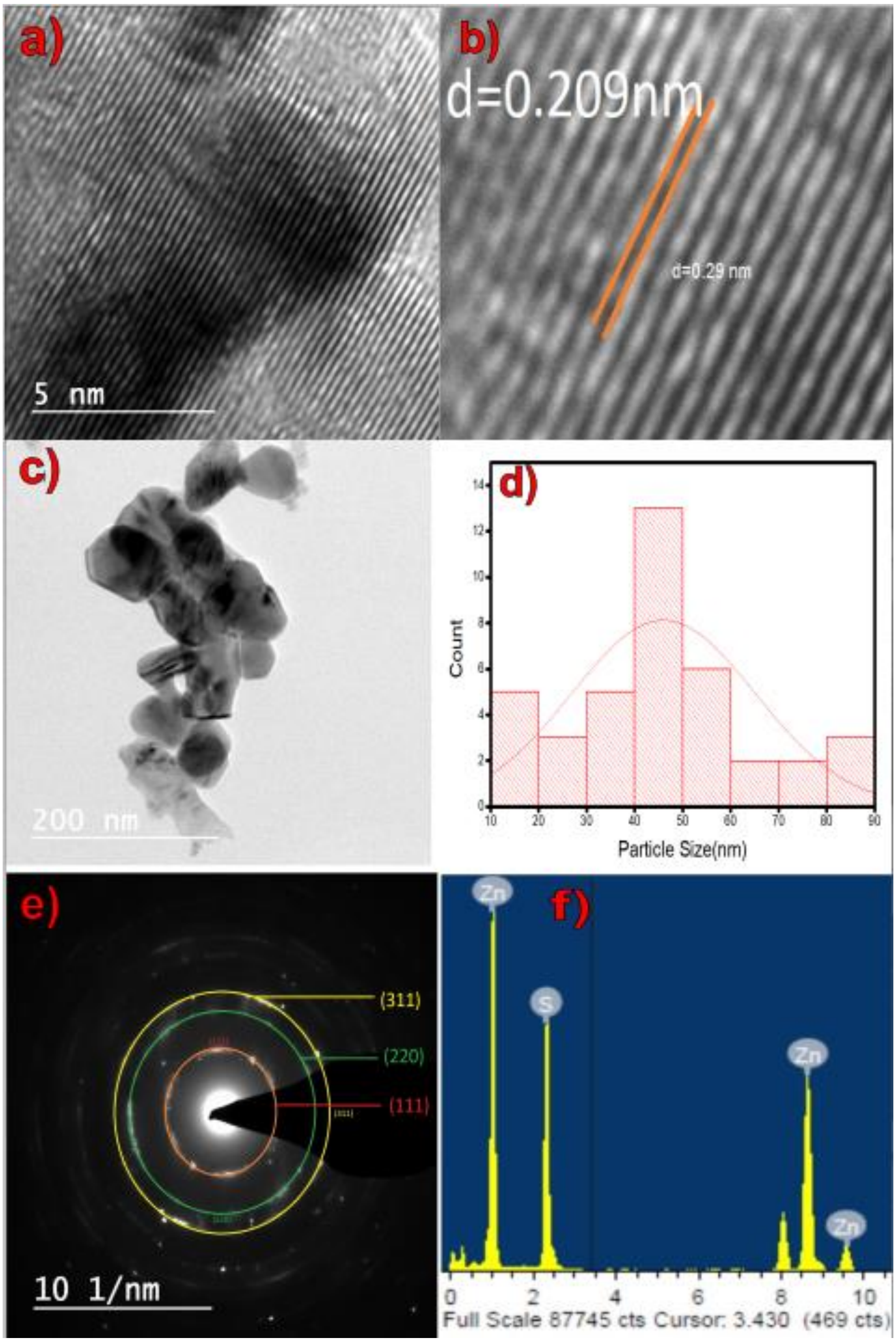

Figure 9.4. a),b) HRTEM image of ZnS b) TEM image of ZnS c) Size Distribution Curve of ZnS e) SAED pattern of ZnS f) EDAX Spectrum of ZnS

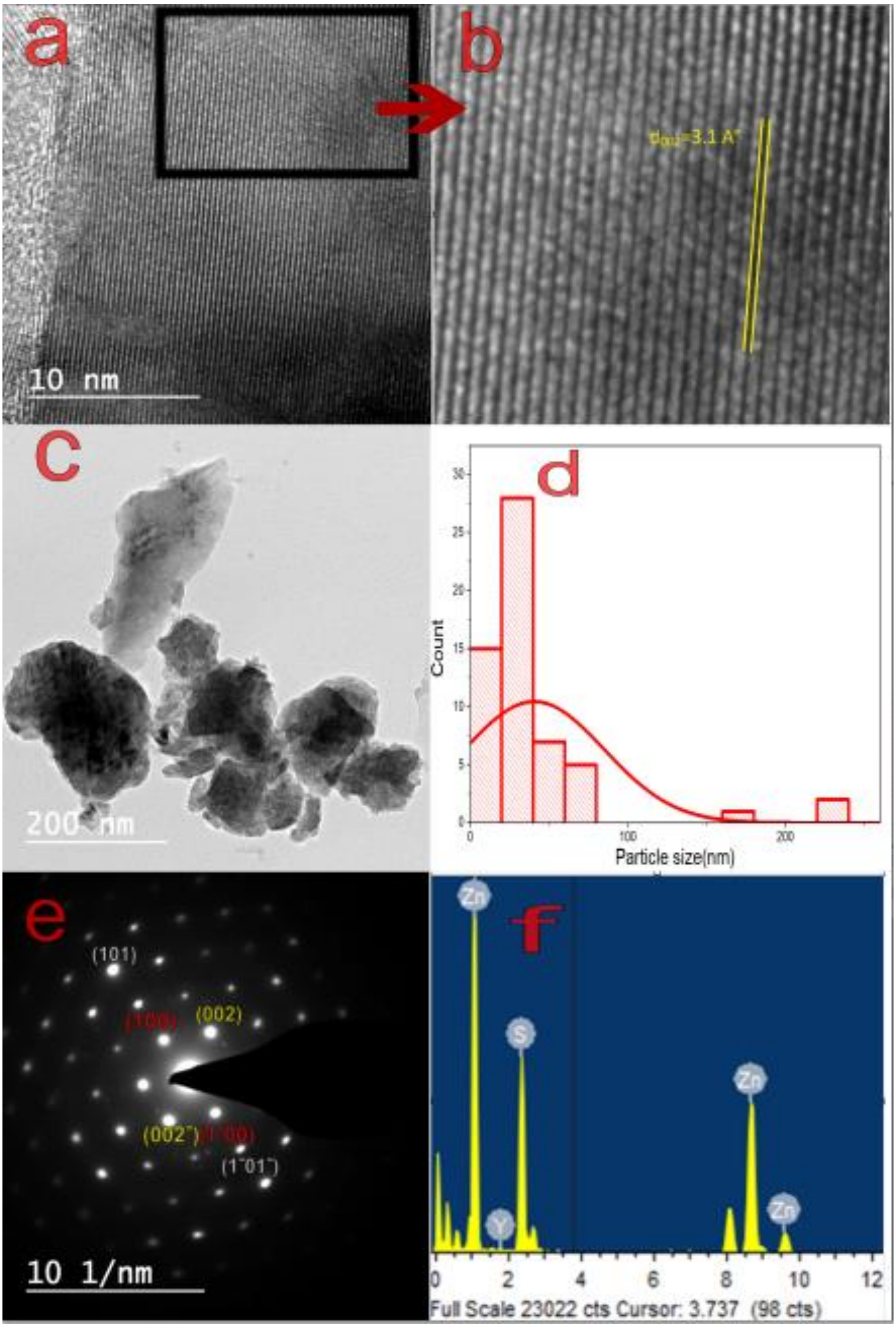

Figure 9.5. a), b) HRTEM image of 5% Y doped ZnS & c) TEM image of 5% Y doped ZnS d) Size Distribution Curve of 5% Y doped ZnS e) SAED pattern of 5% Y doped ZnS f) EDAX Spectrum of 5% Y doped ZnS

9.2.2.5 Raman Spectra Analysis

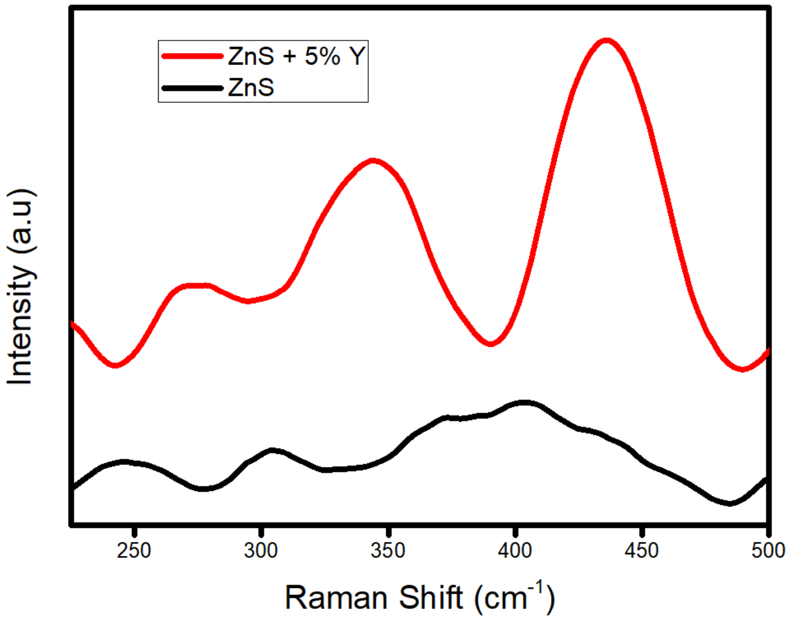

Figure 9.6. Vibrational Raman Spectra of ZnS and 5% Y doped ZnS

Raman analysis was used to assess the vibrational properties of both pure ZnS and 5 %Y-doped ZnS and is shown in Figure 9.6. Peak modes were seen in the case of pure ZnS, including a TO peak mode at around 276 cm^{-1} and a LO peak mode at about 337 cm^{-1}[125]. A peak at 248 cm^{-1} revealed the transverse optical phonon mode's overtone[147], while a peak at 308 cm^{-1} confirmed the presence of a lattice defect-induced phonon mode at the X-W-L point, indicating the influence of structural defects on the vibrational characteristics of the material[388]. The raman spectra of the material additionally showed a peak at 401 cm^{-1}, which corresponds to TO+LA vibrations[388]. The vibrational spectra of the material revealed the cubic structure of ZnS, which was validated by XRD investigation. From the Raman studies of Y doped a small peak located at 219 cm^{-1} in the low-frequency domain is attributed to LA overtones along the M-K[147]. Y-doped ZnS observed peaks at 270 cm^{-1}, suggesting the presence of the TO phonon mode's A1 or E1 vibration[147][503][504]. Moreover, the LO phonon mode-related A1 and E1 vibrational modes were identified as the sources of peaks at 343 cm^{-1}[147][503][504]. The hexagonal ZnS lattice's TA+LO vibration modes were linked to the peaks at 435 cm^{-1}[147][503][504]. In accordance with the findings of the XRD and SAED investigations, the Raman spectroscopy data offered more proof that the Y-doped ZnS sample had the hexagonal crystal structure.

9.2.2.6 Photoluminascence Studies

Several identical peaks and characteristics in the emission spectra of pure ZnS and yttrium doped ZnS have been observed by photoluminescence studies corresponding to an excitation wavelength 320 nm. ZnS nanoparticles may have defect states called stoichiometric vacancies or interstitial impurities on their surface, as evident from the peaks at 362 nm, 383 nm and 390 nm that were seen in the PL spectra (Figure 9.7a) of both pure and doped ZnS samples[397][515]. At the same shutter slit, the intensity approached saturation at 1% Y doping as shown in inset of Figure 9.7b. In order to avoid saturation and enable a more precise assessment of the PL intensity, this change reduced the amount of light that reached the detector and new PL spectra shown in Figure 9.7b. In the emission spectrum, the deconvoluted wide asymmetric peak about 470 nm is composed of peaks at 423 nm, 437 nm, 473 nm and 525 nm (Figure 9.7c). The existence of dangling sulphur bonds on the ZnS grain interface is responsible for the peak at 473 nm, whereas sulphur vacancies in the ZnS nanoparticles are responsible for the peak at 423 nm[399]. Furthermore, structural defects such point defects may be connected to the green emission centred at 525 nm, which may cause deep-level emission.

It had been found that the intensity of the peak in the emission spectra of yttrium doped ZnS at 362 nm enhanced with Y doping and was highest at 1% Y doping. The increase in the rate of radiative recombination in the luminescent process at lower doping percentages is responsible for this intensity enhancement[519]. But when the doping concentration becomes even higher, interactions between the Y atoms result in energy transfer processes that lower the luminescence intensity. Concentration quenching is the term for this phenomenon, in which dopant atoms are near to one another and form non-radiative energy transfer pathways that reduce brightness[399]. Consequently, concentration quenching was seen at doping percentages higher than 1.

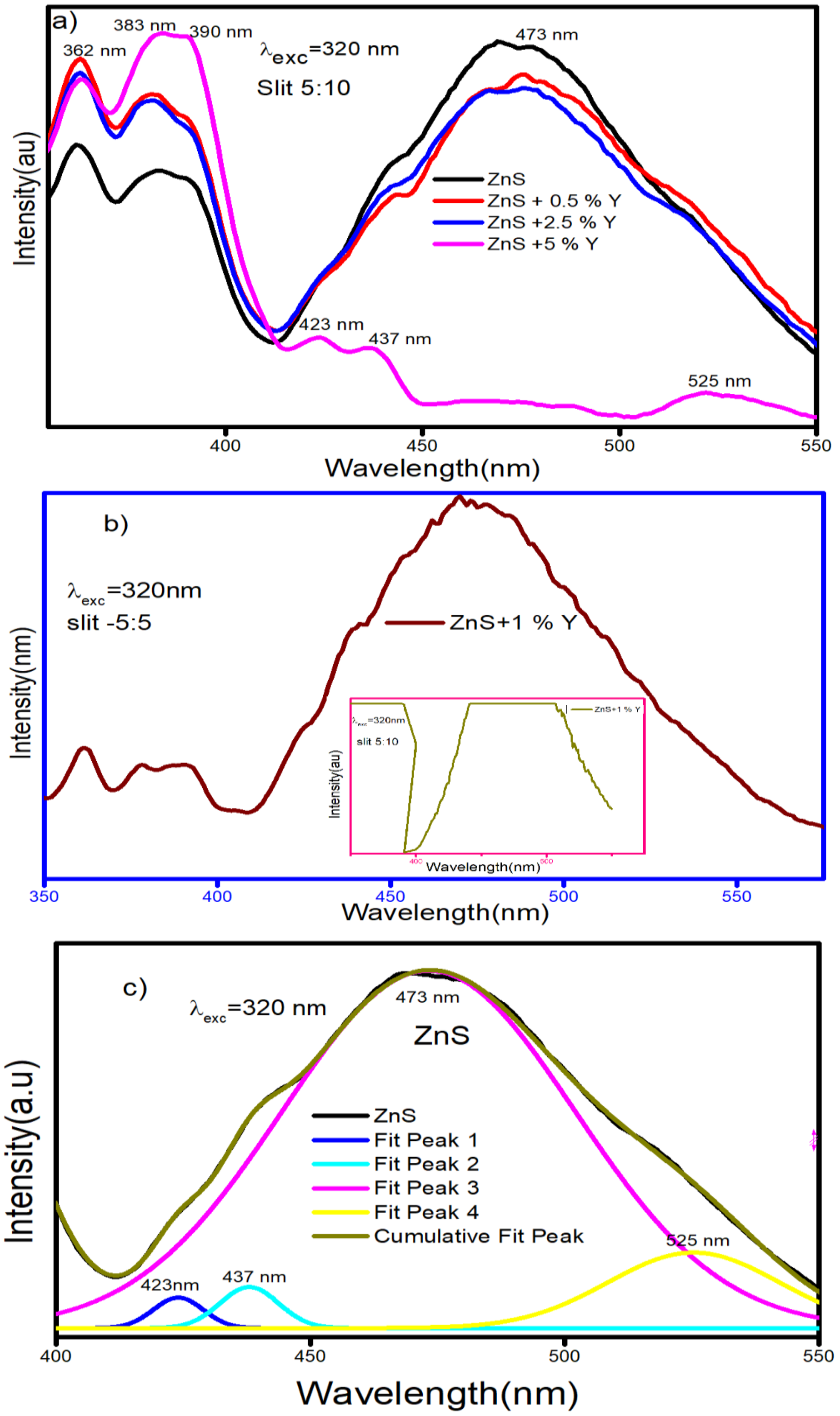

Figure 9.7. a) PL Spectra of ZnS and 0.5,1,2.5% Y doped ZnS nano structures b) PL Spectra of 5% ZnS c) Deconvolution of PL spectra of ZnS

The Luminescence quenching happened for the peaks 383 nm and 390 nm at the same 1 % Y doping. The photoluminescence (PL) emission intensity increases once again at a doping dose of 5%. This can be explained by the fact that there are more radiative recombination centres than nonradiative ones at this concentration[518]. It has been observed that the strength of the peak at 470 nm drastically decreased as the doping % increased. This reduction in intensity may be ascribed to both the removal of interstitial ions like S_i and Zn_i and the deformation of the lattice structure brought about by the Y ion doping[579]. This is because of how the dopants are arranged specifically on the host material and how widely distributed they are in space. A nonuniform rise in emission intensity was seen with an increase in Y concentration. These results underline the need of optimising the doping concentration to attain the intended luminous features and offer insightful information on the doping-dependent luminescence behaviour of yttrium doped ZnS nanoparticles. The presence of several defect states and their contributions to the overall photoluminescence behaviour are highlighted in these studies, which offer important insights into the emission characteristics of pure ZnS and yttrium doped ZnS nanoparticles. The emission spectra of Y-doped ZnS samples may be dominated by the strong luminescence peaks of pure ZnS at 363 and 473 nm, making it difficult to see and identify the luminescence 5d-4f transition of Y at wavelengths of around 363,469 and 601nm[196].

9.2.2.7 Photocatalytic Studies

Photocatalysis is the process of initiating chemical processes by absorption of photons, often from ultraviolet or visible light, by a catalyst[580]. TiO_2 and ZnO, two semiconductor materials with strong photocatalytic properties[581][582][583][584], are often used in many applications. There are many different uses for photocatalysis, including surface disinfection[585], organic pollutant degradation[586] and environmental remediation procedures including water and air cleaning[587]. The photocatalytic activity studies of Yttrium (Y) doped Zinc sulphide (ZnS) in visible light have become more attractive in the field of innovative materials for energy and environmental applications [588][589][125]. The PL spectra of Y-doped ZnS nanoparticles synthesized using the hydrothermal method do exhibit transitions from sulphur vacancy to dangling sulphur bonds. These sulphur defect states in the hydrothermal samples act as trapping sites for charge carriers generated by visible light, contributing to their photocatalytic activity. It was found in the investigation of the photocatalytic characteristics of ZnS and Y-doped ZnS that the photodegradation efficiency increased as the Y doping percentage increased up to 1% as shown in the Figure 9.8a. Beyond this optimal doping percentage, the efficiency gradually decreased. This phenomenon might be explained by the creation of unwanted Y-related recombination centres or changes in the electronic structure of the ZnS lattice[523]. When the dopant concentration is too high, the recombination rate rises and competes with redox activities as the distance between trapping sites decreases [562] [561]. These findings emphasize the significance of optimizing the doping level carefully to achieve the maximum photocatalytic efficiency in ZnS-based materials. The photodegredation of MB dye is shown in Figure 9.8b.

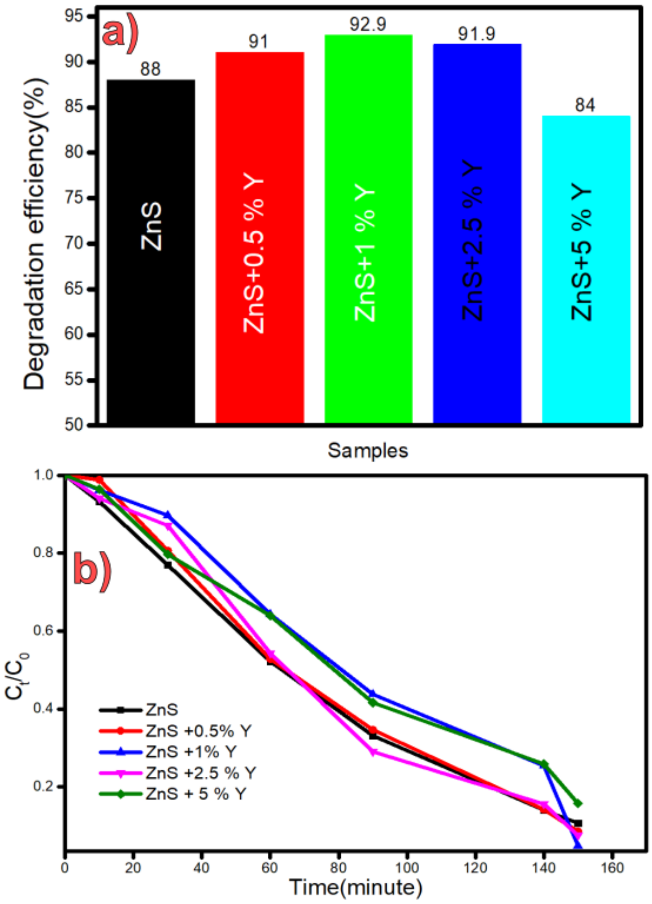

Figure 9.8 a) Photodegradation Efficiency of present photocatalyst b) Photodegradation of MB Dye solution with ZnS and Y doped ZnS catalyst

9.3 Conclusion

In this Chapter , we discussed the hydrothermal synthesis of ZnS and Y-doped ZnS, revealing their structural, morphological and optical properties as in Chapter 5,6,7 and 8. ZnS in its pure form showed a cubic phase, while ZnS doped with 5% Y experienced a transition to a wurtzite phase, according to the analysis of XRD patterns. Interestingly, moderate Y-doping concentrations (0.5%, 1% and 2.5%) resulted in mixed phase samples. Raman studies and TEM SAED patterns strongly confirmed these findings, providing a complete understanding of the structural modifications. Studies on the morphology of the synthesised materials using TEM and SEM yielded more insightful data. Band gap studies utilising the Kubelka-Munk relation revealed a significant trend in optical characteristics with Y doping. The presence of defect states was demonstrated by photoluminescence analysis, with the strength of these states corresponding to Y doping concentrations. The observed photoluminescence behaviour in the ZnS samples, particularly the variation in intensity of various luminescence peaks with doping percentage, highlights the potential uses of these materials in optoelectronic devices and semiconductor technology.The effective integration of Y into the samples was validated by EDAX analysis. Significantly, our visible light photocatalytic investigations revealed 1% Y-doped ZnS to have an extraordinary 93% photodegradation efficiency. In addition to advancing our knowledge of the structural and optical properties of doped ZnS, this work presents a new, low-temperature, energy-saving technique to synthesise Wurtzite ZnS nanoparticles.

Chapter-10

Summary and Recommendations

10.1 Summary

This thesis investigated the effects of point defects on ZnS nanoparticles which were synthesised using two methods namely the hydrothermal and microwave assisted co-precipitation. The point defects were introduced in the crystal lattice by changing the stochiometric ratio and by doping with rare earth elements. The structural, optical and photocatalytic properties of defect induced ZnS nanoparticles are studied.

In our first work, using a low-temperature hydrothermal method, ZnS nanoparticles with various S/Zn molar ratios have been synthesised. By introducing Zn and S defects into the ZnS crystal using defect engineering, the band structure of the material was effectively modified. The existence of defects on the surface of the synthesised nanoparticles were verified by RAMAN, XPS and PL analysis. Using XRD, Raman analysis, Scherrer method, W-H model and the size strain plot, the effect of crystal defects on the structural properties of ZnS nanoparticles were investigated. The photocatalysis degradation activity was very high for Sulphur defect-rich sample ZnS0.67 and Zn defect-rich ZnS3 samples. From the photoluminescence studies, it is clear that the broad and intense blue emission is caused by the recombination of holes at the surface state (SS) and electrons trapped by Sulphur vacancy (Vs) sites. These two defect sites are responsible for the visible photocatalytic activity of samples.

In the second work, Quantum dots-like ZnS nanoparticles were effectively synthesised utilising microwave assisted co-precipitation method with variable CTAB concentrations, resulting in the monophasic ZnS with very small dimensions, which was confirmed using FT-Raman spectroscopy and X-ray diffraction. The energy gap of the ZnS nanoparticles varied depending on the CTAB concentration. ZnS nanoparticles have high dielectric constant values, low loss values and enhanced electrical conductivity with frequency, making them appropriate for optoelectronic devices. ZnS nanoparticles were synthesised using microwave assisted method did not exhibit photocatalytic activity.

The point defects were introduced in to the ZnS crystal lattice synthesised using microwave assisted co-precipitation method by doping with Er in the third work. Several characterisation techniques were used to assess the structural, morphological, optical, dielectric and photoluminescent properties of the synthesised samples. When excited at 320 and 400 nm wavelengths, the Er-doped ZnS samples showed strong luminescence, with emission peaks corresponding to Er transitions, making them appropriate for optoelectronic devices. The emission peaks in the blue region are less intense and narrower compared to the luminescence spectrum of ZnS nanoparticles synthesised using hydrothermal method. This indicates the absence or less density of sulphur vacancy and dangling sulphur bonds on the surface. Due to the absence of these defect states, Er doped ZnS samples have shown no photocatalytic activity either in UV or in Visible region. Er doping has shown tunable influence on the dielectric values, which has slightly lower than those of the pure ZnS nanoparticles.

In the fourth work, we have used Pr doping for the introduction of point defects. Similar to the Er-doped samples, the formation of point defects on ZnS nanoparticles with Pr doping led to the growth of nanoparticles in the cubic phase, as seen by the XRD pattern, FESEM and HRTEM analysis. The photoluminescence emission peaks correspond to Pr^{3+} transitions are observed in the PL spectra. The dielectric study indicated low loss values and high dielectric constant values and the electrical conductivity enhanced with frequency and Pr concentration, making the Pr-doped samples suitable for optoelectronic devices, similar to the Er-doped samples. Pr doped ZnS samples synthesised using microwave assisted coprecipitation method not showing PC activity like Er doped ZnS Samples.

In the Fifth, sixth and seventh work we have used hydrothermal method for the synthesis of ZnS nanoparticle and point defects introduced by doping with La, Ce and Y respectively. The doping caused a phase shift from cubic to wurtzite structure, which was verified by XRD and Raman spectroscopy. Although the PL spectra do not show dopant-specific transitions, the host material could still have an impact on the general luminescence of nanoparticles, but we can tune the intensity of luminescence emission by doping with La, Ce and Y. When ZnS is doped with La, the band gap widens first. The Burstein-Moss effect is the reason for bandgap widening. The bandgap narrows further as the doping percentage increases due to the bandgap renormalization process. The Y-doped ZnS samples exhibit the similar rise in band gap energy, initially due to the Burstein-Moss effect, followed by shrinkage. For ZnS samples doped with Ce, doping does not significantly alter the bandgap energy. The broad highly intense blue luminescence emissions show the presence of defects state responsible for the photocatalytic activity. The optimum doping percentage for high photodegradation efficiency also determined.

ZnS NPs synthesised using microwave-assisted method has smaller size, compared to that of nanoparticles synthesised using hydrothermal method. When we dope using hydrothermal method, these doped nanoparticles experienced a phase shift from cubic to hexagonal and showed excellent luminescence and photocatalytic activity. Retaining the cubic phase in microwave assisted method while doping, they show transition corresponding to dopant but did not exhibit photocatalytic activity either in UV or Visible region. The ZnS nanoparticles synthesised using microwave assisted method is suitable for optoelectronic applications, while the ZnS nanoparticles synthesised using hydrothermal method are prominent for making Optoelectronic devices and for water purification.

10.2 Recommendations

- In this thesis we doped Ce, La and Y in ZnS by hydrothermal method and Er and Pr in ZnS by microwave assisted method. The doping of Er and Pr in ZnS using the hydrothermal method, along with Ce, La, and Y doping via the microwave-assisted method, offers significant potential for further investigation to enhance the properties of ZnS nanoparticles for advanced applications.

- Co-doping: To enhance the photocatalytic activity and luminous properties of ZnS nanoparticles, study the impacts of co-doping them with different elements. This might include investigating the synergistic impact of several dopants on the structural, optical and electrical characteristics of nanoparticles.

- Thin film: Investigate the use of ZnS nanoparticles that have been synthesised in the development of thin films. Spray pyrolysis, chemical vapour deposition, or spin coating may be used to deposit nanoparticles onto various surfaces. The structural, optical and electrical characteristics of the thin films can then be investigated further.

- Buffer layers: Use of ZnS thin film in solar cell as a buffer layer between the absorber layer and the transparent conducting oxide layer to provide a suitable band alignment for efficient separation of photo-generated carriers and to protect the absorber layer from damage caused by physical deposition of the TCO layer a buffer layer

- Device Fabrication: Examine how the synthesised ZnS thin films and nanoparticles could be used in optoelectronic devices. Developing ZnS-based solar cells, sensors, or light-emitting diodes (LEDs) might be examples of this. This performance of devices may be measured by examining their efficiency, stability and reactivity to external stimuli.

- The utilisation of ZnS thin films and nanoparticles as coatings for diverse purposes should be investigated. Solar panel anti-reflective coatings, optical lens protective coatings and photocatalytic water purification coatings are all examples of this.

- Surface modification: Examine the methods for improving the characteristics of ZnS thin films and nanoparticles. This could be done including more elements by surface doping or functionalizing the surface with organic compounds. Subsequently, the altered nanoparticles and films can be assessed for enhanced luminescence, photocatalysis, or sensing capabilities

- Investigate scalability and possible industrial uses for synthesised ZnS nanoparticles and thin films. This might include optimising the synthesis parameters for large-scale production, examining the economic feasibility of the methods and testing the performance of materials in real-world scenarios.

References

[1] I. Khan, K. Saeed and I. Khan, *Arab. J. Chem.*, 2019, **12**, 908–931.

[2] F. Ghribi, L. El Mir, K. Omri and K. Djessas, *Opt. - Int. J. Light Electron Opt.*, 2016, **127**, 3688–3692.

[3] C. Wang, B. Hu, L. Chen, N. Liu and J. Li, *Optik (Stuttg).*, , DOI:10.1016/j.ijleo.2020.165673.

[4] D. Saikia, J. P. Borah, M. Jangra and A. Puzari, *Indian J. Phys.*, 2016, **90**, 549–555.

[5] X. Fang, T. Zhai, U. K. Gautam, L. Li, L. Wu, Y. Bando and D. Golberg, *Prog. Mater. Sci.*, 2011, **56**, 175–287.

[6] *Handbook of Nanotechnology Applications*, Elsevier, 2021.

[7] A. M. Smith and S. Nie, *Acc. Chem. Res.*, 2010, **43**, 190–200.

[8] H. Zeng, J. Zhao, A.-Q. Cheng, L. Zhang, Z. He and R.-S. Chen, *Nanotechnology*, 2018, **29**, 075201.

[9] A. Adewuyi and W. J. Lau, in *Handbook of Nanotechnology Applications*, Elsevier, 2021, pp. 67–97.

[10] K. J. J. Mayrhofer, B. B. Blizanac, M. Arenz, V. R. Stamenkovic, P. N. Ross and N. M. Markovic, *J. Phys. Chem. B*, 2005, **109**, 14433–14440.

[11] A. B. Asha and R. Narain, in *Polymer Science and Nanotechnology*, Elsevier, 2020, pp. 343–359.

[12] M. Chen, L. Zhu, Q. Chen, N. Miao, C. Si, J. Zhou and Z. Sun, *J. Mater. Chem. C*, 2020, **8**, 721–733.

[13] T. Radsar, H. Khalesi and V. Ghods, *Opt. Quantum Electron.*, 2021, **53**, 178.

[14] M. A. Uddin, F. Bayram, G. Koley, Y. Zhu, A. Singh and I. Jahangir, in *2016 IEEE SENSORS*, IEEE, 2016, pp. 1–3.

[15] X. Li and J. Wang, *InfoMat*, 2020, **2**, 3–32.

[16] H. Häkkinen, *Chem. Soc. Rev.*, 2008, **37**, 1847.

[17] K. Harun, N. Mansor, Z. A. Ahmad and A. A. Mohamad, *Procedia Chem.*, 2016, **19**, 125–132.

[18] D. Guo, G. Xie and J. Luo, *J. Phys. D. Appl. Phys.*, 2014, **47**, 013001.

[19] J. Piella, N. G. Bastús, E. Casals and V. Puntes, *J. Phys. Conf. Ser.*, 2013, **429**, 012040.

[20] G. D. Moon, S. Ko, Y. Min, J. Zeng, Y. Xia and U. Jeong, *Nano Today*, 2011, **6**, 186–203.

[21] M. Singh, M. Goyal and K. Devlal, *J. Taibah Univ. Sci.*, 2018, **12**, 470–475.

[22] S. P. Gubin, Y. A. Koksharov, G. B. Khomutov and G. Y. Yurkov, *Russ. Chem. Rev.*, 2005, **74**, 489–520.

[23] N. Zheng, *Univ. Tennessee, Knoxv.*, 2008, 1–7.

[24] T. Dietl, *Nat. Mater.*, 2010, **9**, 965–974.

[25] N. Hossain, M. H. Mobarak, M. A. Mimona, M. A. Islam, A. Hossain, F. T. Zohura and M. A. Chowdhury, *Results Eng.*, 2023, **19**, 101347.

[26] M. Rizwan, A. Shoukat, A. Ayub, B. Razzaq and M. B. Tahir, in *Nanomaterials: Synthesis, Characterization, Hazards and Safety*, Elsevier, 2021, pp. 31–54.

[27] Lorelle Mansfield/NIST, Semiconductor Nanowires, https://www.nist.gov/image/nanotechnologyelectronicsnanowiresthatemituvlightjpg.

[28] Michael Marquardt, The Rise of Carbon Nanotube Electronics, https://data.embeddedcomputing.com/uploads/resize/320/200/external/data.embeddedcomputing.com/uploads/articles/primary_images/1644427182.png.

[29] Z. Tian, H. Hu and Y. Sun, *Int. J. Heat Mass Transf.*, 2013, **61**, 577–582.

[30] F. Zhang, X. Ji, W. Liang, Y. Li, Z. Ma, M. Wang, Y. Wang, D. Wu, X. Chen, D. Yang, X. Li, C. Shan and Z. Shi, *Mater. Horizons*, 2021, **8**, 3432–3442.

[31] C. Kloeffel and D. Loss, *Annu. Rev. Condens. Matter Phys.*, 2013, **4**, 51–81.

[32] J. Mirzaei, M. Reznikov and T. Hegmann, *J. Mater. Chem.*, 2012, **22**, 22350.

[33] U. e Kalsoom, R. Yi, J. Qu and L. Liu, *Front. Phys.*, , DOI:10.3389/fphy.2021.612070.

[34] M. Chern, J. C. Kays, S. Bhuckory and A. M. Dennis, *Methods Appl. Fluoresc.*, 2019, **7**, 012005.

[35] M. Benelmekki and A. Erbe, 2019, pp. 1–34.

[36] R. Kumar, G. Kumar, O. Al-Dossary and A. Umar, *Mater. Express*, 2015, **5**, 3–23.

[37] G. Guisbiers, S. Mejía-Rosales and F. Leonard Deepak, *J. Nanomater.*, 2012, **2012**, 1–2.

[38] M. Ahumada, C. Lazurko and E. I. Alarcon, in *Photoactive Inorganic Nanoparticles*, Elsevier, 2019, pp. 1–19.

[39] S. M. Woodley, G. M. Day and R. Catlow, *Philos. Trans. R. Soc. A Math. Phys. Eng. Sci.*, 2020, **378**, 20190600.

[40] A. Shaji and A. K. Zachariah, in *Thermal and Rheological Measurement Techniques for Nanomaterials Characterization*, Elsevier, 2017, pp. 197–231.

[41] H. J. Imran, K. A. Hubeatir, K. A. Aadim and D. S. Abd, *J. Phys. Conf. Ser.*, 2021, **1818**, 012127.

[42] J. K. Patra and K.-H. Baek, *J. Nanomater.*, 2014, **2014**, 1–12.

[43] D. Rembelski, J. P. Viricelle, L. Combemale and M. Rieu, *Fuel Cells*, 2012, **12**, 256–264.

[44] G. Karthik Pandiyan and T. Prabaharan, *Mater. Today Proc.*, 2020, **33**, 2681–2685.

[45] A. Corma and H. Garcia, *Chem. Soc. Rev.*, 2008, **37**, 2096.

[46] P. Dasta, A. Pratap Singh and A. Pratap Singh, *Mater. Today Proc.*, 2022, **52**, 751–757.

[47] M. I. Zaki, N. E. Fouad, G. A. H. Mekhemer, T. C. Jagadale and S. B. Ogale, *Colloids Surfaces A Physicochem. Eng. Asp.*, 2011, **385**, 195–200.

[48] J. Solla-Gullón, F. J. Vidal-Iglesias, A. López-Cudero, E. Garnier, J. M. Feliu and A. Aldaz, *Phys. Chem. Chem. Phys.*, 2008, **10**, 3689.

[49] F. D. Sanij, P. Balakrishnan, P. Leung, A. Shah, H. Su and Q. Xu, *Int. J. Hydrogen Energy*, 2021, **46**, 14596–14627.

[50] D. L. Huber, *Small*, 2005, **1**, 482–501.

[51] M. Martins, C. Mourato, S. Sanches, J. P. Noronha, M. T. B. Crespo and I. A. C. Pereira, *Water Res.*, 2017, **108**, 160–168.

[52] D. Chen, X. Qiao, X. Qiu and J. Chen, *J. Mater. Sci.*, 2009, **44**, 1076–1081.

[53] E. Trave, V. Bello, F. Enrichi, G. Mattei, E. Borsella, M. Carpanese, M. Falconieri, C. Abate, N. Herlin-Boime, K. Jursiokova, F. Costa, L. Costa and L. Gini, *Opt. Mater. (Amst).*, 2005, **27**, 1014–1019.

[54] T. Yusaf, A. S. F. Mahamude, K. Farhana, W. S. W. Harun, K. Kadirgama, D. Ramasamy, M. K. Kamarulzaman, S. Subramonian, S. Hall and H. A. Dhahad, *Sustainability*, 2022, **14**, 12336.

[55] F. Capasso, *Science (80-.).*, 1987, **235**, 172–176.

[56] M. S. Chavali and M. P. Nikolova, *SN Appl. Sci.*, 2019, **1**, 607.

[57] J.-S. Lee, *Gold Bull.*, 2010, **43**, 189–199.

[58] S. A. Kulkarni, S. G. Mhaisalkar, N. Mathews and P. P. Boix, *Small Methods*, , DOI:10.1002/smtd.201800231.

[59] P. Av. Al. A. et Al, *Plasmonics*, 2012, 525–534.

[60] J. H. Jun, H. Seong, K. Cho, B.-M. Moon and S. Kim, *Ceram. Int.*, 2009, **35**, 2797–2801.

[61] X. Mao, J. Xu and H. Cui, *WIREs Nanomedicine and Nanobiotechnology*, 2016, **8**, 814–841.

[62] K. Wang, X. He, X. Yang and H. Shi, *Acc. Chem. Res.*, 2013, **46**, 1367–1376.

[63] P. Couvreur, *Adv. Drug Deliv. Rev.*, 2013, **65**, 21–23.

[64] M. Pöttler, I. Cicha, H. Unterweger, C. Janko, R. P. Friedrich and C. Alexiou, *Nanomedicine*, 2019, **14**, 1929–1933.

[65] S. S. Patil, U. U. Shedbalkar, A. Truskewycz, B. A. Chopade and A. S. Ball,

Environ. Technol. Innov., 2016, **5**, 10–21.

[66] P. Koedrith, T. Thasiphu, J.-I. Weon, R. Boonprasert, K. Tuitemwong and P. Tuitemwong, *Sci. World J.*, 2015, **2015**, 1–12.

[67] Y. Wu, H. Pang, Y. Liu, X. Wang, S. Yu, D. Fu, J. Chen and X. Wang, *Environ. Pollut.*, 2019, **246**, 608–620.

[68] W. Yan, H.-L. Lien, B. E. Koel and W. Zhang, *Environ. Sci. Process. Impacts*, 2013, **15**, 63–77.

[69] I. Ojea-Jiménez, X. López, J. Arbiol and V. Puntes, *ACS Nano*, 2012, **6**, 2253–2260.

[70] R. Hong, T. Pan, J. Qian and H. Li, *Chem. Eng. J.*, 2006, **119**, 71–81.

[71] S. Basiruddin, A. Saha, N. Pradhan and N. R. Jana, *J. Phys. Chem. C*, 2010, **114**, 11009–11017.

[72] J. Zhao and D. Xie, *J. Compos. Mater.*, 2009, **43**, 2739–2752.

[73] M. Islam, M. R. Azhar, N. Fredj, T. D. Burleigh, O. R. Oloyede, A. A. Almajid and S. Ismat Shah, *Surf. Coatings Technol.*, 2015, **261**, 141–148.

[74] E. Barna, B. Bommer, J. Kürsteiner, A. Vital, O. v. Trzebiatowski, W. Koch, B. Schmid and T. Graule, *Compos. Part A Appl. Sci. Manuf.*, 2005, **36**, 473–480.

[75] M. E. El-Naggar, A. G. Hassabo, A. L. Mohamed and T. I. Shaheen, *J. Colloid Interface Sci.*, 2017, **498**, 413–422.

[76] A. A. Javidparvar, B. Ramezanzadeh and E. Ghasemi, *Prog. Org. Coatings*, 2016, **90**, 10–20.

[77] R. R. Choudhury, J. M. Gohil, S. Mohanty and S. K. Nayak, *J. Mater. Chem. A*, 2018, **6**, 313–333.

[78] D. Xu, Y. Su, L. Zhao, F. Meng, C. Liu, Y. Guan, J. Zhang and J. Luo, *J. Biomed. Mater. Res. Part A*, 2017, **105**, 531–538.

[79] L. Xu, R. G. Karunakaran, J. Guo and S. Yang, *ACS Appl. Mater. Interfaces*, 2012, **4**, 1118–1125.

[80] A. Polakiewicz, H. Dodiuk and S. Kenig, *J. Adhes. Sci. Technol.*, 2014, **28**, 466–478.

[81] C.-C. Chang, C.-P. Chen, T.-H. Wu, C.-H. Yang, C.-W. Lin and C.-Y. Chen, *Nanomaterials*, 2019, **9**, 861.

[82] H. Jans and Q. Huo, *Chem. Soc. Rev.*, 2012, **41**, 2849–2866.

[83] S. Malik, J. Singh, R. Goyat, Y. Saharan, V. Chaudhry, A. Umar, A. A. Ibrahim, S. Akbar, S. Ameen and S. Baskoutas, *Heliyon*, 2023, **9**, e19929.

[84] F. Canfarotta, M. J. Whitcombe and S. A. Piletsky, *Biotechnol. Adv.*, 2013, **31**, 1585–1599.

[85] F. Wang, D. Banerjee, Y. Liu, X. Chen and X. Liu, *Analyst*, 2010, **135**, 1839.

[86] Aaromal Venugopal et.al, .

[87] A. Kaur and U. Gupta, *J. Mater. Chem.*, 2009, **19**, 8279.

[88] M. S. Draz and H. Shafiee, *Theranostics*, 2018, **8**, 1985–2017.

[89] M. Jouyandeh, S. M. Sajadi, F. Seidi, S. Habibzadeh, M. T. Munir, O. Abida, S. Ahmadi, D. Kowalkowska-Zedler, N. Rabiee, M. Rabiee, G. Heidari, M. Hassanpour, E. Nazarzadeh Zare and M. R. Saeb, *OpenNano*, 2022, **8**, 100104.

[90] S. Santra, K. Wang, R. Tapec and W. Tan, *J. Biomed. Opt.*, 2001, **6**, 160.

[91] X. He, H. Deng and H. Hwang, *J. Food Drug Anal.*, 2019, **27**, 1–21.

[92] Z. Hua, T. Yu, D. Liu and Y. Xianyu, *Biosens. Bioelectron.*, 2021, **179**, 113076.

[93] K. Kraśniewska, S. Galus and M. Gniewosz, *Int. J. Mol. Sci.*, 2020, **21**, 698.

[94] G. Guleria, S. Thakur, M. Shandilya, S. Sharma, S. Thakur and S. Kalia, *Plant Physiol. Biochem.*, 2023, **194**, 533–549.

[95] M. Rani, U. Shanker and V. Jassal, *J. Environ. Manage.*, 2017, **190**, 208–222.

[96] K. Warriner, S. M. Reddy, A. Namvar and S. Neethirajan, *Trends Food Sci. Technol.*, 2014, **40**, 183–199.

[97] S. Jafarzadeh and S. M. Jafari, *Crit. Rev. Food Sci. Nutr.*, 2021, **61**, 2640–2658.

[98] R. Liu and R. Lal, *Sci. Total Environ.*, 2015, **514**, 131–139.

[99] E. Mehrazar, M. Rahaie and S. Rahaie, *Int. J. Nanoparticles*, 2015, **8**, 1.

[100] N. Zhang, C. Gao and Y. Xiong, *J. Energy Chem.*, 2019, **37**, 43–57.

[101] J. Wang, X. Zhao, G. Zou, L. Zhang, S. Han, Y. Li, D. Liu, C. Fernandez, L. Li, L. Ren and Q. Peng, *Mater. Today Nano*, 2023, **22**, 100336.

[102] W. Peng, Z. Lin, W. Cao, K. Zhang, W. Heng, Z. Pang, S. Qian, Y. Gao, J. Zhang and Y. Wei, *Int. J. Pharm.*, 2024, **652**, 123837.

[103] K. Komatsu, T. Hayakawa and H. Fudouzi, *Adv. Powder Technol.*, 2022, **33**, 103594.

[104] X. Yang, Z. Xiang, J. Wu, P. He, Y. Qi, S. Chen, Y. Lu, R. Xie, Z. Liu and C. He, *Fuel*, 2024, **355**, 129440.

[105] W. B. Fowler, in *Encyclopedia of Condensed Matter Physics*, Elsevier, 2024, pp. 184–189.

[106] H. Zhang, T. Zheng, B. Gnade and K. Cho, *Comput. Mater. Sci.*, 2015, **104**, 172–176.

[107] R. REIDY and G. SIMKOVICH, *Solid State Ionics*, 1993, **62**, 85–97.

[108] J. M. Howe, in *Physical Metallurgy*, Elsevier, 2014, pp. 1317–1451.

[109] R. Dierk, in *Computational Materials Engineering*, Elsevier, 2007, pp. 267–316.

[110] ANTHONY KELLY and KEVIN M. KNOWLES, *Crystallography and Crystal Defects*, 2012.

[111] X. Liu, H. Wang, H. Lu, X. Liu, Z. Zhao, C. Hou, L. Gu and X. Song, *Adv. Powder Mater.*, 2023, **2**, 100130.

[112] R. V. Vovk, N. R. Vovk and O. V. Dobrovolskiy, *Adv. Condens. Matter Phys.*, 2013, **2013**, 1–7.

[113] W. J. Wang, K. C. Yung, H. S. Choy, T. Y. Xiao and Z. X. Cai, *Appl. Surf. Sci.*, 2018, **443**, 167–175.

[114] A. Gurevich, *Appl. Phys. Lett.*, 2001, **78**, 1891–1893.

[115] J. J.W. Morris, Defects in Crystals.

[116] K. Zhong, R. Bu, F. Jiao, G. Liu and C. Zhang, *Chem. Eng. J.*, 2022, **429**, 132310.

[117] K. S. Jones, S. Prussin and E. R. Weber, *Appl. Phys. A Solids Surfaces*, 1988, **45**, 1–34.

[118] J. S. Williams, *Mater. Sci. Eng. A*, 1998, **253**, 8–15.

[119] X. Zhang, K. Hattar, Y. Chen, L. Shao, J. Li, C. Sun, K. Yu, N. Li, M. L. Taheri, H. Wang, J. Wang and M. Nastasi, *Prog. Mater. Sci.*, 2018, **96**, 217–321.

[120] Y. Park, J. S. Choi, T. Choi, M. J. Lee, Q. Jia, M. Park, H. Lee and B. H. Park, *Sci. Rep.*, 2015, **5**, 9390.

[121] D. Setman, E. Schafler, E. Korznikova and M. J. Zehetbauer, *Mater. Sci. Eng. A*, 2008, **493**, 116–122.

[122] H. F. M. Mohamed, J. Kwon, Y.-M. Kim and W. Kim, *Nucl. Instruments Methods Phys. Res. Sect. B Beam Interact. with Mater. Atoms*, 2007, **258**, 429–434.

[123] W. L. Brown, W. M. Augustyniak and T. R. Waite, *J. Appl. Phys.*, 1959, **30**, 1258–1268.

[124] J. Silcox and P. B. Hirsch, *Philos. Mag.*, 1959, **4**, 72–89.

[125] E. M. Jubeer, M. A. Manthrammel, P. A. Subha, M. Shkir, K. P. Biju and S. A. AlFaify, *Sci. Rep.*, 2023, **13**, 16820.

[126] T.-H. An, Y. S. Lim, H.-S. Choi, W.-S. Seo, C.-H. Park, G.-R. Kim, C. Park, C. H. Lee and J. H. Shim, *J. Mater. Chem. A*, 2014, **2**, 19759–19764.

[127] S. Manzoor, S. Husain, A. Somvanshi, M. Fatema and N. Zarrin, *Appl. Phys. A*, 2019, **125**, 509.

[128] K. Chen, M. Song, Y.-Y. Sun, H. Xu, D.-C. Qi, Z. Su, X. Gao, Q. Xu, J. Hu, J. Zhu, R. Zhang, J. Wang, L. Zhang, L. Cao, Y. Han and Y. Xiong, *Appl. Phys. Lett.*, , DOI:10.1063/5.0005170.

[129] M. Li, Q. Sun, S. Xu, M. Hong, W. Lyu, J. Liu, Y. Wang, M. Dargusch, J. Zou and Z. Chen, *Adv. Mater.*, 2021, **33**, 273–288.

[130] X. Wang, J. Shi, Z. Feng, M. Li and C. Li, *Phys. Chem. Chem. Phys.*, 2011, **13**, 4715–4723.

[131] X. Hao, Y. Wang, J. Zhou, Z. Cui, Y. Wang and Z. Zou, *Appl. Catal. B Environ.*, 2018, **221**, 302–311.

[132] Z. Fang, S. Weng, X. Ye, W. Feng, Z. Zheng, M. Lu, S. Lin, X. Fu and P. Liu, *ACS Appl. Mater. Interfaces*, 2015, **7**, 13915–13924.

[133] X. Yang, W. Gu, C. Yuan, Z. Yang, S. Shi, Z. Liu, S. Liang and F. Teng, *CrystEngComm*, 2021, **23**, 1999–2005.

[134] X. Xue, R. Chen, H. Chen, Y. Hu, Q. Ding, Z. Liu, L. Ma, G. Zhu, W. Zhang, Q. Yu, J. Liu, J. Ma and Z. Jin, *Nano Lett.*, 2018, **18**, 7372–7377.

[135] C.-G. Wu, C.-C. Chao and F.-T. Kuo, *Catal. Today*, 2004, **97**, 103–112.

[136] X. Wu, T. Liu, W. Ni, H. Yang, H. Huang, S. He, C. Li, H. Ning, W. Wu, Q. Zhao and M. Wu, *J. Colloid Interface Sci.*, 2022, **623**, 9–20.

[137] L. Li, Z. Qin, L. Ries, S. Hong, T. Michel, J. Yang, C. Salameh, M. Bechelany, P. Miele, D. Kaplan, M. Chhowalla and D. Voiry, *ACS Nano*, 2019, **13**, 6824–6834.

[138] W. Cui, L. Chen, J. Li, Y. Zhou, Y. Sun, G. Jiang, S. C. Lee and F. Dong, *Appl. Catal. B Environ.*, 2019, **253**, 293–299.

[139] D. Maarisetty and S. S. Baral, *J. Mater. Chem. A*, 2020, **8**, 18560–18604.

[140] X. Hao, D. Xiang and Z. Jin, *ChemCatChem*, 2021, **13**, 4738–4750.

[141] Z. Hong, B. Shen, Y. Chen, B. Lin and B. Gao, *J. Mater. Chem. A*, 2013, **1**, 11754.

[142] H. S. Kim, Y.-J. Kim, Y. R. Son, V. N. Pham, K. Kim, C. W. Kim, Y.-S. Youn, O.-H. Kwon and H. Lee, *Sci. Rep.*, 2022, **12**, 11295.

[143] T. Han, Y. Luo and C. Wang, *Acta Mech. Solida Sin.*, 2015, **28**, 618–625.

[144] Y. Jia, L. Zhang, A. Du, G. Gao, J. Chen, X. Yan, C. L. Brown and X. Yao, *Adv. Mater.*, 2016, **28**, 9532–9538.

[145] U. Farooq, U. Ali Shah, M. Ishaq, J.-G. Hu, S. Ahmed, S. Chen, Z.-H. Zheng, Z.-H. Su, P. Fan and G.-X. Liang, *Chem. Eng. J.*, 2023, **451**, 139109.

[146] S. Suresh, *Int. J. Phys. Sci.*, 2013, **8**, 1121–1127.

[147] Y. C. Cheng, C. Q. Jin, F. Gao, X. L. Wu, W. Zhong, S. H. Li and P. K. Chu, *J. Appl. Phys.*, , DOI:10.1063/1.3270401.

[148] M. Durandurdu, *J. Phys. Chem. Solids*, 2009, **70**, 645–649.

[149] H. Labiadh and S. Hidouri, *J. King Saud Univ. - Sci.*, 2017, **29**, 444–450.

[150] J. S. and M. R. Navneet Kaur, Sukhmeen Kaur, *J. Bioelectron. Nanotechnol.*, 2016,

1, 1–5.

[151] P. Iranmanesh, S. Saeednia and M. Nourzpoor, *Chinese Phys. B*, 2015, **24**, 046104.

[152] V. M. Longo, J. R. Sambrano, E. Longo, J. Andrés, M. S. Li and J. A. Varela, *J. Alloys Compd.*, , DOI:10.1016/j.jallcom.2012.12.081.

[153] Z. G. Chen, L. Cheng, H. Y. Xu, J. Z. Liu, J. Zou, T. Sekiguchi, G. Q. Lu and H. M. Cheng, *Adv. Mater.*, 2010, **22**, 2376–2380.

[154] G. Malloci, L. Chiodo, A. Rubio and A. Mattoni, *J. Phys. Chem. C*, 2012, **116**, 8741–8746.

[155] B. Zns, N. In, C. S. Heterostructures, U. K. Gautam, X. Fang, Y. Bando, J. Zhan and D. Golberg, 2008, **2**, 1015–1021.

[156] J. Huang, Y. Yang, S. Xue, B. Yang, S. Liu and J. Shen, *Appl. Phys. Lett.*, 1997, **70**, 2335–2337.

[157] M. Bredol and M. Kaczmarek, *J. Phys. Chem. A*, 2010, **114**, 3950–3955.

[158] E. Mohagheghpour, M. Rabiee, F. Moztarzadeh, M. Tahriri, M. Jafarbeglou, D. Bizari and H. Eslami, *Mater. Sci. Eng. C*, 2009, **29**, 1842–1848.

[159] L. Hu, J. Yan, M. Liao, H. Xiang, X. Gong and L. Zhang, 2012, 2305–2309.

[160] L. Bao, S. Ali, C. Dai, Q. Zeng, C. Zeng, Y. Jia, X. Liu, P. Wang, X. Ren, T. Yang, M. Bououdina, Z.-H. Lu, Y. Wei, X. Yu and Y. Zhou, *ACS Nano*, , DOI:10.1021/acsnano.3c12773.

[161] L. A. Ramos-Huerta, O. Aguilar-Martínez, V. Santes, F. J. Tzompantzi Morales and C. E. Santolalla-Vargas, *Chem. Eng. Sci.*, 2024, **294**, 120067.

[162] Y. Piña- Pérez, O. Aguilar- Martínez, C. E. Santolalla- Vargas, E. Samaniego-Benítez, Á. Mantilla, F. González, F. Tzompantzi and V. Santes, *ChemistrySelect*, , DOI:10.1002/slct.202402184.

[163] M. M. Khan and K. O. Abdulwahab, *Mater. Sci. Semicond. Process.*, 2024, **181**, 108634.

[164] Stephen B. Castor and James B. Hedrick, *Industrial Minerals and Rocks*, 2006.

[165] T. Liu and J. Chen, *Sep. Purif. Technol.*, 2021, **276**, 119263.

[166] *Prog. Phys. Met.*, 2023, **24**, 157–172.

[167] C. Zhang, *J. Mater. Sci. Chem. Eng.*, 2023, **11**, 8–18.

[168] V. I. Komarewsky, *Ind. Eng. Chem.*, 1957, **49**, 264–265.

[169] A. Mehtab, J. Ahmed, S. M. Alshehri, Y. Mao and T. Ahmad, *Nanotechnology*, 2022, **33**, 142001.

[170] A. Sudha, I. Manimehan and P. Sakthivel, *Results Opt.*, 2024, **16**, 100727.

[171] K. Dawngliana, Lalruatpuia, L. Ralte and S. Rai, *J. Non. Cryst. Solids*, 2024, **632**,

122871.

[172] A. Manikandan, E. Manikandan, B. Meenatchi, S. Vadivel, S. K. Jaganathan, R. Ladchumananandasivam, M. Henini, M. Maaza and J. S. Aanand, *J. Alloys Compd.*, 2017, **723**, 1155–1161.

[173] K. Elayakumar, A. Dinesh, A. Manikandan, M. Palanivelu, G. Kavitha, S. Prakash, R. Thilak Kumar, S. K. Jaganathan and A. Baykal, *J. Magn. Magn. Mater.*, 2019, **476**, 157–165.

[174] K. Paulraj, S. Ramaswamy, M. Shkir, I. S. Yahia, M. S. Hamdy and S. AlFaify, *J. Mater. Sci. Mater. Electron.*, 2020, **31**, 1817–1827.

[175] S. Zhao, Y. Shen, A. Li, Y. Chen, S. Gao, W. Liu and D. Wei, *Ceram. Int.*, 2021, **47**, 24218–24226.

[176] R. Pradheepa, I. Manimehan and P. Sakthivel, *Mater. Sci. Eng. B*, 2024, **306**, 117463.

[177] L. S. Archana, D. N. Rajendran and J. Cyriac, *Inorg. Chem. Commun.*, 2024, **160**, 111936.

[178] M. Xin, *Eur. Phys. J. Plus*, 2024, **139**, 745.

[179] P. Hrubovčák, A. Zeleňáková, A. Berkutova, N. Mielnik, N. Kiraly, J. Szücsova, M. Lisnichuk, L. Nagy, J. Bednarčík, V. Girman and V. Zeleňák, *J. Magn. Magn. Mater.*, 2022, **560**, 169677.

[180] C. C. Baker, E. J. Friebele, C. G. Askins, M. P. Hunt, B. A. Marcheschi, J. Fontana, J. R. Peele, W. Kim, J. Sanghera, J. Zhang, R. K. Pattnaik, L. D. Merkle, M. Dubinskii, Y. Chen, I. A. Dajani and C. Mart, ed. J. Ballato, 2016, p. 97280T.

[181] M. Kumari and M. C. Bhatnagar, *J. Supercond. Nov. Magn.*, 2019, **32**, 1027–1033.

[182] X. Li, H. Liu, J. Wang, H. Cui and F. Han, *Mater. Res. Bull.*, 2004, **39**, 1923–1930.

[183] A. A. Ansari, S. F. Adil, M. Alam, N. Ahmad, M. E. Assal, J. P. Labis and A. Alwarthan, *Sci. Rep.*, 2020, **10**, 15012.

[184] P. Kowalik, J. Mikulski, A. Borodziuk, M. Duda, I. Kamińska, K. Zajdel, J. Rybusinski, J. Szczytko, T. Wojciechowski, K. Sobczak, R. Minikayev, M. Kulpa-Greszta, R. Pazik, P. Grzaczkowska, K. Fronc, M. Lapinski, M. Frontczak-Baniewicz and B. Sikora, *J. Phys. Chem. C*, 2020, **124**, 6871–6883.

[185] N. Nithya, G. Bhoopathi, G. Magesh and O. N. Balasundaram, *Mater. Sci. Semicond. Process.*, 2019, **99**, 14–22.

[186] K. Shingange, H. C. Swart and G. H. Mhlongo, *J. Alloys Compd.*, 2019, **797**, 284–301.

[187] Y. Kakinuma, Y. Konuma, M. Fukuta and K. Tanaka, *CIRP Ann.*, 2019, **68**, 345–348.

[188] A. Iqbal, Y. Iqbal, L. Chang, S. Ahmed, Z. Tang and Y. Gao, *J. Nanoparticle Res.*, 2012, **14**, 1206.

[189] M. Xin, L.-M. Liao and F. Han, *J. Lumin.*, 2021, **238**, 118074.

[190] M. Jothibas, S. Suganya, A. Muthuvel and E. Paulson, *Inorg. Chem. Commun.*, 2023, **150**, 110511.

[191] X. Zhou, Q. Yang, H. Wang, F. Huang, J. Zhang and S. Xu, *J. Mater. Sci. Mater. Electron.*, 2019, **30**, 1089–1099.

[192] B. Poornaprakash, P. T. Puneetha, M. S. P. Reddy and Y. L. Kim, 2023, **20**, 85–90.

[193] B. Poornaprakash, U. Chalapathi, M. Kumar, S. Ramu, S. V. Prabhakar Vattikuti and S. H. Park, *Mater. Lett.*, 2020, **273**, 127887.

[194] J. Kaur, K. G. P. Kahagalla and S. Rani, 2020, **07**, 3640–3645.

[195] N. Suganthi and K. Pushpanathan, *J. Mater. Sci. Mater. Electron.*, 2018, **29**, 13970–13983.

[196] R. Viswanath, H. S. B. Naik, Y. K. G. Somalanaik, P. K. P. Neelanjeneallu, K. N. Harish and M. C. Prabhakara, *J. Nanotechnol.*, 2014, **2014**, 1–8.

[197] A. B. Alwany, G. M. Youssef, E. Eisa, O. M. Samir, M. A. Algradee and A. Alnehia, *Optik (Stuttg).*, 2022, **260**, 169124.

[198] J. W. Lee, K. Cho, H. Kim, J. H. Kim, B. Park, T. Noh, S. S. H. Kim and S. S. H. Kim, *Japanese J. Appl. Physics, Part 1 Regul. Pap. Short Notes Rev. Pap.*, 2005, **44**, 7694–7697.

[199] S. J. Xu, S. J. Chua, B. Liu, L. M. Gan, C. H. Chew and G. Q. Xu, *Appl. Phys. Lett.*, 1998, **73**, 478–480.

[200] L. Wang, X. Xu and X. Yuan, *J. Lumin.*, 2010, **130**, 137–140.

[201] G. Li, L. H. Li, L. S. Yang and J. L. Huang, *Adv. Mater. Res.*, 2013, **800**, 402–405.

[202] Y. Hanifehpour, B. Soltani, A. R. Amani-Ghadim, B. Hedayati, B. Khomami and S. W. Joo, *J. Ind. Eng. Chem.*, 2016, **34**, 41–50.

[203] A. A. Bol, R. Van Beek and A. Meijerink, *Chem. Mater.*, 2002, **14**, 1121–1126.

[204] H. Yang, L. Yu, L. Shen and L. Wang, *Mater. Lett.*, 2004, **58**, 1172–1175.

[205] M. Ahmadi, S. Javadpour, A. Khosravi and A. Gharavi, *Jpn. J. Appl. Phys.*, 2008, **47**, 5089–5092.

[206] P. Yang, M. Lü, D. Xü, D. Yuan and G. Zhou, *J. Lumin.*, 2001, **93**, 101–105.

[207] N. Joudeh and D. Linke, *J. Nanobiotechnology*, 2022, **20**, 262.

[208] N. Abid, A. M. Khan, S. Shujait, K. Chaudhary, M. Ikram, M. Imran, J. Haider, M. Khan, Q. Khan and M. Maqbool, *Adv. Colloid Interface Sci.*, 2022, **300**, 102597.

[209] H. K. Lin, T.-H. Yan, S. Bashir and J. L. Liu, in *Advanced Nanomaterials and Their Applications in Renewable Energy*, Elsevier, 2022, pp. 61–110.

[210] S. A. M. Zobir, S. A. Rashid and T. Tan, in *Synthesis, Technology and Applications*

of Carbon Nanomaterials, Elsevier, 2019, pp. 77–107.

[211] X. Jia, W. Khan, Z. Wu, J. Choi and A. C. K. Yip, *Adv. Powder Technol.*, 2019, **30**, 467–484.

[212] T. Prasad Yadav, R. Manohar Yadav and D. Pratap Singh, *Nanosci. Nanotechnol.*, 2012, **2**, 22–48.

[213] W. Jung, S. Jang, S. Cho, H. Jeon and H. Jung, *Adv. Mater.*, , DOI:10.1002/adma.201907101.

[214] K. A. Peck, J. Lien, M. Su, A. D. Stacy and T. Guo, *ACS Omega*, 2023, **8**, 42667–42677.

[215] B. K. Teo and X. H. Sun, *J. Clust. Sci.*, 2006, **17**, 529–540.

[216] R. G. Hobbs, N. Petkov and J. D. Holmes, *Chem. Mater.*, 2012, **24**, 1975–1991.

[217] H. Lu, S.-Y. Tang, G. Yun, H. Li, Y. Zhang, R. Qiao and W. Li, *Biosensors*, 2020, **10**, 165.

[218] A. Karatutlu, A. Barhoum and A. Sapelkin, in *Emerging Applications of Nanoparticles and Architecture Nanostructures*, Elsevier, 2018, pp. 1–28.

[219] Y. X. Gan, A. H. Jayatissa, Z. Yu, X. Chen and M. Li, *J. Nanomater.*, 2020, **2020**, 1–3.

[220] D. O’Hare, in *Encyclopedia of Materials: Science and Technology*, Elsevier, 2001, pp. 3989–3992.

[221] B. Lu, Y. Oumi, K. Itabashi and T. Sano, *Microporous Mesoporous Mater.*, 2005, **81**, 365–374.

[222] T. A. K. Byrappaa,*, *Prog. Cryst. Growth Charact. Mater.*, 2007, **53**, 117–166.

[223] S.-J. Young and Y.-L. Chu, *IEEE Trans. Electron Devices*, 2021, **68**, 1886–1891.

[224] M. M. Smart, C. A. Moore, C. D. McMillen and J. W. Kolis, *Crystals*, 2023, **13**, 1257.

[225] B. S. Damasceno, A. F. V. da Silva, M. C. Ferreira, A. N. de Melo, D. M. G. Leite and A. C. V. de Araújo, *Colloids Surfaces A Physicochem. Eng. Asp.*, 2023, **670**, 131528.

[226] by W. and A. T. Luo, *Nanomaterials*, 2021, **11**, 365.

[227] M. A. Malik, M. Y. Wani and M. A. Hashim, *Arab. J. Chem.*, 2012, **5**, 397–417.

[228] A. Hu, Z. Yao and X. Yu, *J. Appl. Polym. Sci.*, 2009, **113**, 2202–2208.

[229] M. Sanchez-Dominguez and M. Boutonnet, *Catalysts*, 2015, **6**, 4.

[230] A. K. Ganguli, T. Ahmad, S. Vaidya and J. Ahmed, *Pure Appl. Chem.*, 2008, **80**, 2451–2477.

[231] A. Kumar, Y. Kuang, Z. Liang and X. Sun, *Mater. Today Nano*, 2020, **11**, 100076.

[232] V. Chikan and E. McLaurin, *Nanomaterials*, 2016, **6**, 85.

[233] M. Tsuji, *ChemistrySelect*, 2017, **2**, 805–819.

[234] V. Polshettiwar, M. N. Nadagouda and R. S. Varma, *Aust. J. Chem.*, 2009, **62**, 16.

[235] R. K. Singh, R. Kumar, D. P. Singh, R. Savu and S. A. Moshkalev, *Mater. Today Chem.*, 2019, **12**, 282–314.

[236] H. Xu, B. W. Zeiger and K. S. Suslick, *Chem. Soc. Rev.*, 2013, **42**, 2555–2567.

[237] P. K. Khanna, K. Kate, K. Dhanabalan, S. Banerjee, N. Reji, S. D. Shinde and G. H. Jain, *J. Nanosci. Nanotechnol.*, 2012, **12**, 2791–2796.

[238] A. Dey, S. Noyel Victoria, M. S. Gaikwad and A. Sao, *Mater. Lett.*, 2024, **361**, 136093.

[239] K. Nejati, M. Dadashpour, T. Gharibi, H. Mellatyar and A. Akbarzadeh, *J. Clust. Sci.*, 2022, **33**, 1–16.

[240] A. Hassanjani-Roshan, M. R. Vaezi, A. Shokuhfar and Z. Rajabali, *Particuology*, 2011, **9**, 95–99.

[241] D. Elfadil, S. Palmieri, F. Silveri, F. Della Pelle, M. Sergi, M. Del Carlo, A. Amine and D. Compagnone, *Microchem. J.*, 2022, **180**, 107634.

[242] S. Głowniak, B. Szczęśniak, J. Choma and M. Jaroniec, *Molecules*, 2023, **28**, 2639.

[243] M. A. Behnajady, H. Eskandarloo, N. Modirshahla and M. Shokri, *Desalination*, 2011, **278**, 10–17.

[244] M. Alagiri, S. Ponnusamy and C. Muthamizhchelvan, *J. Mater. Sci. Mater. Electron.*, 2012, **23**, 728–732.

[245] A. M. Ismail, A. A. Menazea, H. A. Kabary, A. E. El-Sherbiny and A. Samy, *J. Mol. Struct.*, 2019, **1196**, 332–337.

[246] R. Mahdavi and S. S. Ashraf Talesh, *Ultrason. Sonochem.*, 2017, **39**, 504–510.

[247] Z. Li, B. Hou, Y. Xu, D. Wu, Y. Sun, W. Hu and F. Deng, *J. Solid State Chem.*, 2005, **178**, 1395–1405.

[248] M. Shahjahan, *Nanosci. Nanometrology*, 2017, **3**, 34.

[249] S. V. Lazareva, N. V. Shikina, L. E. Tatarova and Z. R. Ismagilov, *Eurasian Chem. J.*, 2017, **19**, 295.

[250] W.-F. Chen, S. S. Mofarah, D. A. H. Hanaor, P. Koshy, H.-K. Chen, Y. Jiang and C. C. Sorrell, *Inorg. Chem.*, 2018, **57**, 7279–7289.

[251] M. Parashar, V. K. Shukla and R. Singh, *J. Mater. Sci. Mater. Electron.*, 2020, **31**, 3729–3749.

[252] J. Livage, F. Babonneau, M. Chatry and L. Coury, *Ceram. Int.*, 1997, **23**, 13–18.

[253] K. Kajihara, *J. Asian Ceram. Soc.*, 2013, **1**, 121–133.

[254] J. Livage, *Bull. Mater. Sci.*, 1999, **22**, 201–205.

[255] T. Saragi, B. L. Depi, S. Butarbutar, B. Permana and Risdiana, *J. Phys. Conf. Ser.*, 2018, **1013**, 012190.

[256] J. Tian, W. Qian, H. Zhang, H. Ma and W. Ying, *RSC Adv.*, 2023, **13**, 13902–13910.

[257] *Advances and Avenues in the Development of Novel Carriers for Bioactives and Biological Agents*, Elsevier, 2020.

[258] Z. J. Yu, M. R. Kumar, D. L. Sun, L. T. Wang and R. Y. Hong, *Mater. Lett.*, 2016, **166**, 284–287.

[259] A. Kumar, N. Yadav, D. S. Rana, P. Kumar, M. Arora and R. P. Pant, *J. Magn. Magn. Mater.*, 2015, **394**, 379–384.

[260] S. Thambidurai, P. Gowthaman, M. Venkatachalam, S. Suresh and M. Kandasamy, *J. Alloys Compd.*, 2021, **852**, 156997.

[261] C. F. Holder and R. E. Schaak, *ACS Nano*, 2019, **13**, 7359–7365.

[262] S. Fatimah, R. Ragadhita, D. F. Al Husaeni and A. B. D. Nandiyanto, *ASEAN J. Sci. Eng.*, 2021, **2**, 65–76.

[263] Significance of Bragg’s Equation, https://qsstudy.com/significance-braggs-equation).

[264] A. A. Bunaciu, E. gabriela Udriştioiu and H. Y. Aboul-Enein, *Crit. Rev. Anal. Chem.*, 2015, **45**, 289–299.

[265] A. Chauhan, *J. Anal. Bioanal. Tech.*, , DOI:10.4172/2155-9872.1000212.

[266] J. Pina, A. Dias and J. . Lebrun, *Mater. Sci. Eng. A*, 2003, **347**, 21–31.

[267] B. J. Inkson, in *Materials Characterization Using Nondestructive Evaluation (NDE) Methods*, Elsevier, 2016, pp. 17–43.

[268] P. Echlin and U. Cambridge Analytical Microscopy, *Handbook of Sample Preparation for Scanning Electron Microscopy and X-Ray Microanalysis*, springer, 2009.

[269] Sulabha K. Kulkarni, *Nanotechnology: Principles and Practices*, Springer, USA, 2014.

[270] A. K. Datye, P. L. Hansen and S. Helveg, in *Handbook of Heterogeneous Catalysis*, Wiley, 2008, pp. 803–833.

[271] M. Suga, S. Asahina, Y. Sakuda, H. Kazumori, H. Nishiyama, T. Nokuo, V. Alfredsson, T. Kjellman, S. M. Stevens, H. S. Cho, M. Cho, L. Han, S. Che, M. W. Anderson, F. Schüth, H. Deng, O. M. Yaghi, Z. Liu, H. Y. Jeong, A. Stein, K. Sakamoto, R. Ryoo and O. Terasaki, *Prog. Solid State Chem.*, 2014, **42**, 1–21.

[272] M. M. Nasef and H. Saidi, *Appl. Surf. Sci.*, 2006, **252**, 3073–3084.

[273] L. C. Gomes and F. J. Mergulhão, *Scanning*, 2017, **2017**, 1–7.

[274] A. C. Mohan and B. Renjanadevi, *Procedia Technol.*, 2016, **24**, 761–766.

[275] M. A. Haque and M. T. A. Saif, *Sensors Actuators A Phys.*, 2002, **97**–**98**, 239–245.

[276] SALSA School of Analytical Sciences Adlershof, https://fakultaeten.hu-berlin.de/en/mnf/forschung_internationales/grs/salsa/p-a-labs/application-lab/instrumentation/a-labs-sem.

[277] *Sch. Community Encycl.*

[278] L. Reimer H. Kohl, *Transmission Electron Microscopy Physics of Image Formation*, Springer US, 2008.

[279] C. Y. Tang and Z. Yang, in *Membrane Characterization*, Elsevier, 2017, pp. 145–159.

[280] M. D. Eddleston, E. G. Bithell and W. Jones, *J. Pharm. Sci.*, 2010, **99**, 4072–4083.

[281] M. Rezaei, A. Soheili, S. A. Ziai, A. Fakharian, H. Toreyhi, M. Pourabdollah, J. Ghorbani, M. Karimi-Galougahi, S. A. Mahdaviani, M. Hasanzad, A. Eslaminejad, H. A. Ghaffaripour, S. Mahmoudian, Z. Rodafshani, M. S. Mirenayat, M. Varahram, M. Marjani, P. Tabarsi, D. Mansouri, H. R. Jamaati and A. A. Velayati, *Sci. Rep.*, 2022, **12**, 2375.

[282] B Schrade, *Infrared and Raman spectroscopy: methods and applications*, VCH, NewYork, 2008.

[283] R. P. Van Duyne and C. L. Haynes, in *Encyclopedia of Physical Science and Technology*, Elsevier, 2003, pp. 845–866.

[284] G. S. Bumbrah and R. M. Sharma, *Egypt. J. Forensic Sci.*, 2016, **6**, 209–215.

[285] C. Moura, P. Carvalho, F. Vaz, L. Cunha and E. Alves, *Thin Solid Films*, 2006, **515**, 1132–1137.

[286] D. López-Díaz, M. López Holgado, J. L. García-Fierro and M. M. Velázquez, *J. Phys. Chem. C*, 2017, **121**, 20489–20497.

[287] The Raman Spectrophotometer, https://www.sas.upenn.edu/~crulli/TheRamanSpectrophotometer.html.

[288] G. Kortüm, W. Braun and G. Herzog, *Angew. Chemie Int. Ed. English*, 1963, **2**, 333–341.

[289] A. J. Moy and J. W. Tunnell, in *Imaging in Dermatology*, Elsevier, 2016, pp. 203–215.

[290] A. O. Murzin, A. Y. Samsonova, C. C. Stoumpos, N. I. Selivanov, A. V. Emeline and Y. V. Kapitonov, *Molecules*, 2023, **28**, 350.

[291] M. Nowak, B. Kauch and P. Szperlich, *Rev. Sci. Instrum.*, , DOI:10.1063/1.3103603.

[292] B. J. Fernandes, P. Murahari, S. Chahal and K. Ramesh, 2020, p. 030231.

[293] S. Rajan, P. M. M. Gazzali, L. Okrasa and G. Chandrasekaran, *J. Mater. Sci. Mater.*

Electron., 2018, **29**, 11215–11228.

[294] Mahmood Aliofkhazraei, *Handbook of Nanoparticles*, Springer International Publishing Switzerland, 2015.

[295] T. Yamashita and P. Hayes, *Appl. Surf. Sci.*, 2008, **254**, 2441–2449.

[296] D. N. G. Krishna and J. Philip, *Appl. Surf. Sci. Adv.*, 2022, **12**, 100332.

[297] C. R. Brundle, G. Conti and P. Mack, *J. Electron Spectros. Relat. Phenomena*, 2010, **178**–**179**, 433–448.

[298] J. Baltrusaitis, P. M. Jayaweera and V. H. Grassian, *Phys. Chem. Chem. Phys.*, 2009, **11**, 8295.

[299] J. F. Watts, *Surf. Interface Anal.*, 2010, **42**, 358–362.

[300] A. MOHAMMED1 and Avin ABDULLAH2, *Proc. 2018 Int. Conf. Hydraul. Pneum. - HERVEX*, 1982, 77–85.

[301] A. Fayyaz, J. Iqbal, H. Asghar, T. A. Alrebdi, A. M. Alshehri, W. Ahmed and N. Ahmed, *Metals (Basel).*, 2023, **13**, 1188.

[302] Z. Xiao and A. R. Laplante, *Miner. Eng.*, 2004, **17**, 961–979.

[303] S. Pandey, V. Kumar, V. K. Sharma and K. D. Mandal, *Mater. Chem. Phys.*, 2020, **253**, 123384.

[304] M. Yasutake, S. Hiki, Y. Andou, H. Nishida and T. Endo, *Macromolecules*, 2003, **36**, 5974–5981.

[305] C. Ledda, V. Rapisarda, M. Bracci, L. Proietti, M. Zuccarello, R. Fallico, M. Fiore and M. Ferrante, *J. Occup. Med. Toxicol.*, 2013, **8**, 23.

[306] S. Ridolfi, *Insight - Non-Destructive Test. Cond. Monit.*, 2018, **60**, 37–41.

[307] K. Pye and D. Croft, *Forensic Sci. Int.*, 2007, **165**, 52–63.

[308] O. Dobrozhan, O. Diachenko, M. Kolesnyk, A. Stepanenko, S. Vorobiov, P. Baláž, S. Plotnikov and A. Opanasyuk, *Mater. Sci. Semicond. Process.*, 2019, **102**, 104595.

[309] D. Alonso- Álvarez, D. Ross, E. Klampaftis, K. R. McIntosh, S. Jia, P. Storiz, T. Stolz and B. S. Richards, *Prog. Photovoltaics Res. Appl.*, 2015, **23**, 479–497.

[310] P. M. V. R. & A. R. Barron and R. U. via O. CNX, *LIBREtextschemistry*.

[311] J. P. Leitão, N. M. Santos, P. A. Fernandes, P. M. P. Salomé, A. F. da Cunha, J. C. González, G. M. Ribeiro and F. M. Matinaga, *Phys. Rev. B*, 2011, **84**, 024120.

[312] M. Yoshikawa, M. Kunzer, J. Wagner, H. Obloh, P. Schlotter, R. Schmidt, N. Herres and U. Kaufmann, *J. Appl. Phys.*, 1999, **86**, 4400–4402.

[313] M. Grossberg, J. Krustok, J. Raudoja and T. Raadik, *Appl. Phys. Lett.*, , DOI:10.1063/1.4750249.

[314] M. Karimi, M. Raeisi, M. Bagherzadeh and F. Payami, *SN Appl. Sci.*, 2019, **1**, 635.

[315] P. J. Dean, *Prog. Cryst. Growth Charact.*, 1982, **5**, 89–174.

[316] F. Messina, L. Sciortino, G. Buscarino, S. Agnello, F. Gelardi and M. Cannas, *Mater. Today Proc.*, 2016, **3**, S258–S265.

[317] J. Z. Zhang, *Optical Properties and Spectroscopy of Nanomaterials*, WORLD SCIENTIFIC, 2009.

[318] S. K. Sharma, T. Tingberg, I. Carrasco, M. Bettinelli, D. Kuylenstierna and M. Karlsson, *ECS J. Solid State Sci. Technol.*, 2020, **9**, 016004.

[319] T. Trupke, B. Mitchell, J. W. Weber, W. McMillan, R. A. Bardos and R. Kroeze, *Energy Procedia*, 2012, **15**, 135–146.

[320] A. Alipour, M. Mansour Lakouraj and H. Tashakkorian, *Sci. Rep.*, 2021, **11**, 1913.

[321] J. N. Miller, *J. Pharm. Biomed. Anal.*, 1983, **1**, 525–535.

[322] A. C. Ribes, S. Damaskinos, A. E. Dixon, G. E. Carver, C. Peng, P. M. Fauchet, T. K. Sham and I. Coulthard, *Appl. Phys. Lett.*, 1995, **66**, 2321–2323.

[323] S. G. Chou, F. Plentz, J. Jiang, R. Saito, D. Nezich, H. B. Ribeiro, A. Jorio, M. A. Pimenta, G. G. Samsonidze, A. P. Santos, M. Zheng, G. B. Onoa, E. D. Semke, G. Dresselhaus and M. S. Dresselhaus, *Phys. Rev. Lett.*, 2005, **94**, 127402.

[324] R. Saravanan, F. Gracia and A. Stephen, 2017, pp. 19–40.

[325] L. Zhang, H. H. Mohamed, R. Dillert and D. Bahnemann, *J. Photochem. Photobiol. C Photochem. Rev.*, 2012, **13**, 263–276.

[326] L. G. Devi and R. Kavitha, *Appl. Catal. B Environ.*, 2013, **140**–**141**, 559–587.

[327] S. J. Phang, V.-L. Wong, L.-L. Tan and S.-P. Chai, *Appl. Mater. Today*, 2020, **20**, 100741.

[328] B. D. Deshpande, P. S. Agrawal, M. K. N. Yenkie and S. J. Dhoble, *Nano-Structures & Nano-Objects*, 2020, **22**, 100442.

[329] Landrigan et al, *Lancet*, 2018, **391**, 462–512.

[330] L. Hermabessiere, A. Dehaut, I. Paul-Pont, C. Lacroix, R. Jezequel, P. Soudant and G. Duflos, *Chemosphere*, 2017, **182**, 781–793.

[331] P. Chowdhary, R. N. Bharagava, S. Mishra and N. Khan, in *Environmental Concerns and Sustainable Development*, Springer Singapore, Singapore, 2020, pp. 235–256.

[332] G. J. Lee and J. J. Wu, *Powder Technol.*, 2017, **318**, 8–22.

[333] D. Li and W. Shi, *Chinese J. Catal.*, 2016, **37**, 792–799.

[334] X. Ruan, H. Hu, H. Che, G. Che, C. Li, C. Liu and H. Dong, *J. Alloys Compd.*, 2019, **773**, 1089–1098.

[335] F. Meng, Z. Hong, J. Arndt, M. Li, M. Zhi, F. Yang and N. Wu, *Nano Res.*, 2012, **5**, 213–221.

[336] A. B. Djurišić, Y. He and A. M. C. Ng, *APL Mater.*, 2020, **8**, 030903.

[337] A. Khandelwal, D. Maarisetty and S. S. Baral, *Renew. Sustain. Energy Rev.*, 2022, **167**, 112693.

[338] K. Sharma, P. Raizada, V. Hasija, P. Singh, A. Bajpai, V.-H. Nguyen, S. Rangabhashiyam, P. Kumar, A. K. Nadda, S. Y. Kim, R. S. Varma, T. T. N. Le and Q. Van Le, *J. Water Process Eng.*, 2021, **43**, 102217.

[339] C. Liu, C. Kong, F. J. Zhang, C. M. Kai, W. Q. Cai, X. Y. Sun and W. C. Oh, *J. Korean Ceram. Soc.*, 2021, **58**, 135–147.

[340] Z. Wang, M. Xiao, J. You, G. Liu and L. Wang, *Accounts Mater. Res.*, 2022, **3**, 1127–1136.

[341] D. Maarisetty and S. S. Baral, *ACS Appl. Mater. Interfaces*, 2021, **13**, 60002–60017.

[342] I. Daskalakis, I. Vamvasakis, I. T. Papadas, S. Tsatsos, S. A. Choulis, S. Kennou and G. S. Armatas, *Inorg. Chem. Front.*, 2020, **7**, 4687–4700.

[343] X. Hao, Y. Wang, J. Zhou, Z. Cui, Y. Wang and Z. Zou, *Appl. Catal. B Environ.*, 2018, **221**, 302–311.

[344] T. Arai, S. I. Senda, Y. Sato, H. Takahashi, K. Shinoda, B. Jeyadevan and K. Tohji, *Chem. Mater.*, 2008, **20**, 1997–2000.

[345] M. Jothibas, C. Manoharan, S. J. Jeyakumar, P. Praveen, I. K. Punithavathy and J. P. Richard, *Sol. Energy*, 2018, **159**, 434–443.

[346] Y. Wang, J. Wu, J. Zheng and R. Xu, *Catal. Sci. Technol.*, 2011, **1**, 940–947.

[347] H. Sun, X. Zhao, L. Zhang and W. Fan, 2011, 2218–2227.

[348] A. Manuscript, , DOI:10.1039/C4CP03736G.

[349] F. P. Yu, S. L. Ou, P. C. Yao, B. R. Wu and D. S. Wuu, *J. Nanomater.*, , DOI:10.1155/2014/594952.

[350] Z. Q. Li, J. H. Shi, Q. Q. Liu, Z. A. Wang, Z. Sun and S. M. Huang, *Appl. Surf. Sci.*, 2010, **257**, 122–126.

[351] T. Dedova, M. Krunks, I. Gromyko, V. Mikli, I. Sildos, K. Utt and T. Unt, *Phys. Status Solidi Appl. Mater. Sci.*, 2014, **211**, 514–521.

[352] J. Liu, J. Ma, Y. Liu, Z. Song, Y. Sun, J. Fang and Z. Liu, *J. Alloys Compd.*, 2009, **486**, 40–43.

[353] Y. C. Zhang, G. Y. Wang, X. Y. Hu and W. W. Chen, *Mater. Res. Bull.*, 2006, **41**, 1817–1824.

[354] S. Vijayan, C. S. Dash, G. Umadevi, M. Sundararajan and R. Mariappan, *J. Clust. Sci.*, 2021, **32**, 1601–1608.

[355] N. V Desai, I. A. Shaikh, A. V Raval, K. G. Raval and D. V Shah, *IOP Conf. Ser. Mater. Sci. Eng.*, 2021, **1126**, 012058.

[356] A. A. Markov and I. A. Filimonov, *AIP Conf. Proc.*, , DOI:10.1063/1.5135672.

[357] C. Liu and X. Wu, *Micro Nano Lett.*, 2018, **13**, 157–159.

[358] X. Fang, Y. Bando, M. Liao, U. K. Gautam, C. Zhi, B. Dierre, B. Liu, T. Zhai, T. Sekiguchi, Y. Koide and D. Golberg, *Adv. Mater.*, 2009, **21**, 2034–2039.

[359] X. Fang, Y. Bando, C. Ye, G. Shen and D. Golberg, *J. Phys. Chem. C*, 2007, **111**, 8469–8474.

[360] A. Hikavyy, K. Neyts, G. Stuyven, D. Poelman and P. De Visschere, *J. Soc. Inf. Disp.*, 2002, **10**, 255.

[361] F. H. Su, Z. L. Fang, B. S. Ma, K. Ding, G. H. Li and S. J. Xu, *J. Appl. Phys.*, 2004, **95**, 3344–3349.

[362] S. Anandan, A. Vinu, K. L. P. Sheeja Lovely, N. Gokulakrishnan, P. Srinivasu, T. Mori, V. Murugesan, V. Sivamurugan and K. Ariga, *J. Mol. Catal. A Chem.*, 2007, **266**, 149–157.

[363] D. Sridevi and K. V. Rajendran, *Chalcogenide Lett.*, 2010, **7**, 397–401.

[364] Z. He, Y. Su, Y. Chen, D. Cai, J. Jiang and L. Chen, *Mater. Res. Bull.*, 2005, **40**, 1308–1313.

[365] W. G. Becker and A. J. Bard, *J. Phys. Chem.*, 1983, **87**, 4888–4893.

[366] S. Biswas and S. Kar, *Nanotechnology*, , DOI:10.1088/0957-4484/19/04/045710.

[367] Z. Wei, Y. Lu, J. Zhao, S. Zhao, R. Wang, N. Fu, X. Li, L. Guan and F. Teng, *ACS Omega*, 2018, **3**, 137–143.

[368] E. M. Jubeer, M. A. Manthrammel, M. Shkir, P. A. Subha, I. S. Yahia and A. Alfaify, *Optik (Stuttg).*, 2021, **240**, 166812.

[369] T. T. Quynh Hoa, L. Van Vu, T. D. Canh and N. N. Long, *J. Phys. Conf. Ser.*, , DOI:10.1088/1742-6596/187/1/012081.

[370] X. Zhou, Q. Yang, H. Wang, F. Huang, J. Zhang and S. Xu, *J. Mater. Sci. Mater. Electron.*, 2019, **30**, 1089–1099.

[371] M. Thambidurai, N. Murugan, N. Muthukumarasamy, S. Agilan, S. Vasantha and R. Balasundaraprabhu, *J. Mater. Sci. Technol.*, 2010, **26**, 193–199.

[372] P. Bindu and S. Thomas, *J. Theor. Appl. Phys.*, 2014, **8**, 123–134.

[373] G. Arandhara, J. Bora and P. K. K. Saikia, *Mater. Chem. Phys.*, 2020, **241**, 122277.

[374] A. Alqahtani, S. Husain, A. Somvanshi and W. Khan, *J. Alloys Compd.*, 2019, **804**, 401–414.

[375] V. D. Mote, Y. Purushotham and B. N. Dole, *J. Theor. Appl. Phys.*, 2012, **6**, 2–9.

[376] K. A. Aly, N. M. Khalil, Y. Algamal and Q. M. A. Saleem, *J. Alloys Compd.*, 2016, **676**, 606–612.

[377] M. A. Nawaz, M. Asghar, M. Y. Shahid, N. U. L. Ain, F. Iqbal, F. Malik and H. E. Ruda, 2016, **11**, 537–546.

[378] K. Maniammal, G. Madhu and V. Biju, *Phys. E Low-Dimensional Syst. Nanostructures*, 2017, **85**, 214–222.

[379] M. Xin, L. M. Liao and F. Han, *J. Lumin.*, 2021, **238**, 118074.

[380] J. Madhavi, *SN Appl. Sci.*, 2019, **1**, 1–12.

[381] T. M. K. Thandavan, S. M. A. Gani, C. S. Wong and R. M. Nor, *J. Nondestruct. Eval.*, 2015, **34**, 1–9.

[382] A. Khorsand Zak, W. H. Abd. Majid, M. E. Abrishami and R. Yousefi, *Solid State Sci.*, 2011, **13**, 251–256.

[383] M. Riazian and M. Yousefpoor, *Int. J. Smart Nano Mater.*, 2020, **11**, 47–64.

[384] J. Zhou, J. Zhao and R. Liu, *Appl. Catal. B Environ.*, 2020, **278**, 119265.

[385] W. G. Nilsen, *Phys. Rev.*, 1969, **182**, 838–850.

[386] Z. Ye, L. Kong, F. Chen, Z. Chen, Y. Lin and C. Liu, *Optik (Stuttg).*, 2018, **164**, 345–354.

[387] S. Dhara, A. K. Arora, J. Ghatak, K. H. Chen, C. P. Liu, L. C. Chen, Y. Tzeng and B. Raj, 1–12.

[388] J. Serrano, A. Cantarero, M. Cardona, N. Garro, R. Lauck, R. E. Tallman, T. M. Ritter and B. A. Weinstein, *Phys. Rev. B - Condens. Matter Mater. Phys.*, 2004, **69**, 1–11.

[389] M. M. El-Desoky, G. A. El-Barbary, D. E. El Refaey and F. El-Tantawy, *Optik (Stuttg).*, 2018, **168**, 764–777.

[390] C. Morrison, H. Sun, Y. Yao, R. A. Loomis and W. E. Buhro, *Chem. Mater.*, 2020, **32**, 1760–1768.

[391] A. Goudarzi, G. M. Aval, S. S. Park, M.-C. Choi, R. Sahraei, M. H. Ullah, A. Avane and C.-S. Ha, *Chem. Mater.*, 2009, **21**, 2375–2385.

[392] X. Yang, W. Gu, C. Yuan, Z. Yang, S. Shi, Z. Liu, S. Liang and F. Teng, *CrystEngComm*, 2021, **23**, 1999–2005.

[393] M. Shobana and S. R. Meher, *Thin Solid Films*, 2019, **683**, 97–110.

[394] A. K. Shahi, B. K. Pandey, B. P. Singh, B. K. Gupta, S. Singh and R. Gopal, *Electron. Mater. Lett.*, 2017, **13**, 160–167.

[395] H. Aydin, C. Aydin, A. A. Al-Ghamdi, W. A. Farooq and F. Yakuphanoglu, *Optik (Stuttg).*, 2016, **127**, 1879–1883.

[396] S. Ilican, Y. Caglar, M. Caglar and F. Yakuphanoglu, *J. Alloys Compd.*, 2009, **480**, 234–237.

[397] B. L. Devi, K. M. Rao, D. Kekuda and D. Ramananda, *Appl. Phys. A Mater. Sci. Process.*, 2018, **124**, 0.

[398] K. Manzoor, S. R. Vadera, N. Kumar and T. R. N. Kutty, *Mater. Chem. Phys.*, 2003, **82**, 718–725.

[399] H. Y. Lu, S. Y. Chu and S. S. Tan, *J. Cryst. Growth*, 2004, **269**, 385–391.

[400] M. Wang, J. Wang, C. Xi, C. Cheng, C. Zou, R. Zhang, Y. Xie, Z. Guo, C. Tang, C. Dong, Y. Chen and X. Du, *Angew. Chemie Int. Ed.*, 2020, **59**, 11510–11515.

[401] H. Li, J. Li, Z. Ai, F. Jia and L. Zhang, *Angew. Chemie Int. Ed.*, 2018, **57**, 122–138.

[402] D. Xue, H. Xia, W. Yan, J. Zhang and S. Mu, *Nano-Micro Lett.*, 2021, **13**, 5.

[403] B. Xiao, T. Lv, J. Zhao, Q. Rong, H. Zhang, H. Wei, J. He, J. Zhang, Y. Zhang, Y. Peng and Q. Liu, *ACS Catal.*, 2021, **11**, 13255–13265.

[404] C. Du, Q. Zhang, Z. Lin, B. Yan, C. Xia and G. Yang, *Appl. Catal. B Environ.*, 2019, **248**, 193–201.

[405] J. Lee, S. Ham, D. Choi and D.-J. Jang, *Nanoscale*, 2018, **10**, 14254–14263.

[406] X. Hao, Z. Cui, J. Zhou, Y. Wang, Y. Hu, Y. Wang and Z. Zou, *Nano Energy*, 2018, **52**, 105–116.

[407] T. Mahvelati-Shamsabadi and E. K. Goharshadi, *Ultrason. Sonochem.*, 2017, **34**, 78–89.

[408] H. Zhang, X. Chen, Z. Li, J. Kou, T. Yu and Z. Zou, *J. Phys. D. Appl. Phys.*, 2007, **40**, 6846–6849.

[409] Z. Wang, Y. Liu, B. Huang, Y. Dai, Z. Lou, G. Wang, X. Zhang and X. Qin, *Phys. Chem. Chem. Phys.*, 2014, **16**, 2758–2774.

[410] R. N. Juine, B. K. Sahu and A. Das, *New J. Chem.*, 2021, **45**, 5845–5854.

[411] G. Wang, B. Huang, Z. Li, Z. Lou, Z. Wang, Y. Dai and M. H. Whangbo, *Sci. Rep.*, 2015, **5**, 1–7.

[412] F. Chen, Y. Cao and D. Jia, *Ceram. Int.*, 2015, **41**, 6645–6652.

[413] Z. Fang, S. Weng, X. Ye, W. Feng, Z. Zheng, M. Lu, S. Lin, X. Fu and P. Liu, *ACS Appl. Mater. Interfaces*, 2015, **7**, 13915–13924.

[414] S. Ummartyotin and Y. Infahsaeng, *Renew. Sustain. Energy Rev.*, 2016, **55**, 17–24.

[415] Y. Q. Yu, L. B. Luo, Z. F. Zhu, B. Nie, Y. G. Zhang, L. H. Zeng, Y. Zhang, C. Y. Wu, L. Wang and Y. Jiang, *CrystEngComm*, 2013, **15**, 1635–1642.

[416] H. wa Yu, J. Wang, X. an Yan, J. Wang, P. fei Cheng and C. juan Xia, *Optik (Stuttg).*, 2019, **185**, 990–996.

[417] J. Mao, J. Zhao, L. Li, T. Chen, Q. Lv and Y. Li, *Chinese J. Phys.*, 2020, **63**, 163–167.

[418] A. Najafi and S. Ghasemi, *J. Alloys Compd.*, 2017, **720**, 423–431.

[419] S. Hajimirzaee, S. Chansai, C. Hardacre, C. E. Banks and A. M. Doyle, *J. Solid State Chem.*, 2019, **276**, 345–351.

[420] Y. Miao, Z. Zhang, Y. Gong, Q. Zhang and G. Yan, *Biosens. Bioelectron.*, 2014, **52**, 271–276.

[421] P. Praus, R. Dvorský, P. Horínková, M. Pospíšil and P. Kovář, *J. Colloid Interface Sci.*, 2012, **377**, 58–63.

[422] B. Hu, H. Cheng, C. Huang, M. K. Aslam, L. Liu, C. Xu, P. Chen, D. Yu and C. Chen, *Solid State Ionics*, 2019, **342**, 115059.

[423] J. Zhu, M. Zhou, J. Xu and X. Liao, *Mater. Lett.*, 2001, **47**, 25–29.

[424] J. Q. Sun, X. P. Shen, K. M. Chen, Q. Liu and W. Liu, *Solid State Commun.*, 2008, **147**, 501–504.

[425] S. K. Panda, A. Datta and S. Chaudhuri, 2007, **440**, 235–238.

[426] D. R. b B. Lalithadevi a, K. Mohan Rao a, *Chem. Phys. Lett.*, 2018, **700**, 74–79.

[427] M. Shkir, A. Khan, M. S. Hamdy and S. AlFaify, *Mater. Res. Express*, 2020, **6**, 1250e6.

[428] D. Xue and K. Kitamura, *Solid State Commun.*, 2002, **122**, 537–541.

[429] J. Koaib, N. Bouguila, H. Abassi, N. Moutia, M. Kraini, A. Timoumi, C. Vázquez-Vázquez, K. Khirouni and S. Alaya, *RSC Adv.*, 2020, **10**, 9549–9562.

[430] G. He, S. Li, K. Yang, J. Liu, P. Liu, L. Zhang and J. Peng, *Minerals*, 2017, **7**, 31.

[431] M. Shkir, S. AlFaify, I. S. Yahia, M. S. Hamdy, V. Ganesh and H. Algarni, *J. Nanoparticle Res.*, 2017, **19**, 328.

[432] N. Dushyantha, N. Batapola, I. M. S. K. Ilankoon, S. Rohitha, R. Premasiri, B. Abeysinghe, N. Ratnayake and K. Dissanayake, *Ore Geol. Rev.*, 2020, **122**, 103521.

[433] X. Song, M.-H. Chang and M. Pecht, *JOM*, 2013, **65**, 1276–1282.

[434] B. Wang, K. Li, J. Liu, T. Zhang, T. Yang and N. Zhang, *Int. J. Hydrogen Energy*, 2024, **61**, 216–225.

[435] W. Xu, G. Bai, E. Pan, D. Li, J. Zhang and S. Xu, *Mater. Des.*, 2024, **238**, 112698.

[436] D. B. Malavekar, V. V. Magdum, S. D. Khot, J. H. Kim and C. D. Lokhande, *J. Alloys Compd.*, 2023, **960**, 170601.

[437] M. M. Abdelrazek, A. E. Hannora, R. M. Kamel, D. E. El Refaay and M. M. El-Desoky, *Mater. Sci. Eng. B*, 2024, **302**, 117215.

[438] J. Ren, J. X. Wu and P. P. Liu, *Phys. B Condens. Matter*, 2023, **652**, 414661 Contents.

[439] A. Tiwari and S. J. Dhoble, *RSC Adv.*, 2016, **6**, 64400–64420.

[440] M. Banuprakash, R. Bairy and M. S. Murari, *Mater. Today Proc.*, , DOI:10.1016/j.matpr.2023.05.679.

[441] V. S. Ganesha Krishna and M. G. Mahesha, *Phys. B Condens. Matter*, 2022, **628**, 413628.

[442] Z. Zhao, L. Zhang, Y. Zhuang, Y. Guo, H. Zhang and W. Jiao, *Vacuum*, 2023, **215**, 112334.

[443] I. M. Mehedi, A. I. Iskanderani, M. S. Islam, H. Shah, V. Shrotriya and M. B. Zaman, *Ceram. Int.*, 2024, **50**, 16131–16141.

[444] J. Sahu, S. Kumar, V. S. Vats, P. A. Alvi, B. Dalela, D. M. Phase, M. Gupta, S. Kumar and S. Dalela, *J. Mater. Sci. Mater. Electron.*, 2022, **33**, 21546–21568.

[445] D. Daksh and Y. K. Agrawal, *Rev. Nanosci. Nanotechnol.*, 2016, **5**, 1–27.

[446] Y. Tong, F. Cao, J. Yang, M. Xu, C. Zheng, X. Zhu, D. Chen, M. Zhang, F. Huang, J. Zhou and L. Wang, *Mater. Chem. Phys.*, 2015, **151**, 357–363.

[447] X. Li, K. Yang, C. Yu, S. Yang, K. Zhang, W. Dai, H. Ji, L. Zhu, W. Huang and S. Ouyang, *J. Mater. Chem. C*, 2019, **7**, 8053–8062.

[448] N. Eryong, L. Donglai, Z. Yunsen, B. Xue, Y. Liang, J. Yong, J. Zhifeng and S. Xiaosong, *Appl. Surf. Sci.*, 2011, **257**, 8762–8766.

[449] G. Rajender and P. K. Giri, *J. Alloys Compd.*, 2016, **676**, 591–600.

[450] K. A. Aly, N. M. Khalil, Y. Algamal and Q. M. A. Saleem, *Mater. Chem. Phys.*, , DOI:10.1016/j.matchemphys.2017.01.059.

[451] C. Demirel and A. Kabutey, , DOI:10.1088/1742-6596/1317/1/012052.

[452] B. Anugop, S. Prasanth, D. Rithesh Raj, T. V. Vineeshkumar, S. Pranitha, V. P. Mahadevan Pillai and C. Sudarsanakumar, *Opt. Mater. (Amst).*, 2016, **62**, 297–305.

[453] B. Choudhury, M. Dey and A. Choudhury, *Int. Nano Lett.*, 2013, **3**, 2–9.

[454] S. Prasanth, P. Irshad, D. R. Raj, T. V. Vineeshkumar, R. Philip and C. Sudarsanakumar, *J. Lumin.*, 2015, **166**, 167–175.

[455] X. Zeng, S. S. Pramana, S. K. Batabyal, S. G. Mhaisalkar, X. Chen and K. B. Jinesh, *Phys. Chem. Chem. Phys.*, 2013, **15**, 6763–6768.

[456] M. Chang, X. L. Cao, X. J. Xu and L. Zhang, *Phys. Lett. Sect. A Gen. At. Solid State Phys.*, 2008, **372**, 273–276.

[457] K. Manojkumar, B. Prasad, Y. Kranthi, J. S. K. Varma, K. Vinay, D. Amaranatha Reddy and K. Subramanyam, *J. Supercond. Nov. Magn.*, 2019, **32**, 2489–2500.

[458] M. L. Frej, E. Valdez, C. B. De Araújo, Y. Ledemi and Y. Messaddeq, *J. Appl. Phys.*, , DOI:10.1063/1.3493239.

[459] G. M. Whyte, C. Awada, P. O. Offor, F. U. Otung, A. Alshoaibi, A. Aljaafari, A. B. C. Ekwealor, M. Maaza and F. I. Ezema, *Opt. Mater. (Amst).*, 2020, **99**, 109556.

[460] S. Jayakiruba, G. Kumar and N. Lakshminarasimhan, *Solid State Sci.*, 2016, **55**, 121–124.

[461] C. C. Yu, .

[462] Virpal, A. Hastir, S. Sharma and R. C. Singh, *Appl. Surf. Sci.*, 2016, **372**, 57–62.

[463] N. Baraz, İ. Yücedağ, Y. Azizian-Kalandaragh and Ş. Altındal, *J. Mater. Sci. Mater. Electron.*, 2017, **28**, 1315–1321.

[464] M. Mehedi Hassan, W. Khan, A. Azam and A. H. Naqvi, *J. Ind. Eng. Chem.*, 2015, **21**, 283–291.

[465] C. C. Vidyasagar and Y. Arthoba Naik, *Arab. J. Chem.*, 2016, **9**, 507–510.

[466] P. V. R. B. Sreenivasulu, S. Venkatramana Reddy, *J. Nanotechnol. Mater. Sci.*, 2017, **4**, 1–8.

[467] P. Raja, P. Rajkumar, P. Jegatheesan, A. S. Amalraj and A. J. Lourdu Rajah, *J. Indian Chem. Soc.*, 2023, **100**, 100855.

[468] A. Kapoor, N. Kumar, N. Aggarwal, V. Sharma, J. K. Sharma, S. K. Sharma and S. Kumar, *Phys. B Condens. Matter*, 2023, **652**, 414660.

[469] Y. Chen, G. F. Huang, W. Q. Huang, B. S. Zou and A. Pan, *Appl. Phys. A Mater. Sci. Process.*, 2012, **108**, 895–900.

[470] M. Kuppayee, G. K. V. Nachiyar and V. Ramasamy, *Mater. Sci. Semicond. Process.*, 2012, **15**, 136–144.

[471] R. Balakarthikeyan, A. Santhanam, S. Vinoth, A. A. Abdeltawab, S. Z. Mohammady, M. Ubaidullah, S. F. Shaikh, M. Shahzad, M. A. Manthrammel and M. Shkir, *Mater. Sci. Eng. B*, 2023, **289**, 116213.

[472] Q. Zhang, S. Ma, R. Zhang, K. Zhu, Y. Tie and S. Pei, *J. Alloys Compd.,* 2019, **807**, 151650.

[473] Y. H. Lee, B. K. Ju, M. H. Song, T. S. Hahn, M. H. Oh and D. H. Kim, *J. Appl. Phys.*, 1996, **79**, 8717–8724.

[474] Q. Fang, C. Huang, Y. Zhang, C. Zhao, S. Cai, S. Li and Y. Hang, *Opt. Laser Technol.*, 2023, **159**, 109021.

[475] M. J. E, M. A. Manthrammel, P. A. Subha, M. Shkir and S. A. Alfaify, *Luminescence*, , DOI:10.1002/bio.4577.

[476] S. Cholan, N. Shanmugam, N. Kannadasan, K. Sathishkumar and K. Deivam, *J. Mater. Res. Technol.*, 2014, **3**, 222–227.

[477] D. Nath, F. Singh and R. Das, *Mater. Chem. Phys.*, 2020, **239**, 122021.

[478] A. A. Othman, M. A. Osman, M. A. Ali and E. M. M. Ibrahim, *Mater. Sci. Eng. B Solid-State Mater. Adv. Technol.*, 2021, **270**, 115195.

[479] I. S. Yahia, M. Shkir, S. AlFaify, V. Ganesh, H. Y. Zahran and M. Kilany, *Mater.*

Sci. Eng. C, 2017, **72**, 472–480.

[480] M. Shkir, I. S. Yahia and A. M. A. Al-Qahtani, *Mater. Chem. Phys.*, 2016, **184**, 12–22.

[481] K. Vijai Anand, *J. Clust. Sci.*, 2021, **32**, 155–161.

[482] H. Takashima, K. Ueda and M. Itoh, *Appl. Phys. Lett.*, 2006, **89**, 1–4.

[483] F. Ramos-Brito, M. García-Hipólito, R. Martínez-Martínez, E. Martínez-Sánchez and C. Falcony, *J. Phys. D. Appl. Phys.*, , DOI:10.1088/0022-3727/37/5/L01.

[484] Y. Jin, Y. Hu, L. Chen, Y. Fu, Z. Mu, T. Wang and J. Lin, *J. Alloys Compd.*, 2014, **616**, 159–165.

[485] T. Q. Hoa Tran, M. H. Hoang, T. A. T. Do, A. T. Le, T. H. Nguyen, T. D. Nguyen and M. T. Man, *J. Lumin.*, 2021, **237**, 118162.

[486] V. Reddy Prasad, S. Damodaraiah, S. N. Devara and Y. C. Ratnakaram, *J. Mol. Struct.*, 2018, **1160**, 383–392.

[487] Y. Su, X. Ji and Y. He, *Adv. Mater.*, 2016, **28**, 10567–10574.

[488] Z. Tang, X. Li, Y. Zhao, L. Chen, F. Ren and S. Tang, *Phys. Lett. A*, 2023, **483**, 129042.

[489] O. El Khouja, I. Boukhoubza, I. Derkaoui, I. Assahsahi, M. Achehboune, A. Talbi, Y. Khaaissa, M. Makha, M. Ebn Touhami and K. Nouneh, *Mater. Chem. Phys.*, 2024, **313**, 128707.

[490] A. G. Abd-Elrahim, D.-M. Chun, E. M. M. Ibrahim and M. A. Ali, *Phys. B Condens. Matter*, 2023, **670**, 415408.

[491] C. Bozkaplan, Y. S. Ocak and K. Akkilic, *Opt. Mater. (Amst).*, 2021, **117**, 111126.

[492] H. Liu, Z. Chen, X. Yang, S. Hong, Z. Zhang, Z. Yang and J. Cai, *J. Electroanal. Chem.*, 2023, **932**, 117252.

[493] T. Mori, *Solid State Ionics*, 2002, **154–155**, 461–466.

[494] M. V. Zdorovets and A. L. Kozlovskiy, *Vacuum*, 2019, **168**, 108838.

[495] S. K. Gupta, K. Sudarshan and R. M. Kadam, *Mater. Today Commun.*, 2021, **27**, 102277.

[496] W. F. Krupke, *Phys. Rev.*, 1966, **145**, 325–337.

[497] P. Sakthivel, P. Kumar, M. Dhavamurthy, A. Thirumurugan and S. Sridhar, *J. Mol. Struct.*, 2023, **1288**, 135723.

[498] H.-Q. Xie, Y. Chen, W.-Q. Huang, G.-F. Huang, P. Peng, L. Peng, T.-H. Wang and Y. Zeng, *Chinese Phys. Lett.*, 2011, **28**, 027806.

[499] S. Shahi, S. Saeednia, P. Iranmanesh and M. Hatefi Ardakani, *Luminescence*, 2021, **36**, 180–191.

[500] M. Riazian, *Phys. Scr.*, 2023, **98**, 065956.

[501] L. Tairi, Y. Messai, R. Bourzami, A. Chetoui, M. Sebais, T. Tahraoui, T. Bouarroudj, H. Bezzi and D. E. Mekki, *Phys. B Condens. Matter*, 2022, **631**, 413713.

[502] B. Poornaprakash, U. Chalapathi, M. Reddeppa and S.-H. Park, *Superlattices Microstruct.*, 2016, **97**, 104–109.

[503] O. Brafman and S. S. Mitra, *Phys. Rev.*, 1968, **171**, 931–934.

[504] J. Schneider and R. D. Kirby, *Phys. Rev. B*, 1972, **6**, 1290–1294.

[505] J. Díaz-Reyes, R. S. Castillo-Ojeda, R. Sánchez-Espíndola, M. Galván-Arellano and O. Zaca-Morán, *Curr. Appl. Phys.*, 2015, **15**, 103–109.

[506] Z. M. Gibbs, A. LaLonde and G. J. Snyder, *New J. Phys.*, 2013, **15**, 075020.

[507] Q. Zhu, J. Lu, Y. Wang, F. Qin, Z. Shi and C. Xu, *Sci. Rep.*, 2016, **6**, 36194.

[508] Q.-C. Sun, L. Yadgarov, R. Rosentsveig, G. Seifert, R. Tenne and J. L. Musfeldt, *ACS Nano*, 2013, **7**, 3506–3511.

[509] P. Li, X. Wang, X. Zhang, L. Zhang, X. Yang and B. Zhao, *Front. Chem.*, , DOI:10.3389/fchem.2019.00144.

[510] J. Hasanzadeh, A. Taherkhani and M. Ghorbani, *Chinese J. Phys.*, 2013, **51**, 540–550.

[511] K. Joshi, M. Rawat, S. K. Gautam, R. G. Singh, R. C. Ramola and F. Singh, *J. Alloys Compd.*, 2016, **680**, 252–258.

[512] J. Wallentin, K. Mergenthaler, M. Ek, L. R. Wallenberg, L. Samuelson, K. Deppert, M.-E. Pistol and M. T. Borgström, *Nano Lett.*, 2011, **11**, 2286–2290.

[513] A. Goktas, *Appl. Surf. Sci.*, 2015, **340**, 151–159.

[514] M. M. El-Desoky, G. A. El-Barbary, D. E. El Refaey and F. El-Tantawy, *Optik (Stuttg).*, 2018, **168**, 764–777.

[515] A. Goudarzi, G. M. Aval, S. S. Park, M. C. Choi, R. Sahraei, M. H. Ullah, A. Avane and C. S. Ha, *Chem. Mater.*, 2009, **21**, 2375–2385.

[516] H.-Y. Lu, S.-Y. Chu and S.-S. Tan, *J. Cryst. Growth*, 2004, **269**, 385–391.

[517] Z. Ma, F. Ren, Y. Deng and A. A. Volinsky, *Optik (Stuttg).*, 2020, **219**, 165204.

[518] B. Choudhury, B. Borah and A. Choudhury, *Photochem. Photobiol.*, 2012, **88**, 257–264.

[519] X. Chen, Q. Xie and J. Li, *Ceram. Int.*, 2020, **46**, 2309–2316.

[520] H. Reza, A. Norozi, M. Hossein and A. Semnani, 2009, **162**, 674–681.

[521] P. K. Labhane, G. H. Sonawane and S. H. Sonawane, *Green Process. Synth.*, 2018, **7**, 360–371.

[522] A. Baig, A. Baig, V. Rathinam and J. Palaninathan, *J. Iran. Chem. Soc.*, , DOI:10.1007/s13738-020-02000-2.

[523] D. A. Links, 2011, 14937–14945.

[524] A. M. El-Khawaga, A. Zidan and A. I. A. A. El-Mageed, *J. Mol. Struct.*, 2023, **1281**, 135148.

[525] S. K. Dubey, A. Dey, G. Singhvi, M. M. Pandey, V. Singh and P. Kesharwani, *Colloids Surfaces B Biointerfaces*, 2022, **214**, 112440.

[526] A. Lassoued and J. F. Li, *J. Mol. Struct.*, 2022, **1262**, 133021.

[527] B. Mahipal, N. Venkatesh, D. R. Kumar and P. Veerasomaiah, *J. Mol. Struct.*, 2023, **1277**, 134843.

[528] K. Tamilarasi, P. Aji Udhaya and M. Meena, *Mater. Today Proc.*, 2022, **64**, 1671–1678.

[529] L.-C. Cheng, X. Jiang, J. Wang, C. Chen and R.-S. Liu, *Nanoscale*, 2013, **5**, 3547.

[530] B. S. Yadav, A. C. Badgujar and S. R. Dhage, in *Smart Multifunctional Nano-inks*, Elsevier, 2023, pp. 249–276.

[531] N. A. Basher and A. Abdulkhabeer, *Mater. Today Proc.*, 2022, **49**, 2842–2850.

[532] K. Kristinaitytė, L. Dagys, J. Kausteklis, V. Klimavicius, I. Doroshenko, V. Pogorelov, N. R. Valevičienė and V. Balevicius, *J. Mol. Liq.*, 2017, **235**, 1–6.

[533] X. Feng, L. Gu, N. Wang, Q. Pu and G. Liu, *J. Mater. Sci. Technol.*, 2023, **135**, 54–64.

[534] C. Solans and M. J. García-Celma, in *Cosmetic Science and Technology*, Elsevier, 2017, pp. 507–518.

[535] S. K. Dhoke, *Results Chem.*, 2023, **5**, 100771.

[536] T. A. Saleh, *Environ. Technol. Innov.*, 2020, **20**, 101067.

[537] C. A. Pawar, A. K. Sharma, N. R. Prasad, S. S. Suryawanshi, G. M. Nazeruddin, V. S. Shaikh, A. N. Kulkarni, A. G. Al-Sehemi and Y. I. Shaikh, *Curr. Res. Green Sustain. Chem.*, 2022, **5**, 100311.

[538] T. Takata and K. Domen, *J. Phys. Chem. C*, 2009, **113**, 19386–19388.

[539] S. Ramu and R. P. Vijayalakshmi, *J. Supercond. Nov. Magn.*, 2017, **30**, 1921–1925.

[540] M. S. Khan, L. Shi, B. Zou and H. Ullah, *Optik (Stuttg).*, 2020, **204**, 164162.

[541] H. Hu and W. Zhang, *Opt. Mater. (Amst).*, 2006, **28**, 536–550.

[542] C. S. Pathak, V. Agarwala and M. K. Mandal, *Phys. B Condens. Matter*, 2012, **407**, 3309–3312.

[543] H. Hedjar, S. Meskine, A. Boukortt, H. Bennacer and M. R. Benzidane, *Comput. Condens. Matter*, 2022, **30**, e00632.

[544] N. T. Hien, N. X. Ca, N. T. Kien, N. T. Luyen, P. V. Do, L. D. Thanh, H. T. Van, S. Bharti, Y. Wang, N. T. M. Thuy and P. M. Tan, *J. Phys. Chem. Solids*, 2020, **147**, 109638.

[545] M. Dharani Devi, A. Vimala Juliet, R. Ade, M. Thirumoorthi, P. Diana, S. Saravanakumar, V. Ganesh, Y. Bitla and H. Algarni, *Mater. Sci. Semicond. Process.*, 2022, **144**, 106572.

[546] A. J. Jebathew, M. Karunakaran, K. D. Arun Kumar, S. Valanarasu, V. Ganesh, M. Shkir, I. S. Yahia, H. Y. Zahran and A. Kathalingam, *Phys. B Condens. Matter*, 2019, **574**, 411674.

[547] A. J. Jebathew, M. Karunakaran, M. Shkir, H. Algarni, S. AlFaify, A. Khan, N. Alotaibi and T. Alshahrani, *Opt. Mater. (Amst).*, 2021, **122**, 111649.

[548] R. Kumar and S. K. Mishra, in *Ceramic Science and Engineering*, Elsevier, 2022, pp. 263–294.

[549] N. SUGANTHI and K. PUSHPANATHAN, *Trans. Nonferrous Met. Soc. China*, 2019, **29**, 811–820.

[550] N. Shanmugam, S. Cholan, N. Kannadasan, K. Sathishkumar and G. Viruthagiri, *Solid State Sci.*, 2014, **28**, 55–60.

[551] L. A. González, V. Sánchez-Cardona, J. Escorcia-García and M. A. Meléndez-Lira, *Ceram. Int.*, , DOI:10.1016/j.ceramint.2023.01.144.

[552] P. Kumari, K. P. Misra, S. Samanta, A. Rao, A. Bandyopadhyay and S. Chattopadhyay, *J. Lumin.*, 2022, **251**, 119258.

[553] L. Wang, S. Huang and Y. Sun, *Appl. Surf. Sci.*, 2013, **270**, 178–183.

[554] A. K. Kole and P. Kumbhakar, *RESULTS Phys.*, 2012, **2**, 150–155.

[555] S. D. Scott and H. L. Barnes, *Geochim. Cosmochim. Acta*, 1972, **36**, 1275–1295.

[556] Y. Li, W. Tan and Y. Wu, *J. Eur. Ceram. Soc.*, , DOI:10.1016/j.jeurceramsoc.2019.12.045.

[557] Q. Xiong, J. Wang, O. Reese, L. C. Lew Yan Voon and P. C. Eklund, *Nano Lett.*, 2004, **4**, 1991–1996.

[558] N. Prasad and B. Karthikeyan, *Nanoscale*, 2019, **11**, 4948–4958.

[559] K. R. Bindu and E. I. Anila, *J. Lumin.*, 2017, **192**, 123–128.

[560] M. Jothibas, C. Manoharan, S. Johnson Jeyakumar, P. Praveen, I. Kartharinal Punithavathy and J. Prince Richard, *Sol. Energy*, 2018, **159**, 434–443.

[561] P. K. Labhane, G. H. Sonawane and S. H. Sonawane, 2018, 360–371.

[562] M. Shamsipur and H. Reza, *Spectrochim. ACTA PART A Mol. Biomol. Spectrosc.*, 2014, **122**, 260–267.

[563] N. Hossain, H. Mobarak, M. Akter, A. Islam, A. Hossain, F. Tuz and M.

Asaduzzaman, *Results Eng.*, 2023, **19**, 101347.

[564] V. Pillay, R. Remya, S. Parani, J. V Rajendran, R. Maluleke, T. C. Lebepe, O. A. Aladesuyi, S. Thomas and O. S. Oluwafemi, *Mater. Sci. Eng. B*, 2023, **297**, 116726.

[565] S. F. Hathot, S. I. Abbas, H. A. T. AlOgaili and A. A. Salim, *Optik (Stuttg).*, , DOI:10.1016/j.ijleo.2022.169056.

[566] K. O. Olumurewa, B. Taleatu, V. A. Owoeye, O. Fasakin and M. A. Eleruja, *Appl. Surf. Sci. Adv.*, 2023, **13**, 100370.

[567] M. Khodamorady and K. Bahrami, *Heliyon*, 2023, **9**, e16397.

[568] M. H. Majeed, M. Aycibin and A. G. Imer, *Optik (Stuttg).*, 2022, **258**, 168949.

[569] A. Madani, M. Alghamdi, B. Alamri and S. Althobaiti, *Opt. Mater. (Amst).*, 2023, **137**, 113480.

[570] N. Anh Tien, V. O. Mittova, B. V. Sladkopevtsev, V. Quang Mai, I. Y. Mittova and B. Xuan Vuong, *Solid State Sci.*, 2023, **138**, 107149.

[571] R. Kırkgeçit, H. Özlü Torun, F. Kılıç Dokan and E. Öztürk, *J. Rare Earths*, 2022, **40**, 1619–1627.

[572] M. Shkir and T. Alshahrani, *Sensors Actuators A Phys.*, 2023, **351**, 114169.

[573] L. S. Archana and D. N. Rajendran, *Mater. Today Proc.*, 2021, **41**, 461–467.

[574] C. Li, R. Hu, T. Zhou, H. Wu, K. Song, X. Liu and R. Wang, *Mater. Lett.*, 2014, **124**, 81–84.

[575] R. Ram Prasanth, P. Manikandan, J. Muthukumar, K. Sowmiya, E. Veeramanipriya, R. Jayasri and P. Dhivya, *Mater. Today Proc.*, 2023, **74**, 923–933.

[576] B. Mandal, R. Roy and P. Mitra, *J. Alloys Compd.*, 2021, **879**, 160432.

[577] T. M. Abdalkreem, H. C. Swart and R. E. Kroon, *Nano-Structures and Nano-Objects*, 2023, **35**, 101026.

[578] S. . Scott and H. . Barnes, *Geochim. Cosmochim. Acta*, 1972, **36**, 1275–1295.

[579] N. SUGANTHI and K. PUSHPANATHAN, *Surf. Rev. Lett.*, 2018, **25**, 1850063.

[580] R. M. Navarro, F. del Valle, J. A. Villoria de la Mano, M. C. Álvarez-Galván and J. L. G. Fierro, 2009, pp. 111–143.

[581] M. Dell'Edera, C. Lo Porto, I. De Pasquale, F. Petronella, M. L. Curri, A. Agostiano and R. Comparelli, *Catal. Today*, 2021, **380**, 62–83.

[582] C. Liu, J. Bai, S. Zhang, Z. Yang and M. Luo, *J. Phys. Conf. Ser.*, 2021, **2011**, 012049.

[583] Y. Sun, W. Zhang, Q. Li, H. Liu and X. Wang, *Adv. Sens. Energy Mater.*, 2023, **2**, 100069.

[584] C. B. Ong, L. Y. Ng and A. W. Mohammad, *Renew. Sustain. Energy Rev.*, 2018, **81**,

536–551.

[585] O. K. Dalrymple, E. Stefanakos, M. A. Trotz and D. Y. Goswami, *Appl. Catal. B Environ.*, 2010, **98**, 27–38.

[586] C.-C. Wang, J.-R. Li, X.-L. Lv, Y.-Q. Zhang and G. Guo, *Energy Environ. Sci.*, 2014, **7**, 2831–2867.

[587] M. Pavel, C. Anastasescu, R.-N. State, A. Vasile, F. Papa and I. Balint, *Catalysts*, 2023, **13**, 380.

[588] N. Suganthi and K. Pushpanathan, *Int. J. Environ. Sci. Technol.*, 2019, **16**, 3375–3388.

[589] I. Ahmad, M. S. Akhtar, M. F. Manzoor, M. Wajid, M. Noman, E. Ahmed, M. Ahmad, W. Q. Khan and A. M. Rana, *J. Rare Earths*, 2021, **39**, 440–445.